

SYNTHESIS, PHOTOPHYSICS, REVERSE SATURABLE ABSORPTION, AND
PHOTODYNAMIC THERAPY OF IRIDIUM(III) COMPLEXES BEARING DIFFERENT
DEGREES OF π -CONJUGATION ON THE LIGANDS

A Dissertation
Submitted to the Graduate Faculty
of the
North Dakota State University
of Agriculture and Applied Science

By

Bingqing Liu

In Partial Fulfillment of the Requirements
for the Degree of
DOCTOR OF PHILOSOPHY

Major Department:
Chemistry and Biochemistry

February 2019

Fargo, North Dakota

North Dakota State University
Graduate School

Title

Synthesis, Photophysics, Reverse Saturable Absorption, and Photodynamic
Therapy of Iridium(III) Complexes Bearing Different Degrees of π -
conjugation on The Ligands

By

Bingqing Liu

The Supervisory Committee certifies that this *disquisition* complies with North Dakota
State University's regulations and meets the accepted standards for the degree of

DOCTOR OF PHILOSOPHY

SUPERVISORY COMMITTEE:

Dr. Wenfang Sun

Chair

Dr. Gregory Cook

Dr. Pinjing Zhao

Dr. D.K., Srivastava

Dr. Sanku Mallik

Approved:

02/27/2019

Date

Dr. Gregory Cook

Department Chair

ABSTRACT

Octahedral d^6 iridium(III) complexes possess rich photophysical properties. The most distinct photophysical properties of the Ir(III) complexes are their high triplet excited-state formation quantum yields, long-lived triplet excited states, and feasible structural modifications. To better understand the impact of ligand π -conjugation on the photophysics and reverse saturable absorption (RSA) or PDT of the Ir(III) complexes, six series of Ir(III) complexes bearing various bidentate or terdentate ligands were designed and synthesized in this dissertation.

In Chapter 1, the photophysical principles, typical electronic transitions in Ir(III) complexes, the prototypes of the tris-bidentate and bis-terdentate Ir(III) complexes, the state-of-art on exploring Ir(III) complexes for RSA and PDT, and the materials design criteria are reviewed.

In Chapters 2 and 3, sixteen cyclometalated cationic Ir(III) complexes were synthesized and investigated to understand how the benzannulation site on diimine ligands influences the characteristics of the excited states of these complexes. The site-dependent benzannulation influenced the spectral feature and intensity of the triplet transient absorption (TA) and T_1 lifetimes, and their RSA strength.

In Chapter 4, ten 2-phenylpyridine based Ir(III) complexes with varied degrees of π -conjugation and sites of benzannulation were synthesized. Benzannulation at the different sites of 2-phenylpyridine exerted a different effect on the energies of the S_1 and T_1 excited states, the TA spectral features, and the RSA performances of the complexes.

In Chapter 5, the synthesis, photophysics, and RSA of three Ir(III) complexes with different degrees of π -conjugation on the diimine ligands were discussed. The impact of this structural variation on the RSA at 532 nm was demonstrated.

In Chapter 6, five Ir(III) complexes bearing terpyridine-capped fluorenyl bridging ligands and different terminal terdentate ligands were investigated to reveal the effects of different terminal ligands on the S_1 and T_1 excited states. Their *in vitro* theranostic PDT effects toward the SKMEL28 cells were evaluated.

In Chapter 7, the photophysics and *in vitro* PDT studies of five neutral Ir(III) complexes incorporating BODIPY-substituted *N*-heterocyclic carbene (NHC) ligands were studied. The attachment position of the BODIPY substituent did not alter the photophysical properties significantly but changed the dark- and photo- cytotoxicity of these complexes toward SKMEL28 cells.

ACKNOWLEDGEMENTS

This dissertation was personally and professionally supported by many people who I would like to express my deep appreciation.

Firstly, I sincerely appreciate my advisor, Dr. Wenfang Sun, for providing me the opportunity to pursue my Ph.D. dream in her group. Her inspiration, suggestions, guidance, and constructive comments encouraged me to go through the difficulties in my research and helped me to complete this dissertation.

Secondly, I deeply appreciate my committee members Dr. Pinjing Zhao, Dr. Gregory Cook, Dr. D. K. Srivastava, Dr. Jayaraman Sivaguru, and Dr. Sanku Mallik for taking the time out of their busy schedule to attend my committee meetings and for their precious suggestions and affirmative comments. I would like to thank my course instructors for their valuable instructions. I am very grateful to Dr. Svetlana Killina, Levi Lystrom, and Mohammed Javed for the DFT calculations they performed for all of my research projects. I am also very grateful to Dr. Sherri McFarland at the University of North Carolina at Greensboro and Susan Monro at Acadia University for the photobiological studies they carried out for the projects described in Chapters 6 and 7. I would like to thank Dr. Alex Parent for training me to use the cyclic voltammetry. I also want to thank Dr. Angel Ugrinov for helping me using the mass spectrometer and analyzing the crystal structures. I would like to thank Amy Kain and Cole Larson for their kind helps in scheduling my seminars and chemical ordering. Many thanks to my labmates Wei Xu and Wan Xu for them to create an active and fun lab environment. I would also like to thank my previous labmates: Dr. Li Wang, Dr. Hui Li, Dr. Xiaolin Zhu, Chengzhe Wang, Senqiang Zhu, and Liya Sun, for their support and accompany.

I would like to acknowledge the National Science Foundation, the U.S. Army Research Laboratory, and the Department of Chemistry and Biochemistry at North Dakota State University for supporting me as a research assistant or teaching assistant during my time at NDSU.

Last, but not least, I cannot say enough thank you to my wife, Qiaobin Li, and my parents. Without their constant love, encouragement, and support in these years , I could not have finished my Ph.D. study smoothly.

DEDICATION

This thesis is dedicated to my parents.

TABLE OF CONTENTS

ABSTRACT.....	iii
ACKNOWLEDGEMENTS.....	v
DEDICATION.....	vii
LIST OF TABLES.....	xiv
LIST OF FIGURES.....	xvii
LIST OF SCHEMES.....	xxiv
LIST OF CHARTS.....	xxv
1. INTRODUCTION.....	1
1.1. Basic photophysical concepts.....	2
1.1.1. Light.....	2
1.1.2. The absorption of light in materials.....	3
1.1.3. Fluorescence and phosphorescence.....	6
1.1.4. Heavy atom effect.....	8
1.1.5. RSA.....	8
1.1.6. PDT.....	10
1.2. Basic photophysics and representative examples for Ir(III) complexes.....	11
1.2.1. Photophysics of Ir(III) complexes.....	11
1.2.2. Three typical prototypes of Ir(III) complexes.....	13
1.2.3. Cyclometalated Ir(III) complexes with different π -conjugation on ligands.....	15
1.2.4. Bis-terdentate Ir(III) complexes.....	21
1.3. Cyclometalated Ir(III) complexes for RSA applications.....	27
1.4. Applications of heteroleptic Ir(III) complexes in PDT.....	36
1.5. Synthesis of Ir(III) complexes.....	40
1.6. Designing criteria for reverse saturable absorbers.....	43

1.7. Designing criteria for photosensitizer in PDT research	44
1.8. Objectives of my dissertation	45
1.9. References	46
2. TUNING THE GROUND STATE AND EXCITED STATE PROPERTIES OF MONO-CATIONIC IRIIDIUM(III) COMPLEXES BY VARYING THE SITE OF BENZANNULATON ON DIIMINE LIGAND.....	52
2.1. Introduction	52
2.2. Experimental section	54
2.2.1. Materials and synthesis.....	54
2.2.2. Photophysical studies	59
2.2.3. Computational methods.....	60
2.2.4. Electrochemical measurements	61
2.3. Results and discussion.....	61
2.3.1. Electronic absorption.....	61
2.3.2. Electrochemical properties	70
2.3.3. Photoluminescence	72
2.3.4. Transient absorption (TA).....	75
2.4. Conclusion.....	80
2.5. References	81
3. IMPACT OF BENZANNULATION SITE AT THE DIIMINE (N^N) LIGAND ON THE PHOTOPHYSICS AND REVERSE SATURABLE ABSORPTION OF CYCLOMETALATED MONOCATIONIC IRIIDIUM(III) COMPLEXES	87
3.1. Introduction	87
3.2. Experimental section	90
3.2.1. Materials and synthesis.....	90
3.2.2. Photophysical studies	94
3.2.3. Nonlinear transmission measurement.....	95

3.2.4. Computational methods.....	96
3.3. Results and discussion.....	96
3.3.1. Electronic absorption.....	96
3.3.2. Photoluminescence	114
3.3.3. Transient absorption (TA).....	119
3.3.4. Reverse saturable absorption.....	123
3.4. Conclusions	125
3.5. References	126
4. EFFECTS OF VARYING THE BENZANNULATION SITE AND π CONJUGATION OF THE CYCLOMETALATING LIGAND ON THE PHOTOPHYSICS AND REVERSE SATURABLE ABSORPTION OF MONOCATIONIC IRIIDIUM(III) COMPLEXES	131
4.1. Introduction	131
4.2. Experimental section	134
4.2.1. Materials and synthesis.....	134
4.2.2. Photophysical and nonlinear transmission measurements	139
4.2.3. Quantum chemistry calculations	140
4.3. Results and discussion.....	141
4.3.1. Effect of benzannulation on the ground-state equilibrium geometry.....	141
4.3.2. Electronic absorption.....	143
4.3.3. Photoluminescence	158
4.3.4. TA.....	163
4.3.5. RSA	167
4.4. Conclusion.....	169
4.5. References	170

5. MONOCATIONIC IRIDIUM(III) COMPLEXES WITH FAR-RED CHARGE TRANSFER ABSORPTION AND NEAR-IR EMISSION: SYNTHESIS, PHOTOPHYSICS, AND REVERSE SATURABLE ABSORPTION	175
5.1. Introduction	175
5.2. Experimental section	177
5.2.1. Materials and synthesis.....	177
5.2.2. General procedure for the synthesis of 5-1 – 5-3	178
5.2.3. Photophysical and nonlinear transmission measurements	180
5.2.4. Computational methodology	181
5.3. Results and discussion.....	181
5.3.1. Electronic absorption.....	181
5.3.2. Photoluminescence	188
5.3.3. Transient absorption (TA)	190
5.3.4. Reverse saturable absorption.....	192
5.4. Conclusions	194
5.5. References	195
6. PHOTOPHYSICAL AND PHOTOBIOLOGICAL PROPERTIES OF DINUCLEAR IRIDIUM(III) BIS-TRIDENTATE COMPLEXES	200
6.1. Introduction	200
6.2. Experimental section	204
6.2.1. Synthesis and characterizations	204
6.2.2. Photophysical studies	208
6.2.3. Singlet oxygen quantum yields	209
6.2.4. DFT calculations	209
6.2.5. Photobiological activity studies.....	211
6.3. Results and discussion.....	211

6.3.1. Electronic absorption.....	211
6.3.2. Photoluminescence	215
6.3.3. Transient absorption	218
6.3.4. Singlet oxygen generation	220
6.3.5. Cytotoxicity and photocytotoxicity	222
6.3.6. Cellular imaging	226
6.3.7. DNA interactions.....	229
6.4. Conclusions	232
6.5. References	233
7. SYNTHESIS, NEUTRAL IRIDIUM(III) COMPLEXES BEARING BODIPY-SUBSTITUTED <i>N</i>-HETEROCYCLIC CARBENE (NHC) LIGANDS: SYNTHESIS, PHOTOPHYSICS, AND PHOTOBIOLOGICAL ACTIVITIES	241
7.1. Introduction	241
7.2. Experimental	245
7.2.1. Materials and synthesis.....	245
7.2.2. Synthesis of precursor compounds 2 – 5 and 8 – 10.....	247
7.2.3. General synthetic procedure for ligands L7-1 – L7-5	249
7.2.4. General synthetic procedure for iridium complexes 7-1 – 7-5.....	251
7.2.5. Photophysical studies	253
7.2.6. Computational methodology	254
7.2.7. Cellular assays	255
7.2.8. Cell culture	255
7.2.9. Cytotoxicity and photocytotoxicity cell assays	256
7.2.10. Confocal microscopy.....	257
7.2.11. Bacterial survival assays.....	258
7.2.12. Measurement of ROS in SKMEL-28 cells.....	260

7.3. Results and discussion.....	261
7.3.1. Electronic absorption.....	261
7.3.2. Photoluminescence	268
7.3.3. Transient absorption (TA).....	272
7.3.4. Singlet oxygen generation	273
7.3.5. Cytotoxicity and photocytotoxicity toward cancer cells	274
7.3.6. Cytotoxicity and photocytotoxicity toward bacteria	278
7.4. Conclusions	279
7.5. References	281

LIST OF TABLES

<u>Table</u>	<u>Page</u>
2.1. Electronic absorption, emission, and triplet excited-state absorption parameters for complexes 2-1 – 2-6.	62
2.2. Natural transition orbitals (NTOs) representing singlet transitions contributing to the low-energy absorption bands of complexes 2-1 – 2-6 in CH ₂ Cl ₂	63
2.3. Characterization of molecular orbitals for the first five HOMOs and LUMOs of complexes 2-1 – 2-6 in CH ₂ Cl ₂	64
2.4. HOMO and LUMO of 2-1 – 2-6 in CH ₂ Cl ₂	66
2.5. Percentage of HOMO-LUMO transition contributing to S ₁ of complexes 2-1 – 2-6 calculated in CH ₂ Cl ₂ solvent.	68
2.6. Electrochemical properties of Ir(III) complexes 2-1 – 2-6.	72
2.7. NTOs representing transitions corresponding to the triplet emission of 2-1 to 2-6 in CH ₂ Cl ₂ calculated by TDDFT-based Δ SCF.	74
3.1. Electronic absorption, emission, and triplet excited-state absorption parameters for complexes 3-1–3-10.	100
3.2. NTOs of the low-energy transitions contributing to the 400–500 nm absorption band of complexes 3-1 – 3-10 in CH ₂ Cl ₂	100
3.3. NTOs for the optical transitions at 300 – 400 nm for 3-1 – 3-10 in CH ₂ Cl ₂ . The isovalue is set to 0.03.	103
3.4. NTOs for the high energy optical transitions (<300 nm) of 3-1 – 3-10 in CH ₂ Cl ₂ . The isovalue is set to 0.03.	108
3.5. HOMOs and LUMOs of 3-1 – 3-10 in CH ₂ Cl ₂ and the contribution of HOMO→LUMO transition to the S ₁ state.	110
3.6. Emission characteristics of complexes 3-1 – 3-10 in different solvents at room temperature.	115
3.7. NTOs representing the lowest triplet transitions (T ₁) of 3-1 – 3-10 in CH ₂ Cl ₂	116
3.8. NTOs for the second triplet excited states (T ₂) of 3-1 – 3-10 in CH ₂ Cl ₂	119
3.9. Ground-state absorption cross sections (σ_0) and Δ OD values of 3-1 – 3-10 at 532 nm.	124

4.1. Geometrical characteristics of complexes 4-1 – 4-10: bond length (B), dihedral angle (D) and bond angle (A) between atoms numbered in the Chart 4-1.	143
4.2. Electronic absorption, emission, and excited-state absorption parameters for complexes 4-1 – 4-10.	144
4.3. NTOs contributing to the lowest-energy singlet transitions (S_1) of complexes 4-1 – 4-10 in CH_2Cl_2	146
4.4. NTOs representing singlet transitions responsible for the low-energy absorption bands of complexes 4-1 – 4-10 in CH_2Cl_2	146
4.5. NTOs representing singlet transitions responsible for the medium energy absorption bands of complexes 4-1 – 4-10 in CH_2Cl_2	149
4.6. NTOs representing singlet transitions responsible for the main absorption bands of complexes 4-1 – 4-10 in CH_2Cl_2	152
4.7. Electron density distribution plots for HOMOs and LUMOs of complexes 4-1 – 4-10 in CH_2Cl_2 and the percentage contribution of the HOMO-LUMO transition to the S_1 excited state.	154
4.8. Emission characteristic of complexes 4-1 – 4-10 in different solvents at room temperature. ^a	161
4.9. Spin-density for the single and triplet SCF calculations for 4-1 – 4-10. The red translucent isosurface represents the electron distribution, whereas the blue translucent isosurface represents the hole for the transition from T_1 to S_0	161
4.10. NTOs representing the triplet transitions contributing to the emission of complexes 4-1 – 4-10 in CH_2Cl_2^a . The NTOs were calculated by TDDFT using the triplet minimum-energy geometry optimized by unrestricted DFT as described in the quantum chemistry calculations section.	163
4.11. Ground-state absorption cross sections (σ_0) and ΔOD values of 4-1 – 4-10 in CH_3CN at 532 nm	168
5.1. Photophysical properties of complexes 5-1 – 5-3.	182
5.2. Natural transition orbitals (NTOs) corresponding to the transitions contributing to the low-energy absorption bands of 5-1 – 5-3 in CH_2Cl_2	184
5.3. Natural transition orbitals (NTOs) representing singlet transitions contributing to the medium energy transitions of 5-1 – 5-3 in CH_2Cl_2	185
5.4. Natural transition orbitals (NTOs) representing singlet transitions contributing to the high energy transitions of 5-1 – 5-3 in CH_2Cl_2	187

5.5. Emission characteristics of 5-1 – 5-3 in different solvents at room temperature. ^a	190
5.6. NTOs representing the transitions contributing to the T ₁ states of 5-1 – 5-3 in CH ₂ Cl ₂ calculated by TDDFT Δ SCF method.	190
6.1. Electronic absorption, emission, and triplet excited-state absorption parameters, as well as singlet oxygen quantum yields for complexes 6-1 – 6-5.	213
6.2. NTOs for low energy transitions of 6-1 – 6-5. For transitions with quasi-degenerate transition orbitals, only one pair of transition densities are shown and are indicated by *.	213
6.3. Natural transition orbitals (NTOs) for high energy transitions for 6-1 – 6-5. Transition with quasi-degenerate transition orbitals only one pair of transition densities are shown and are indicated by *.	214
6.4. Emission characteristics of complexes 6-1 – 6-5 in different solvents at room temperature.	217
6.5. Comparison of EC ₅₀ values (μ M) for SK-MEL-28 cancer cells and CCD-1064Sk normal skin fibroblasts dosed with complexes 6-1 – 6-5.	223
7.1. Photophysical parameters for complexes 7-1 – 7-5.	263
7.2. NTOs for lowest-energy transitions of complexes 7-1 – 7-5 in toluene.	265
7.3. NTOs of the hole and electron of the moderate energy absorption band transitions of complexes 7-1 – 7-5, calculated by the TD-DFT method with PBE1PBE functional, LANL2DZ/6-31G* basis and toluene as a solvent.	265
7.4. NTOs of the hole and electron of the high energy absorption band transitions of complexes 7-1 – 7-5, calculated by the TD-DFT method with PBE1PBE functional, LANL2DZ/6-31G* basis using toluene as the solvent.	267
7.5. Emission characteristics of complexes 7-1 – 7-5 in different solvents at r.t.	269
7.6. NTOs corresponding to the optimized S ₁ and T ₂ states of complexes 7-1 – 7-5 in toluene.	271
7.7. NTOs of the optimized 1 st triplet state. All excited state calculations were done with the PBE1 functionals with LAN2DZ/6-31G* basis set and toluene as a solvent.	271
7.8. Comparison of EC ₅₀ values (μ M) for SKMEL28 cancer cells dosed with complexes 7-3 and 7-5.	274
7.9. Comparison of EC ₅₀ values (μ M) for <i>streptococcus aureus</i> dosed with 7-3 or 7-5.	279

LIST OF FIGURES

<u>Figure</u>	<u>Page</u>
1.1. Frank–Condon energy diagram.	4
1.2. Jablonski diagram of molecules. IC: internal conversion, ISC: intersystem crossing, ESA: excited state absorption.....	6
1.3. Typical pathway for a photosensitizer to generate ¹ O ₂ and ROS.	10
1.4. Schematic energy–level diagram for a typical cationic heteroleptic Ir(III) complex.....	13
1.5. Absorption spectra of complexes Ir1–Ir6 (Ir1 = 1, Ir2 = 2, Ir3 = 3, Ir4 = 4, Ir5 = 5, Ir6 = 6) in CH ₂ Cl ₂ at room temperature. Reprinted with permission from Ref. 48.....	17
1.6. Photoluminescence spectra of complexes Ir1–Ir6 (Ir1 = 1, Ir2 = 2, Ir3 = 3, Ir4 = 4, Ir5 = 5, Ir6 = 6) in degassed CH ₂ Cl ₂ at room temperature. Reprinted with permission from Ref. 48.	17
1.7. Room–temperature absorption (left) and photoluminescence (right) spectra of complexes Ir7–Ir9 (Ir7 = 1, Ir8 = 2, Ir9 = 3) in degassed CH ₂ Cl ₂ . The spectra were recorded on a Jobin Yvon fluorospectrophotometer (FluoroMax-3), by using the manufacturer’s procedure. Reprinted with permission from Ref. 49.....	18
1.8. Absorption spectra of complexes Ir10–Ir13 (Ir10 = 1, Ir11 = 2, Ir12 = 3, Ir13 = 4) in CH ₂ Cl ₂ at room temperature. Reprinted with permission from Ref. 22.....	19
1.9. Photoluminescence spectra of complexes Ir10–Ir13 (Ir10 = 1, Ir11 = 2, Ir12 = 3, Ir13 = 4) in degassed CH ₂ Cl ₂ at room temperature. Reprinted with permission from Ref. 22.	19
1.10. Experimental UV–vis absorption spectra of Ir14–Ir19 (Ir14 = 1, Ir15 = 2, Ir16 = 3, Ir17 = 4, Ir18 = 5, Ir19 = 6) in CH ₂ Cl ₂ . Reprinted with permission from Ref. 20.	20
1.11. Normalized emission spectra of Ir14–Ir19 (Ir14 = 1, Ir15 = 2, Ir16 = 3, Ir17 = 4, Ir18 = 5, Ir19 = 6) in deaerated CH ₂ Cl ₂ solution, $c = 1 \times 10^{-5}$ mol L ⁻¹ . Reprinted with permission from Ref. 20.	21
1.12. The ground–state absorption spectra for complexes Ir20–Ir24 (Ir20 = 1, Ir21 = 2, Ir22 = 3, Ir23 = 4, Ir24 = 5) in CH ₃ CN at room temperature. Reprinted with permission from Ref. 57.	23
1.13. The proposed ILCT transition in Ir22. Reprinted with permission from Ref. 57.....	23
1.14. Emission spectra for complexes Ir20–Ir24 (Ir20 = 1, Ir21 = 2, Ir22 = 3, Ir23 = 4, Ir24 = 5) in degassed CH ₃ CN (left) and aqueous (right) at room temperature. Reprinted with permission from Ref. 57.....	23

1.15. The UV–vis absorption (solid line) and emission (dash line) spectra for complexes Ir25 and Ir26 (Ir25 = IrN ₆ ³⁺ , Ir26 = IrN ₄ C ₂ ⁺) in aerated CH ₃ CN solutions at room temperature. Reprinted with permission from Ref. 58.	24
1.16. Luminescence spectra of (A) Ir25 and (B) Ir26 excited at 350 nm with increased concentration of dGMP. Inset: The obtained Stern–Volmer plots for complexes Ir25 and Ir26 measured at wavelength of 560 and 514 nm, respectively. Reprinted with permission from Ref. 58.	25
1.17. The absorption spectra of Ir28 in aqueous solution at different pH values (5.3, 6.7, 7.6, 8.3, 9.0, 10.1).	25
1.18. The luminescence spectra of the air-equilibrated aqueous solutions of Ir27–Ir31 (Ir27 = 1, Ir28 = 2, Ir29 = 3, Ir30 = 4, Ir31 = 5) at pH 6.0 at room temperature ($\lambda_{\text{ex}} = 364$ nm).	26
1.19. UV-vis spectra of Ir32 (solid line) and Ir33 (dashed line) in acetonitrile.	26
1.20. Emission spectra of Ir32 (a) and Ir33 (b). Solid lines are at room temperature (in MeCN), and dotted lines are at 77 K (in DMF-MeOH-EtOH [1:5:5(v/v)]).	27
1.21. (a) TA spectra of Ir34 in deoxygenated THF solution (b) transmittance of pulsed beam at 1064 nm of Ir34 in degassed THF solution at various concentrations. Reprinted with permission from Ref. 21.	29
1.22. Experimental (a) and calculated (b) ground–state absorption spectra of all complexes (Ir35 = 1, Ir36 = 2, Ir37 = 3, Ir38 = 4, Ir39 = 5) in CH ₂ Cl ₂ . Reprinted with permission from Ref. 51.	30
1.23. Normalized emission spectra of all complexes in degassed CH ₂ Cl ₂ . Reprinted with permission from Ref. 51.	30
1.24. Reverse saturable absorption for complexes (Ir35 = 1, Ir36 = 2, Ir37 = 3, Ir38 = 4, Ir39 = 5) in 2 mm thick toluene (80% linear transmission) for 532 nm 4.1 ns laser pulses at room temperature. Reprinted with permission from Ref. 51.	31
1.25. Experimental ground–state absorption spectra of (a) C ^N ligands (1: benzo[H]quinoline; 2: 1–phenylisoquinoline, 3: 1–(2–pyridyl)naphthalene, 4: 2–(2–pyridyl)–naphthalene, 5: 1–(2–pyridyl)pyrene, 6: 1,2–diphenyl–pyreno[4,5–d]imidazole, 7: 3–(2–pyridyl)perylene) and (b) complexes Ir40–Ir46 (Ir40 = 1, Ir41 = 2, Ir42 = 3, Ir43 = 4, Ir44 = 5, Ir45 = 6, Ir46 = 7) in CH ₂ Cl ₂ at room temperature and (c) calculated UV–vis spectra all complexes in CH ₂ Cl ₂ at 0 K. Reprinted with permission from Ref. 50.	32
1.26. Nanosecond triplet TA spectra of complexes Ir40–Ir46 (Ir40 = 1, Ir41 = 2, Ir42 = 3, Ir43 = 4, Ir44 = 5, Ir45 = 6, Ir46 = 7) at zero–time decay in acetonitrile. Reprinted with permission from Ref. 50.	32

1.27. Nonlinear transmission plot of Ir40–Ir46 (Ir40 = 1, Ir41 = 2, Ir42 = 3, Ir43 = 4, Ir44 = 5, Ir45 = 6, Ir46 = 7) at the linear transmittance of 80% in CH ₂ Cl ₂ solution in a 2 mm cuvette for 532 nm 4.1 ns laser. Reprinted with permission from Ref. 50.....	33
1.28. Reverse saturable absorption for Ir47–Ir50 (Ir47= 1, Ir48 = 2, Ir49 = 3, Ir50 = 4) in CH ₂ Cl ₂ in a 2 mm cuvette for 532 nm nanosecond laser pulses. Reprinted with permission from Ref. 18.	33
1.29. Time-resolved triplet TA spectra of Ir14–Ir19 (Ir14 = 1, Ir15 = 2, Ir16 = 3, Ir17 = 4, Ir18 = 5, Ir19 = 6) in toluene solution in a 1-cm cuvette ($\lambda_{\text{ex}} = 355 \text{ nm}$, $A_{355} = 0.4$). Reprinted with permission from Ref. 20.....	35
1.30. Reverse saturable absorption for complexes Ir14–Ir18 (Ir14 = 1, Ir15 = 2, Ir16 = 3, Ir17 = 4, Ir18 = 5) for 4.1 ns laser pulses at 532 nm in 2-mm thick toluene solution. Reprinted with permission from Ref. 20.....	35
2.1. UV–vis absorption spectra of 2-1 – 2-6 in CH ₂ Cl ₂	62
2.2. The ground–state molecular orbital diagram for 2-1 – 2-6 in CH ₂ Cl ₂ , and HOMO and LUMO plots for 2-1.	67
2.3. Frontier molecular orbital mixing between 2-1 and 1,3–butadiene to give rise to 2-2, 2-3 and 2-5.....	69
2.4. Frontier molecular orbital mixing between 2-2, 2-3, 2-5 and 1,3-butadiene.	70
2.5. Normalized emission spectra of 2-1 – 2-6 at room temperature in CH ₂ Cl ₂ . The spectra of 2-1 – 2-4 were measured on a HORIBA FluoroMax 4 fluorometer/phosphorometer with a Hamamatsu PMT R928 as the detector, while the spectra of 2-5 and 2-6 were detected with an InGaAs sensor from 670 nm to 1225 nm ($\lambda_{\text{ex}} = 473 \text{ nm}$) with a 500 nm long pass filter. The vertical lines represent the triplet emission wavelengths calculated by TDDFT based ΔSCF method.....	74
2.6. Nanosecond transient difference absorption spectra of complexes 2-1 – 2-6 in acetonitrile immediately after 355 nm laser pulse excitation. $A_{355} = 0.4$ in a 1-cm cuvette.	77
2.7. Nanosecond time-resolved transient differential absorption spectra of 2-1 – 2-6 in acetonitrile. $\lambda_{\text{ex}} = 355 \text{ nm}$, $A_{355} = 0.4$ in a 1-cm cuvette.	78
2.8. Nanosecond time-resolved transient differential absorption spectra of L2-1 – L2-6 in acetonitrile. $\lambda_{\text{ex}} = 355 \text{ nm}$, $A_{355} = 0.4$ in a 1-cm cuvette.	79
2.9. Calculated triplet excited state energy diagram for complexes 2-1 – 2-6 in CH ₃ CN.....	80
3.1. UV–vis absorption spectra of 3-1–3-10 in CH ₂ Cl ₂ at room temperature. The insets are the expanded spectra in the region of 450–625 nm.....	98

3.2. Normalized experimental absorption spectra of 3-1 – 3-10 in different solvents.....	99
3.3. Ground–state molecular orbital diagram for 3-1 – 3-10 in CH ₂ Cl ₂ (HOMO and LUMO of 3-1 are plotted as representative).	112
3.4. Frontier molecular orbital mixing between <i>cis</i> -1,3–butadiene or ethene and parent molecules.	112
3.5. Normalized emission spectra of 3-1 – 3-10 in CH ₂ Cl ₂ at room temperature. (λ_{ex} = 438 nm for 3-1, 430 nm for 3-2, 439 nm for 3-3, 436 nm for 3-4, 438 nm for 3-5, 437 nm for 3-6, 440 nm for 3-7, 428 nm for 3-8, 436 nm for 3-9, and 437 nm for 3-10.	114
3.6. Comparing experimental emission spectra to TDDFT Δ SCF energy for 3-1 – 3-10 in dichloromethane.	118
3.7. Triplet excited state energy diagram for 3-1 – 3-10 in CH ₂ Cl ₂	118
3.8. Nanosecond transient differential absorption spectra of complexes 3-1 – 3-10 in acetonitrile solution immediately after laser pulse excitation ($A_{355} = 0.4$ in a 1–cm cuvette, $\lambda_{\text{ex}} = 355$ nm).	121
3.9. Nanosecond time-resolved transient differential absorption spectra of 3-1 – 3-10 at zero-time decay in acetonitrile. $\lambda_{\text{ex}} = 355$ nm, $A_{355} = 0.4$ in a 1-cm cuvette.	121
3.10. Nanosecond time-resolved transient absorption (TA) spectra of the diimine ligands used in complexes 3-2 – 3-4, 3-6 – 3-8 and 3-10 and their corresponding ZnCl ₂ complexes in CH ₃ CN. The diimine ligands used in 3-1, 3-5 and 3-9 and their corresponding ZnCl ₂ complexes did not show any TA signals. $\lambda_{\text{ex}} = 355$ nm, and $A_{355} = 0.4$ in a 1-cm cuvette.....	122
3.11. Transmission vs incident energy curves for 3-1 – 3-10 at the linear transmittance of 80% in 2 mm cuvette (in acetonitrile solution) using the 532 nm 4.1 ns laser pulses. The radius of the beam at the focal point was approximately 96 μm	124
4.1. Experimental UV-vis absorption spectra of (a) 4-0 – 4-4, (b) 4-5 – 4-7 and (c) 4-0, 4-1, and 4-8 – 4-10 at room temperature in dichloromethane. The inset shows the expanded spectra at 500-800 nm.	145
4.2. HOMO and LUMO plots for 4-0 and ground-state molecular orbital diagram for 4-0 – 4-10 in CH ₂ Cl ₂	154
4.3. FMO mixing between the HOMO of the parent complex 4-0 and the HOMO–1 or HOMO of <i>cis</i> -1,3-butadiene to generate the FMOs of 4-1 (a), 4-2 (b), 4-5 (c), or 4-6 (d), respectively.	156

4.4. FMO mixing between the HOMO of the parent complex 4-0 and HOMO-1/LUMO of <i>cis</i> -1,3-butadiene or HOMO of ethane to generate the FMOs of 4-3 and 4-4, respectively.....	157
4.5. FMO mixing between the HOMO of the parent complex 4-5 or 4-6 and HOMO-1/LUMO or HOMO of <i>cis</i> -1,3-butadiene to generate the FMOs of 4-7.	157
4.6. FMO mixing between the HOMO of the parent complex 4-1 and HOMO-1/LUMO of <i>cis</i> -1,3-butadiene to generate the FMOs of 4-8 and 4-9.	157
4.7. FMO mixing between the HOMO of the parent complex 4-8 or 4-9 and HOMO or HOMO-1/LUMO of <i>cis</i> -1,3-butadiene to generate the FMOs of 4-10.	158
4.8. Experimental emission spectra of 4-1 – 4-10 at room temperature in dichloromethane. The spectra of 4-1 – 4-7 and 4-9 were measured on a HORIBA FluoroMax 4 fluorometer /phosphorometer with a Hamamatsu PMT R928 as the detector, while the spectra of 4-8 and 4-10 were detected with an InGaAs sensor from 670 to 1225 nm ($\lambda_{\text{ex}} = 473$ nm) with a 500 nm long pass filter.	159
4.9. Normalized emission spectra of 4-1 – 4-10 (1–10) in different solvents ($\lambda_{\text{ex}} = 436$ nm).....	160
4.10. Comparison of the nanosecond TA difference spectra of complexes 4-1 – 4-10 in a CH ₃ CN solution immediately after laser excitation (the top figure) and the time-resolved TA spectra of complexes 4-1 – 4-3, 4-5, 4-8, and 4-10 in CH ₃ CN ($\lambda_{\text{ex}} = 355$ nm; $A_{355} = 0.4$ in a 1 cm cuvette).	164
4.11. Nanosecond time-resolved transient difference absorption spectra of 4-4, 4-6, 4-7, and 4-9 in acetonitrile. $\lambda_{\text{ex}} = 355$ nm, $A_{355} = 0.4$ in a 1-cm cuvette.	165
4.12. Nonlinear transmission plots of 4-1 – 4-10 at 80% linear transmittance in a 2-mm cuvette in CH ₃ CN solutions for 532 nm 4.1 ns laser pulses.....	168
5.1. Experimental (a) and theoretical (b) UV/Vis absorption spectra of 5-1 – 5-3 at room temperature in CH ₂ Cl ₂ . The inset in panel (a) shows the expanded spectra in the regions of 450 – 800 nm. The B3LYP functional was used in the TDDFT calculations and the calculated transitions were broadened by a Gaussian distribution with a linewidth of 0.05 eV.	182
5.2. Normalized emission spectra of 5-1 – 5-3 in CH ₂ Cl ₂ at room temperature.	189
5.3. Normalized experimental emission spectra of 5-1 – 5-3 at room temperature in different solvents.	189
5.4. Time-resolved nanosecond TA spectra of complexes 5-1 – 5-3 in deoxygenated acetonitrile solution (a–c), and comparison of the TA spectra of 5-1 – 5-3 immediately after laser excitation. $A_{355} = 0.4$ in a 1 cm cuvette, $\lambda_{\text{ex}} = 355$ nm.....	192

5.5. Nonlinear transmission plot of 5-1 – 5-3 at the linear transmittance of 80% in 2 mm cuvette in acetonitrile solution using the 4.1 ns laser pulses duration at 532 nm.	193
6.1. Experimental (a) and theoretical (b) UV–vis absorption spectra of 6-1 – 6-5 at room temperature in acetonitrile. The inset in panel (a) is the expansion of the spectra in the region of 450–800 nm. The theoretical spectra were computed using ω B97XD with mixed basis set. A redshift of 0.55 eV for the theoretical spectra in panel (b) was applied for better comparison with the experimental spectra.	212
6.2. Normalized experimental absorption spectra of 6-1 – 6-5 in different solvents.	212
6.3. Experimental emission spectra of 6-1 ($\lambda_{\text{ex}} = 426$ nm), 6-2 ($\lambda_{\text{ex}} = 420$ nm), 6-3 ($\lambda_{\text{ex}} = 405$ nm), 6-4 ($\lambda_{\text{ex}} = 413$ nm), and 6-5 ($\lambda_{\text{ex}} = 415$ nm) at room temperature in deoxygenated acetonitrile ($c = 1 \times 10^{-5}$ mol·L ⁻¹).	217
6.4. Normalized emission spectra of 6-1 – 6-5 in different solvents ($\lambda_{\text{ex}} = 436$ nm).	217
6.5. Nanosecond transient absorption (TA) spectra of complexes 6-1 – 6-5 in deoxygenated acetonitrile at zero delay after 355 nm excitation. The inset shows the TA spectra of 6-3 at different delay time after excitation. $A_{355 \text{ nm}} = 0.4$ in a 1-cm cuvette.	219
6.6. Nanosecond time-resolved transient differential absorption spectra of 6-1 – 6-5 at zero-time decay in acetonitrile. $\lambda_{\text{ex}} = 355$ nm, $A_{355} = 0.4$ in a 1-cm cuvette.	220
6.7. <i>In-vitro</i> dose-response curves for complexes 6-1 (a), 6-2 (b), 6-3 (c), 6-4 (d), and 6-5 (e) in SK-MEL-28 cells treated in the dark (black) and with visible (blue) or red (red) light activation.	224
6.8. Activity plot for complexes 6-1 – 6-5 in SK-MEL-28 and CCD-1064Sk cells treated in the dark (black) and with visible (blue) or red (red) light activation.	224
6.9. Confocal luminescence images of SK-MEL-28 cells dosed with 6-1 – 6-5 (a-e, 50 μ M) in the dark (left) and with visible light (50 J·cm ⁻²) (right).	228
6.10. DNA photocleavage of pUC19 DNA (20 μ M) dosed with metal complex (MC) 6-1 (a), 6-2 (b), 6-3 (c), 6-4 (d), 6-5 (e) and visible light (14 J·cm ⁻²). Gel mobility shift assays employed 1% agarose gels (0.75 μ g·mL ⁻¹ ethidium bromide) electrophoresed in 1× TAE at 8 V·cm ⁻¹ for 30 min. Lane 1, DNA only (- $h\nu$); lane 2, DNA only (+ $h\nu$); lane 3, 0.5 μ M MC (+ $h\nu$); lane 4, 1 μ M MC (+ $h\nu$); lane 5, 2 μ M MC (+ $h\nu$); lane 6, 3 μ M MC (+ $h\nu$); lane 7, 5 μ M MC (+ $h\nu$); lane 8, 8 μ M MC (+ $h\nu$); lane 9, 10 μ M MC (+ $h\nu$); lane 10, 12 μ M MC (+ $h\nu$); lane 11, 15 μ M MC (+ $h\nu$); lane 12, 20 μ M MC (+ $h\nu$); lane 13, 50 μ M MC (+ $h\nu$); lane 14, 100 μ M MC (+ $h\nu$); lane 15, 100 μ M MC (- $h\nu$). Forms I, II and IV DNA refer to supercoiled plasmid, nicked circular plasmid, and aggregated plasmid, respectively.	230
7.1. UV–vis absorption spectra of 7-1 – 7-5 in toluene at room temperature.	262

7.2. Normalized UV-vis absorption spectra of 7-1 – 7-5 in different solvents.	262
7.3. Normalized experimental and calculated absorption spectra with the respective oscillation strength. All absorption spectra are calculated by using the linear response time dependent DFT (TD-DFT) with the PBE1 functional and LAN2DZ/6-31G* basis set. Toluene are used as a solvent. Vertical bar indicates the oscillation strength of the transitions.	264
7.4. Normalized experimental emission spectra of 7-1 – 7-5 in deaerated toluene at room temperature. The excitation wavelength was 543 nm for 7-1 and 7-3, 530 nm for 7-2, and 535 nm for 7-4 and 7-5. The open-headed lines represent the calculated S ₁ fluorescence and the solid-headed lines represent the calculated T ₂ phosphorescence. The inset shows the comparison of emission intensity in air-saturated and deaerated toluene solutions for 7-1.....	270
7.5. Normalized emission spectra of complexes 7-1 – 7-5 in different solvents at r.t. ($\lambda_{\text{ex}} = 436 \text{ nm}$).....	270
7.6. Nanosecond transient difference absorption spectra of complexes 7-1 – 7-5 in toluene at room temperature immediately after 355 nm laser pulse excitation. $A_{355} = 0.4$ in a 1-cm cuvette.	272
7.7. In vitro dose-response curves for complexes 7-3 (left) and 7-5 (right) in SKMEL28 cells treated in the dark (black) and with visible (blue) or red (red) light activation.....	274
7.8. Reactive oxygen species assay results for SKMEL28 cells treated with 7-3 (a), 7-5 (b), or the positive control <i>tert</i> -butyl hydrogen peroxide TBHP (c) using DCFH-DA as a ROS probe. Cells were treated in the dark (black bars) or with 50 J cm ⁻¹ visible light (blue bars). ROS production was measured at 120 min post-treatment.....	276
7.9. Laser scanning confocal microscopy images of SKMEL28 cells dosed with 50 μM 7-3 (top row) or 7-5 (bottom row) in the dark (a) or with 50 J cm ⁻² visible light (b).	278
7.10. Bacterial cell survival dose-response bar graphs for complexes 7-3 (a) and 7-5 (b) in <i>Streptococcus aureus</i> , treated in the dark (black) or with 35 J cm ⁻¹ visible (blue) light.	279

LIST OF SCHEMES

<u>Scheme</u>	<u>Page</u>
2.1. Synthetic routes for ligands L2-4 – L2-6 and complexes 2-1 – 2-6.	55
4-1. Synthetic routes for Ir(III) complexes.	135
5-1. Synthetic route for Ir(III) complexes 5-1 – 5-3.	178
6-1. Synthetic routes for complexes 6-1 – 6-5.	205
7-1. Synthetic route for ligands L7-1–L7-5 and complexes 7-1 – 7-5 ^a	246

LIST OF CHARTS

<u>Chart</u>	<u>Page</u>
1.1. Three common prototypes of Ir(III) complexes.....	14
1.2. Representative biscyclometalated monocationic iridium(III) complexes with different conjugation lengths on the ligands.	16
1.3. Selected examples of bis-terdentate iridium(III) complexes.	22
1.4. Selected examples of cyclometalated iridium (III) complexes for RSA study.....	28
1.5. Selected examples of cyclometalated iridium(III) complexes for phototherapeutic studies.....	37
1.6. General synthesis route for tris-bidentate cyclometalated Ir(III) complexes.....	41
1.7. General synthesis route for bis-tridentate Ir(III) complexes.	42
2.1. Structures of complexes 2-1 – 2-6.	54
3.1. Structures of complexes 3-1 – 3-10.	90
4.1. Structures of heteroleptic cationic Ir(III) complexes 4-0 – 4-10.	133
6.1. The molecule structure of target dinuclear Ir(III) complexes.....	203
7.1. Molecular structures of BODIPY-NHC-Ir(III) complexes 7-1 – 7-5.....	245

1. INTRODUCTION

Iridium, a third-row transition noble metal with oxidation states of -3 to $+9$, was firstly discovered in 1803. To date, investigations of the photochemical, photophysical, and electrochemical properties of organoiridium compounds have attracted intense and sustained interests. Owing to the commercially-available hydrated iridium trichloride and ammonium hexachloroiridate as the precursors, diverse octahedral d^6 Ir(III) complexes were synthesized, which have potential applications in organic light emitting diodes (OLEDs),¹⁻⁴ light-emitting electrochemical cells (LECs),⁵⁻⁷ luminescent biological labeling,⁸⁻¹⁰ photocatalysts,¹¹⁻¹³ photodynamic therapy (PDT),¹⁴⁻¹⁷ and nonlinear optics.¹⁸⁻²² These applications are based on their striking structural and spectroscopic characteristics, i.e. tunable triplet excited states, photo- and thermal-stability, and high quantum efficiency for triplet excited-state formation, etc..²³⁻²⁵

Among the variety of potential applications reported for the Ir(III) complexes, reverse saturable absorption (RSA) and photodynamic therapy (PDT) are the two emerging areas. RSA refers to a nonlinear optical phenomenon in which the absorbance of the excited state is stronger than that of the ground state at the same wavelength.^{26,27} RSA has applications in optical limiting,⁶⁷ laser pulse shaping,⁶⁸ optical switching,⁶⁹ and spatial light modulation,⁷⁰ etc. RSA can be achieved by materials that possess large ratios of the excited-state absorption (ESA) cross section (σ_{ex}) to that of the ground state (σ_0) at the same wavelength. Thus, weaker ground-state absorption accompanied with stronger excited-state absorption are the basic requirements for reverse saturable absorbers. For RSA of the nanoseconds and longer laser pulses, the longer-lived triplet excited states play the major role. In such a case, the quantum yield of the triplet-excited state formation and the triplet lifetime are also important parameters for improving the RSA.

PDT is an emerging therapeutic modality for cancers that combines three non-toxic components, i.e. a photosensitizer (PS) that is non-toxic in dark but becomes phototoxic upon light activation, a light source, and oxygen.²⁸⁻³⁰ Upon light irradiation, the non-toxic ground-state oxygen ($^3\text{O}_2$) becomes toxic singlet oxygen ($^1\text{O}_2$) and/or reactive oxygen species (ROS) through interacting with the excited PSs, which destroy the cancer cells directly, damage the vascular system in the surrounding tissues to avoid the recurrence of tumors, and may stimulate the immune system. To obtain a high PDT activity against cancers, PSs that are capable of efficient $^1\text{O}_2$ and/or ROS generation in hypoxic cancerous environment remain to be the most desirable ones.

The above discussion shows that the applications of the Ir(III) complexes are closely related to their photophysical properties. In order to improve the device performances, optimization of the photophysical properties of the individual complex plays a key role. To realize this goal, understanding the structure-property correlations holds the key. In this chapter, the basic concepts in photophysics will be reviewed first. Then, the synthesis, photophysics, and the current status of utilizing Ir(III) complexes in RSA and PDT will be reviewed.

1.1. Basic photophysical concepts

Various photophysical processes originate from the interactions between light and molecules. The basic principles on the photophysical processes are discussed in this chapter.

1.1.1. Light

Light, associated with our daily life, is a type of electromagnetic radiation with a speed of approximately 300,000 km/s in vacuum. The relationship between the light and energy is governed by the Planck's equation:

$$E = h\nu = hc/\lambda \quad (1.1)$$

Where E stands for the photon energy, h is Planck's constant (6.63×10^{-34} joule-seconds), ν is the frequency of light, c is the speed of light, and λ is the wavelength of light. The nature of light has a wave-particle duality, due to both the wave-like and particle-like features. Since the wave-particle duality character shared by both photons and electrons, an intimate connection between light and electrons has been developed as a foundation for modern photophysical research. In view of the two areas of applications of the Ir(III) complexes will be potentially applied to, the following discussion in this dissertation will be focused on a molecular level.

1.1.2. The absorption of light in materials

The absorption of light in molecules is always accompanied with electronic transitions. To further understand the natures of these transitions, Frank-Condon principle needs to be explained, which is a well-established theory in quantum chemistry and spectroscopy (Figure 1.1)³¹. In simple terms, this principle can be exploited to explain the intensity of vibronic transitions and absorption of photons.

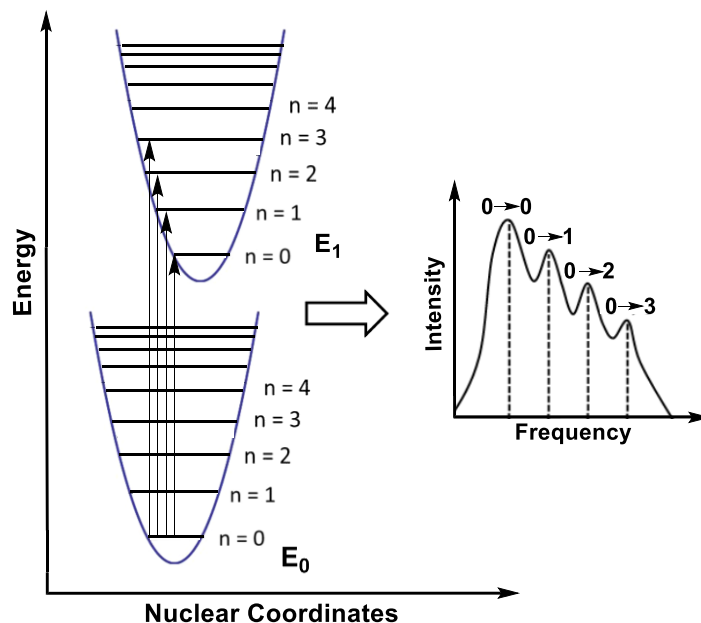


Figure 1.1. Frank–Condon energy diagram.

As depicted in Figure 1.1, electrons at the ground state (E_0) are vertically excited to an excited state (E_1) within a femtosecond timescale ($\sim 10^{-15}$ s) upon light irradiation. Compared to the electrons, atomic nuclei are much heavier. Thus, the atomic nuclei cannot be moved and readjusted in femtoseconds during the absorption. Each energy level is marked as a solid line. The electronic transitions are expressed as upward arrows. Among them, the energy of absorption is equivalent to the length of the arrow. Based on the above Planck's equation, the frequency of an absorption peak is governed by the potential energy gap between the initial and final states.

When a light beam enters a sample solution, attenuation of the light can be observed, which is associated with the ability of the material's absorption. According to the Lambert–Beer law, a linear relationship between the absorbance and the intrinsic properties of the absorbing species is expressed in the following equations:³²

$$T = I/I_0 \quad (1.2)$$

$$A = -\log T = -\log (I/I_0) = \varepsilon * l * c \quad (1.3)$$

where T is the transmittance of the light, I_0 is the initial light intensity, I is the intensity of the transmitted light, A is the measured absorbance, ϵ ($\text{M}^{-1} \cdot \text{cm}^{-1}$) is the molar extinction coefficient, l (cm) is the path length of the sample, and c (mol/L) is the concentration of the sample solution. Accordingly, modern ultraviolet–visible (UV-Vis) spectroscopy is usually utilized to measure the absorbance and subsequently deduce the ϵ values of a tested sample with a known concentration.

Jablonski diagram, as an energy diagram, illustrates the electronic states and possible excited state pathways in a molecule, which is shown in Figure 1.2.³³ By absorbing a photon, a molecule can be populated to its lowest singlet excited state (S_1). Note that electrons can be excited to higher energy singlet excited states (S_n) and then relax back to S_1 *via* internal conversion (IC) (known as a thermal process), due to the overlapping vibrational and electronic energy states. The S_1 state will release that energy to go back to the ground state (S_0) *via* radiative (fluorescence) or non–radiative (heat) transitions (Figure 1.2). Radiative and nonradiative transitions are denoted as straight and sinuate arrows, respectively. In comparison to the S_n states, the corresponding triplet excited states (T_n) located at lower energy levels because of the electron–electron repulsion. Since electron spins are paired in S_n states, the unpaired excited electrons in the triplet states lead the excitation to a triplet state involving a spin–forbidden transition. Except for the spin–allowed process ($S_1 \rightarrow S_0$), S_1 can relax and populate to the lowest-energy triplet excited state (T_1) *via* a spin–forbidden nonradiative transition known as intersystem crossing (ISC). After a spin flip of an electron, the T_1 deactivate to S_0 through a radiative decay or nonradiative decay pathways, which are known as phosphorescence or ISC.

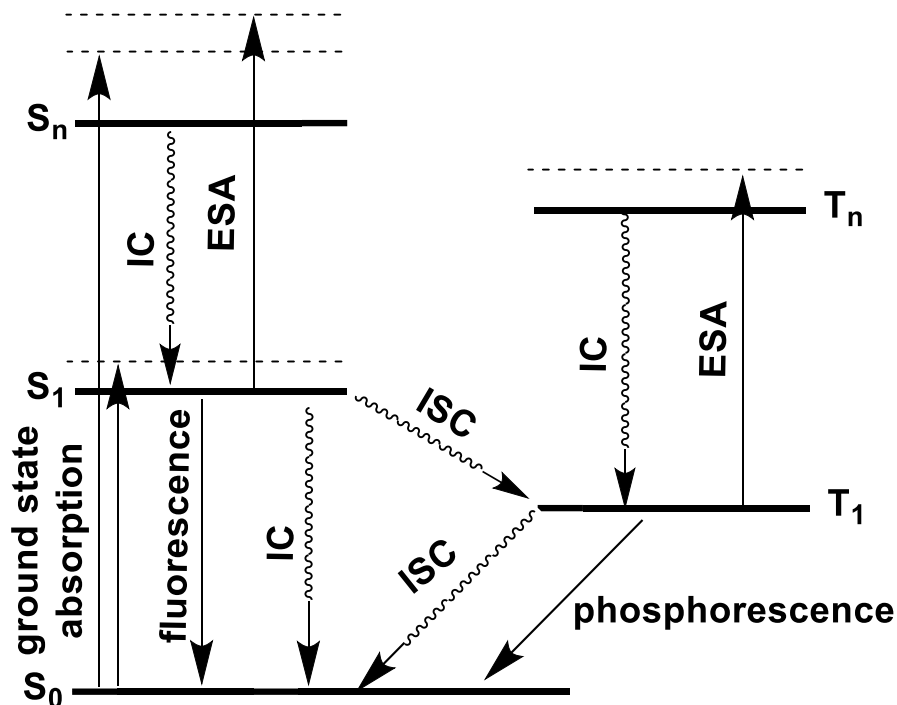


Figure 1.2. Jablonski diagram of molecules. IC: internal conversion, ISC: intersystem crossing, ESA: excited state absorption.

1.1.3. Fluorescence and phosphorescence

Based on the aforementioned discussion, fluorescence and phosphorescence are the radiative decay pathways from the S_1 and T_1 states respectively (Figure 1.2). The S_1 state, which has a higher potential energy, gives a shorter wavelength of fluorescence in contrast to the phosphorescence from the T_1 state. As a result of vibrational relaxation within the excited states, the energies of both the fluorescence and phosphorescence are typically lower than that of the excitation energy. The energy difference between an emitted photon and an absorbed photon appears as the Stokes shift between the excitation and emission spectra.³⁴

Fluorescence, a spin-allowed process, is a short-lived emission (the lifetime (τ) typically ranged from 10 ns to 700 ns).⁷¹ Phosphorescence, however, is a spin-forbidden transition, which lifetime is much longer than that of fluorescence ($\tau \approx 1$ ns - 1 ms). The lifetime of luminescence can be measured by time-resolved spectroscopy and fitting the obtained decay curves. Because of

the presence of ISC and IC, the shortened lifetime of radiative transition is observed. Therefore, the intrinsic lifetimes of S₁ (τ_{S_1}) and T₁ (τ_{T_1}) can be written as:³⁵

$$\tau_{S_1} = \frac{1}{k_r^f + k_{nr}^{S_1}} \quad (1.4)$$

$$\tau_{T_1} = \frac{1}{k_r^p + k_{nr}^{T_1}} \quad (1.5)$$

where k_r^f , $k_{nr}^{S_1}$, k_r^p , and $k_{nr}^{T_1}$ are the rate constant of fluorescence, nonradiative decay from the S₁ state, phosphorescence, and non-radiative decay from the T₁ state, respectively.

The emission quantum yield can be expressed as the ratio between the number of emitted photons and the number of absorbed photons. For fluorescence, the relationship of the quantum yield (Φ_f), the rate constant of fluorescence (k_f), and the rate constant of nonradiative decay (k_{nr}) from S₁ can be written as:³⁶

$$\Phi_f = \frac{k_f}{k_f + k_{nr}} \quad (1.6)$$

For phosphorescence, however, the quantum yield is susceptible to both ISC and quenching pathways. Thus, the phosphorescence quantum yield (Φ_p) can be expressed as:³⁷

$$\Phi_p = \frac{\Phi_{ISC} k_p}{k_p + k_{nr}} \quad (1.7)$$

where Φ_{ISC} , k_p , and k_{nr} stand for the quantum yield of ISC, the rate constant of phosphorescence, and rate constant of nonradiative decay from T₁, respectively.

The obtained phosphorescence quantum yields in this dissertation were calculated using the relative actinometry method.⁷² A degassed acetonitrile solution of [Ru(bpy)₃]Cl₂ ($\Phi_R = 0.097$) is used as the reference (R) for the quantum yield calculations of the samples (S) following the equation:

$$\Phi_S = \Phi_R * \frac{A_S}{A_R} * \frac{I_R}{I_S} * \frac{(n_S)^2}{(n_R)^2} \quad (1.8)$$

where Φ , A , I , and n are the phosphorescence quantum yield, the integrated area of the emission spectra, ground-state absorbance of the solution at the excitation wavelength, and the refractive index of the used solvent, respectively. The subscript S refers to the samples, and R refers to the reference.

1.1.4. Heavy atom effect

The property of T_1 plays a vital role in the applications for both RSA and PDT. According to the above discussion, T_1 state can be heavily populated through the nonradiative passway between the S_1 and T_1 states when the rate constant of ISC is high. However, the coupling and quantization of angular momentum and orbital angular momentum is separated, which results in a forbidden spin change of electron. For most organic compounds without heavy atoms, ISC yield is low. An increased overlap of spin angular momentum and orbital angular momentum of the electron can be obtained by the presence of a heavy atom. Consequently, the spin-orbit coupling enhances ISC yield, which is called the heavy atom effect.³⁸ In the periodic table, the atoms beyond the third row are defined as heavy atoms.

In this dissertation, strong spin-orbit coupling effect and high ISC rate are anticipated for all synthesized complexes due to the presence of Ir(III) ion. For example, , the rate constant of ISC is $6.9 \times 10^{12} \text{ s}^{-1}$ for complex *fac*-Ir(ppy)₃; whereas, the rate constant of fluorescence is about $1 \times 10^6 \text{ s}^{-1}$.³⁹ As a result, a nearly unity population of the T_1 state can occur.

1.1.5. RSA

With the development of laser technology, various laser sources have been employed in photonic and medical applications associated with our daily life. However, an urgent need for

optical limiters in order to protect human eyes or optical sensors from damaging laser beam is emerging. The performance of the optical limiters heavily depends on the optical limiting materials used in the devices. Such materials show excellent linear transmittance for low-intensity light. Under intense laser radiation, however, the transmitted laser pulses can be modulated to a safe intensity below the damaging threshold value. Since linear optical techniques, including absorption, reflection, and diffraction, cannot meet the aforementioned needs, a growing effort is focusing on the nonlinear absorbers.

Among the variety of nonlinear optical phenomena that have been explored for optical limiting applications, multiple photon absorption (MPA) and RSA are two major methods for the protection of human eyes and delicate components under exposure to intense laser beams. With increasing intensity or fluence of the incident laser, the absorptivities of the MPA or RSA materials increase. MPA is a spontaneous process that depends on the intensity of the last beams and typically work better for ps or fs laser pulses. Whereas RSA is a fluence dependent process that dominates the optical limiting for ns or longer pulse width laser beams. As shown in Figure 1.2, an excited molecule populated to the S_1 state can absorb additional photons to be populated to the higher energy S_n state ($S_1 \rightarrow S_n$ absorption). Similarly, the excited molecules at the T_1 state can also absorb photons to reach the T_n states with higher energies ($T_1 \rightarrow T_n$ absorption). With the different lifetimes of S_1 (fs-ns) and T_1 (ns-ms), the $S_1 \rightarrow S_n$ or $T_1 \rightarrow T_n$ absorption will be the major player for the short or long laser pulse induced RSA, respectively. Since a distinct heavy-atom effect can be induced by Ir(III) ion, the ISC rate is greatly enhanced in Ir(III) complexes, which results in dominant $T_1 \rightarrow T_n$ absorption in the RSA possess for Ir(III) complexes.

In order for RSA to occur, σ_{ex} should be larger than σ_0 , which will induce an increased absorptivity with increased laser fluence. Several criteria need to be taken into account when

design an ideal reverse saturable absorbers, such as a large ratio of σ_{ex}/σ_0 , long-lived excited-states, and high triplet excited-state quantum yield.

1.1.6. PDT

As an oxygen-dependent process, PDT is a noninvasive and precise spatiotemporal medical modality, in which PS is nontoxic without light activation but becomes highly phototoxic upon light activation. Therefore, in comparison with other cancer treatment modalities, the photoinitiated PDT has outstanding regioselectivity.

A typical photosensitization diagram displaying the formation of ROS and 1O_2 mediated by PSs is depicted in Figure 1.3.^{40,41} Upon photon absorption, a PS is excited from the ground state (S_0) to its lowest singlet excited state (S_1) and then relaxes to its lowest triplet excited state (T_1). Then, the T_1 of PS interacts with oxygen in its ground state (3O_2) via two pathways: energy transfer to convert 3O_2 to 1O_2 (Type II) and electron transfer to generate ROS, such as O_2^- , $\cdot OH$, H_2O_2 , etc (Type I).

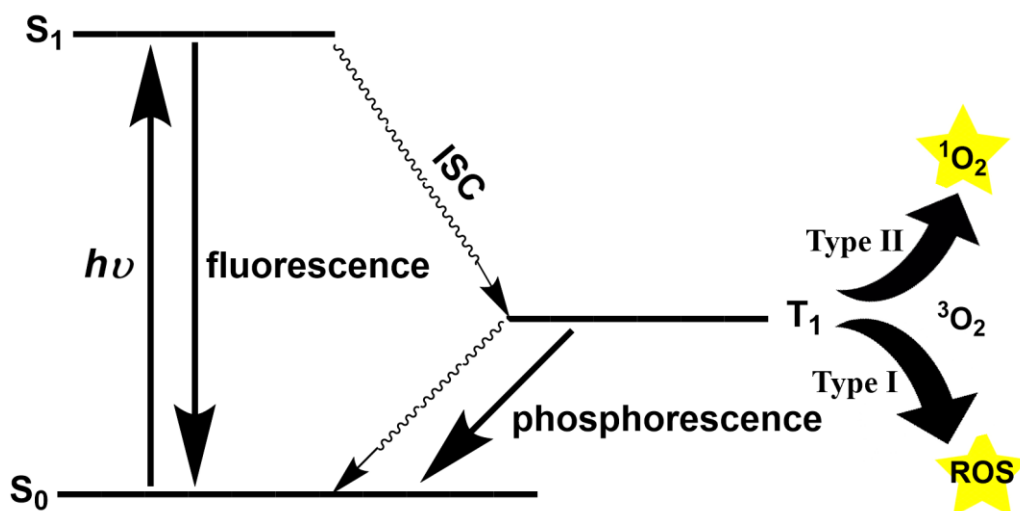


Figure 1.3. Typical pathway for a photosensitizer to generate 1O_2 and ROS.

To date, the most clinically used PDT drugs are still based on hematoporphyrin derivatives (HPD), which suffers from several drawbacks, such as high dark toxicity, inability to be activated by near-IR (NIR) light, low $^1\text{O}_2$ /ROS generation efficiency in hypoxic solid tumors, low cancer selectivity, cutaneous photosensitivity, and water insolubility. To overcome these disadvantages, there is an urgent need for developing new PSs with good tumor-specific targeting, absorb strongly in the NIR region, and long-lived triplet excited state.

Herein, PSs based on transition-metal complexes have prompted significant interest in recent years. In comparison to the organic PSs, transition-metal complex based PSs hold a series of unique merits, *i.e.*, (i) tunable excited-state properties, (ii) high triplet excited-state quantum yields, and (iii) good photostability and cell permeability. Additionally, the phosphorescent heavy transition-metal complexes can be used as targeted bioimaging agents, providing novel theranostic platforms to help investigating the PDT mechanisms and thus optimizing the treatment efficacy by *in situ* monitoring of biodistribution in the tumor cell. Therefore, cationic iridium(III) complexes appear promising for the application of PDT, because their photophysical properties match the requirement of ideal bioimaging-based PSs quite well.

1.2. Basic photophysics and representative examples for Ir(III) complexes

1.2.1. Photophysics of Ir(III) complexes

With an octahedral d^6 electronic configuration, the coordinating ligands of iridium(III) complexes protect the metal center from the environment well. Accordingly, several metal-based nonradiative pathways for transition metal complexes, including ground-state aggregation and solvent binding, can be largely avoided.⁴² Due to the decreased deactivation pathways and the

strong spin-orbit coupling effect induced by iridium ion, population of the triplet states with a high quantum yield can be realized.

Unlike pure organic chromophores, the Ir(III) ion plays a significant role in the photophysical processes of the Ir(III) complexes. The electronic transition diagram for typical biscyclometalated Ir(III) complexes is schematically illustrated in Figure 1.4. The vertical arrows indicate the electronic transitions from different orbitals of complexes. Among them, the fundamental types are listed as following:

(1) Metal-centered (MC) or d,d transitions: the transition between the two metal-localized orbitals.

(2) Ligand-centered (LC) or intraligand (IL) transitions: the $\pi \rightarrow \pi^*$ transitions between the orbitals on the same ligand.

(3) Ligand-to-ligand charge-transfer (LLCT) transitions: the $\pi \rightarrow \pi^*$ transitions between the orbitals on two different ligands.

(4) Metal-to-ligand charge-transfer (MLCT) transitions: the $d \rightarrow \pi^*$ transitions between the metal-centered d orbital and the ligand localized orbital.

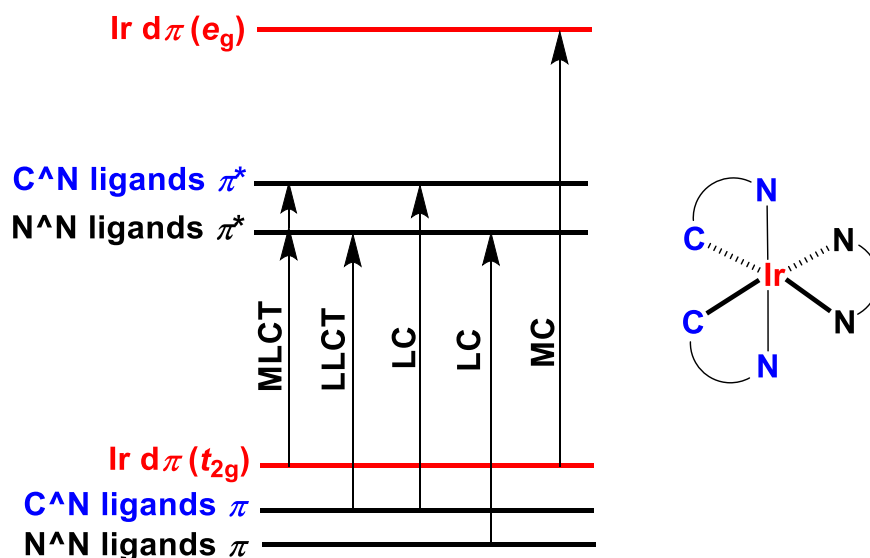


Figure 1.4. Schematic energy–level diagram for a typical cationic heteroleptic Ir(III) complex.

1.2.2. Three typical prototypes of Ir(III) complexes

The rich photophysical properties of Ir(III) complexes attract intense attention. As illustrated in Figure 1.4, ligands localized orbitals can be readily tuned by ligand structural modifications. Bathochromic or hypsochromic shifts may occur in the electronic absorption after adjusting the conjugation length of the ligands. Introducing electron–donating or –withdrawing substituents to the ligands also affects the electronic absorption. Therefore, the development of Ir(III) complexes with various ligands has drawn great interest.

Three common prototypes of Ir(III) complexes, i.e. *fac*-Ir(ppy)₃, [Ir(bpy)(ppy)₂]⁺, and [Ir(tpy)₂]³⁺, are illustrated in Chart 1.1. In these complexes, ppy, bpy, and tpy denote 2–phenylpyridine, 2,2'–bipyridine, and 2,2':6',2''–terpyridine, respectively. The well–known neutral complex, *fac*-Ir(ppy)₃, was first developed by Martin in 1958.⁴³ The metal center is surrounded by three identical ppy ligands where each of the phenyl group carries one formal negative charge and each of the pyridine group is neutral. Based on the subsequent theoretical calculations, the highest occupied molecular orbital (HOMO) in *fac*-Ir(ppy)₃ is delocalized on the

π orbitals of the phenyl rings and the metal d orbitals, while the lowest unoccupied molecular orbital (LUMO) is mainly delocalized on the pyridine rings. Obvious low-energy $^1\text{MLCT}$ band (from 320 to 500 nm) were observed in the absorption spectra, which are assigned to transitions between the HOMO and LUMO orbitals.⁴⁴ The emission spectrum of *fac*-Ir(ppy)₃ resembles the shape of the ligand emission at 77 K, which is indicative of a ligand-localized (π,π^*) lowest excited state. The measured phosphorescence lifetime was ca. 2 μs at room temperature, indicating the emitting state is a mixture of $^3\pi,\pi^*$ and $^3\text{MLCT}$.

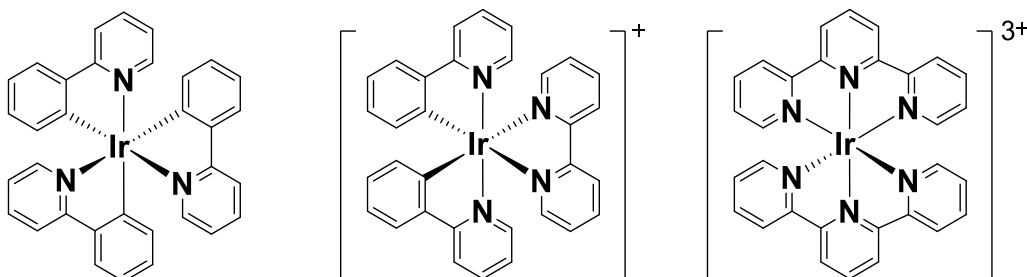


Chart 1.1. Three common prototypes of Ir(III) complexes.

In comparison to the neutral complex Ir(ppy)₃, replacing one cyclometalating (C[^]N) ligand by a diimine (N[^]N) ligand results in the monocationic complex [Ir(bpy)(ppy)₂]⁺. As a prototype, the complex shows intense $^1\pi,\pi^*$ absorption bands in high-energy region ($\lambda < 300$ nm), and moderate $^1\text{MLCT}$ absorption in the UV to blue spectral region.⁴⁵ Interestingly, spin-forbidden $^3\text{MLCT}/^3\text{LLCT}$ transitions exhibit a long and weak absorption tail extending to 550 nm.⁴⁶ With the emission lifetime being hundreds of nanoseconds, the phosphorescence of the complex was assigned predominantly to the low-lying $^3\text{MLCT}$ state.

The homoleptic bis-terpyridine complex, [Ir(tpy)₂]³⁺, features ligand-centered transitions with large extinction coefficients ranged from 200 to 350 nm. Besides, the absorption tail is attributed to $^1\text{MLCT}$ and spin-forbidden ($S_0 \rightarrow T_1$) transitions.⁴⁷ With the emission lifetime being 1

μs and the similarity of the luminescence profiles to that of $\text{Zn}(\text{tpy})_2^{2+}$ at 77 K, the room-temperature vibronically resolved luminescence spectrum was ascribed to tpy-localized $^3\pi,\pi^*$ excited state.

1.2.3. Cyclometalated Ir(III) complexes with different π -conjugation on ligands

Cyclometalated complexes are defined as a type of complexes that contain at least one covalent metal-carbon bond. Thus, the Ir-carbon bond(s) exist(s) in the cyclometalated Ir(III) complexes when C^N ligands are applied. In the past two decades, numerous studies have been focusing on monocationic bis-cyclometalated Ir(III) complexes with a variety of C^N and N^N ligands. Modifications of these ligands via attaching different substituents or extending π -conjugation were then performed. Chart 1.2 illustrates some representative cyclometalated monocationic Ir(III) complexes bearing tris-bidentate ligands with different conjugation lengths.

Huang and coworkers developed a series of monocationic Ir(III) complexes (**Ir1–Ir6**) bearing two identical cyclometalating ligands (1-phenylisoquinoline) but different N^N ligands with varied π -conjugations.⁴⁸ As shown in Figure 1.5, all complexes exhibit intense intraligand $^1\pi,\pi^*$ absorption bands at <400 nm, moderately intense $^1\text{MLCT}/^1\text{LLCT}$ absorption bands at 400 - 500 nm, and weak spin-forbidden $^3\text{MLCT}$ absorption tails beyond 500 nm. Due to the different conjugation lengths on the N^N ligands, the emission energies were tuned from 586 nm for **Ir1** and **Ir2** to 732 nm for **Ir6**. Considering the vibronically resolved photoluminescence spectra of **Ir1** and **Ir2**, the emitting states for these two complexes were attributed to the ligand-centered $^3\pi,\pi^*$ excited states. In contrast, the broad and structureless emission spectra for **Ir3–Ir6** suggested mixed $^3\text{MLCT}/^3\text{LLCT}$ excited states for these complexes (Figure 1.6).

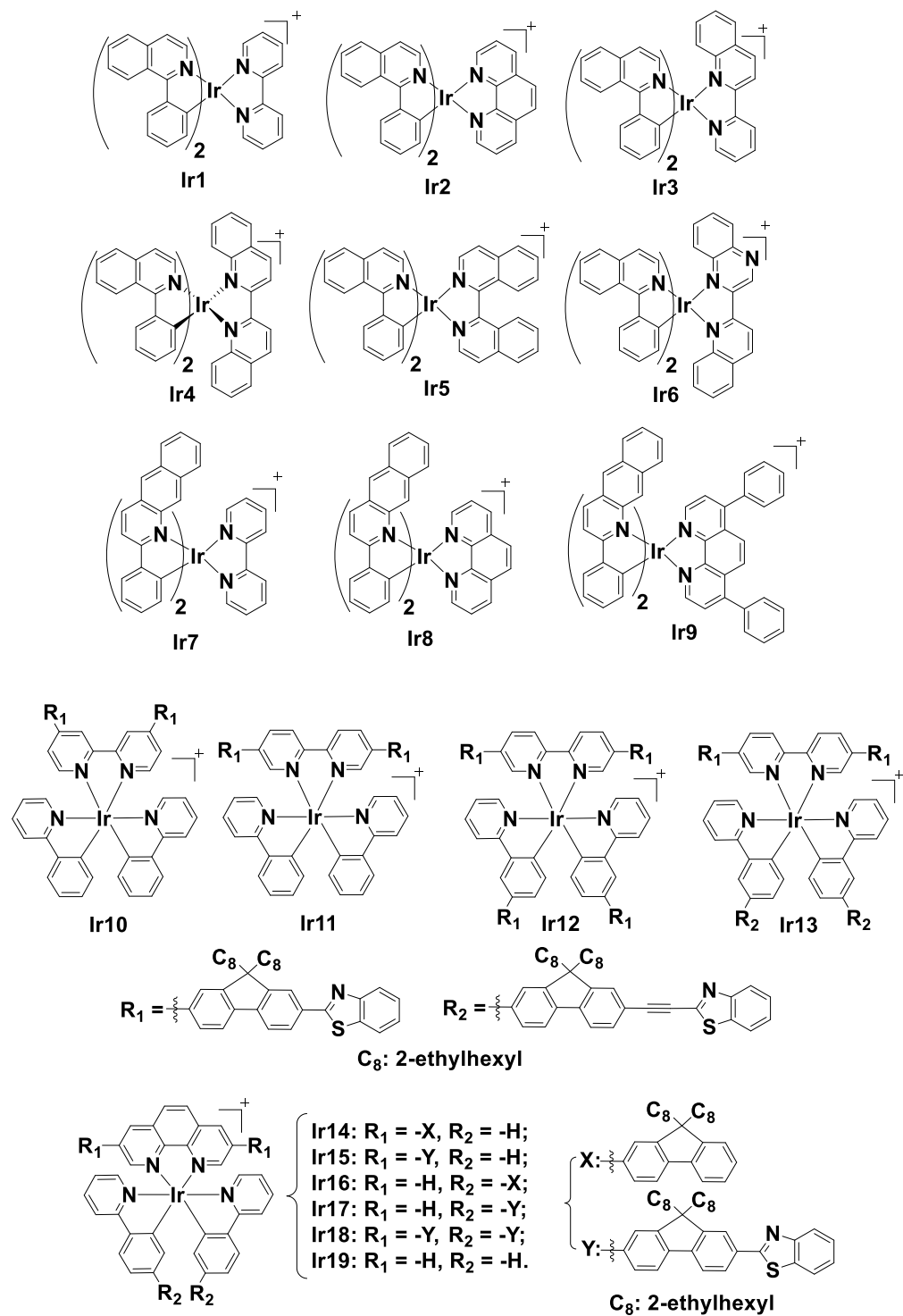


Chart 1.2. Representative biscyclometalated monocationic iridium(III) complexes with different conjugation lengths on the ligands.

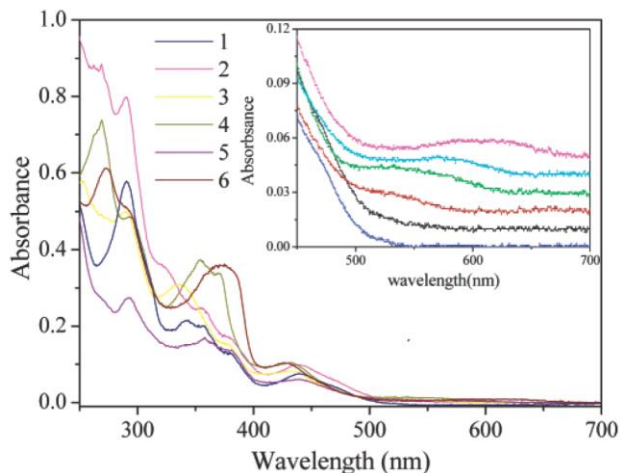


Figure 1.5. Absorption spectra of complexes **Ir1–Ir6** (**Ir1** = 1, **Ir2** = 2, **Ir3** = 3, **Ir4** = 4, **Ir5** = 5, **Ir6** = 6) in CH_2Cl_2 at room temperature. Reprinted with permission from Ref. 48.

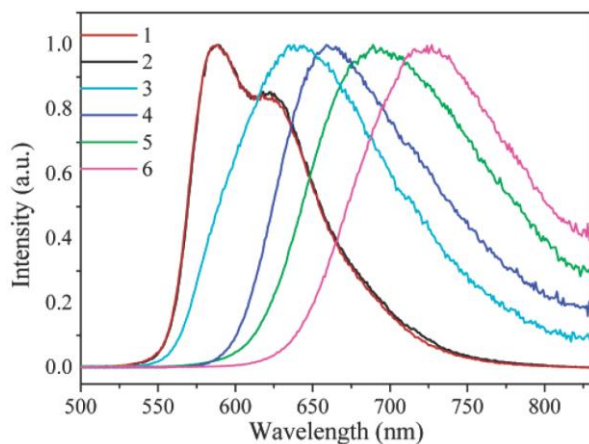


Figure 1.6. Photoluminescence spectra of complexes **Ir1–Ir6** (**Ir1** = 1, **Ir2** = 2, **Ir3** = 3, **Ir4** = 4, **Ir5** = 5, **Ir6** = 6) in degassed CH_2Cl_2 at room temperature. Reprinted with permission from Ref. 48.

Qiao and coworkers reported three near-infrared (NIR) emitting monocationic Ir(III) (**Ir7–Ir9** in Chart 1.2) with different ancillary ligands (**Ir7**: bipyridine; **Ir8**: 1,10-phenanthroline; **Ir9**: 4,7-diphenyl-1,10-phenanthroline), in which large π -conjugated 2-phenylbenzo[*g*]quinoline was used as the cyclometalating ligand.⁴⁹ All complexes hold ligand-centered $^1\pi,\pi^*$ transitions at < 350 nm and mixed $^1\text{MLCT}/^3\text{MLCT}/^3\text{LLCT}$ transitions from 350 to 600 nm. Complexes **Ir7–Ir9** exhibited an emission maximum at 698 nm and a shoulder at

760 nm with a quantum yield of ca. 3%. Since the influence of the different diimine ligands on the emission is limited, the nature of the emitting states was assigned to the C[^]N ligands localized ³ π,π^* mixed with ³CT characters.

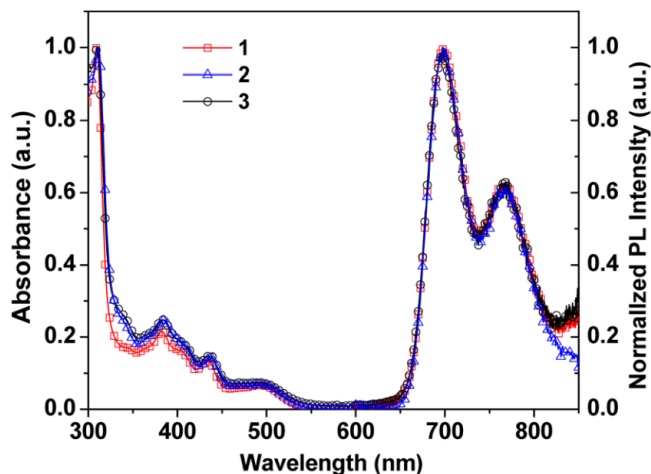


Figure 1.7. Room-temperature absorption (left) and photoluminescence (right) spectra of complexes **Ir7–Ir9** (**Ir7** = 1, **Ir8** = 2, **Ir9** = 3) in degassed CH₂Cl₂. The spectra were recorded on a Jobin Yvon fluorospectrophotometer (FluoroMax-3), by using the manufacturer’s procedure. Reprinted with permission from Ref. 49.

Taking all the aforementioned examples into account, the photophysical properties of the heteroleptic cationic Ir(III) complexes could be easily tuned by changing the degree of π -conjugation of the N[^]N and/or C[^]N ligands. Considering the difficulty of the benzannulation on the ligands, our group adopted another approach to extend the ligand π -conjugation via tethering the π -conjugated substituents to the N[^]N or C[^]N ligands. We reported a systematic study on the photophysics of four cyclometalated Ir(III) complexes (**Ir10–Ir13**) and explored their applications as reverse saturable absorbers.²² The benzothiazolylfluorene motifs were tethered on the bipyridine (**Ir10** and **Ir11**) and the phenylpyridine (**Ir12** and **Ir13**) ligands. The effects of the extended π -conjugation of the N[^]N and/or C[^]N ligands, and the attachment position of the substituents at the N[^]N ligand on the photophysics and RSA strength were investigated. All complexes exhibit spin-allowed intraligand ¹ π,π^* transitions with large extinction coefficient below 475 nm, and very

weak $^1,^3\text{MLCT}$ and $^1,^3\text{LLCT}$ transitions above 475 nm (Figure 1.8). The emission bands of these complexes are attributed to $^3\text{MLCT}/^3\text{LLCT}$ for **Ir1**, $^3\pi, \pi^*$ for **Ir2**, and $^3\text{MLCT}/^3\text{LLCT}/^3\pi, \pi^*$ for **Ir3** and **Ir4**. The variations of the different π -conjugation degrees in ligands alter both the parentage of T_1 states and RSA strength.

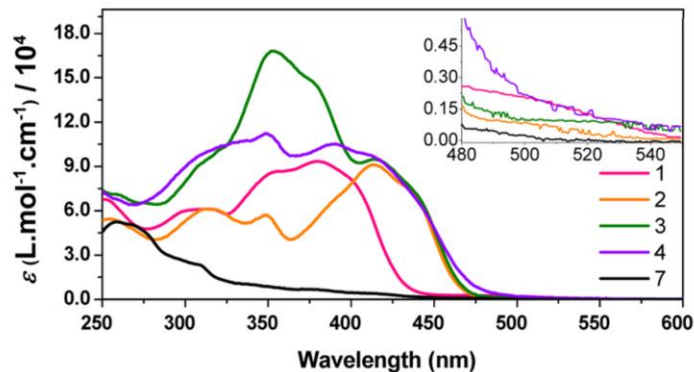


Figure 1.8. Absorption spectra of complexes **Ir10–Ir13** (**Ir10** = 1, **Ir11** = 2, **Ir12** = 3, **Ir13** = 4) in CH_2Cl_2 at room temperature. Reprinted with permission from Ref. 22.

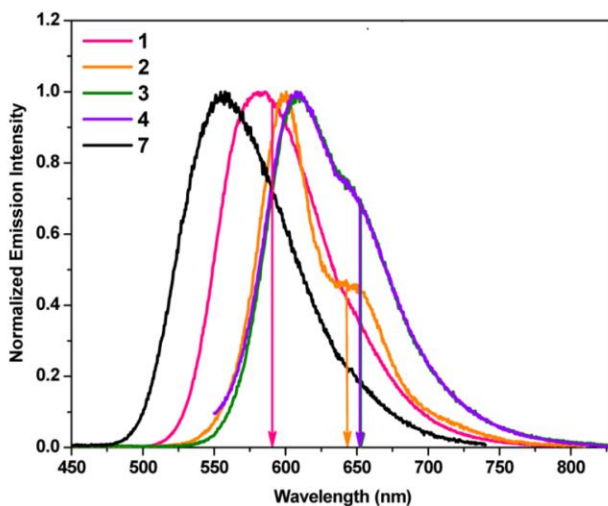


Figure 1.9. Photoluminescence spectra of complexes **Ir10–Ir13** (**Ir10** = 1, **Ir11** = 2, **Ir12** = 3, **Ir13** = 4) in degassed CH_2Cl_2 at room temperature. Reprinted with permission from Ref. 22.

To further understand the influence of extended π -conjugation of the $\text{N}^{\wedge}\text{N}$ or/and $\text{C}^{\wedge}\text{N}$ ligands via tethering π -conjugated substituents on the photophysics of the monocationic Ir(III) complexes, our group studied six other Ir(III) complexes (**Ir14–Ir19**),²⁰ where fluoren-2-yl or 7-

benzothiazolylfluoren-2-yl motifs were attached on the N[^]N or/and C[^]N ligands. The obtained complexes hold N[^]N or C[^]N ligand-localized ¹ $\pi,\pi^*/^1$ ILCT transitions below 450 nm and weak ^{1,3}MLCT/^{1,3}LLCT bands above 450 nm. Modifications of the phenanthroline ligand by introducing fluoren-2-yl or 7-benzothiazolylfluoren-2-yl substituents led to the a red-shift of the main absorption band to 400 and 408 nm for **Ir14** and **Ir15**, respectively. For complexes **Ir16** and **Ir17**, the major absorption bands appear at 325 and 360 nm, respectively. When the 7-benzothiazolylfluoren-2-yl motifs were introduced to both the N[^]N and C[^]N ligands in complex **Ir18**, its absorption spectrum appeared to be a superimposition of the spectra of **Ir15** and **Ir17**. The emission spectra of **Ir14** and **Ir15** were structured and the lifetimes were long (5.6 μ s for **Ir4** and 12.9 μ s for **Ir5**), indicating the substituted phenanthroline-localized ³ π,π^* state being the emitting states. The shorter-lived (0.37-1.38 μ s) and structureless emission spectra of **Ir16**, **Ir17**, and **Ir18** were indicative of the ³CT emitting states. Complexes **Ir14** and **Ir15** with extended π -conjugation at the N[^]N ligand exhibited longer-lived, red-shifted and stronger triplet excited-state absorption in comparison to their respective counterparts **Ir16** and **Ir17** with the π -conjugated substituents at the C[^]N ligands. Therefore, **Ir14** and **Ir15** gave rise to stronger RSA in comparison to **Ir16** and **Ir17**, respectively, at 532 nm.

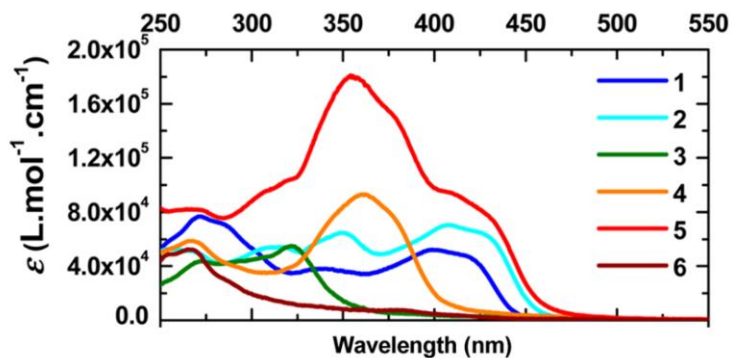


Figure 1.10. Experimental UV–vis absorption spectra of **Ir14–Ir19** (**Ir14** = 1, **Ir15** = 2, **Ir16** = 3, **Ir17** = 4, **Ir18** = 5, **Ir19** = 6) in CH₂Cl₂. Reprinted with permission from Ref. 20.

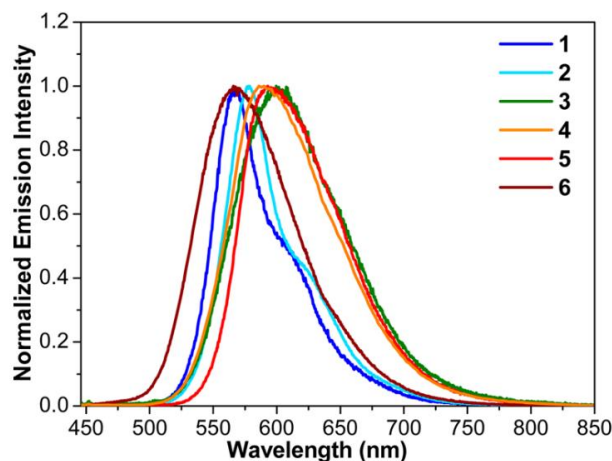


Figure 1.11. Normalized emission spectra of **Ir14–Ir19** (**Ir14** = 1, **Ir15** = 2, **Ir16** = 3, **Ir17** = 4, **Ir18** = 5, **Ir19** = 6) in deaerated CH_2Cl_2 solution, $c = 1 \times 10^{-5} \text{ mol L}^{-1}$. Reprinted with permission from Ref. 20.

1.2.4. Bis–terdentate Ir(III) complexes

Different from the bidentate ligands, terdentate ligands, such as tpy and 2,6–diphenylpyridine, enable one to construct a linearly arranged system of complexes. This could avoid the formation of geometrical *fac*– or *mer*– stereoisomers that was found in the triscyclometalated Ir(III) complexes. These ligands can also be used as building blocks to form multinuclear complexes. Moreover, the photophysical properties of bis–terpyridine Ir(III) complexes ($\text{Ir}(\text{tpy})_2^{3+}$) are greatly influenced by the substituents at the 4-position of tpy. In 1999, the synthetic procedure of a series of $\text{Ir}(\text{tpy})_2^{3+}$ complexes were reported by Collin and coworkers.⁴⁷ Different aryl substituents was attached to the 4-position of tpy ligand. These complexes featured high-lying emitting states ($>2.5 \text{ eV}$) with high efficiencies and long lifetimes (1–2 μs). Based on the published synthetic procedures, several homoleptic and heteroleptic $\text{Ir}(\text{tpy})_2^{3+}$ complexes were designed for a range of applications in recent years. As shown in Chart 1.3, tolyl, benzyl hydroxyphenyl, aniline, methoxyphenyl, or benzoic acid groups were introduced to the 4-position of tpy.

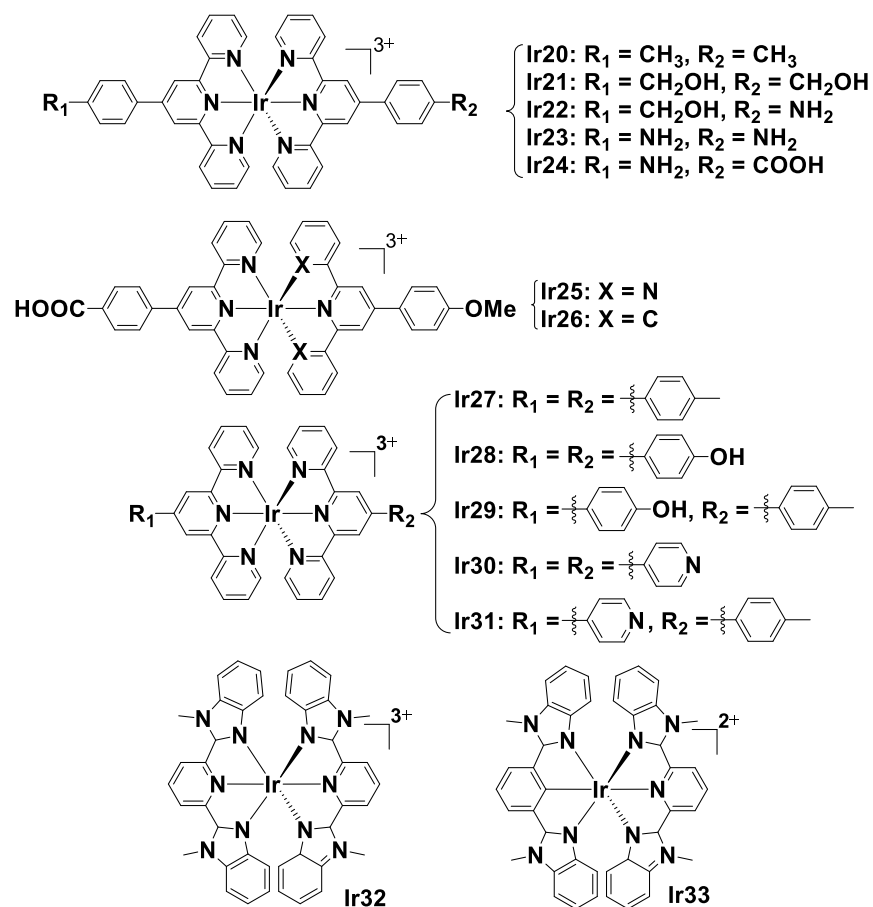


Chart 1.3. Selected examples of bis-terdentate iridium(III) complexes.

For the bis-terpyridine Ir(III) complexes (**Ir20–Ir24**) possessing electron-donating or accepting groups, varied absorption and luminescence properties have been observed.⁵⁷ In contrast to **Ir20** and **Ir21**, the presence of aniline in **Ir22–Ir24** induced strong ¹ILCT absorption bands in the visible spectral region (See Figure 1.12). As presented in Figure 1.13, the electron-donating amino substituent on the phenyl ring increased the energy level of the aryl substituent (π_{ph}) to surpass that of the tpy (π_{tpy}), resulting in ¹ILCT ($\pi_{\text{ph}} \rightarrow \pi_{\text{tpy}}^*$) transition. The homoleptic Ir(III) complex **Ir23** that was incorporated with two amino substituents doubled the intensity of the ¹ILCT absorption band than those in the heteroleptic complexes **Ir22** and **Ir24**. All complexes exhibited emission in both acetonitrile and aqueous solutions originating from the mixed ³ π, π^* ($\pi_{\text{tpy}}^* \rightarrow \pi_{\text{tpy}}$) / ³ILCT ($\pi_{\text{Ar}}^* \rightarrow \pi_{\text{tpy}}$) states (Figure 1.14). Following the energy-gap law, the

low-lying $^3\text{ILCT}$ excited state induced by aniline in complexes **Ir22–Ir24** resulted in a faster nonradiative decay and thus reduced the emission in these complexes. In addition, the emission lifetimes in degassed acetonitrile solutions (3.2–9.6 μs) were shorter than those in degassed aqueous solutions (7.7–21 μs), owing to increased nonradiative decay rates in acetonitrile.

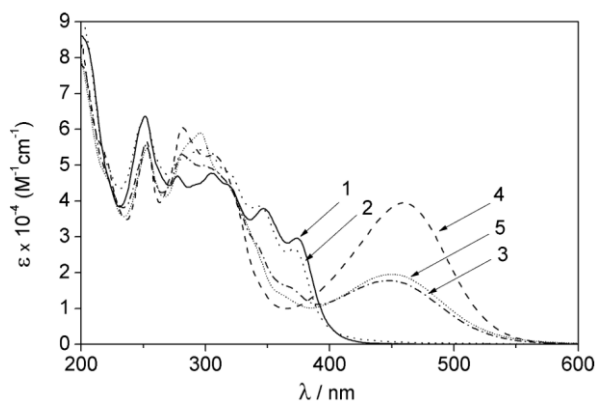


Figure 1.12. The ground-state absorption spectra for complexes **Ir20–Ir24** (**Ir20** = 1, **Ir21** = 2, **Ir22** = 3, **Ir23** = 4, **Ir24** = 5) in CH_3CN at room temperature. Reprinted with permission from Ref. 57.

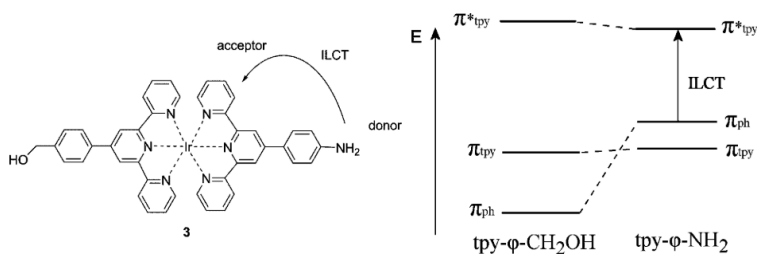


Figure 1.13. The proposed ILCT transition in **Ir22**. Reprinted with permission from Ref. 57.

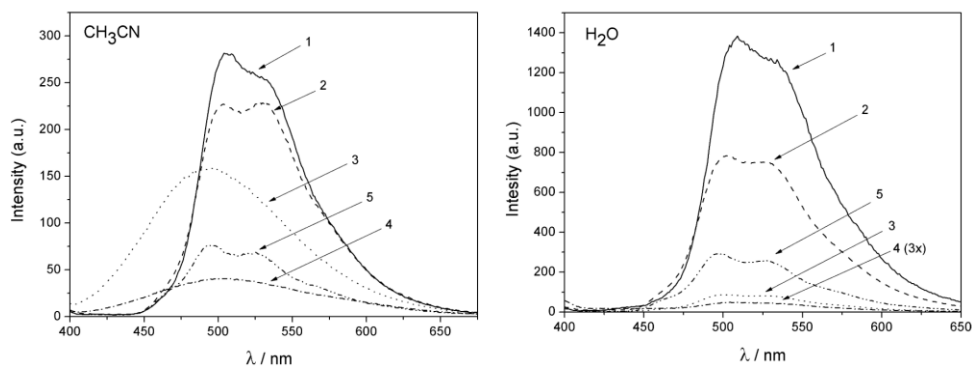


Figure 1.14. Emission spectra for complexes **Ir20–Ir24** (**Ir20** = 1, **Ir21** = 2, **Ir22** = 3, **Ir23** = 4, **Ir24** = 5) in degassed CH_3CN (left) and aqueous (right) at room temperature. Reprinted with permission from Ref. 57.

Two bis-terdentate Ir(III) complexes (**Ir25** and **Ir26**) bearing polypyridyl or cyclometalating ligands for DNA purine bases oxidation were reported by Elias's group.⁵⁸ Electron-withdrawing carboxyl group was introduced to the 4'-position of phtpy and electron-donating methoxy group was incorporated to the 4-phenyl substituent on the other terdentate ligand. In air-saturated solutions, a broad emission band was observed for **Ir25** at 568 nm ($\tau = 470$ ns), whereas dual-emission was observed for **Ir26** at 528 nm ($\tau = 1 \mu\text{s}$) and 697 nm ($\tau = 260$ ns), respectively (Figure 1.15). In the presence of a guanine unit (dGMP), the emission was quenched by a photo-induced electron-transfer process (Figure 1.16). A linear Stern-Volmer correlation between the dGMP's concentration and the luminescence intensity was obtained, which is indicative of the pure dynamic quenching of the excited state for both complexes (see insets of Figure 1.16). The emission of **Ir25** was oxidatively quenched, suggesting a high oxidizing ability of the excited state.

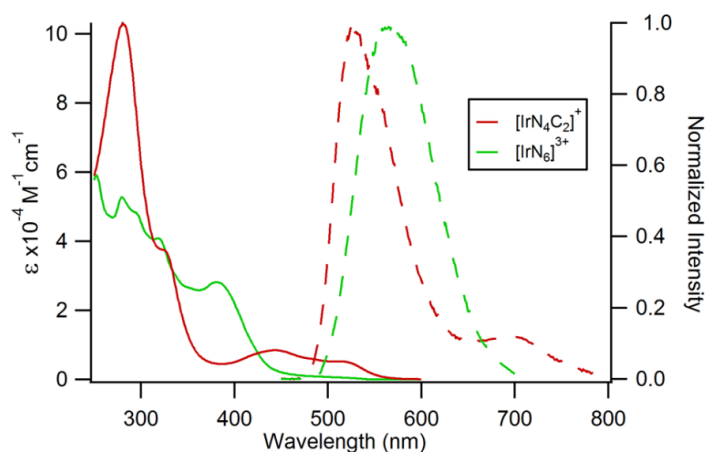


Figure 1.15. The UV-vis absorption (solid line) and emission (dash line) spectra for complexes **Ir25** and **Ir26** (**Ir25** = IrN_6^{3+} , **Ir26** = IrN_4C_2^+) in aerated CH_3CN solutions at room temperature. Reprinted with permission from Ref. 58.

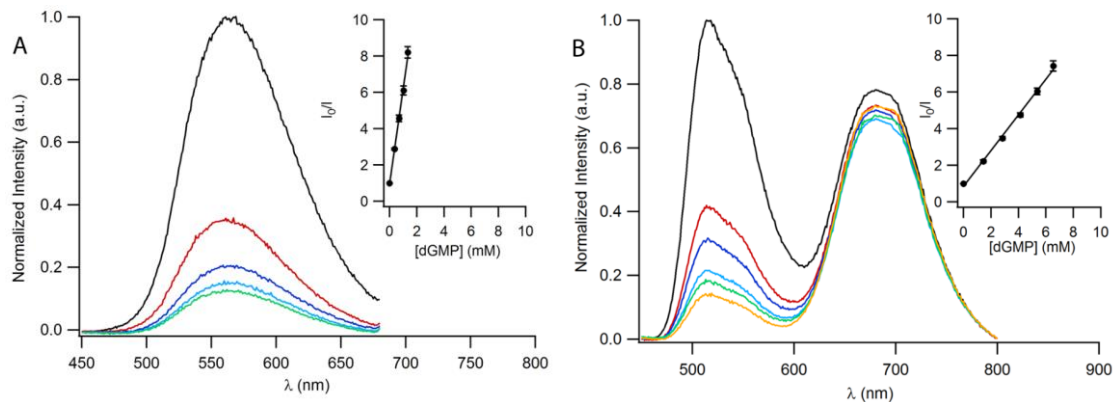


Figure 1.16. Luminescence spectra of (A) **Ir25** and (B) **Ir26** excited at 350 nm with increased concentration of dGMP. Inset: The obtained Stern–Volmer plots for complexes **Ir25** and **Ir26** measured at wavelength of 560 and 514 nm, respectively. Reprinted with permission from Ref. 58.

Williams and coworkers reported a family of bis-terpyridine Ir(III) complexes (**Ir27–Ir31**), in which pyridyl or phenolic groups were attached to the para-position of the central pyridine ring in 2,2':6',2''-terpyridine.⁷³ The phenolic-substituted complexes (**Ir28** and **Ir29**) showed a significant red-shift of the ¹MLCT bands upon protonation (Figure 1.17). The appearance of the solution of **Ir28** became deep orange by increasing the pH to 10, due to the appearance of the band at 468 nm in the absorption spectrum. The spectra of complexes **Ir29** and **Ir31** were similar to that of **Ir27** (Figure 1.18). In addition, the weakly emissive complex **Ir28** was found to be quenched by deprotonating of the phenol ring.

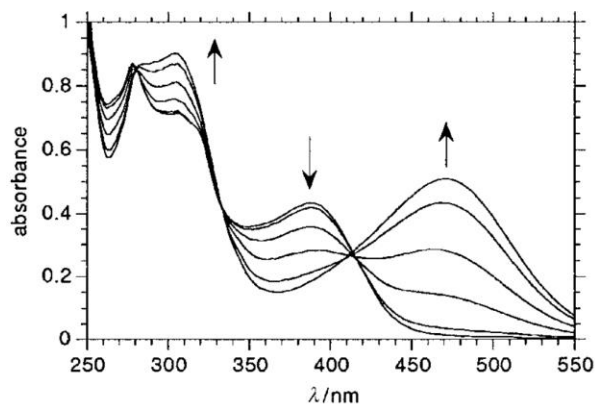


Figure 1.17. The absorption spectra of **Ir28** in aqueous solution at different pH values (5.3, 6.7, 7.6, 8.3, 9.0, 10.1).

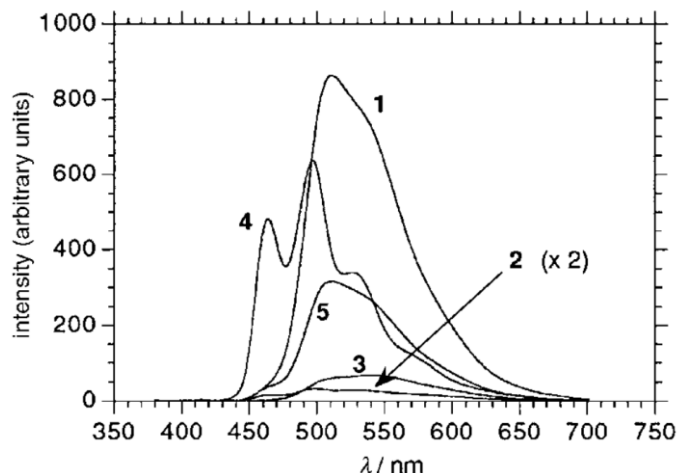


Figure 1.18. The luminescence spectra of the air-equilibrated aqueous solutions of **Ir27–Ir31** (**Ir27** = 1, **Ir28** = 2, **Ir29** = 3, **Ir30** = 4, **Ir31** = 5) at pH 6.0 at room temperature ($\lambda_{\text{ex}} = 364$ nm).

Haga and coworkers developed two bis-terdentate Ir(III) complexes (**Ir32** and **Ir33**), in which 2,6-bis(1-methyl-benzimidazol-2-yl)pyridine and 1,3-bis-(1-methyl-benzimidazol-2-yl)benzene were used as the coordination ligands. As shown in Figure 1.19, **Ir32** and **Ir33** possessed weak absorption bands in a low-energy region (>400 nm), which emanated from the $^1,^3\text{MLCT}$ -based transitions. All Ir(III) complexes exhibited emissions at ca. 600 nm at room temperature (Figure 1.20). The emission spectra of **Ir32** and **Ir33** displayed vibrational progressions at 77 K.

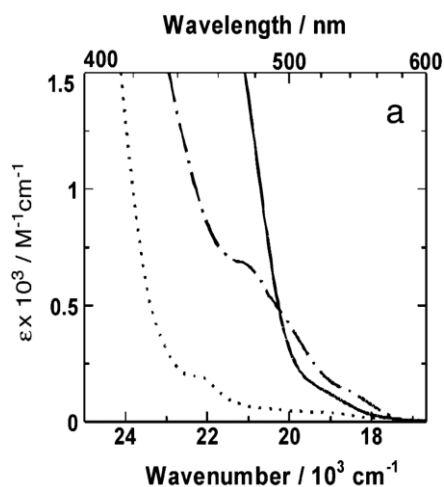


Figure 1.19. UV-vis spectra of **Ir32** (solid line) and **Ir33** (dashed line) in acetonitrile.

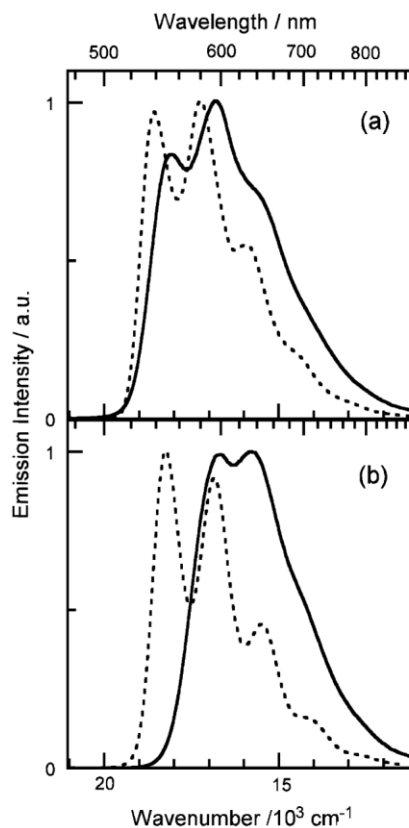


Figure 1.20. Emission spectra of **Ir32** (a) and **Ir33** (b). Solid lines are at room temperature (in MeCN), and dotted lines are at 77 K (in DMF-MeOH-EtOH [1:5:5(v/v)]).

1.3. Cyclometalated Ir(III) complexes for RSA applications

As discussed in the previous section, the ground-state and excited-state properties of the cyclometalated Ir(III) complexes are readily tuned by structural modifications of the N[^]N and/or C[^]N ligands. Moreover, the broad and weaker charge transfer ground-state absorption but much stronger excited-state absorption in the visible spectral region, the high triplet excited-state formation quantum yield, and the long triplet lifetime associated with the cyclometalated Ir(III) complexes match the requirements for RSA quite well. Therefore, RSA of the cyclometalated Ir(III) complexes has been extensively investigated by our group and other groups in the past 15 years. As shown in Chart 1.4, the RSA of several representative cyclometalated Ir(III) complexes will be discussed in the following part.

for ns laser at 1064 nm, which was the result of two-photon absorption (TPA) initiated excited-state absorption (ESA) (Figure 1.21(b)).

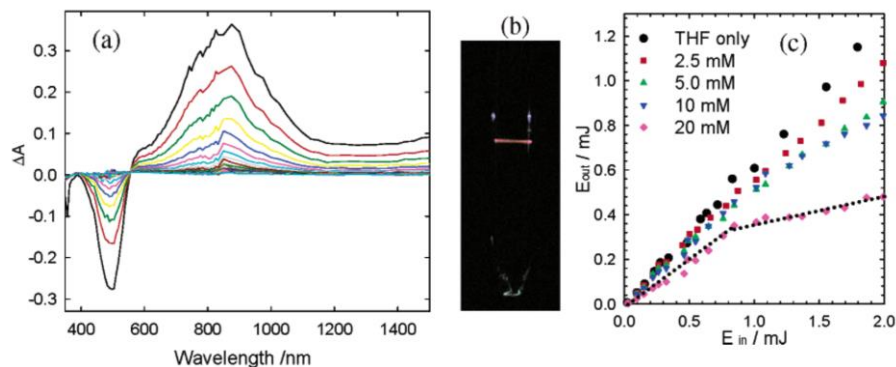


Figure 1.21. (a) TA spectra of **Ir34** in deoxygenated THF solution (b) transmittance of pulsed beam at 1064 nm of **Ir34** in degassed THF solution at various concentrations. Reprinted with permission from Ref. 21.

To understand the effect of extended π -conjugation of the N[^]N ligand on the photophysics and RSA of Ir(III) complexes, our group studied complexes **Ir35–Ir39** in which 2-{3-[7-(benzothiazol-2-yl)fluoren-2-yl]phenyl}pyridine and various diimine ligands, i.e., 2-(pyridin-2-yl)quinoline (**Ir35**), 1,10-phenanthroline (**Ir36**), 2,2'-biquinoline (**Ir37**), and 1,1'-biisoquinoline (**Ir38**), were employed as the C[^]N and N[^]N ligand(s), respectively.⁵¹ Additionally, complex **Ir39** bearing 2-(pyridin-2-yl)quinoline and 2-phenylpyridine ligands was chosen as the reference complex. In the UV-vis absorption spectra, all complexes displayed $^1\pi,\pi^*$ transitions below 400 nm, $^1\text{MLCT}/^1\text{LLCT}$ transitions in the range from 400 to 450 nm, and spin-forbidden $^3\text{MLCT}/^3\text{LLCT}$ transitions above 450 nm (see Figure 1.22). Owing to the extended π -conjugation in the N[^]N ligands, the $^3\text{MLCT}/^3\text{LLCT}$ absorption bands were gradually bathochromically shifted with enhanced extinction coefficients. The emission of these complexes was centered at the wavelengths from 584 to 672 nm in CH₂Cl₂ at room temperature, which was assigned to $^3\text{MLCT}/^3\text{LLCT}$ states (see Figure 1.23). Upon ns laser pulses excitation at 532 nm, all

complexes exhibited very strong RSA effect. The RSA strength followed the trend of **Ir35** \approx **Ir36** > **Ir38** > **Ir37** > **Ir39**, which paralleled the cross-section ratios between the excited-state and ground-state absorption at 532 nm (see Figure 1.24).

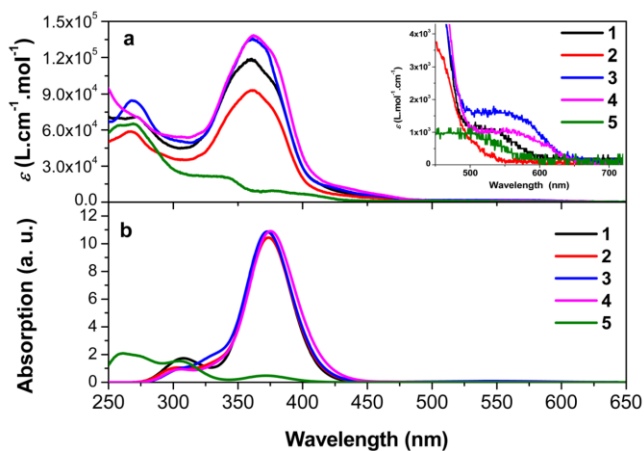


Figure 1.22. Experimental (a) and calculated (b) ground-state absorption spectra of all complexes (**Ir35** = 1, **Ir36** = 2, **Ir37** = 3, **Ir38** = 4, **Ir39** = 5) in CH₂Cl₂. Reprinted with permission from Ref. 51.

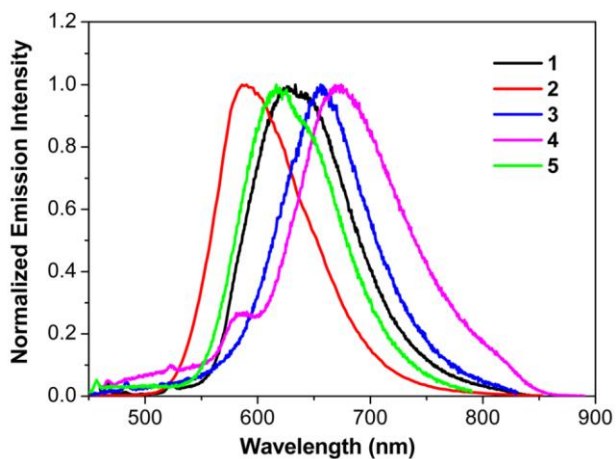


Figure 1.23. Normalized emission spectra of all complexes in degassed CH₂Cl₂. Reprinted with permission from Ref. 51.

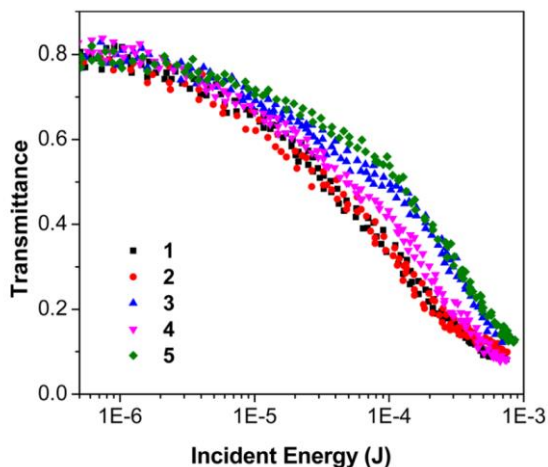


Figure 1.24. Reverse saturable absorption for complexes (**Ir35** = 1, **Ir36** = 2, **Ir37** = 3, **Ir38** = 4, **Ir39** = 5) in 2 mm thick toluene (80% linear transmission) for 532 nm 4.1 ns laser pulses at room temperature. Reprinted with permission from Ref. 51.

Unlike extending the π -conjugation on the N[^]N ligands, our group reported seven Ir(III) complexes (**Ir40–Ir46**) bearing 2,2'-bipyridine ligand but varying the π -conjugation of the cyclometalating C[^]N ligands.⁵⁰ As depicted in Figure 1.25, all complexes displayed intense high-energy ligand-localized $^1\pi,\pi^*$ transitions and lower-energy $^1\text{MLCT}$ / $^1\text{LLCT}$ transitions in the UV-vis absorption spectra. The emission bands of these complexes could be tuned from 500 to 670 nm with the emitting states being $^3\pi,\pi^*/^3\text{MLCT}$ for **Ir40**, $^3\pi,\pi^*/^3\text{MLCT}/^3\text{LMCT}$ for **Ir41**, **Ir42**, and **Ir43**, $^3\pi,\pi^*$ transitions for **Ir44** and **Ir45**, and $^3\pi,\pi^*/^3\text{MLCT}/^3\text{LMCT}/^3\text{LLCT}$ for **Ir46**. Besides, these complexes possessed broadband transient absorption, as illustrated in Figure 1.26. The long-lived transient species in complexes **Ir41**, **Ir42**, **Ir44**, and **Ir45** with varied TA spectra were measured, suggesting the C[^]N ligand-centered $^3\pi,\pi^*$ nature of the lowest triplet excited states. The complexes **Ir40**, **Ir41**, and **Ir46** hold short-lived transient absorption, which are indicative of more ^3CT characters in their transient species. Except for **Ir46**, all complexes exhibited strong RSA effects. The obtained RSA strength followed the trend of **Ir46** < **Ir40** < **Ir43**

$\text{Ir45} < \text{Ir44} \approx \text{Ir42} \approx \text{Ir41}$, which was approximately associated with the ΔOD values at 532 nm (Figure 1.27).

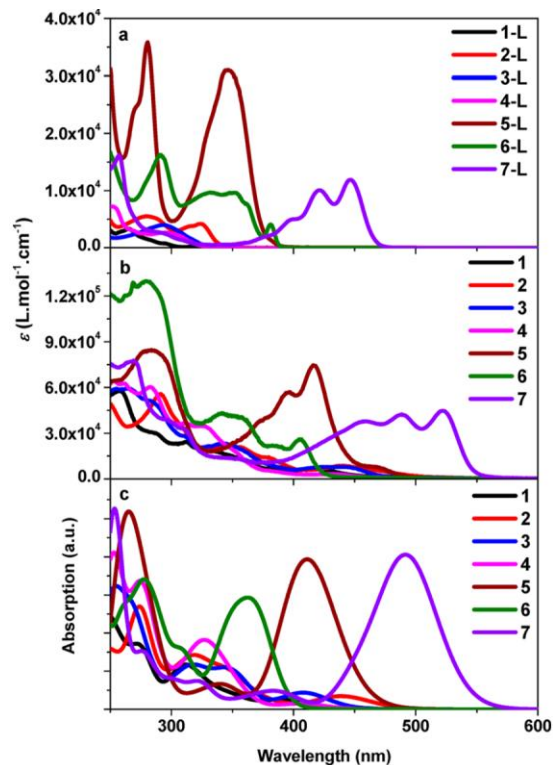


Figure 1.25. Experimental ground-state absorption spectra of (a) C^N ligands (1: benzo[H]quinoline; 2: 1-phenylisoquinoline, 3: 1-(2-pyridyl)naphthalene, 4: 2-(2-pyridyl)naphthalene, 5: 1-(2-pyridyl)pyrene, 6: 1,2-diphenyl-pyreno[4,5-d]imidazole, 7: 3-(2-pyridyl)perylene) and (b) complexes **Ir40–Ir46** (**Ir40** = 1, **Ir41** = 2, **Ir42** = 3, **Ir43** = 4, **Ir44** = 5, **Ir45** = 6, **Ir46** = 7) in CH₂Cl₂ at room temperature and (c) calculated UV-vis spectra all complexes in CH₂Cl₂ at 0 K. Reprinted with permission from Ref. 50.

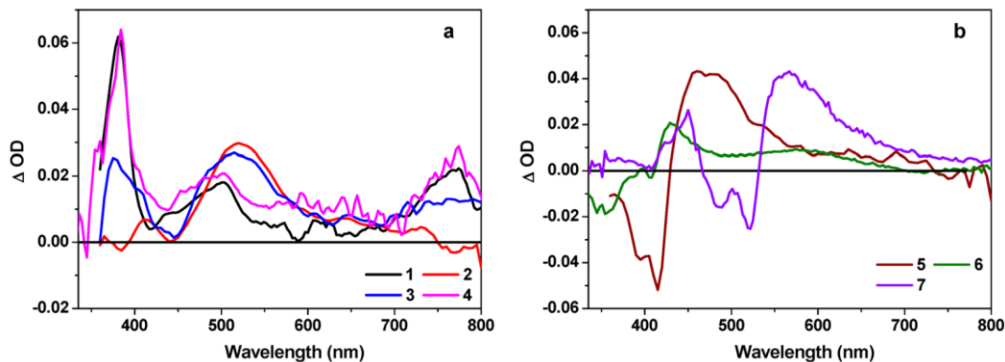


Figure 1.26. Nanosecond triplet TA spectra of complexes **Ir40–Ir46** (**Ir40** = 1, **Ir41** = 2, **Ir42** = 3, **Ir43** = 4, **Ir44** = 5, **Ir45** = 6, **Ir46** = 7) at zero-time decay in acetonitrile. Reprinted with permission from Ref. 50.

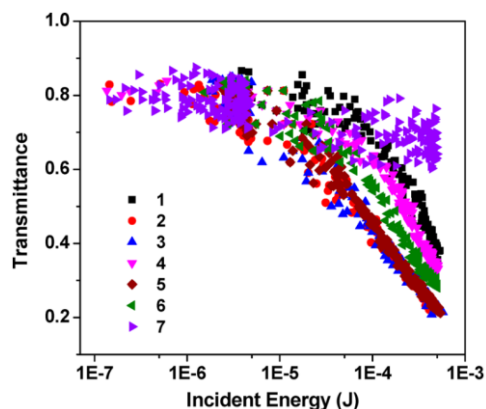


Figure 1.27. Nonlinear transmission plot of **Ir40–Ir46** (**Ir40** = 1, **Ir41** = 2, **Ir42** = 3, **Ir43** = 4, **Ir44** = 5, **Ir45** = 6, **Ir46** = 7) at the linear transmittance of 80% in CH₂Cl₂ solution in a 2 mm cuvette for 532 nm 4.1 ns laser. Reprinted with permission from Ref. 50.

In contrast to the benzannulation, our group also reported the photophysics and RSA study of complexes **Ir47–Ir50** with different π -conjugation lengths on the C^N ligands via tethering large π -conjugated motifs.¹⁸ As discussed in the previous section, all complexes exhibit positive TA absorption at 532 nm, indicating stronger excited-state absorption than that of the ground state. Compared to the *para*-substitution, the *meta*-substitution results in a higher phosphorescence intensity and longer-lived triplet excited state. The RSA strength followed the order of **Ir50** > **Ir49** \approx **Ir48** > **Ir47** (Figure 1.28), suggesting the complex with *para*-substituted C^N ligands displayed a stronger RSA at 532 nm.

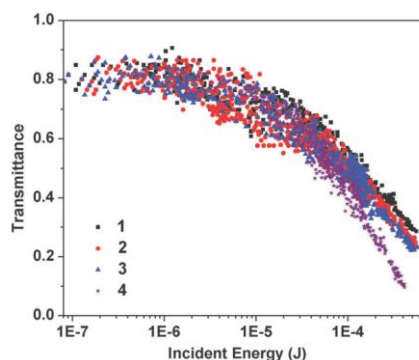


Figure 1.28. Reverse saturable absorption for **Ir47–Ir50** (**Ir47**= 1, **Ir48** = 2, **Ir49** = 3, **Ir50** = 4) in CH₂Cl₂ in a 2 mm cuvette for 532 nm nanosecond laser pulses. Reprinted with permission from Ref. 18.

We also reported the TA and RSA studies of cationic heteroleptic Iridium(III) complexes (**Ir14–Ir19**) with a tethered fluoren-2-yl or 7-benzothiazolylfluoren-2-yl substituent on the 2-phenylpyridine and/or phenanthroline ligands.²⁰ As shown in the TA spectra (Figure 1.29), complexes **Ir14–Ir19** possessed positive absorption signals at 532 nm, indicating that RSA could occur at this wavelength. The transient absorption absorption of **Ir14** and **Ir15** are attributed to the substituted phenanthroline ligand-localized $^3\pi,\pi^*$ states, while the observed TA of **Ir16–Ir19** was attributed to predominantly the $^3\text{MLCT}/^3\text{LLCT}$ states. The RSA strength decreased as **Ir18** \approx **Ir15** > **Ir17** \approx **Ir14** > **Ir16**, which coincided with the $\sigma_{\text{ex}}/\sigma_0$ ratios for most of the complexes (Figure 1.30). In comparison to **Ir16** and **Ir17** bearing π -conjugated substituents at the C^N ligands, tethering the π -conjugated substituents to the N^N ligand (**Ir14**, **Ir15**, and **Ir18**) not only caused the red-shifted major ground-state and triplet excited-state absorption bands, but also enhanced the RSA strength.

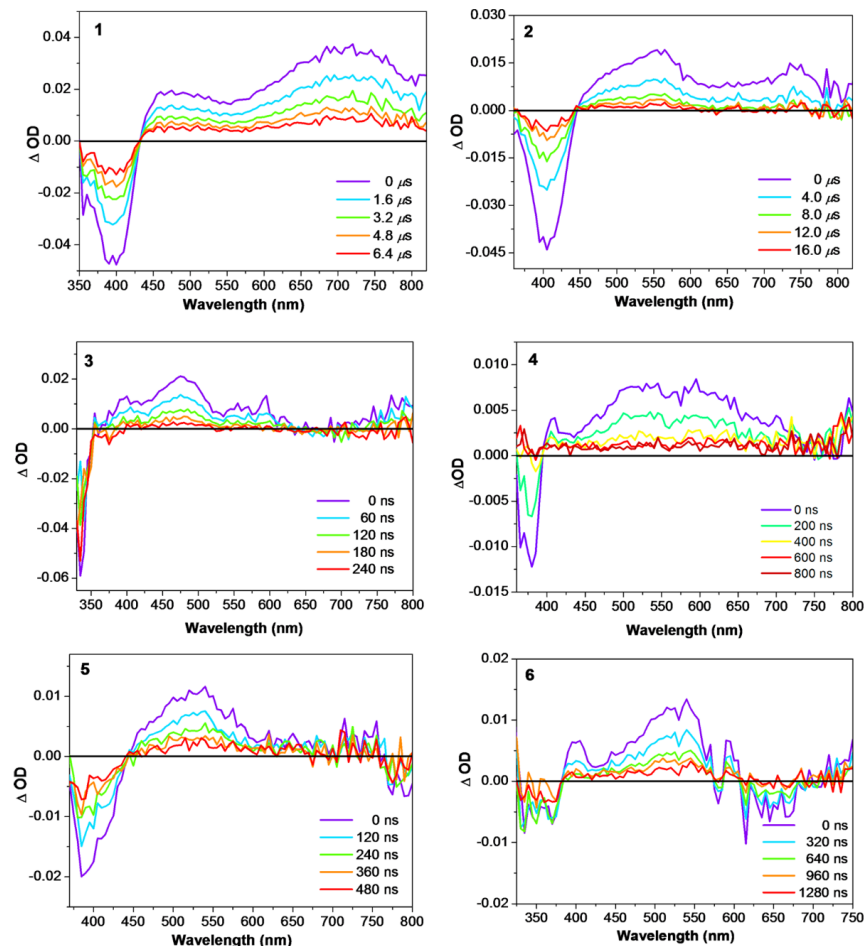


Figure 1.29. Time-resolved triplet TA spectra of Ir14–Ir19 (Ir14 = 1, Ir15 = 2, Ir16 = 3, Ir17 = 4, Ir18 = 5, Ir19 = 6) in toluene solution in a 1-cm cuvette ($\lambda_{\text{ex}} = 355 \text{ nm}$, $A_{355} = 0.4$). Reprinted with permission from Ref. 20.

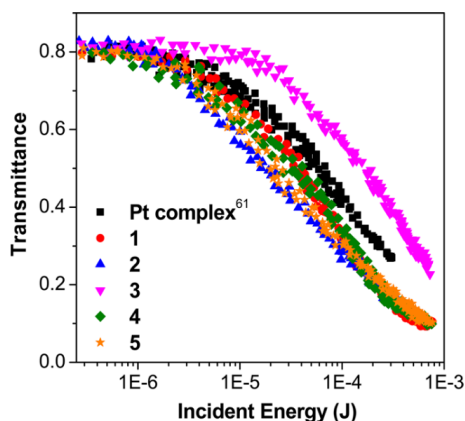


Figure 1.30. Reverse saturable absorption for complexes Ir14–Ir18 (Ir14 = 1, Ir15 = 2, Ir16 = 3, Ir17 = 4, Ir18 = 5) for 4.1 ns laser pulses at 532 nm in 2-mm thick toluene solution. Reprinted with permission from Ref. 20.

1.4. Applications of heteroleptic Ir(III) complexes in PDT

To date, high quantum yields for triplet excited state formation and long-lived triplet excited states for efficient ROS generation even if under hypoxia have been reported for some Ir(III) complexes. Meanwhile, Ir(III) complexes were found to be specifically localized in mitochondria, lysosomes, endoplasmic reticulum, or nuclei in a variety of the cancer cell lines. More interestingly, due to their luminescence properties, these Ir(III) complexes can also be utilized as biomolecular probes and cellular imaging reagents.

Because of these fascinating photophysical properties, Ir(III) complexes were explored as photosensitizers for PDT. To date, a variety of cyclometalated Ir(III) complexes were reported to exhibit high singlet oxygen generation efficiency and organelle-targeting ability.⁶²⁻⁶⁵ For the examples of cyclometalated Ir(III) complexes shown in Chart 1.5, their photophysical and biological properties can be substantially tuned by the peripheral ligands, which will be discussed below.

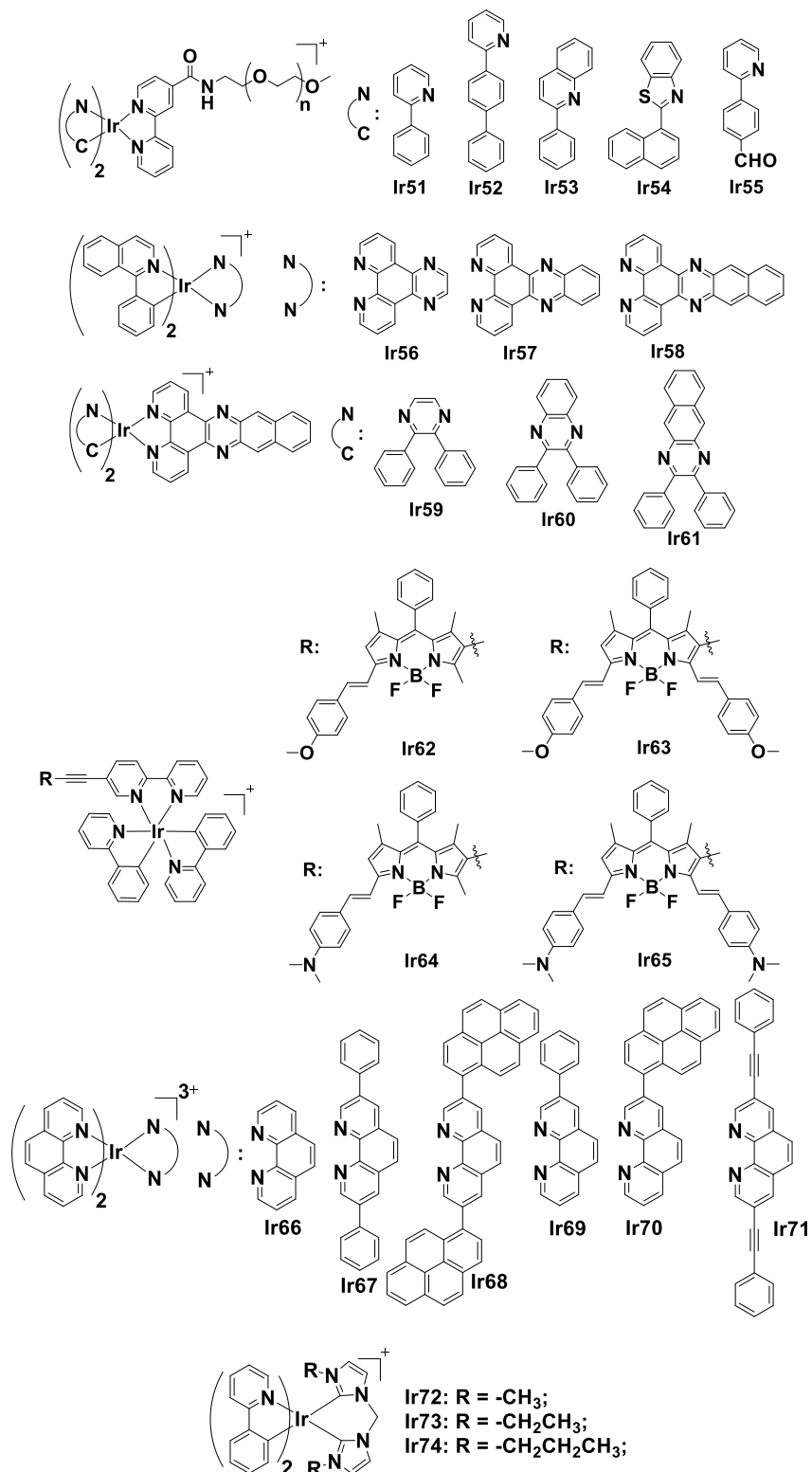


Chart 1.5. Selected examples of cyclometalated iridium(III) complexes for phototherapeutic studies.

Lo et al. developed several phosphorescent water-soluble Ir(III) complexes (**Ir51 – Ir55**), in which photophysical and photochemical characteristics were adjusted through altering the cyclometalating ligands.⁶² The attachment of PEG chains could help to minimize the cytotoxicity in the dark due to the decreased unfavorable interactions between PSs and biomolecules. The observed emission wavelengths ranged from green to orange-red due to the varied energy levels of the emitting states. The short-lived ³CT state and long-lived ³IL state were found to be the lowest triplet excited states for **Ir51 – Ir53** and **Ir54 – Ir55**, respectively. Therefore, the quantum yield of ¹O₂ generation increased following **Ir51 < Ir52 < Ir53 < Ir55 < Ir54**, which is dependent on the triplet excited-state lifetimes of these complexes. All reagents showed very low dark toxicity toward HeLa cells, indicating these PEG-based PSs were noncytotoxic in the dark. Their IC₅₀ values upon 365 nm light irradiation were in the range of 3.4 to 23.2 μM.

To red-shift the ground-state absorption and meanwhile keep a long-lived triplet excited state, our group reported six Ir(III) complexes (**Ir56 – Ir61**) with different π-conjugation lengths on both the N[^]N and the C[^]N ligands as PSs for PDT.⁶³ Red-shifted ground-state absorption and prolonged triplet excited states were observed in **Ir59 – Ir61** via extending the π-conjugation on the C[^]N ligands. In complexes **Ir56 – Ir58**, benzannulation at the N[^]N ligands did not alter the lowest ground-state absorption bands but significantly prolonged the lowest triplet excited state. Without light activation, **Ir56 – Ir58** were accumulated on the membrane, whereas **Ir59 – Ir61** localized on the whole cancer cell. Among them, **Ir61** presented the largest phototherapeutic indices (PI) toward SK-MEL-28 (Dark IC₅₀: 144 ± 56.9 μM, Vis IC₅₀: 0.354 ± 0.066 μM, PI = 407) and HL60 (Dark IC₅₀: 83.9 ± 1.40 μM, Vis IC₅₀: 0.588 ± 0.052 μM, PI = 143) cell lines upon broadband visible light (400-700 nm) activation. Such a high photosensitization efficiency of **Ir57**

can be attributed to its broad absorption from the visible to the NIR region and its extremely long-lived $^3\pi,\pi^*$ -based lowest triplet excited states.

To further red-shift the ground-state absorption to the far-red or NIR regions, Zhao and coworkers⁶⁴ designed four cyclometalated Ir(III) complexes (**Ir62** – **Ir65**) with a monostyryl/distyryl-substituted BODIPY motif attached to the 2,2'-bipyridine ligand. All complexes showed strong absorption in the regions of 644–729 nm. Owing to a stronger electron-donating ability of the dimethylamino group at the BODIPY (**Ir64** and **Ir65**) motif, NIR absorption bands were observed in **Ir64** and **Ir65**. These complexes were found to possess very long-lived BODIPY-based $^3\pi,\pi^*$ states, i.e. 106.6 μs for **Ir62**, 156.5 μs for **Ir63**, 92.5 μs for **Ir64**, and 31.4 μs for **Ir65**, which paralleled their singlet oxygen generation efficiencies, i.e. 0.53 for **Ir62**, 0.81 for **Ir63**, 0.06 for **Ir64**, and 0.02 for **Ir65**. However, their *in vitro* PDT effects were marginal due to the high dark toxicity ($\text{IC}_{50} = 8.16 - 16.70 \mu\text{M}$ toward 1121 or LLC cell lines) and small PI values (1.3-3.8).

Recently, our group developed a family of tricationic heteroleptic Ir(III) complexes (**Ir66** – **Ir71**) incorporating tris-diimine ligands.⁶⁵ All complexes possessed two phenanthroline (phen) ligands and one R-phen ligand (R = H, phenyl, pyrenyl, phenylethynyl). With the increased π -conjugation of the R substituent, the triplet lifetimes of **Ir68** and **Ir70** became much longer (>30 μs). The singlet oxygen generation quantum yields for **Ir68** and **Ir70** were 81% and 72%, respectively. Their PIs toward SK-MEL-28 cells were 248 (Dark IC_{50} : $67.0 \pm 0.9 \mu\text{M}$, Vis IC_{50} : $0.27 \pm 0.01 \mu\text{M}$) for **Ir68** and >435 (Dark IC_{50} : >300 μM , Vis IC_{50} : $0.69 \pm 0.01 \mu\text{M}$) for **Ir70**.

Three cyclometalated Ir(III) complexes (**Ir72** – **Ir74**) containing *N*-heterocyclic carbene (NHC) ligands were reported by Mao and coworkers, which were used as mitochondria-targeting PSs for PDT study.⁶⁶ Different alkyl substituents were attached on the N1 position of the NHC

ligand (methyl for **Ir72**, ethyl for **Ir73**, and propyl for **Ir74**). All complexes exhibited weak charge-transfer absorption bands at >360 nm, which are attributed to the $^1,^3\text{MLCT}$ transitions. The $^1\text{O}_2$ generation capability of these complexes decreased in the following order: **Ir74** ($\Phi_{\Delta} = 0.62$) $>$ **Ir73** ($\Phi_{\Delta} = 0.59$) $>$ **Ir72** ($\Phi_{\Delta} = 0.58$). In view of the anticancer activities, these Ir(III) complexes exhibited much higher cytotoxicity upon irradiation at 365 nm toward different cell lines, including HeLa, MCF-7, A549, A549R, HepG2, and LO2, which are better than cisplatin. The mitochondrial damage in HeLa cells was confirmed for **Ir72** – **Ir74** upon irradiation. Notably, PI value of **Ir74** against A549R cells is up to 3488 (Dark IC_{50} : $3.0 \pm 0.2 \mu\text{M}$, Vis IC_{50} : $0.00086 \pm 0.00002 \mu\text{M}$). However, these complexes can only be activated by the UV light, which prevents their potential applications as PDT reagents.

1.5. Synthesis of Ir(III) complexes

Generally, it is relatively challenging to carry out a coordination reaction on Ir(III) because of its inertness. Compared to the Ru(II) complexes, harsher reaction conditions are required for formation of Ir(III) complexes. To activate the metal center, a variety of methods have been explored for coordination of the Ir(III) ion. One feasible method is adding silver salts, such as AgOTf, AgNO₃, and Ag₂O, to remove the chloride and enhance the coordination activity of the center metal. Another commonly used method is increasing the reaction temperature for the coordination reaction. In this dissertation, the employed synthetic procedures for the tris–bidentate cyclometalated Ir(III) complexes and the bis–terdentate Ir(III) complexes are presented in Chart 1.6 and Chart 1.7, respectively.^{50,38}

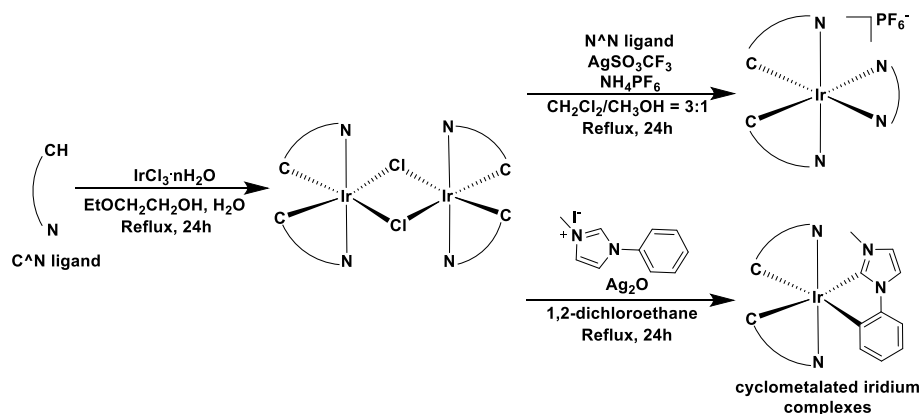


Chart 1.6. General synthesis route for tris-bidentate cyclometalated Ir(III) complexes.

For the synthesis of tris-bidentate cyclometalated Ir(III) complexes bearing N^N or N-heterocyclic carbene (NHC) ligands, the dinuclear [Ir(ppy)₂(μ-Cl)]₂ intermediates were first prepared by using Ir(III) chloride hydrate and two equivalents of cyclometalating ligands in the mixture of 2-ethoxyethanol and water ($v/v = 3/1$) under reflux for 24 hours. Then, the obtained dinuclear complex precursor was treated with two equivalence of N^N (or NHC) ligand in a mixed solvent of CH₂Cl₂ and methanol ($v/v = 3/1$) for the N^N ligand or 1,2-dichloroethane for the NHC ligand to afford the target cyclometalated cationic (or neutral) Ir(III) complexes. To reduce the formation of by-products, these two-step reactions should be protected from light and oxygen.

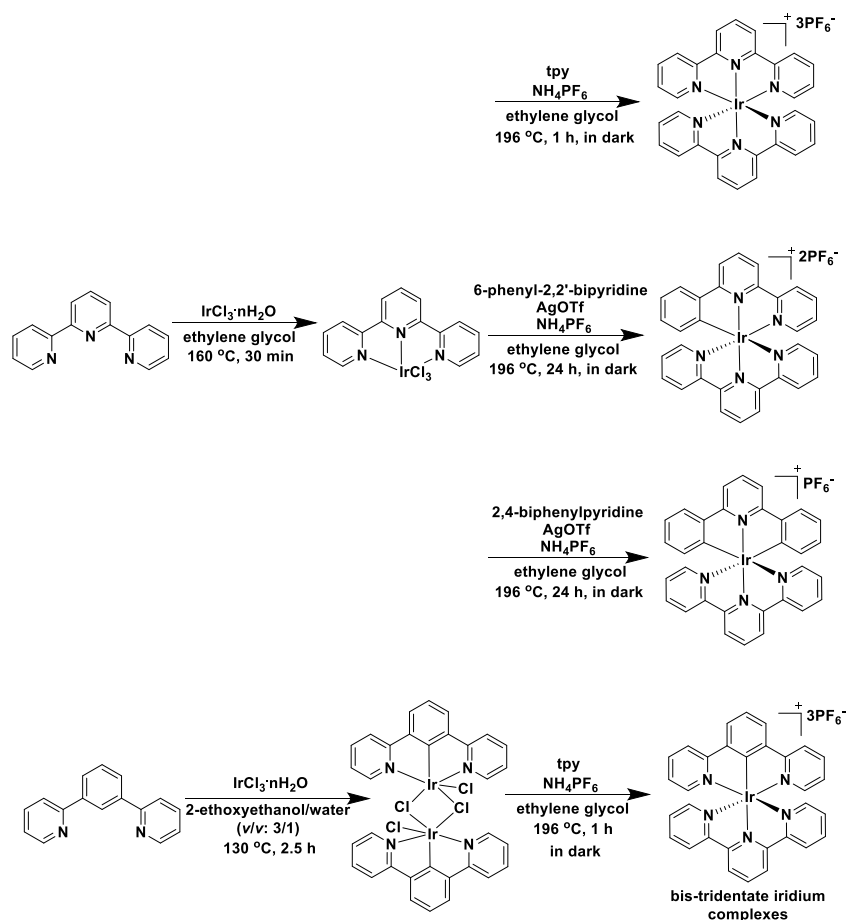


Chart 1.7. General synthesis route for bis-tridentate Ir(III) complexes.

The synthesis of bis-tridentate Ir(III) complexes is illustrated in Chart 1.7.^{47,59,60,61} In this procedure, tpy was treated with Ir(III) chloride hydrate in ethylene glycol for 30 min at 160 °C in dark to afford tpy-IrCl₃ as the intermediate. To obtain the Ir(tpy)₂³⁺ based complexes, tpy-IrCl₃ reacts with another tpy ligands in ethylene glycol under reflux for 1 hour under N₂ atmosphere and avoid light. In contrast, synthesis of the other two types of bis-tridentate Ir(III) complexes, i.e. (C[^]N[^]N)Irtpy²⁺ and (C[^]N[^]C)Irtpy⁺ needs harsher reaction conditions, which involves Ag⁺ catalyst and longer reaction times, due to the poorer coordination ability of carbon. For the (N[^]C[^]N)Irtpy²⁺ complexes, however, 1,3-di(pyrid-2-yl)benzene should first react with iridium trichloride hydrate in mixed solvent of 2-ethoxyethanol and water (v/v = 3/1) to form a

[Ir(dpyb)Cl(μ -Cl)]₂ as the reactive dimer. The subsequent reaction involved the dimer and tpy ligand in refluxed ethylene glycol for 1 h, which was similar to the synthesis of Ir(tpy)₂³⁺. Similar to the synthesis of tris-bidentate complexes, these two-step reactions need to be carried out under noble gas atmosphere without direct light exposure.

1.6. Designing criteria for reverse saturable absorbers

In the past two decades, our group has been focusing on develop Ir(III) complexes for RSA based optical limiting applications. To effectively decrease the transmittance of lasers at high intensity, complexes with suitable photophysical properties are required. Generally, to optimize the RSA strength, these complexes need a large ratio of ESA cross section (σ_{ex}) relative to that of the ground state (σ_0). To augment the $\sigma_{\text{ex}}/\sigma_0$ values, a low intensity of ground-state absorption (not zero) but strong ESA at the interested wavelengths is desired. Meanwhile, long-lived excited-states capable of undergoing a long-time light absorption before decay to its ground state, is another desired preliminary property. Based on the discussion in the previous sections, Ir(III) complexes hold spin-allowed ligand-centered ¹ π,π^* transitions with high intensity in the UV spectral region and ¹MLCT/¹LLCT transitions with low intensity in the visible spectral region. To increase the RSA strength over a broad spectral region, expanding the weakly absorptive ¹CT bands is our ultimate interest.

In view of the metal center, the ligand field strength of transition metal partially dominates its excited-state properties, which increases from the first-row to the third-row metals. Generally, the first-row transition metal complexes commonly possess a short-lived triplet excited state due to the readily accessible non-radiative d,d state. As a third-row transition metal, a long-lived

excited state was obtained for most of the Ir(III) complexes, in which d,d state is elevated to a higher energy. Herein, RSA are expected for Ir(III) complexes incorporating appropriate ligands.

1.7. Designing criteria for photosensitizer in PDT research

The application of PDT to cancers mainly depends on the development of more effective PSs. To date, developing new PSs with tumor-specific targeting, strong absorption in the NIR region, long-lived triplet excited state, and high ROS production efficiency in hypoxia still remains to be a challenge. In general, several clinically relevant criteria need to be considered for designing new PSs.⁴²

(1) Toxicity. An appropriate PS should be capable of efficient $^1\text{O}_2$ and/or ROS generation upon light irradiation at an appropriate wavelength, namely it should be highly phototoxic. Meanwhile, it should be non-toxic or have low toxicity without light activation. The photo- and dark-toxicities are closely related to the structures of PSs.

(2) Amphiphilicity. PSs with good water-solubility travel human body easily. To meet this requirement, compounds with multiple charges and/or hydrophilic moieties are desired. On the other hand, a PS needs to pass the cell membrane to enter the cell, which requires some lipophilicity. Therefore, an suitable PS should be amphiphilic.

(3) Penetration depths. In biological tissues, penetration of the light is proportional to its wavelength. For instance, the penetration depth for light at a wavelength of 400 nm is 1 mm; whereas, light at a wavelength of 630 nm results in about 10 mm depth. To utilize PDT for the treatment of deep-seated tumors, red- (or NIR-) light activatable PSs are desired. By using dyes-tethered molecules, the absorption wavelength of PSs can be tuned to the desired spectral region.

(4) T₁ state. Long-lived T₁ state with an appropriate energy level and a high quantum yield of formation is the most important feature for an PS to effectively convert photon energy into ¹O₂ and/or ROS. For the development of Ir(III) complex PSs, π, π^* nature for the T₁ state yields long T₁ lifetime, which can be realized by tethering π -conjugated organic chromophores to the Ir(III) complex or extending the π -conjugation for the ligands.

(5) Targetability. Accumulation of PSs on tumors rather than normal tissues, and specific targeting of certain organelles inside of cancer cells, such as mitochondria, lysosomes, and nuclei, are beneficial to improve the PDT efficiency and reduce the side effects.

(6) Cost. An effective PS at a reasonable cost will help the treatment of cancer patients.

With all of the aforementioned criteria in mind, new PS design should fulfill as many of them as possible with the understanding that some compromises need to be made at times.

1.8. Objectives of my dissertation

By design and synthesis of Ir(III) complexes with different types of ligands, three major goals are anticipated to be realized in this dissertation: (1) To establish a structure-property correlation via modification of the ligand π -conjugation and/or attaching π -conjugated organic chromophores to the core ligands. To realize this goal, spectroscopic measurement, such as the UV-vis absorption, emission, and transient absorption studies, and computational simulation of the optical spectra for the synthesized complexes were carried out; (2) Optimizing the RSA strength of the Ir(III) complexes at 532 nm and developing some broadband reverse saturable absorbers; (3) Developing red or NIR absorbing PSs with optimized triplet excited-state properties for theranostic PDT applications. To fulfill these objectives, six series of Ir(III) complexes bearing a variety of N^N or C^N ligands were synthesized and investigated:

(1) Tuning the Ground State and Excited State Properties of Monocationic Iridium(III) Complexes by Varying the Site of Benzannulation on Diimine Ligand.

(2) Impact of Benzannulation Site at the Diimine (N^N) Ligand on the Photophysics and Reverse Saturable Absorption of Cyclometalated Monocationic Iridium(III) Complexes.

(3) Effects of Varying the Benzannulation Site and π -Conjugation of Cyclometalating Ligand on Photophysics and Reverse Saturable Absorption of Monocationic Iridium(III) Complexes.

(4) Monocationic Iridium(III) Complexes with Far-Red Charge Transfer Absorption and Near-IR Emission: Synthesis, Photophysics, and Reverse Saturable Absorption.

(5) Photophysical and Photobiological Properties of Dinuclear Iridium(III) Bis-tridentate Complexes.

(6) Neutral Iridium(III) Complexes Bearing BODIPY-Substituted N-Heterocyclic Carbene (NHC) Ligands: Synthesis, Photophysics, and Photobiological Activities.

1.9. References

- ¹ Kesarkar, S.; Mróz, W.; Penconi, M.; Pasini, M.; Destri, S.; Cazzaniga, M.; Ceresoli, D.; Mussini, P. R.; Baldoli, C.; Giovanella, U.; Bossi, *Angew. Chem. Int. Ed.* **2016**, *55*, 2714.
- ² Wong, W.-Y.; Zhou, G.-J.; Yu, X.-M.; Kwok, H.-S.; Tang, B.-Z. *Adv. Funct. Mater.* **2006**, *16*, 838.
- ³ Rausch, A. F.; Thompson, M. E.; Yersin, H. *J. Phys. Chem. A* **2009**, *113*, 5927.
- ⁴ Lamansky, S.; Djurovich, P.; Murphy, D.; Abdel-Razzaq, F.; Lee, H.-E.; Adachi, C.; Burrows, P. E.; Forrest, S. R.; Thompson, M. E. *J. Am. Chem. Soc.*, **2001**, *123*, 4304.

- ⁵ Momblona, C.; Ertl, C. D.; Pertegás, A.; Junquera–Hernández, J. M.; Bolink, H. J.; Constable, E. C.; Sessolo, M.; Ortí, E.; Housecroft, C. E. *J. Mater. Chem. C* **2018**, *6*, 12679.
- ⁶ González, I.; Dreyse, P.; Cortés–Arriagada, D.; Sundararajan, M.; Morgado, C.; Brito, I.; Roldán–Carmona, C.; Bolink, H. J.; Loeb, B. *Dalton. Trans.* **2015**, *44*, 14771.
- ⁷ Matteucci, E.; Baschieri, A.; Mazzanti, A.; Sambri, L.; Ávila, J.; Pertegás, A.; Bolink, H. J.; Monti, F.; Leoni, E.; Armaroli, N. *Inorg. Chem.* **2017**, *56*, 10584.
- ⁸ Lo, K. K.–W.; Chung, C.–K.; Zhu, N. *Chem. – A Eur. J.* **2003**, *9*, 475.
- ⁹ Lo, K. K.–W.; Chung, C.–K.; Lee, T. K.–M.; Lui, L.–H.; Tsang, K. H.–K.; Zhu, N. *Inorg. Chem.* **2003**, *42*, 6886.
- ¹⁰ Lo, K. K.–W.; Ng, D. C.–M.; Chung, C.–K. *Organometallics*, **2001**, *20*, 4999.
- ¹¹ Sato, S.; Morikawa, T.; Kajino, T.; Ishitani, O. *Angew. Chem.* **2013**, *125*, 1022.
- ¹² Rackl, D.; Kreitmeier, P.; Reiser, O. *Green Chem.* **2016**, *18*, 214.
- ¹³ Lalevée, J.; Tehfe, M.–A.; Dumur, F.; Gigmes, D.; Blanchard, N.; Morlet–Savary, F.; Fouassier, J. P. *ACS Macro Lett.* **2012**, *1*, 286.
- ¹⁴ Ye, R.–R.; Tan, C.–P.; He, L.; Chen, M.–H.; Ji, L.–N.; Mao, Z.–W. *Chem. Commun.* **2014**, *50*, 10945.
- ¹⁵ Maggioni, D.; Galli, M.; D’Alfonso, L.; Inverso, D.; Dozzi, M. V.; Sironi, L.; Iannaccone, M.; Collini, M.; Ferruti, P.; Ranucci, E.; D’Alfonso, G. *Inorg. Chem.* **2015**, *54*, 544.
- ¹⁶ Huang, H.; Banerjee, S.; Sadler, P. J. *ChemBioChem* **2018**, *19*, 1574.
- ¹⁷ Huang, T.; Yu, Q.; Liu, S.; Huang, W.; Zhao, Q. *Dalton. Trans.* **2018**, *47*, 7628.
- ¹⁸ Sun, W.; Pei, C.; Lu, T.; Cui, P.; Li, Z.; McCleese, C.; Fang, Y.; Kilina, S.; Song, Y.; Burda, C. *J. Mater. Chem. C* **2016**, *4*, 5059.
- ¹⁹ Li, Y.; Dandu, N.; Liu, R.; Kilina, S.; Sun, W. *Dalton. Trans.* **2014**, *43*, 1724.

- 20 Li, Y.; Dandu, N.; Liu, R.; Li, Z.; Kilina, S.; Sun, W. *J. Phys. Chem. C* **2014**, *118*, 6372.
- 21 Kim, K.-Y.; Farley, R. T.; Schanze, K. S. *J. Phys. Chem. B* **2006**, *110*, 17302.
- 22 Li, Y.; Dandu, N.; Liu, R.; Hu, L.; Kilina, S.; Sun, W. *ACS Appl. Mater. Interfaces* **2013**, *5*, 6556.
- 23 Balzani, V.; Juris, A.; Venturi, M.; Campagna, S.; Serroni, S. *Chem. Rev.* **1996**, *96*, 759.
- 24 You, Y.; Nam, W. *Chem. Soc. Rev* **2012**, *41*, 7061.
- 25 You, Y.; Park, S. Y. *J. Chem. Soc. Dalton. Trans.* **2009**, 9226, 1267.
- 26 Zhang, B.; Li, Y.; Liu, R.; Pritchett, T. M.; Azenkeng, A.; Ugrinov, A.; Haley, J. E.; Li, Z.; Hoffmann, M. R.; Sun, W. *Chem. – A Eur. J.* **2012**, *18*, 4593.
- 27 Sun, W.; Zhang, B.; Li, Y.; Pritchett, T. M.; Li, Z.; Haley, J. E. *Chem. Mater.* **2010**, *22*, 6384.
- 28 Li, X.; Lee, S.; Yoon, J. *Chem. Soc. Rev.* **2018**, *47*, 1174.
- 29 Celli, J. P.; Spring, B. Q.; Rizvi, I.; Evans, C. L.; Samkoe, K. S.; Verma, S.; Pogue, B. W.; Hasan, T. *Chem. Rev.* **2010**, *110*, 2795.
- 30 Kelland, L. The Resurgence of Platinum-Based Cancer Chemotherapy. *Nat. Rev. Cancer* **2007**, *7*, 573.
- 31 Atkins, P. W. *Molecular Quantum Mechanics*; Oxford University Press, New York, **1983**.
- 32 Ingle, J. D. J.; Crouch, S. R. *Spectrochemical Analysis*. Old Tappan, NJ (US), **1988**.
- 33 Lichtman, J. W.; Conchello, J.-A. *Nat. Methods* **2005**, *2*, 910.
- 34 Ribas Gispert, J. *Coordination Chemistry*; Wiley-VCH, **2008**.
- 35 Wayne, R. P. *Principles and Applications of Photochemistry*; Oxford University Press, New York, **1988**.
- 36 Turro, N. J. *Modern Molecular Photochemistry*; University Science Books, **1991**.

- ³⁷ Gilbert, A.; Baggott, J. E. *Essentials of Molecular Photochemistry*; Blackwell Scientific Publications: Oxford ;;Boston, 1991.
- ³⁸ Koziar, J. C.; Cowan, D. O. *Acc. Chem. Res.* **1978**, *11*, 334.
- ³⁹ Damrauer, N. H.; Cerullo, C. V.; Yeh, J. K.; Boussie; Shank; McCusker. *Science* **1997**, *275*, 54.
- ⁴⁰ Gorman, A.; Killoran, J.; O'shea, C.; Kenna, T.; Gallagher, W. M.; O'shea, D. F. In Vitro Demonstration of the Heavy-Atom Effect for Photodynamic Therapy. *J. Am. Chem. Soc.*, **2004**, *126*, 10619.
- ⁴¹ Dolmans, D. E. J. G. J.; Fukumura, D.; Jain, R. K. *Nat. Rev. Cancer* **2003**, *3*, 380.
- ⁴² Allison, R. R.; Downie, G. H.; Cuenca, R.; Hu, X.-H.; Childs, C. J.; Sibata, C. H. *Photodiagnosis Photodyn. Ther.* **2004**, *1*, 27.
- ⁴³ Martin, B.; Waind, G. M. *J. Chem. Soc.* **1958**, 4284.
- ⁴⁴ Sajoto, T.; Djurovich, P. I.; Tamayo, A.; Yousufuddin, M.; Bau, R.; Thompson, M. E.; Holmes, R. J.; Forrest, S. R. *Inorg. Chem.* **2005**, *44*, 7992.
- ⁴⁵ Tamayo, A. B.; Alleyne, B. D.; Djurovich, P. I.; Lamansky, S.; Tsyba, I.; Ho, N. N.; Bau, R.; Thompson, M. E. *J. Am. Chem. Soc.*, **2003**, *125*, 7377.
- ⁴⁶ Wu, S.-H.; Ling, J.-W.; Lai, S.-H.; Huang, M.-J.; Cheng, C. H.; Chen, I.-C. *J. Phys. Chem. A* **2010**, *114*, 10339.
- ⁴⁷ Collin, J.-P.; Dixon, I. M.; Sauvage, J.-P.; Williams, J. A. G.; Barigelletti, F.; Flamigni, L.; *J. Am. Chem. Soc.*, **1999**, *121*, 5009.
- ⁴⁸ Zhao, Q.; Liu, S.; Shi, M.; Wang, C.; Yu, M.; Li, L.; Li, F.; Yi, T.; Huang, C. *Inorg. Chem.* **2006**, *45*, 6152.

- ⁴⁹ Zhang, G.; Zhang, H.; Gao, Y.; Tao, R.; Xin, L.; Yi, J.; Li, F.; Liu, W.; Qiao, J. *Organometallics* **2014**, *33*, 61.
- ⁵⁰ Li, Z.; Cui, P.; Wang, C.; Kilina, S.; Sun, W. *J. Phys. Chem. C* **2014**, *118*, 28764–28775.
- ⁵¹ Liu, R.; Dandu, N.; Chen, J.; Li, Y.; Li, Z.; Liu, S.; Wang, C.; Kilina, S.; Kohler, B.; Sun, W. *J. Phys. Chem. C* **2014**, *118*, 23233.
- ⁵² Tamayo, A. B.; Garon, S.; Sajoto, T.; Djurovich, P. I.; Tsyba, I. M.; Bau, R.; Thompson, M. *E. Inorg. Chem.*, **2005**, *44*, 8723
- ⁵³ Nazeeruddin, Md. K.; Wegh, R. T.; Zhou, Z.; Klein, C.; Wang, Q.; De Angelis, F.; Fantacci, S.; Grätzel, M. *Inorg. Chem.*, **2006**, *45*, 9245.
- ⁵⁴ Hasan, K.; Bansal, A. K.; Samuel, I. D. W.; Roldán–Carmona, C.; Bolink, H. J.; Zysman–Colman, E. *Sci. Rep.* **2015**, *5*, 1.
- ⁵⁵ Pal, A. K.; Cordes, D. B.; Slawin, A. M. Z.; Momblona, C.; Ortí, E.; Samuel, I. D. W.; Bolink, H. J.; Zysman–Colman, E. *Inorg. Chem.* **2016**, *55*, 10361.
- ⁵⁶ Skórka, Ł.; Filapek, M.; Zur, L.; Małecki, J. G.; Pisarski, W.; Olejnik, M.; Danikiewicz, W.; Krompiec, S. *J. Phys. Chem. C* **2016**, *120*, 7284.
- ⁵⁷ Goldstein, D. C.; Cheng, Y. Y.; Schmidt, T. W.; Bhadbhade, M.; Thordarson, P. *Dalton. Trans.* **2011**, *40*, 2053.
- ⁵⁸ Jacques, A.; Kirsch–De Mesmaeker, A.; Elias, B. *Inorg. Chem.* **2014**, *53*, 1507.
- ⁵⁹ Polson, M.; Fracasso, S.; Bertolasi, V.; Ravaglia, M.; Scandola, F. *Inorg. Chem.*, **2004**, *43*, 1950.
- ⁶⁰ Wilkinson, A. J.; Puschmann, H.; Howard, J. A. K.; Foster, C. E.; Williams, J. A. G. *Inorg. Chem.* **2006**, *45*, 8685.

- ⁶¹ Auffrant, A.; Barbieri, A.; Barigelletti, F.; Collin, J. P.; Flamigni, L.; Sabatini, C.; Sauvage, J. P. *Inorg. Chem.* **2006**, *45*, 10990.
- ⁶² Li, S. P.-Y.; Lau, Chris T. -S.; Louie, M. -W.; Lam, Y. -W.; Cheng, S. H.; Lo, K. K. -W. *Biomaterials* **2013**, *34*, 7519.
- ⁶³ Wang, C.; Lystrom, L.; Yin, H.; Hetu, M.; Kilina, S.; McFarland, S.A.; Sun, W. *Dalton Trans.* **2016**, *45*, 16366.
- ⁶⁴ Majumdar, P.; Yuan, X.; Li, S.; Guennic, B. L.; Ma, J.; Zhang, C.; Jacqueminde, D.; Zhao J. *J. Mater. Chem. B*, **2014**, *2*, 2838.
- ⁶⁵ Wang, L.; Monro, S.; Cui, P.; Yin, H.; Liu, B.; Cameron, C. G.; Xu, W.; Hetu, M.; Fuller, A.; Kilina, S.; McFarland, S. A.; Sun, W. *ACS Appl. Mater. Interfaces* **2019**, *11*, 3629.
- ⁶⁶ Li, Y.; Tan, C.-P.; Zhang, W.; He, L.; Ji, L.-N.; Mao, Z.-W. *Biomaterials* **2015**, *39*, 95.
- ⁶⁷ Tutt, L. W.; Boggess, T. F. *Prog. Quantum Electron.* **1993**, *17*, 299.
- ⁶⁸ Robertson, J.; Smith, A.; Duignan, J.; Milsom, P.; Bourhill, G. *Appl. Phys. Lett.* **2001**, *78*, 1183.
- ⁶⁹ Henari, F. Z. *J. Opt. A: Pure Appl. Opt.* **2001**, *3*, 188.
- ⁷⁰ Reddy, K. P. *J. Curr. Sci.* **1991**, *61*, 520.
- ⁷¹ Berezin, M. Y.; Achilefu, S. *Chem. Rev.* **2010**, *110*, 2641.
- ⁷² Demas, J. N.; Crosby, G. A. *J. Phys. Chem.* **1971**, *75*, 991–1024.
- ⁷³ Licini, M.; Williams, J. A. G. *Chem. Commun.*, **1999**, 1943.
- ⁷⁴ Yutaka, T.; Obara, S.; Ogawa, S.; Nozaki, K.; Ikeda, N.; Ohno, T.; Ishii, Y.; Sakai K.; Haga, M.-A. *Inorg. Chem.*, **2005**, *44*, 4737.

2. TUNING THE GROUND STATE AND EXCITED STATE PROPERTIES OF MONOCATIONIC IRIDIUM(III) COMPLEXES BY VARYING THE SITE OF BENZANNULATON ON DIIMINE LIGAND

2.1. Introduction

In the last two decades, octahedral d^6 Ir(III) complexes have attracted extensive interest due to the strong spin-orbit coupling induced by the Ir(III) ion, which increases the triplet excited-state quantum yield and induces strong phosphorescence in fluid solutions at room temperature.¹⁻³ Many of the research has focused on monocationic iridium(III) complexes because of the facile synthesis of these complexes under mild reaction condition and the vast amount of choices for the diimine (N^N) and the cyclometalating (C^N) ligands.⁴⁻⁶ The interesting electronic absorption and emission properties of the Ir(III) complexes make them attractive candidates for applications in organic light emitting diodes (OLEDs), solar energy conversion, luminescent biological labeling, etc.⁷⁻⁹

It has been well understood that the absorption and emission characteristics of the monocationic iridium complexes can be readily tuned by modification of the N^N and/or C^N ligands.¹⁰⁻¹² Extensive electrochemical and/or computational studies show that the lowest unoccupied molecular orbital (LUMO) of these Ir(III) complexes is typically located on the N^N ligand; while the highest occupied molecular orbital (HOMO) is delocalized on the C^N ligands and the d -orbital of the Ir(III) center.¹³⁻¹⁵ Thus electron-donating or withdrawing substituents on the N^N ligand could lead to hypsochromic or bathochromic shifts of the lowest-energy charge transfer transition by destabilization or stabilization of LUMO.¹⁶ On the other hand, introducing π -conjugated substituents on the N^N ligand could alter the nature of the lowest triplet excited

state (T_1 state).¹⁷⁻²⁰ Bryce's group,¹⁷ Schanze's group,¹⁸ and our group^{19,20} had discovered that extending the π -conjugation of the $N^{\wedge}N$ ligand via incorporating π -conjugated substituents admixed the $N^{\wedge}N$ ligand localized $^3\pi,\pi^*$ character with the 3CT (charge transfer) characters in the T_1 state of the Ir(III) complexes, or even switched the T_1 state from the 3CT state to the $^3\pi,\pi^*$ state. This change increased the T_1 lifetime and enhanced the triplet excited-state absorption drastically.

Another commonly used approach to extend the π -conjugation of the ligand is benzannulation. It has been found, however, that benzannulation could cause either blue or red shifts of the absorption and / or emission bands depending on the site of benzannulation.²¹⁻³⁰ Although this phenomenon was mostly observed in various small organic molecules,²¹⁻²⁴ it has been rarely reported in organometallic complexes.²⁵⁻³⁰ Thompson and Gordon groups discovered this phenomenon in a series of $(N^{\wedge}N^{\wedge}N)PtCl$ complexes ($N^{\wedge}N^{\wedge}N = 2,5$ -bis(2-pyridylimino)pyrrolate and its benzannulated analogs) and explained this unusual behavior via molecular orbital theory.²⁵ Balzani's group and Turro's group revealed the blue shifted absorption or emission bands of Ru(II) complexes when benzannulation occurred at the 4,5-position of the bipyridine ligand²⁷ or fusion aromatic ring(s) at the 5,6-position of the phenanthroline ligand.²⁸ In contrast, benzannulation at either the 3,4- or 5,6-position of the bipyridine ligand in Ir(III) complexes caused red shifts of the lowest energy absorption band and the emission band in comparison to the nonbenzannulated complex.^{29,30}

To understand whether the site-selective blue or red-shifts upon benzannulation of the $N^{\wedge}N$ ligand is a general feature that could occur in other transition-metal complexes, we designed and synthesized a series of monocationic Ir(III) complexes (Chart 2.1). These complexes all feature 1,2-diphenyl-9*H*-pyreno[4,5-*d*]imidazole (dppi) as the $C^{\wedge}N$ ligands, but the $N^{\wedge}N$ ligands contain varied degrees of π -conjugation via benzannulation at different positions of 2-(pyridin-2-

yl)quinoline. Dppi was chosen as the C^N ligand because previous work demonstrated that Ir(III) complexes bearing this ligand had dramatically long triplet excited-state lifetimes^{31,32} and broad excited-state absorption,³¹ which is a desirable feature for reverse saturable absorbers^{19,20,31} and triplet photosensitizers for triplet-triplet annihilation upconversion.³²

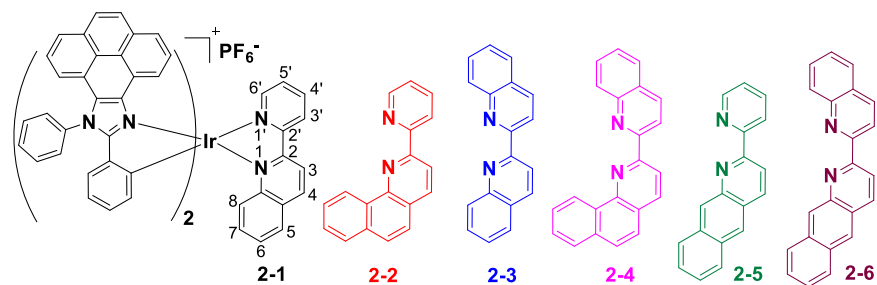


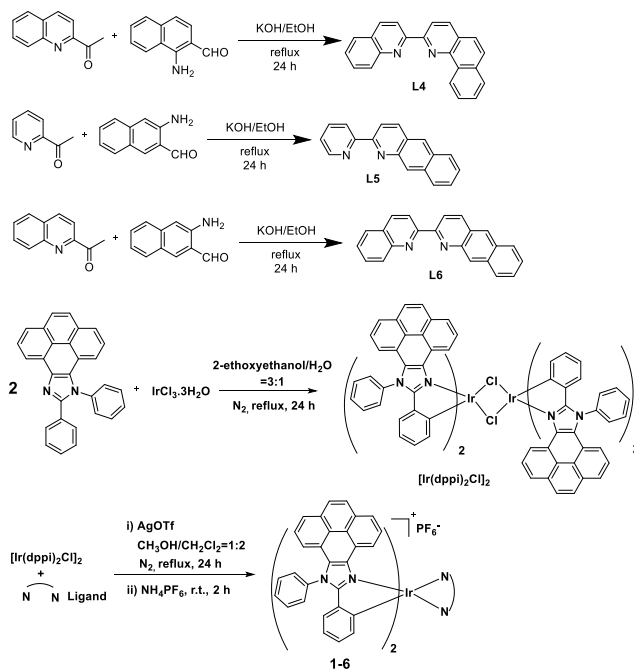
Chart 2.1. Structures of complexes **2-1** – **2-6**.

2.2. Experimental section

2.2.1. Materials and synthesis

All solvents and reagents were obtained from Aldrich or Alfa-Aesar and used as received without further purification unless otherwise stated. Silica gels (230–400 mesh) and Al₂O₃ gels (activated, neutral, Brockmann I) for column chromatography were obtained from Sorbent Technology and Aldrich, respectively. The diimine ligand 2,2'-bisquinoline (**L2-3**) was obtained from Alfa-Aesar. Ligands 2-(pyridin-2-yl)quinoline (**L2-1**) and 2-(pyridin-2-yl)[7,8]benzoquinoline (**L2-2**) were synthesized according to the reported procedures.^{33,35} The other diimine ligands 2-(quinolin-2-yl)[7,8]benzoquinoline (**L2-4**), 2-(pyridin-2-yl)[6,7]benzoquinoline (**L2-5**), and 2-(quinolin-2-yl)[6,7]benzoquinoline (**L2-6**) were prepared by Friedländer Reaction. The C^N ligand dppi and its Ir(III) dimer [Ir(dppi)₂Cl]₂ were synthesized following the literature procedures.³² Complexes **2-1** – **2-6** were synthesized by reaction of the [Ir(dppi)₂Cl]₂ dimer and the corresponding N^N ligand in refluxed CH₂Cl₂/CH₃OH in the presence of AgSO₃CF₃ to abstract chloride from the [Ir(dppi)₂Cl]₂ dimer to move the reaction forward.³²

The Ir(III) complexes **2-1** – **2-6** were characterized by ^1H NMR, ESI-HRMS and elemental analyses. A Varian Oxford-400 or Oxford-500 VNMR spectrometer was used to record the ^1H NMR spectra. ESI-HRMS analyses were conducted on a Bruker BioTOF III mass spectrometer. NuMega Resonance Laboratories, Inc. in San Diego, California carried out the elemental analyses.



Scheme 2.1. Synthetic routes for ligands **L2-4** – **L2-6** and complexes **2-1** – **2-6**.

Ligand L2-4. To a solution of 2-acetylquinoline (500 mg, 4.0 mmol) and 1-aminonaphthalene-2-carboxaldehyde (500 mg, 4.0 mmol) in absolute EtOH (50 mL) was added saturated ethanolic KOH (2 mL). The solution was refluxed under Ar for 24 h. After removal of the solvent, the residue was purified by column chromatography on silica gel, eluted with CH_2Cl_2 /hexanes (1:5, v/v), to provide **L2-4** (580 mg, 65%) as yellow solid. ^1H NMR (400 MHz, CDCl_3) δ 9.58 (d, $J = 8.1$ Hz, 1H), 9.11 (d, $J = 8.6$ Hz, 1H), 9.01 (d, $J = 8.4$ Hz, 1H), 8.40 (t, $J = 8.2$ Hz, 2H), 8.27 (d, $J = 8.5$ Hz, 1H), 8.06 – 7.68 (m, 7H), 7.66 – 7.57 (m, 1H).

Ligand L2-5. To a solution of 2-acetylpyridine (70 mg, 0.58 mmol) and 3-aminonaphthalene-2-carboxaldehyde (100 mg, 0.58 mmol) in absolute EtOH (50 mL) was added

saturated ethanolic KOH (2 mL). The solution was refluxed under Ar for 24h. After the solvent was removed, the residue was purified by column chromatography on alumina gel, eluted with CH₂Cl₂/hexanes (1:9, v/v), to provide **L2-5** (57 mg, 38%) as yellow powder. ¹H NMR (400 MHz, CDCl₃) δ 8.74 (dd, *J* = 11.9, 7.1 Hz, 3H), 8.55 (d, *J* = 8.9 Hz, 1H), 8.47 – 8.37 (m, 2H), 8.09 (d, *J* = 9.7 Hz, 1H), 8.03 (d, *J* = 9.6 Hz, 1H), 7.89 (t, *J* = 6.8 Hz, 1H), 7.57 – 7.46 (m, 2H), 7.40 – 7.34 (m, 1H).

Ligand L2-6. To a solution of 2-acetylquinoline (60 mg, 0.35 mmol) and 3-aminonaphthalene-2-carboxaldehyde (60 mg, 0.35 mmol) in absolute EtOH (50 mL) was added saturated ethanolic KOH (2 mL). The solution was refluxed under Ar for 24h. After removal of the solvent, the residue was purified by column chromatography on alumina gel, eluted with CH₂Cl₂/hexanes (1:3, v/v), to provide **L2-6** (58 mg, 54%) as yellow powder. ¹H NMR (400 MHz, CDCl₃) δ 8.91 (d, *J* = 8.6 Hz, 1H), 8.87 – 8.79 (m, 2H), 8.47 (d, *J* = 8.6 Hz, 1H), 8.44 (s, 1H), 8.34 (d, *J* = 8.7 Hz, 1H), 8.23 (d, *J* = 8.3 Hz, 1H), 8.14 – 8.08 (m, 1H), 8.04 (ddd, *J* = 7.0, 2.6, 0.9 Hz, 1H), 7.91 – 7.85 (m, 1H), 7.75 (ddd, *J* = 8.4, 6.8, 1.4 Hz, 1H), 7.62 – 7.55 (m, 1H), 7.55 – 7.48 (m, 2H).

General Procedure for the Synthesis of 2-1 – 2-6. The [Ir(dppi)₂Cl]₂ dimer (0.03 mmol), diimine ligand (0.06 mmol) and AgSO₃CF₃ (0.06 mmol) were added into the mixed solvent (CH₂Cl₂:MeOH = 2:1 (v/v), 45 mL) and the reaction mixture was degassed and heated to reflux for 24 h. The solution was cooled to room temperature and NH₄PF₆ (0.3 mmol) was added to stir at r.t. for 2 h. After removal of the solvent, the residue was purified by column chromatography on neutral alumina gel, eluted with CH₂Cl₂/hexane (3:1 - 1:0, v/v), followed by recrystallization from dichloromethane and hexanes.

Complex 2-1. A red powder (51 mg) was obtained as the product (yield: 74%). ^1H NMR (CDCl_3 , 400 MHz): δ 8.84 (d, $J = 7.1$ Hz, 1H), 8.42 (d, $J = 4.8$ Hz, 1H), 8.15 – 7.64 (m, 22H), 7.63 – 7.52 (m, 3H), 7.38 (d, $J = 7.7$ Hz, 2H), 7.25 (s, 1H), 7.14 – 7.00 (m, 4H), 6.88 – 6.76 (m, 3H), 6.74 – 6.66 (m, 2H), 6.57 (dd, $J = 12.7, 7.0$ Hz, 3H), 6.34 (d, $J = 7.9$ Hz, 1H), 6.22 (t, $J = 7.9$ Hz, 1H). ESI-HRMS (m/z): calcd. for $[\text{C}_{72}\text{H}_{44}\text{N}_6\text{Ir}]^+$, 1185.3263; found, 1185.3329. Anal. Calcd. for $\text{C}_{72}\text{H}_{44}\text{N}_6\text{IrPF}_6 \cdot 0.6\text{CH}_2\text{Cl}_2 \cdot 1.7\text{C}_6\text{H}_{14}$: C, 65.09; H, 4.55; N, 5.50. Found: C, 64.93; H, 4.69; N, 5.82.

Complex 2-2. An orange powder (46 mg) was obtained as the product (yield: 66%). ^1H NMR (CDCl_3 , 400 MHz): δ 9.52 (d, $J = 7.4$ Hz, 1H), 9.05 (d, $J = 8.9$ Hz, 1H), 8.59 (d, $J = 4.2$ Hz, 1H), 8.26 – 7.88 (m, 13H), 7.87 – 7.78 (m, 1H), 7.78 – 7.51 (m, 8H), 7.37 (d, $J = 8.7$ Hz, 1H), 7.24 (d, $J = 12.9$ Hz, 2H), 7.15 (t, $J = 7.7$ Hz, 1H), 7.07 – 7.00 (m, 2H), 6.97 (d, $J = 8.1$ Hz, 1H), 6.88 (dd, $J = 16.8, 8.1$ Hz, 2H), 6.78 (d, $J = 7.8$ Hz, 2H), 6.73 – 6.54 (m, 4H), 6.47 (d, $J = 8.0$ Hz, 1H), 6.19 – 6.09 (m, 2H), 6.04 (d, $J = 7.6$ Hz, 2H), 5.35 (d, $J = 6.7$ Hz, 1H). ESI-HRMS (m/z): calcd. for $[\text{C}_{76}\text{H}_{46}\text{N}_6\text{Ir}]^+$, 1235.3420; found, 1235.3466. Anal. Calcd. for $\text{C}_{76}\text{H}_{46}\text{N}_6\text{IrPF}_6 \cdot \text{H}_2\text{O}$: C, 65.27; H, 3.46; N, 6.01. Found: C, 64.93; H, 3.23; N, 6.18.

Complex 2-3. A red powder (42 mg) was obtained as the product (yield: 60%). ^1H NMR (CDCl_3 , 400 MHz): δ 8.44 (d, $J = 8.5$ Hz, 2H), 8.19 (d, $J = 7.7$ Hz, 2H), 8.04 (d, $J = 7.8$ Hz, 4H), 7.94 (dd, $J = 17.0, 8.5$ Hz, 4H), 7.88 – 7.66 (m, 12H), 7.64 – 7.55 (m, 4H), 7.45 (t, $J = 7.4$ Hz, 2H), 7.16 (d, $J = 7.9$ Hz, 2H), 7.03 – 6.85 (m, 6H), 6.72 (td, $J = 7.6, 1.1$ Hz, 2H), 6.62 – 6.52 (m, 2H), 6.25 (t, $J = 7.8$ Hz, 2H), 6.17 – 6.08 (m, 2H). ESI-HRMS (m/z): calcd. for $[\text{C}_{76}\text{H}_{46}\text{N}_6\text{Ir}]^+$, 1235.3420; found, 1235.3453. Anal. Calcd. for $\text{C}_{76}\text{H}_{46}\text{N}_6\text{IrPF}_6$: C, 66.13; H, 3.36; N, 6.09. Found: C, 65.76; H, 3.69; N, 5.96.

Complex 2-4. A red powder (44 mg) was obtained as the product (yield: 60%). ^1H NMR (CDCl_3 , 400 MHz): δ 9.16 (d, $J = 7.2$ Hz, 1H), 9.05 (d, $J = 8.1$ Hz, 1H), 8.46-8.43 (m, 2H), 8.27-

8.23 (m, 1H), 8.17 (dd, $J = 7.6, 4.4$ Hz, 2H), 8.12-8.00 (m, 4H), 7.98-7.77 (m, 9H), 7.71 (t, $J = 8.0$ Hz, 2H), 7.64-7.54 (m, 4H), 7.40 (d, $J = 7.6$ Hz, 1H), 7.29-7.20 (m, 3H), 7.19-7.16 (m, 5H), 7.11 (d, $J = 7.6$ Hz, 1H), 6.98-7.91 (m, 3H), 6.72-6.71 (m, 2H), 6.62 (td, $J = 8.0, 1.2$ Hz, 1H), 6.47 (d, $J = 7.8$ Hz, 1H), 6.27 (t, $J = 7.6$ Hz, 1H), 6.15 (t, $J = 7.7$ Hz, 1H), 6.05 (t, $J = 7.6$ Hz, 1H), 5.94 (t, $J = 7.6$ Hz, 1H), 5.33 (dd, $J = 7.9, 1.0$ Hz, 1H). ESI-HRMS (m/z): calcd. for $[\text{C}_{80}\text{H}_{48}\text{N}_6\text{Ir}]^+$, 1285.3578; found, 1285.3622. Anal. Calcd. for $\text{C}_{80}\text{H}_{48}\text{N}_6\text{IrPF}_6$: C, 67.17; H, 3.38; N, 5.88. Found: C, 66.95; H, 3.20; N, 5.83.

Complex 2-5. A dark red powder (43 mg) was obtained as the product (yield: 50%). ^1H NMR (CDCl_3 , 400 MHz): δ 9.18 (d, $J = 7.9$ Hz, 1H), 8.69 (s, 1H), 8.53 (d, $J = 4.7$ Hz, 1H), 8.37 (s, 1H), 8.14 – 7.85 (m, 14H), 7.82 (d, $J = 8.8$ Hz, 1H), 7.78 – 7.72 (m, 1H), 7.72 – 7.59 (m, 5H), 7.49 (ddd, $J = 19.6, 16.1, 6.9$ Hz, 4H), 7.37 (dd, $J = 10.7, 8.7$ Hz, 2H), 7.21 (d, $J = 7.1$ Hz, 1H), 7.18 – 7.13 (m, 1H), 7.09 – 6.84 (m, 6H), 6.84 – 6.74 (m, 3H), 6.65 – 6.59 (m, 1H), 6.23 (d, $J = 6.8$ Hz, 1H), 6.02 (t, $J = 7.8$ Hz, 1H), 5.37 (d, $J = 7.5$ Hz, 1H). ESI-HRMS (m/z): calcd. for $[\text{C}_{76}\text{H}_{46}\text{N}_6\text{Ir}]^+$, 1235.3420; found, 1235.3389. Anal. Calcd. for $\text{C}_{76}\text{H}_{46}\text{N}_6\text{IrPF}_6 \cdot 0.7\text{CH}_2\text{Cl}_2 \cdot 0.2\text{C}_6\text{H}_{14}$: C, 64.21; H, 3.47; N, 5.77. Found: C, 63.88; H, 3.84; N, 6.20.

Complex 2-6. A brown powder (51 mg) was obtained as the product (yield: 61%). ^1H NMR (CDCl_3 , 400 MHz): δ 8.93 (s, 1H), 8.55 (s, 1H), 8.41 (dd, $J = 13.3, 7.9$ Hz, 2H), 8.32 (d, $J = 7.0$ Hz, 1H), 8.26 (d, $J = 8.6$ Hz, 1H), 8.14 – 8.04 (m, 3H), 7.97 (dt, $J = 18.2, 8.8$ Hz, 6H), 7.88 – 7.68 (m, 6H), 7.68 – 7.58 (m, 6H), 7.56 (d, $J = 9.0$ Hz, 2H), 7.52 – 7.40 (m, 2H), 7.34 (d, $J = 7.2$ Hz, 1H), 7.30 (d, $J = 8.2$ Hz, 2H), 7.18 (d, $J = 7.4$ Hz, 1H), 7.11 (d, $J = 7.3$ Hz, 1H), 6.81 (ddd, $J = 13.7, 8.9, 5.2$ Hz, 5H), 6.63 – 6.49 (m, 3H), 6.41 (t, $J = 7.9$ Hz, 1H), 6.06 (t, $J = 7.8$ Hz, 2H), 5.98 (d, $J = 8.9$ Hz, 1H). ESI-HRMS (m/z): calcd. for $[\text{C}_{80}\text{H}_{48}\text{N}_6\text{Ir}]^+$, 1285.3578; found, 1285.3577.

Anal. Calcd. for $C_{80}H_{48}N_6IrPF_6 \cdot 0.8CH_2Cl_2 \cdot 0.1C_6H_{14}$: C, 64.87; H, 3.41; N, 5.58. Found: C, 64.60; H, 3.76; N, 5.68.

2.2.2. Photophysical studies

The UV–vis absorption spectra of complexes **2-1** – **2-6** were recorded using a Cary 50 spectrophotometer in a 1-cm quartz cuvette. The emission spectra of **2-1** – **2-4** were measured on a HORIBA FluoroMax 4 fluorometer/phosphorometer. The spectra of **2-5** and **2-6** were detected with an InGaAs detector from 670 nm to 1225 nm ($\lambda_{ex} = 473$ nm) with a 500 nm long pass filter. The emission quantum yields were obtained using the relative actinometry method in degassed solutions.⁵⁶ The reference used for complexes **2-1** – **2-4** was a degassed acetonitrile solution of $[Ru(bpy)_3]Cl_2$ ($\Phi_{em} = 0.097$, $\lambda_{ex} = 436$ nm).⁵⁷ For complexes **2-5** and **2-6**, IR26 ($\Phi_{em} = 0.0005$)⁵⁸ was used as the reference. The quantum yield reported for **2-5** and **2-6** are only for the emission in the region of 700-850 nm detected by the Hamamatsu Photomultiplier tube (PMT) R928. Acetonitrile solution of $[Ru(bpy)_3]Cl_2$ was used as the reference in this case.

The ns transient absorption (TA) measurements (TA spectra, triplet lifetimes and quantum yields) were conducted on a laser flash photolysis spectrometer (Edinburgh LP920) excited by the third-harmonic output (355 nm) of a Quantel Brilliant Nd:YAG laser with a pulse duration of 4.1 ns and a repetition rate of 1 Hz. Before measurement, all sample solutions were purged with Ar for 30 min. The triplet excited-state molar extinction coefficients (ϵ_T) were determined by the singlet depletion method.⁵⁵ After the ϵ_T value was obtained, the triplet excited-state quantum yield was calculated via the relative actinometry,⁵⁴ using SiNc in benzene as the reference ($\epsilon_{590} = 70,000$ $M^{-1} cm^{-1}$, $\Phi_T = 0.20$).⁵⁹

2.2.3. Computational methods

Gaussian 09 quantum computing software package⁶⁰ was implemented for all calculations, *i.e.* geometry optimization and the electronic structure for ground and excited states. Density functional theory (DFT) and time-dependent DFT (TDDFT) was implemented using the functional PBE1PBE⁶¹ with mixed basis set LANL2DZ for Ir ion⁶² and 6-31G* for light elements (H, C and N).⁶³⁻⁶⁴ Similar methodologies have been proven to successfully describe structural and optical properties of various Ir(III) complexes.^{17,20,30,31,39,65-67} Additionally, the solvent effect was implicitly included by Conductor Polarized Continuum Model (CPCM)^{68,69} for both dichloromethane and acetonitrile. Absorption spectrums were obtained using the TDDFT with the same functional and basis set specified above. The lowest 100 transitions were calculated and then broadened using the Gaussian function with line-width of $\sigma = 0.1$ eV in order to reproduce the thermal broadening correlated with the experimental absorption spectra.

To theoretically investigate the nature of the emitting state for each complex, two approaches were used. The first method is the Δ SCF,^{70,71} where the phosphorescence energies are found by taking the differences between the total energies at the triplet and singlet spin configurations of the complexes. The second method used is a modification of the Δ SCF, where the energies are found from TDDFT using the ground state geometry at the triplet spin configuration. Both methods provide qualitative agreement in phosphorescence energies. Additionally, TDDFT-based Δ SCF provides natural transition orbitals³⁸ (NTOs) used for analysis of the excited state character. To characterize the electronic transitions contributing to absorption and emission, NTOs were calculated using Gaussian 09 and visualized using GaussView 5.09 graphical software⁷² with isovale of 0.02.

2.2.4. Electrochemical measurements

The redox potentials of **2-1** – **2-6** were measured by cyclic voltammetry on a Pine WaveDriver potentiostat/galvanostat voltammetric analyzer in 1×10^{-3} M anhydrous acetonitrile solutions with a scan rate of 50 mV/s. The electrolytic cell used a platinum plate as the working electrode, Ag/AgCl as the reference electrode, and a platinum wire as the counter electrode. The supporting electrolyte was a 0.1 M solution of tetrabutylammonium hexafluorophosphate (TBAPF₆). The electrochemical potentials were recorded in volts against the Ag/AgCl reference electrode with the ferrocenium/ferrocene (Fc⁺/Fc) couple as the internal standard. The reported redox potentials were calculated against the Fc⁺/Fc couple. The solution was deaerated with prepurified argon gas for 15 min before each measurement.

2.3. Results and discussion

2.3.1. Electronic absorption

The UV–vis absorption spectra of complexes **2-1** – **2-6** were recorded in CH₂Cl₂ and are shown in Figure 2.1. The absorption band maxima and molar extinction coefficients are compiled in Table 2.1. The strong absorption bands with large extinction coefficients at wavelengths shorter than 430 nm are assigned to dppi and N[^]N ligands spin–allowed intraligand (IL) ¹π,π* transitions. The tails in the region of 430 – 700 nm are attributed to ^{1,3}MLCT (metal–to–ligand charge transfer) / ^{1,3}LLCT (ligand–to–ligand charge transfer) transitions based on the small extinction coefficients and the DFT calculation results (see the natural transition orbitals (NTOs)³⁸ in Tables 2.2 and 2.3, and discussions in the following paragraphs), which is in line with the reported Ir(III) complexes with extended π–conjugated N[^]N ligand.^{29,30,39,40}

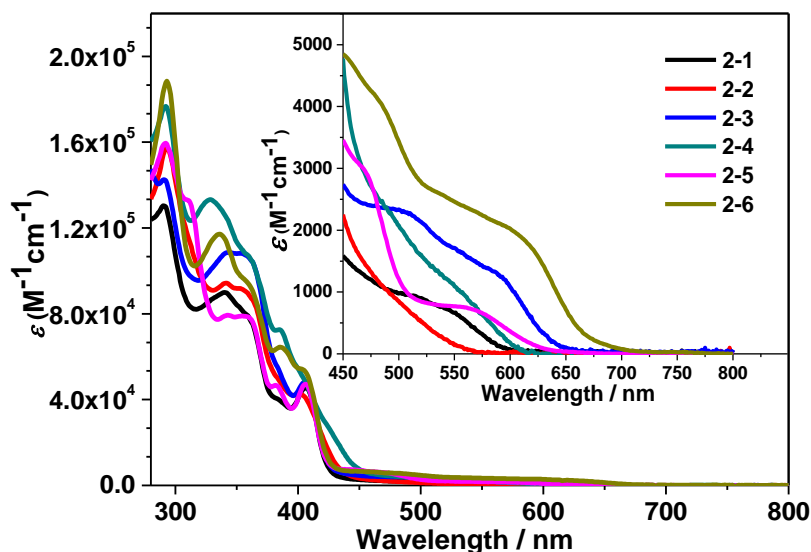


Figure 2.1. UV-vis absorption spectra of **2-1** – **2-6** in CH₂Cl₂.

Table 2.1. Electronic absorption, emission, and triplet excited-state absorption parameters for complexes **2-1** – **2-6**.

	$\lambda_{\text{abs}}/\text{nm}$ ($\log \epsilon$) ^a	$\lambda_{\text{em}}/\text{nm}$ ($\tau_{\text{em}}/\mu\text{s}$); Φ_{em} ^b	$\lambda_{\text{T1-Tn}}/\text{nm}$ ($\tau_{\text{TA}}/\mu\text{s}$; $\log \epsilon_{\text{T1-Tn}}$; Φ_{T}) ^c
2-1	290 (5.12), 340 (4.96), 406 (4.66), 498 (3.00)	625 (0.94); 0.13	775 (0.67; 4.85; 0.091)
2-2	292 (5.20), 339 (4.98), 401 (4.64), 445 (3.60)	593 (0.15); 0.017	545 (16.1; 5.24; 0.075)
2-3	290 (5.15), 344 (5.04), 405 (4.69), 496 (3.37), 580 (3.13)	657 (0.93); 0.12	390 (0.56; 5.01; 0.23)
2-4	291 (5.25), 328 (5.12), 384 (4.86), 485 (3.39)	645 (1.34); 0.085	425 (14.9; 5.17; 0.10)
2-5	292 (5.20), 309 (5.13), 357 (4.90), 405 (4.68), 444 (3.89), 469 (3.48), 550 (2.89)	755 (2.21), 845 (–), 938 (–), 1054 (–); 0.0017	665 (2.82; 5.37; 0.027)
2-6	292 (5.27), 336 (5.07), 386 (4.81), 402 (4.74), 480 (3.62), 599 (3.31)	780 (0.86), 904 (–), 967 (–), 1087 (–); 0.0019	785 (0.87; 5.13; 0.018)

^a Absorption band maxima and molar extinction coefficients of the UV-vis absorption in CH₂Cl₂ at room temperature. ^b Emission band maxima and decay lifetimes in CH₂Cl₂ at room temperature, $c = 1 \times 10^{-5}$ mol/L. The emission characteristics of **2-1** – **2-4** were measured using Hamamatsu R928 PMT as the detector, while an InGaAs array was used to measure the emission of **2-5** and **2-6**. The reference used was a degassed CH₃CN solution of [Ru(bpy)₃]Cl₂ ($\Phi_{\text{em}} = 0.097$, $\lambda_{\text{ex}} = 436$ nm) for **2-1** – **2-4**, and IR26 ($\Phi_{\text{em}} = 0.0005$) for **2-5** and **2-6**. ^c Nanosecond TA band maxima, triplet extinction coefficients, triplet excited-state lifetimes, and quantum yields measured in CH₃CN at room temperature. SiNc in C₆H₆ was used as the reference. ($\epsilon_{590} = 70,000$ L mol⁻¹ cm⁻¹, $\Phi_{\text{T}} = 0.20$).

Table 2.2. Natural transition orbitals (NTOs) representing singlet transitions contributing to the low-energy absorption bands of complexes **2-1** – **2-6** in CH₂Cl₂.

	S_n	Hole	Electron		S_n	Hole	Electron
2-1	S ₁ 527 nm <i>f</i> = 0.001			2-4	S ₁ 545 nm <i>f</i> = 0.006		
	S ₂ 494 nm <i>f</i> = 0.002				S ₂ 513 nm <i>f</i> = 0.017		
	S ₃ 440 nm <i>f</i> = 0.002				S ₃ 454 nm <i>f</i> = 0.015		
2-2	S ₁ 501 nm <i>f</i> = 0.005			2-5	S ₁ 583 nm <i>f</i> = 0.001		
	S ₂ 466 nm <i>f</i> = 0.007				S ₂ 542 nm <i>f</i> = 0.002		
	S ₃ 420 nm <i>f</i> = 0.010				S ₃ 476 nm <i>f</i> = 0.004		
	S ₄ 401 nm <i>f</i> = 0.104				S ₄ 453 nm <i>f</i> = 0.060		
2-3	S ₁ 570 nm <i>f</i> = 0.010			2-6	S ₁ 612 nm <i>f</i> = 0.012		
	S ₂ 540 nm <i>f</i> = 0.019				S ₂ 581 nm <i>f</i> = 0.145		
	S ₃ 468 nm <i>f</i> = 0.011				S ₃ 498 nm <i>f</i> = 0.267		
	S ₄ 425 nm <i>f</i> = 0.031				S ₄ 484 nm <i>f</i> = 0.024		
	S ₅ 420 nm <i>f</i> = 0.034				S ₅ 444 nm <i>f</i> = 0.010		
					S ₆ 439 nm <i>f</i> = 0.015		

Table 2.3. Characterization of molecular orbitals for the first five HOMOs and LUMOs of complexes **2-1** – **2-6** in CH₂Cl₂.

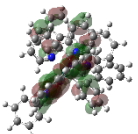
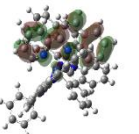
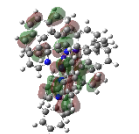
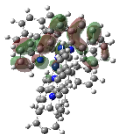
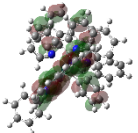
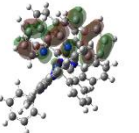
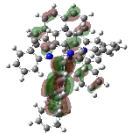
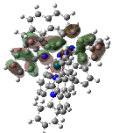
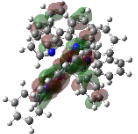
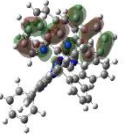
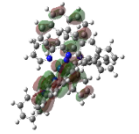
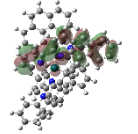
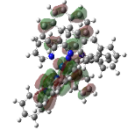
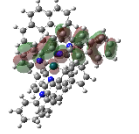
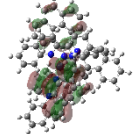
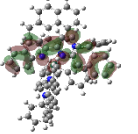
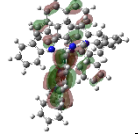
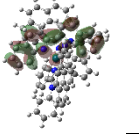
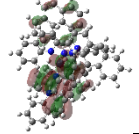
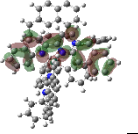
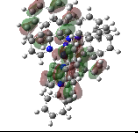
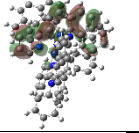
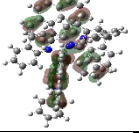
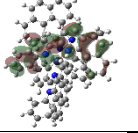
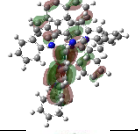
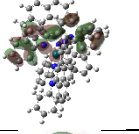
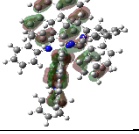
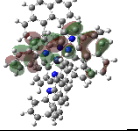
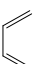
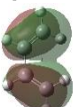
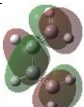
	2-1	2-2	2-3	2-4
LUMO+4	$\pi^*(C^{\wedge}N)$	$\pi^*(C^{\wedge}N)/d(Ir)$	$\pi^{*\dagger}$	$\pi^{*\dagger}$
LUMO+3	$\pi^*(C^{\wedge}N-N^{\wedge}N)$	$\pi^*(C^{\wedge}N)$	$\pi^*(C^{\wedge}N)$	$\pi^*(N)$
LUMO+2	$\pi^*(C^{\wedge}N)$	$\pi^*(pyr)$	$\pi^*(C^{\wedge}N)$	$\pi^{*\dagger}$
LUMO+1	$\pi^*(C^{\wedge}N)$	$\pi^{*\dagger}$	$\pi^*(N^{\wedge}N)$	$\pi^*(N^{\wedge}N)/\pi^*(Ph)$
LUMO	$\pi^*(N^{\wedge}N)$	$\pi^*(N^{\wedge}N)$	$\pi^*(N^{\wedge}N)/d(Ir)$	$\pi^*(N^{\wedge}N)$
HOMO	$d(Ir)/\pi(C^{\wedge}N)$	$d(Ir)/\pi(C^{\wedge}N)$	$d(Ir)/\pi(C^{\wedge}N)$	$d(Ir)/\pi(C^{\wedge}N)$
HOMO-1	$\pi(C^{\wedge}N)/d(Ir)$	$\pi(C^{\wedge}N)$	$\pi(C^{\wedge}N)$	$\pi(C^{\wedge}N)$
HOMO-2	$d(Ir)/\pi(C^{\wedge}N)$	π^{\dagger}	$d(Ir)/\pi(C^{\wedge}N)$	$d(Ir)/\pi(C^{\wedge}N)$
HOMO-3	$d(Ir)/\pi(C^{\wedge}N)$	π^{\dagger}	$d(Ir)/\pi(C^{\wedge}N)$	π^{\dagger}
HOMO-4	$d(Ir)/\pi(C^{\wedge}N)$	π^{\dagger}	$d(Ir)/\pi(C^{\wedge}N)$	$d(Ir)/\pi(C^{\wedge}N)$
	2-5	2-6		
LUMO+4	$\pi^*(C^{\wedge}N)$	$\pi^*(N^{\wedge}N)/d(Ir)$		
LUMO+3	$\pi^*(C^{\wedge}N)$	$\pi^*(C^{\wedge}N)$		
LUMO+2	$\pi^*(C^{\wedge}N)$	$\pi^*(C^{\wedge}N)$		
LUMO+1	$\pi^*(C^{\wedge}N-N^{\wedge}N)$	$\pi^*(N^{\wedge}N)$		
LUMO	$\pi^*(N^{\wedge}N)/d(Ir)$	$\pi^*(N^{\wedge}N)/d(Ir)$		
HOMO	$d(Ir)/\pi(C^{\wedge}N)$	$\pi(C^{\wedge}N)/d(Ir)$		
HOMO-1	$\pi(C^{\wedge}N)/d(Ir)$	$\pi(C^{\wedge}N)$		
HOMO-2	$d(Ir)/\pi(C^{\wedge}N)$	$\pi(N)/d(Ir)/\pi(C^{\wedge}N)$		
HOMO-3	$\pi(C^{\wedge}N)/d(Ir)$	$d(Ir)/\pi(C^{\wedge}N)/\pi(N)$		
HOMO-4	$\pi(C^{\wedge}N)/d(Ir)$	$d(Ir)/\pi(C^{\wedge}N)/\pi(N)$		

Examination of the tails at 450–700 nm for complexes **2-1** – **2-6** revealed that benzannulation at either the 5',6'-position of pyridine or the 6,7-position of quinoline of the N[^]N ligand caused red-shifts of the ^{1,3}MLCT / ^{1,3}LLCT transitions and increased the molar extinction coefficients (**2-3**, **2-5**, and **2-6** vs. **2-1**). In contrast, benzannulation at the 7,8-position of quinoline of the N[^]N ligand induced blue-shifts of the ^{1,3}MLCT / ^{1,3}LLCT transitions in complexes **2-2** and **2-4** with respect to their corresponding complexes **2-1** and **2-3** (*i.e.* **2-2** vs. **2-1** and **2-4** vs. **2-3**). This phenomenon is contrary to the previous findings that expansion of the aromatic π -system led

to red-shifts of the absorption band.^{29,30,41} However, benzannulation at the 5',6'-position of pyridine in complex **2-2** still red-shifted the ^{1,3}MLCT / ^{1,3}LLCT transitions in **2-4**.

To understand the site selective benzannulation effect, DFT calculations were performed for **2-1** – **2-6** in CH₂Cl₂ using Gaussian09 software package and PBE1 functional. The resultant ground-state energy diagram for **2-1** – **2-6** is shown in Figure 2.2. The calculated electron density distributions of HOMO and LUMO are the same for all six complexes (see the representative frontier molecular orbital (FMO) plots for **2-1** in Figure 2.1, and the FMOs for the other complexes in Table 2.4), with the HOMO being delocalized on the dppe ligands and the d-orbital of the Ir(III) ion and the LUMO being exclusively on the diimine ligand. The optimized geometries of these complexes showed that although all complexes adopted similar octahedral geometry around the Ir(III) center, the dihedral angles within the N^N ligand are 8–11 degrees larger in **2-2** and **2-4** compared to the other complexes (Table 2.4) due to the increased steric hindrance from the additional phenyl ring fused at the 7,8-position of quinoline upon coordination. The larger distortion of the N^N ligand in **2-2** and **2-4** could destabilize the N^N ligand localized LUMO, while the HOMO energies remain unchanged. Consequently, the HOMO–LUMO gaps increased in **2-2** and **2-4**, and thus blue-shifts occurred. On the other hand, benzannulation at the 5',6'-position of pyridine or the 6,7-position of quinoline of the N^N ligand stabilized the LUMO in **2-3**, **2-5**, and **2-6**, resulting in decreased HOMO–LUMO gap and red-shifted charge transfer transitions.

Table 2.4. HOMO and LUMO of 2-1 – 2-6 in CH₂Cl₂.

	HOMO	LUMO		HOMO	LUMO	
2-1			2-2			H-L
2-1			2-3			L-L
2-1			2-5			L-L
2-5			2-6			L-L
2-3			2-6			L-L
2-2			2-4			L-L
2-3			2-4			H-L
						

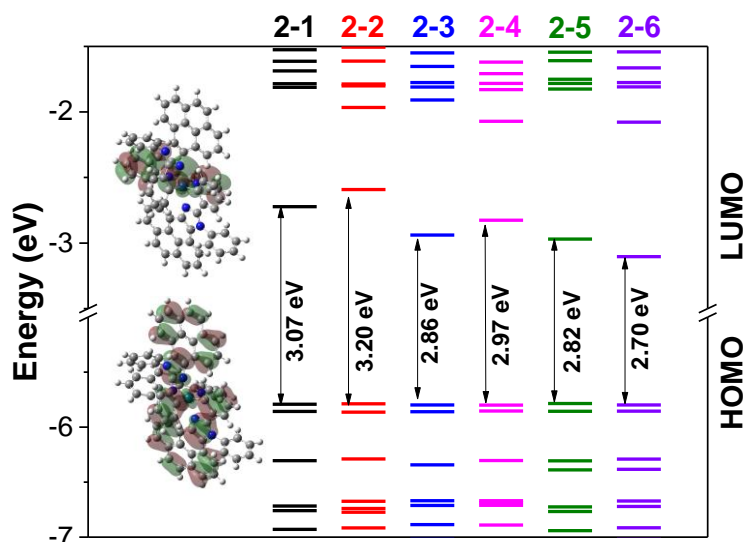


Figure 2.2. The ground-state molecular orbital diagram for **2-1** – **2-6** in CH_2Cl_2 , and HOMO and LUMO plots for **2-1**.

Although the increased distortion of the $\text{N}^{\wedge}\text{N}$ ligands seems reasonably explain the blue-shifts in **2-2** and **2-4**, this does not appear to be able to explain the blue-shifts in the Ru(II) complexes with benzannulation at the 4,5-position of the bipyridine ligand²⁷ or fusion aromatic ring(s) at the 5,6-position of the phenanthroline ligand.²⁸ In both cases, benzannulation did not cause distortion of the $\text{N}^{\wedge}\text{N}$ ligand upon coordination. Therefore, the orbital symmetry analysis method reported by Thompson and Gordon for rationalizing the blue-shifts in $(\text{N}^{\wedge}\text{N}^{\wedge}\text{N})\text{PtCl}$ complexes²⁵ was applied to complexes **2-1** – **2-6**. In this method, benzannulation was considered occurring through interactions of the FMOs of the parent compound with those of 1,3-butadiene or ethene. Depending on the electron density distributions on the FMOs of the parent compound and 1,3-butadiene or ethene and the orbital symmetry at the site of benzannulation, either the HOMO or LUMO of 1,3-butadiene or ethene interacted with the LUMO of the parent compound. These interactions destabilized (when the HOMO of 1,3-butadiene interacted) or stabilized (when the LUMO of 1,3-butadiene interacted) the LUMO of the parent compound while the HOMO was intact, resulting in blue- or red-shifts in absorption.²⁵ Our DFT calculations showed that the

HOMO–LUMO transitions of **2-1** – **2-6** contributed 64–68% (Table 2.5) to the lowest singlet transition (S_1 state), thus the FMO analysis can be used to explain the blue– or red–shifts of **2-1** – **2-6** upon benzannulation. The qualitative orbital diagram of the valence orbitals for **2-1**, **2-2**, **2-3** and **2-5** is provided in Figure 2.3, which represents the cases when benzannulation occurs at the 7,8–position of quinoline (**2-2**) or the 5',6'–position of pyridine (**2-3**) or the 6,7–position of quinoline (**2-5**).

Table 2.5. Percentage of HOMO-LUMO transition contributing to S_1 of complexes **2-1** – **2-6** calculated in CH_2Cl_2 solvent.

	Percent HOMO-LUMO
2-1	67%
2-2	68%
2-3	64%
2-4	68%
2-5	67%
2-6	64%

Because the HOMOs for all complexes are delocalized on one of the dppe ligands and the d -orbital of the Ir(III) ion while the LUMOs being exclusively on the diimine ligands, benzannulation at the $\text{N}^{\wedge}\text{N}$ ligand did not impact the HOMO energy but only altered the energy of LUMO. Depending on the symmetry of MOs at the site of benzannulation, either the HOMO or LUMO of 1,3–butadiene interacts with the LUMO of the $\text{N}^{\wedge}\text{N}$ ligand. As shown in Figure 2.3, when benzannulation occurs at the 7,8–position of quinoline in complex **2-2**, the LUMO symmetry of **2-1** at the annulation site matches the HOMO symmetry of 1,3–butadiene. The LUMO–HOMO interactions raise the LUMO energy in **2-2** and thus cause the blue–shifted CT absorption band. The similar phenomenon occurs from **2-3** to **2-4** (Figure 2.4). In contrast, when benzannulation takes place at the 5',6'–position of pyridine or the 6,7–position of quinoline, the LUMO symmetry at the respective interacting site matches the LUMO symmetry of 1,3–butadiene. The LUMO–

LUMO interactions result in the stabilized LUMOs in **2-3** and **2-5** compared to **2-1**, which consequently induces the red-shifts of the CT transitions in **2-3** and **2-5**. This is the same case for complex **2-6** (Figure 2.4).

It should be pointed out that when considering the degree of orbital mixing between the parent complex and 1,3-butadiene, both the orbital symmetry and orbital energy difference have to be taken into account. In fact, the larger the difference in orbital energies, the smaller their coupling (mixing), despite similarities in orbital symmetry. Our calculations show the energy splitting of > 2 eV between HOMO (-6.66 eV) and HOMO+1 (-8.79 eV), as well as between LUMO (-0.55 eV) and LUMO+1 ($+2.30$ eV) in 1,3-butadiene. Therefore, much larger difference between the LUMO energy of the parent complex and the HOMO-1/LUMO+1 energies of 1,3-butadiene, as compared to the HOMO/LUMO energies of 1,3-butadiene. This larger energy difference leads to negligible contributions of HOMO-1/LUMO+1 to the orbital mixing. As such, only the HOMO and LUMO of 1,3-butadiene were considered in analyzing the stabilization/destabilization of the LUMO of the parent complex.

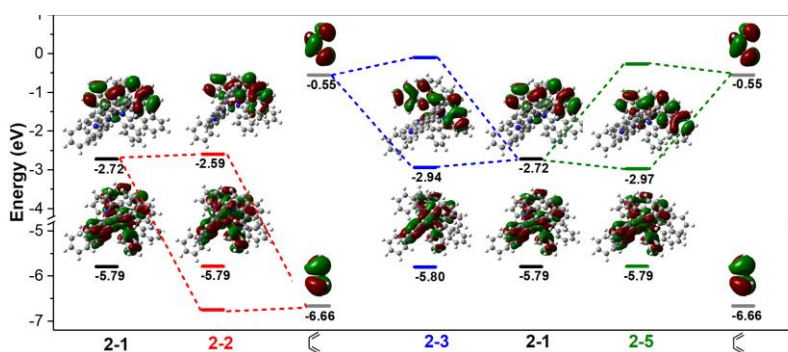


Figure 2.3. Frontier molecular orbital mixing between **2-1** and 1,3-butadiene to give rise to **2-2**, **2-3** and **2-5**.

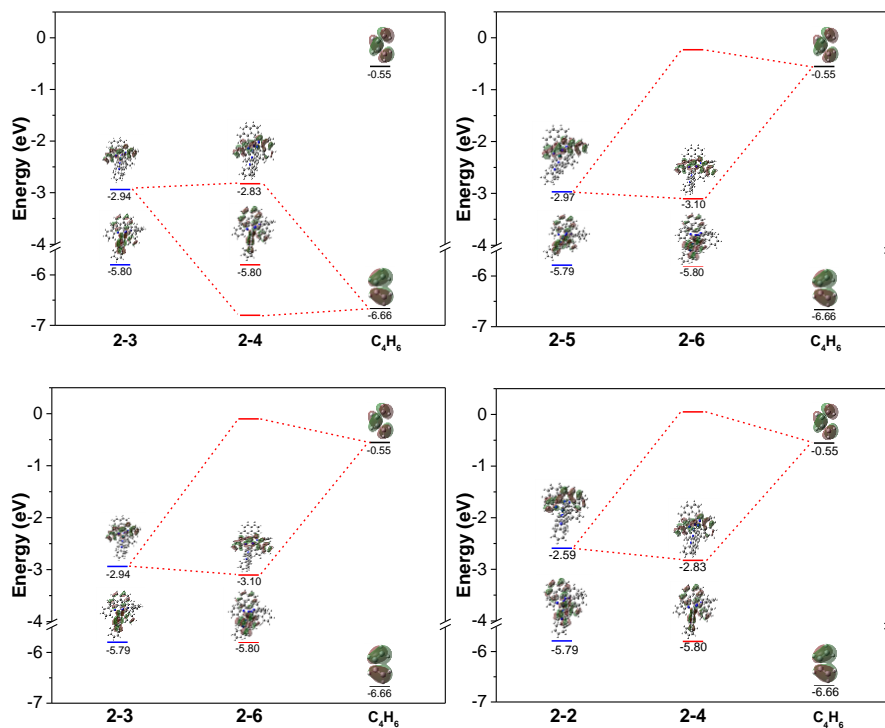


Figure 2.4. Frontier molecular orbital mixing between **2-2**, **2-3**, **2-5** and 1,3-butadiene.

2.3.2. Electrochemical properties

To confirm the impact of site-dependent benzannulation on the HOMO–LUMO gaps in **2-1** – **2-6**, electrochemical properties of **2-1** – **2-6** were investigated in degassed anhydrous CH_3CN solutions by cyclic voltammetry (CV) using ferrocenium/ferrocene (Fc^+/Fc) couple as the internal standard. The cyclic voltammograms of **2-1** and **2-3** are presented in Figure 2.4. The obtained redox potentials vs Fc^+/Fc are listed in Table 2.6. While all of the other complexes exhibited irreversible oxidation processes with the cathodic peaks of the first oxidation waves occurring at approximately 0.8 V, complex **2-3** showed a reversible oxidation process with a half-wave potential of 0.83 V. It appears that the oxidation potentials of **2-1** – **2-6** are essentially the same, which is consistent with the same nature of their HOMOs obtained from the DFT calculations, *i.e.* $\text{C}^{\wedge}\text{N}$ ligands and *d*-orbital based HOMOs. These values are also in line with the half-wave

oxidation potential of 0.83 V for $[\text{Ir}(\text{ppy})_2(\text{dtb-bpy})]\text{PF}_6$ reported in the literature¹⁵ and can be attributed to the oxidation of Ir(III) to Ir(IV), with some contributions from the C[^]N ligand oxidation. For complexes **2-1** – **2-5**, there were additional oxidation peak(s) around 1 V or at > 1 V, which could be ascribed to further oxidation of the cyclometalating ligands.

In contrast, the first reduction waves for all complexes except **2-2** and **2-4** were reversible, and the reduction potentials varied significantly among these complexes. The half-wave reduction potentials decreased from **2-1**, **2-3**, **2-5** to **2-6**; while the anodic reduction potentials for the first reduction waves of **2-2** and **2-4** increased compared to those of **2-1** and **2-3**, respectively. However, the $E_{\text{red}}^{\text{pa}}$ value of **2-4** decreased from that of **2-2**. These trends match the trends obtained from the DFT calculation for the LUMOs in these complexes, confirming that the LUMOs of these complexes are indeed localized on the corresponding N[^]N ligands. Benzannulation at the 5',6'-position of pyridine or the 6,7'-position of quinoline of the N[^]N ligand stabilized the LUMOs in **2-3**, **2-5**, and **2-6**; while benzannulation at the 7,8'-position of quinoline of the N[^]N ligand destabilized the LUMOs in **2-2** and **2-4** with respect to those in **2-1** and **2-3**. The second reduction wave around -2.0 V can be assigned to the reduction of the cyclometalating ligands. The trend of the electrochemical energy gaps (E_{gap}) of these complexes matches well with the trend of the calculated HOMO-LUMO gaps although there appears to be some discrepancy in the absolute values of the calculated HOMO-LUMO gaps with the experimental electrochemical band gaps. Therefore, the DFT calculations clearly confirm and explain the trend in energy level shifts upon benzannulation at different sites. A similar discrepancy between the calculated HOMO-LUMO gaps and the electrochemical energy gaps was reported in $[\text{Ir}(\text{ppy})_2(\text{dtb-bpy})]\text{PF}_6$ and other fluorinated cationic iridium complex.^{14,43} In addition, the electrochemical measurements were

carried out in CH₃CN, while the DFT calculations used CH₂Cl₂ as the solvent. The different solvents may make minor contribution to the discrepancy as well.

Table 2.6. Electrochemical properties of Ir(III) complexes **2-1** – **2-6**.

	$E_{\text{ox}}^{1/2}$ (V) ^a	$E_{\text{ox}}^{\text{pc}}$ (V)	$E_{\text{red}}^{1/2}$ (V)	$E_{\text{red}}^{\text{pa}}$ (V)	E_{gap} (V) ^b
2-1	irr	0.81; 1.02	-1.57 [37]	-1.59, -2.32	2.40
2-2	irr	0.76; 0.92; 1.22; 1.34	irr	-1.72; -2.21; -2.34	2.48
2-3	0.83 [69]	0.81; 1.00	-1.41 [75]; -2.06 [77]	-1.43; -2.05	2.24
2-4	irr	0.77; 1.11	irr	-1.68; -2.25	2.45
2-5	irr	0.81; 1.02	-1.41 [67]	-1.39; -2.07	2.20
2-6	irr	0.88	-1.27 [85]	-1.26; -1.91	2.14

^a $E^{1/2} = (E^{\text{pa}} + E^{\text{pc}})/2$, where E^{pa} and E^{pc} are the anodic and cathodic peak potentials vs ferrocinium/ferrocene (Fc) couple measured in CH₃CN and $\Delta E_{\text{p}} = |E_{\text{pa}} - E_{\text{pc}}|$. ^b $E_{\text{gap}} = (\text{first wave}) E_{\text{ox}}^{\text{pa}} - (\text{first wave}) E_{\text{red}}^{\text{pc}}$.

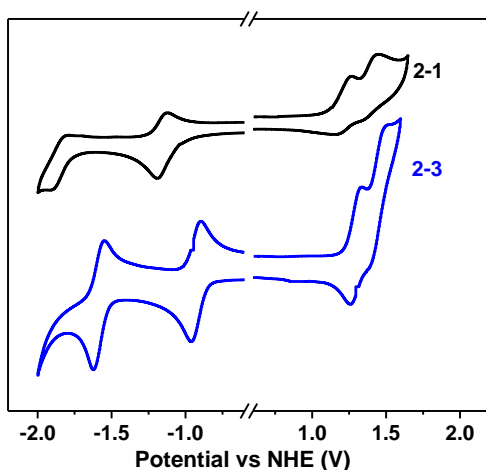


Figure 2.4. Cyclic voltammograms of **2-1** and **2-3** in degassed anhydrous CH₃CN solutions (1×10^{-3} M) in the presence of 0.1 M tetrabutylammonium hexafluorophosphate as the supporting electrolyte and ferrocenium/ferrocene (Fc⁺/Fc) couple as the internal standard. The potentials were recorded against an Ag/AgCl reference electrode.

2.3.3. Photoluminescence

To understand the effects of site-selective benzannulation on the triplet excited states, the emission characteristics of **2-1** – **2-6** at room temperature were investigated. Figure 2.5 displays

the normalized emission spectra of **2-1** – **2-6** in CH₂Cl₂. The emission band maxima and lifetimes are summarized in Table 2.1. The emission of **2-1** – **2-6** is relatively long-lived (~100 ns – 2.2 μs), quite sensitive to oxygen quenching, and exhibit obvious red-shifts in comparison to their corresponding excitation wavelengths. Thus, they are phosphorescence from the triplet excited states, which is in line with the other reported Ir(III) complexes.^{1-20,29-32,37,39,44,45} However, the spectral features of **2-1** – **2-4** are distinctively different from those of **2-5** and **2-6**. The spectra of **2-1** – **2-4** are broad and featureless, while the spectra of **2-5** and **2-6** exhibit clear vibronic progressions. According to that reported for other Ir(III) complexes^{44,45} and the triplet NTOs shown in Table 2.7, the emission of **2-1** – **2-4** is attributed to ³MLCT / ³LLCT phosphorescence in nature, mixed with minor N[^]N ligand-centered ³π,π* character. In contrary, with the extended π-conjugation along the 5',6'-position of pyridine or 6,7-position of quinoline, the N[^]N ligand-centered ³π,π* states became the lowest triplet excited states in **2-5** and **2-6**. Thus, the emission of **2-5** and **2-6** emanates from the ligand-center ³π,π* state. The emission was clearly blue-shifted upon benzannulation at the 7,8-position of quinoline (**2-2** vs **2-1**, and **2-4** vs **2-3**). Opposed to this trend, benzannulation at the 5',6'-position of pyridine or the 6,7-position of quinoline caused salient red-shifts going from **2-1** to **2-3** to **2-5** and **2-6** although the natures of the emitting states of **2-5** and **2-6** are distinct from those of **2-1** – **2-4**. This trend is consistent with that observed for the low-energy electronic absorption bands. Thus, the site-dependent benzannulation effect applies not only to the lowest singlet excited states, but also to the lowest triplet excited states.

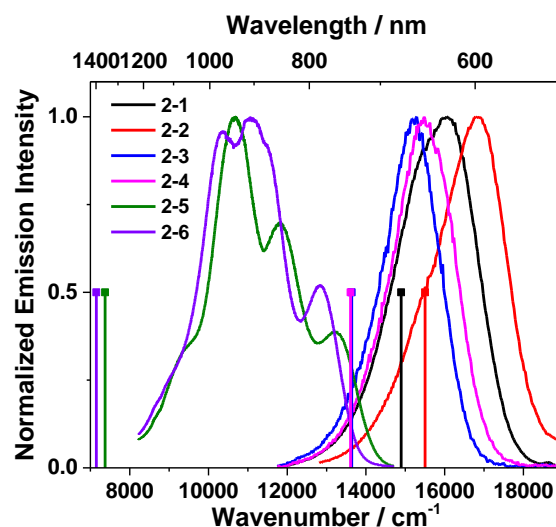


Figure 2.5. Normalized emission spectra of **2-1** – **2-6** at room temperature in CH_2Cl_2 . The spectra of **2-1** – **2-4** were measured on a HORIBA FluoroMax 4 fluorometer/phosphorometer with a Hamamatsu PMT R928 as the detector, while the spectra of **2-5** and **2-6** were detected with an InGaAs sensor from 670 nm to 1225 nm ($\lambda_{\text{ex}} = 473$ nm) with a 500 nm long pass filter. The vertical lines represent the triplet emission wavelengths calculated by TDDFT based ΔSCF method.

Table 2.7. NTOs representing transitions corresponding to the triplet emission of **2-1** to **2-6** in CH_2Cl_2 calculated by TDDFT-based ΔSCF .

Complexes	T_1 / nm	Hole	Electron
2-1	671 (656)		
2-2	645 (638)		
2-3	733 (714)		
2-4	735 (702)		
2-5	1356 (765)		
2-6	1398 (804)		

2.3.4. Transient absorption (TA)

The nanosecond TA spectra of **2-1** – **2-6** were studied in acetonitrile to further understand the triplet excited state characteristics. The triplet excited-state lifetimes, extinction coefficients, and quantum yields are deduced or calculated, and the results are summarized in Table 2.1. The nanosecond TA spectra of **2-1** – **2-6** in acetonitrile immediately after 355 nm laser pulse excitation are presented in Figure 2.6, and the time-resolved spectra for each complex are provided in Figure 2.7. For comparison purpose, the time-resolved TA spectra of the corresponding N^N ligand for each complex (**L2-1** – **L2-6**) were measured in acetonitrile as well and the spectra are shown in Figure 2.8.

Complexes **2-1** – **2-6** all possessed broad positive absorption bands in the region of 400–800 nm, except that **2-1** – **2-3** exhibited a sharp bleaching band at 403–416 nm. The spectral features of **2-1** and **2-3**, and **2-2** and **2-4** resembled each other. However, the spectral of **2-5** and **2-6** differed from each other and from those of **2-1** – **2-4**. For complexes **2-1**, **2-3**, **2-5**, and **2-6** that have benzannulation at the 5',6'-position of pyridine or the 6,7-position of quinoline of the diimine ligand, the triplet lifetimes deduced from the decay of TA are consistent with those obtained from the decay of emission in CH₃CN (Table 2.1). Thus, the excited states giving rise to the observed TA in these four complexes should be their emitting states, *i.e.* predominantly ³MLCT / ³LLCT state for **2-1** and **2-3**, and ³ π,π^* localized on the N^N ligand for **2-5** and **2-6**. This conclusion is further supported by the fact that the TA spectra of **2-5** and **2-6** resembled those of their respective N^N ligands shown in Figure 2.8. The intensity difference in the 350–450 nm region in these two complexes compared to those of their ligands should arise from the stronger ground-state absorption in this region that is much weaker or absent in their corresponding ligand.

For **2-2** and **2-4** that have benzannulation occurred at 7,8–position of quinoline, the major absorption band at 400–480 nm was blue–shifted compared to those of **2-1** and **2-3**, respectively. However, a broad and strong absorption band appeared at 480–700 nm in **2-2** and **2-4**. The TA spectral features of **2-2** and **2-4** resemble those of their corresponding N[^]N ligands (Figure 2.8). More strikingly, the transient species in **2-2** and **2-4** exhibited one order of magnitude longer lifetimes than those of **2-1** and **2-3**, and the TA lifetimes were 1–2 orders of magnitude longer than their emission lifetimes. These features suggest that the transient absorbing excited states in **2-2** and **2-4** differ from their emitting states. As discussed in the photoluminescence section, the emitting states in **2-2** and **2-4** predominantly have the ³MLCT / ³LLCT character. However, the much longer TA lifetimes and the drastically different TA spectral features at 480–800 nm in **2-2** and **2-4** with respect to those of **2-1** and **2-3** suggest that the transient absorbing states in these two complexes are likely to be the N[^]N ligand based ³ π, π^* state. Although such a phenomenon is rare, it has been reported for other Ir(III),⁴⁶ Pt(II),^{47,48} and Ru(II)⁴⁹⁻⁵² complexes, in which those complexes possessed a short–lived ³CT emitting state and a long–lived nonemissive ligand–localized ³ π, π^* transient absorbing state. Our TDDFT calculations for the triplet excited states of **2-1** – **2-6** revealed that the T₂ states in **2-2** and **2-4** predominantly had the N[^]N ligand localized ³ π, π^* character in nature (Figure 2.8). Due to the increased energy of the T₁ states in **2-2** and **2-4** upon benzannulation at the 7,8–position of quinoline, as reflected by the blue–shifted emission in these two complexes, the T₁ states became more closer to the ³ π, π^* dominated T₂ state (Figure 2.9). This could facilitate the mixing of the T₁ and T₂ states in these two complexes and led to the transient absorbing species in **2-2** and **2-4** having more N[^]N ligand–centered ³ π, π^* character. Alternatively, for reasons that are not clearly understood at this time, the nonemissive T₂ states in **2-2** and **2-4** gave rise to the observed TA.

It is interesting to note that the triplet quantum yields for these complexes all appeared to be quite low, which is inconsistent to that expected for heavy-metal containing transition-metal complexes, in which heavy-metal induced strong spin-orbit coupling should result in almost unity intersystem crossing. This phenomenon can be rationalized by the following factors: (1) When the π -conjugation of the ligand increases, the contribution of the d -orbital to the FMOs of the complexes decreases, which reduces the spin-orbit coupling as reported by Schanze and co-workers for phenylene vinylene platinum(II) acetylides;⁵³ (2) When intersystem cross occurs in transition-metal complexes, it is possible to populate two triplet excited states simultaneously.^{46–52} However, the triplet quantum yields were measured from the TA measurements, which did not take into account the population of the other triplet excited state that does not contribute to the observed TA; (3) The triplet quantum yields were obtained using the relative actinometry,⁵⁴ in which the triplet excited-state absorption coefficient had to be known. In our studies, we used the singlet depletion method⁵⁵ to estimate the triplet excited-state absorption coefficients, which assumed that the compound had no excited-state absorption at the valley of the bleaching band and no ground-state absorption at the peak of the TA band. If these conditions can't be fully met, the errors in the obtained triplet excited state absorption coefficient could be large. This may influence the calculated triplet quantum yield as well.

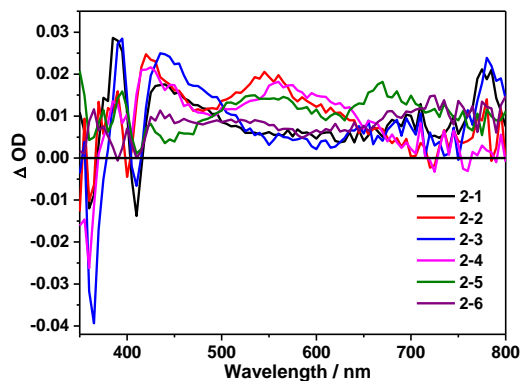


Figure 2.6. Nanosecond transient difference absorption spectra of complexes **2-1** – **2-6** in acetonitrile immediately after 355 nm laser pulse excitation. $A_{355} = 0.4$ in a 1-cm cuvette.

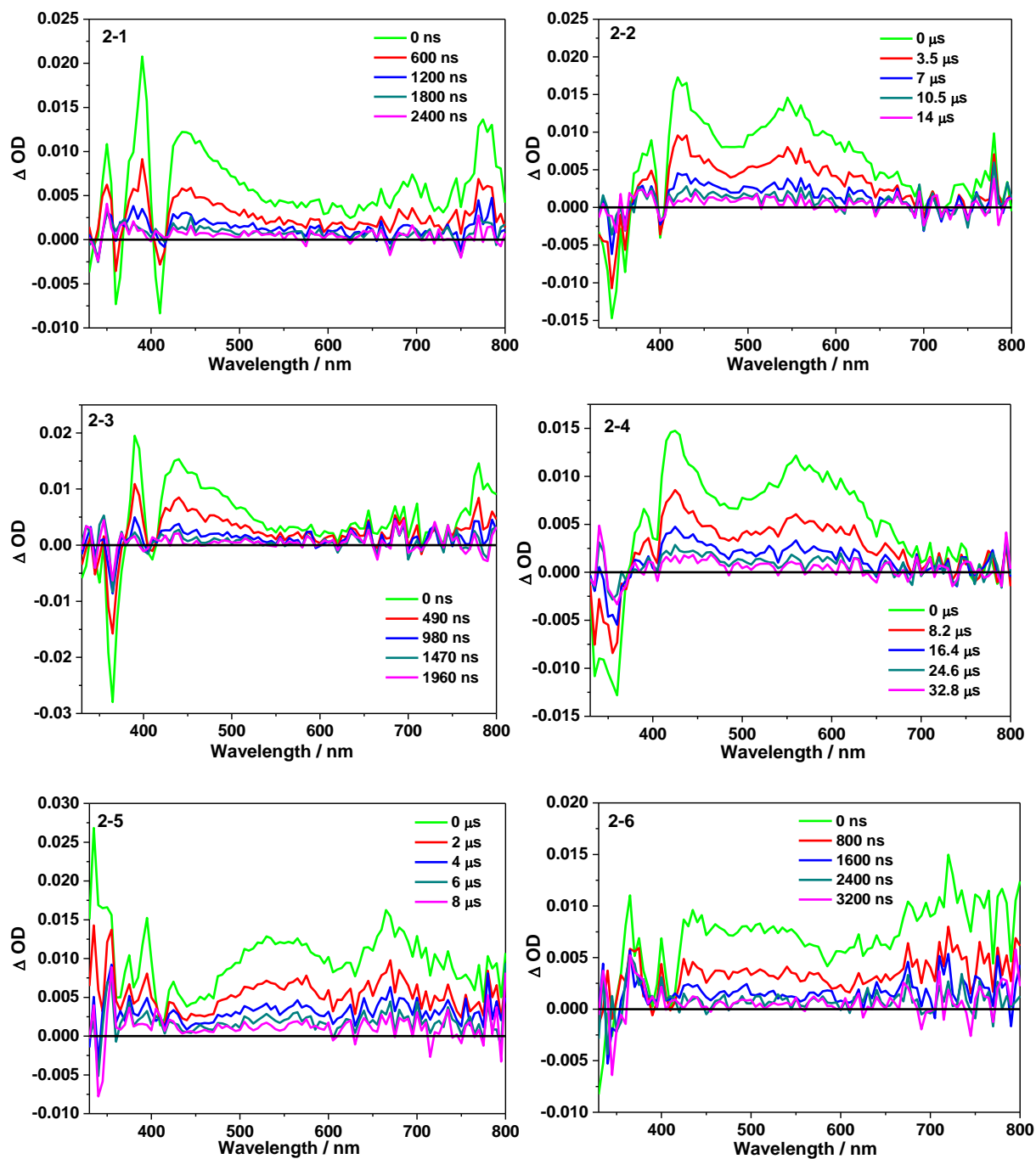


Figure 2.7. Nanosecond time-resolved transient differential absorption spectra of 2-1 – 2-6 in acetonitrile. $\lambda_{\text{ex}} = 355 \text{ nm}$, $A_{355} = 0.4$ in a 1-cm cuvette.

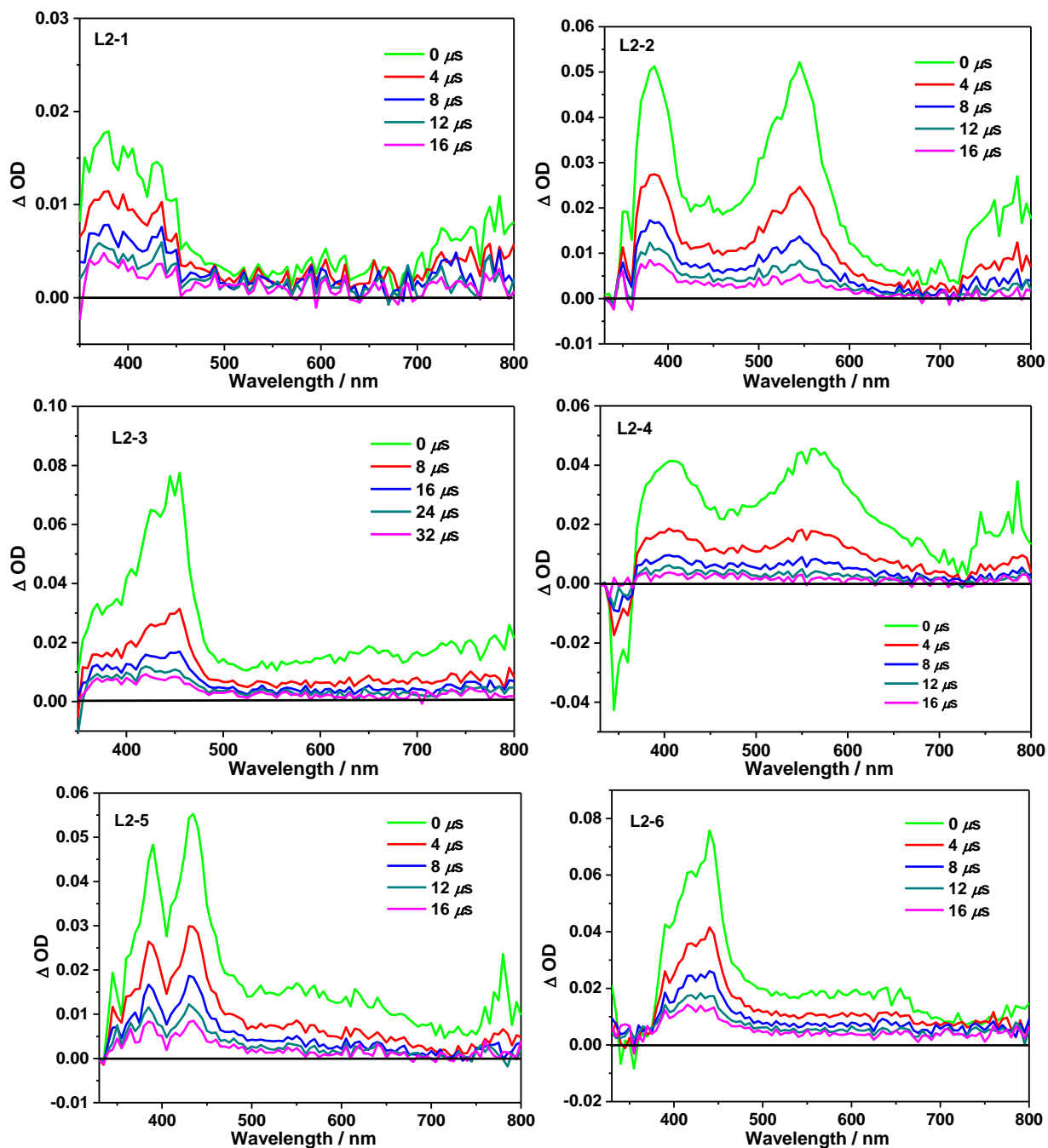


Figure 2.8. Nanosecond time-resolved transient differential absorption spectra of L2-1 – L2-6 in acetonitrile. $\lambda_{ex} = 355$ nm, $A_{355} = 0.4$ in a 1-cm cuvette.

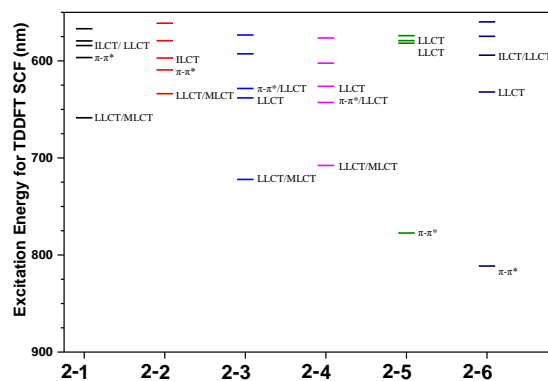


Figure 2.9. Calculated triplet excited state energy diagram for complexes **2-1** – **2-6** in CH₃CN.

2.4. Conclusion

We demonstrated the first time that extending the π -conjugation of that N[^]N ligand could cause either blue- or red-shifts of the lowest-energy absorption and emission bands depending on the site of benzannulation in Ir(III) complexes. Molecular orbital symmetry analysis was applied to rationalize this unusual phenomenon. The site-dependent destabilization or stabilization of the LUMO (or LUTO in cases of excited state) upon benzannulation appears to be a general feature for small organic molecules and transition-metal complexes. The site-dependent benzannulation also influences the triplet excited-state absorption drastically. This discovery would enable a rational design of organic or organometallic compounds that require a pre-determined absorption and/or emission energies and could potentially advance the photonic fields such as OLED, solar energy conversion, luminescent biological labeling, etc. In addition, the complexes reported in this paper exhibited weak ground-state absorption at 430 – 700 nm, but stronger triplet excited-state absorption in this spectral region. Therefore, they have the potential to be developed into broadband reverse saturable absorbers. This study is currently undergoing and will be reported in the near future.

2.5. References

- ¹ Jung, Y.; Lippard, S. J. *Chem. Rev.* **2007**, *107*, 1387.
- ² Dixon, I. M.; Collin, J.-P.; Sauvage, J.-P.; Flamigni, L.; Encinas, S.; Barigelletti, F. *Chem. Soc. Rev.* **2000**, *29*, 385.
- ³ Goldsmith, J. I.; Hudson, W. R.; Lowry, M. S.; Anderson, T. H.; Bernhard, S. *J. Am. Chem. Soc.* **2005**, *127*, 7502.
- ⁴ Gärtner, F.; Cozzula, D.; Losse, S.; Boddien, A.; Anilkumar, G.; Junge, H.; Schulz, T.; Marquet, N.; Spannenberg, A.; Gladiali, S.; Beller, M. *Chem. Eur. J.* **2011**, *17*, 6998.
- ⁵ Goswami, S.; Sengupta, D.; Paul, N. D.; Mondal, T. K.; Goswami, S. *Chem. Eur. J.* **2014**, *20*, 6103.
- ⁶ Radwan, Y. K.; Maity, A.; Teets, T. S. *Inorg. Chem.* **2015**, *54*, 7122.
- ⁷ Zhao, J.; Wu, W.; Sun, J.; Guo, S. *Chem. Soc. Rev.* **2013**, *42*, 5323.
- ⁸ Stimpson, S.; Jenkinson, D. R.; Sadler, A.; Latham, M.; Wragg, A.; Meijer, A. J. H. M.; Thomas, J. A. *Angew. Chem. Int. Ed.* **2015**, *54*, 3000.
- ⁹ Mydlak, M.; Bizzarri, C.; Hartmann, D.; Sarfert, W.; Schmid, G.; De Cola, L. *Adv. Funct. Mater.* **2010**, *20*, 1812.
- ¹⁰ Costa, R. D.; Ortí, E.; Bolink, H. J.; Monti, F.; Accorsi, G.; Armaroli, N. *Angew. Chem. Int. Ed.* **2012**, *51*, 8178.
- ¹¹ Romanenko, I.; Gajan, D.; Sayah, R.; Crozet, D.; Jeanneau, E.; Lucas, C.; Leroux, L.; Veyre, L.; Lesage, A.; Emsley, L.; Lacôte, E.; Thieuleux, C. *Angew. Chem. Int. Ed.* **2015**, *127*, 13129.
- ¹² Schulze, M.; Steffen, A.; Würthner, F. *Angew. Chem. Int. Ed.* **2015**, *54*, 1570.
- ¹³ Okada, S.; Okinaka, K.; Iwawaki, H.; Furugori, M.; Hashimoto, M.; Mukaide, T.; Kamatani, J.; Igawa, S.; Tsuboyama, A.; Takiguchi, T.; Ueno, K. *Dalton Trans.* **2005**, *9*, 1583.

- ¹⁴ Nazeeruddin, Md. K.; Wegh, R. T.; Zhou, Z.; Klein, C.; Wang, Q.; Angelis, F. De; Fantacci, S.; Graetzel; M. *Inorg. Chem.* **2006**, *45*, 9245.
- ¹⁵ Sunesh, C. D.; Mathai, G.; Choe, Y. *ACS Appl. Mater. Interfaces* **2014**, *6*, 17416.
- ¹⁶ Zollinger, H. *Color Chemistry*, 3rd ed., Wiley-VCH: Zurich, **2001**, p550.
- ¹⁷ Zeng, X.; Tavasli, M.; Perepichka, I. F.; Batsanov, A. S.; Bryce, M. R.; Chiang, C.-J.; Rothe, C.; Monkman, A. P. *Chem. Eur. J.* **2008**, *14*, 933.
- ¹⁸ Kim, K.-Y.; Farley, R. T.; Schanze, K. S. An Iridium(III) Complex that Exhibits Dual Mechanism Nonlinear Absorption. *J. Phys. Chem. B* **2006**, *110*, 17302–17304.
- ¹⁹ Li, Y.; Dandu, N.; Liu, R.; Li, Z.; Kilina, S.; Sun, W. *J. Phys. Chem. C* **2014**, *118*, 6372.
- ²⁰ Li, Y.; Dandu, N.; Liu, R.; Hu, L.; Kilina, S.; Sun, W. *ACS Appl. Mater. Interfaces.* **2013**, *5*, 6556.
- ²¹ Adachi, M.; Murata, Y. *J. Phys. Chem. A* **1998**, *102*, 841.
- ²² Adachi, M.; Nagao, Y. *Chem. Mater.* **2001**, *13*, 662.
- ²³ Martin, N.; Segura, J. L.; Seoane, C. *J. Mater. Chem.* **1997**, *7*, 1661.
- ²⁴ Jensen, B. S.; Parker, V. D. *J. Am. Chem. Soc.* **1975**, *97*, 5211.
- ²⁵ Hanson, K.; Roskop, L.; Djurovich, P. I.; Zahariev, F.; Gordon, M. S.; Thompson, M. E. *J. Am. Chem. Soc.* **2010**, *132*, 16247.
- ²⁶ Wen, H.-M.; Wu, Y.-H.; Fan, Y.; Zhang, L.-Y.; Chen, C.-N.; Chen, Z.-N. *Inorg. Chem.* **2010**, *49*, 2210.
- ²⁷ Juris, A.; Barigelletti, F.; Balzani, V.; Belser, P.; Von Zelewsky, A. *Inorg. Chem.* **1985**, *24*, 202–206.
- ²⁸ Sun, Y.; Joyce, L. E.; Dickson, N. M.; Turro, C. *Chem. Commun.*, **2010**, *46*, 2426.

- ²⁹ Zhao, Q.; Liu, S.; Shi, M.; Wang, C.; Yu, M.; Li, L.; Li, F.; Yi, T.; Huang, C. *Inorg. Chem.* **2006**, *45*, 6152.
- ³⁰ Liu, R.; Dandu, N.; Chen, J.; Li, Y.; Li, Z.; Liu, S.; Wang, C.; Kilina, S.; Kohler, B.; Sun, W. *J. Phys. Chem. C* **2014**, *118*, 23233.
- ³¹ Li, Z.; Cui, P.; Wang, C.; Kilina, S.; Sun, W. *J. Phys. Chem. C* **2014**, *118*, 28764.
- ³² Yi, X.; Yang, P.; Huang, D.; Zhao, J. *Dyes Pigm.* **2013**, *96*, 104.
- ³³ Riesgo, E. C.; Hu, Y.-Z.; Bouvier, F.; Thummel, R. P. *Inorg. Chem.* **2001**, *40*, 3413.
- ³⁴ Marco-Contelles, J.; Pérez-Mayoral, E.; Samadi, A.; Carreiras, M. D.; Soriano, E. Recent Advances in the Friedländer Reaction. *Chem. Rev.* **2009**, *109*, 2652.
- ³⁵ Li, A. H.; Beard, D. J.; Coate, H.; Honda, A.; Kadalbajoo, M.; Kleinberg, A.; Sherman, D. *Synthesis* **2010**, *10*, 1678.
- ³⁶ Nonoyama, M. *Bull. Chem. Soc. Jpn.* **1974**, *47*, 767.
- ³⁷ Mauro, M.; De Paoli, G.; Otter, M.; Donghi, D.; D'Alfonso, G.; De Cola, L. *Dalton Trans.* **2011**, *40*, 12106.
- ³⁸ Martin, R. L. *J. Chem. Phys.* **2003**, *118*, 4775–4777.
- ³⁹ Sun, W.; Pei, C.; Lu, T.; Cui, P.; Li, Z.; McCleese, C.; Fang, Y.; Kilina, S.; Song, Y.; Burda, C. *J. Mater. Chem. C* **2016**, *4*, 5059.
- ⁴⁰ Wu, S.-H.; Ling, J.-W.; Lai, S.-H.; Huang, M.-J.; Cheng, C. H.; Chen, I.-C. *J. Phys. Chem. A* **2010**, *114*, 10339.
- ⁴¹ Rogers, J. E.; Nguyen, K. A.; Hufnagle, D. C.; McLean, D. G.; Su, W.; Gossett, K. M.; Burke, A. R.; Vinogradov, S. A.; Pachter, R.; Fleitz, P. A. *J. Phys. Chem. A* **2003**, *107*, 11331.
- ⁴² Slinker, J. D.; Gorodetsky, A. A.; Lowry, M. S.; Wang, J.; Parker, S.; Rohl, R.; Bernhard, S.; Malliaras, G. G. *J. Am. Chem. Soc.* **2004**, *126*, 2763.

- ⁴³ Lowry, M. S.; Goldsmith, J. I.; Slinker, J. D.; Rohl, R.; Pascal, R. A.; Malliaras, G. G.; Bernhard, S. *Chem. Mater.* **2005**, *17*, 5712.
- ⁴⁴ Tsuboyama, A.; Iwawaki, H.; Furugori, M.; Mukaide, T.; Kamatani, J.; Igawa, S.; Moriyama, T.; Miura, S.; Takiguchi, T.; Okada, S.; Hoshino, M.; Ueno, K. *J. Am. Chem. Soc.* **2003**, *125*, 12971.
- ⁴⁵ Ladouceur, S.; Fortin, D.; Zysman-Colman, E. *Inorg. Chem.* **2010**, *49*, 5625–5641.
- ⁴⁶ Wang, C.; Lystrom, L.; Yin, H.; Hetu, M.; Kilina, S.; McFarland, S. A.; Sun, W. *Dalton Trans.* **2016**, *45*, 16366.
- ⁴⁷ Liu, R.; Li, Y.; Li, Y.; Zhu, H.; Sun, W. *J. Phys. Chem. A* **2010**, *114*, 12639.
- ⁴⁸ Liu, R.; Dandu, N.; Li, Y.; Kilina, S.; Sun, W. *Dalton Trans.* **2013**, *42*, 4398.
- ⁴⁹ Sun, Y.; Joyce, L. E.; Dickson, N. M.; Turro, C. *Chem. Commun.* **2010**, *46*, 2426.
- ⁵⁰ Liu, Y.; Hammitt, R.; Lutterman, D. A.; Joyce, L. E.; Thummel, R. P.; Turro, C. *Inorg. Chem.* **2009**, *48*, 375.
- ⁵¹ Foxon, S. P.; Metcalfe, C.; Adams, H.; Webb, M.; Thomas, J. A. *Inorg. Chem.* **2007**, *46*, 409-416.
- ⁵² Foxon, S. P.; Alamiry, M. A. H.; Walker, M. G.; Meijer, A. J. H. M.; Sazanovich, I. V.; Weinstein, J. A.; Thomas, J. A. *J. Phys. Chem. A* **2009**, *113*, 12754.
- ⁵³ Dubinina, G. G.; Price, R. S.; Abboud, K. A.; Wicks G.; Wnuk, P.; Stepanenko, Y.; Drobizhev, M.; Rebane, A.; Schanze, K. S. *J. Am. Chem. Soc.* **2012**, *134*, 19346.
- ⁵⁴ Kumar, C. V.; Qin, L.; Das, P. K. *J. Chem. Soc., Faraday Trans. 2* **1984**, *80*, 783.
- ⁵⁵ Carmichael, I.; Hug, G. L. *Phys. Chem. Ref. Data* **1986**, *15*, 1.
- ⁵⁶ Demas, J. N.; Crosby, G. A. *J. Phys. Chem.* **1971**, *75*, 991.

- ⁵⁷ Suzuki, K.; Kobayashi, A.; Kaneko, S.; Takehira, K.; Yoshihara, T.; Ishida, H.; Shiina, Y.; Oishi, S.; Tobita, S. *Phys. Chem. Chem. Phys.* **2009**, *11*, 9850.
- ⁵⁸ Semonin, O. E.; Johnson, J. C.; Luther, J. M.; Midgett, A. G.; Nozik, A. J.; Beard, M. C. *J. Phys. Chem. Lett.* **2010**, *1*, 2445.
- ⁵⁹ Firey, P. A.; Ford, W. E.; Sounik, J. R.; Kenney, M. E.; Rodgers, M. A. J. *J. Am. Chem. Soc.* **1988**, *110*, 7626.
- ⁶⁰ Frisch, M. J.; Trucks, G. W.; Schlegel, H. B.; Scuseria, G. E.; Robb, M. A.; Cheeseman, J. R.; Scalmani, G.; Barone, V.; Mennucci, B.; Peterson, G. A.; Nakatsuji, H.; Caricato, M.; Li, X.; Hratchian, H. P.; Izmaylov, A. F.; Bloino, J.; Zheng, G.; Sonnenberg, J. L.; Hada, M.; Ehara, M.; Toyota, K.; Fukuda, R.; Hasegawa, J.; Ishida, M.; Nakajima, T.; Honda, Y.; Kitao, O.; Nakai, H.; Vreven, T.; Montgomery, J. A., Jr.; Peralta, J. E.; Ogliaro, F.; Bearpark, M.; Heyd, J. J.; Brothers, E.; Kudin, K. N.; Staroverov, V. N.; Kobayashi, R.; Normand, J.; Raghavachari, K.; Rendell, A.; Burant, J. C.; Iyengar, S. S.; Tomasi, J.; Cossi, M.; Rega, N.; Millam, J. M.; Klene, M.; Knox, J. E.; Cross, J. B.; Bakken, V.; Adamo, C.; Jaramillo, J.; Gomperts, R.; Stratmann, R. E.; Yazyev, O.; et al. *Gaussian 09*, revision B.1; Gaussian, Inc.: Wallingford, CT, **2009**.
- ⁶¹ Perdew, J. P.; Burke, K.; Ernzerhof, M. *Phys. Rev. Lett.* **1996**, *77*, 3865.
- ⁶² Hay, P. J.; Wadt, W. R. *J. Chem. Phys.* **1985**, *82*, 270.
- ⁶³ Francel, M. M.; Pietro, W. J.; Hehre, W. J.; Binkley, J. S.; Gordon, M. S.; DeFrees, D. J.; Pople, J. A. *J. Chem. Phys.* **1982**, *77*, 3654.
- ⁶⁴ Krishnan, R.; Binkley, J. S.; Seeger, R.; Pople, J. A. *J. Chem. Phys.* **1980**, *72*, 650.
- ⁶⁵ Pei, C.; Cui, P.; McCleese, C.; Kilina, S.; Burda, C.; Sun, W. *Dalton Trans.* **2015**, *44*, 2176.
- ⁶⁶ Li, Z.; Li, H.; Gifford, B. J.; Peiris, W. D. N.; Kilina, S.; Sun, W. *RSC Advances* **2016**, *6*, 41214.

- ⁶⁷ Li, Y.; Dandu, N.; Liu, R.; Kilina, S.; Sun, W. *Dalton Trans.* **2014**, *43*, 1724.
- ⁶⁸ Barone, V.; Cossi, M.; Tomasi, J. *J. Comput. Chem.* **1998**, *19*, 404.
- ⁶⁹ Cossi, M.; Barone, V.; Cammi, R.; Tomasi, J. *Chem. Phys. Lett.* **1996**, *255*, 327.
- ⁷⁰ Guillon, T.; Boggio-Pasqua, M.; Alary, F.; Heully, J.; Lebon, E.; Sutra, P.; Igau, A. *Inorg. Chem.* **2010**, *49*, 8862.
- ⁷¹ Zhang, T.; Qi, X.; Jia, J.; Wu, H. *J. Mol. Model* **2012**, *18*, 4615.
- ⁷² Dennington, R. II; Keith, T.; Millam, J. GaussView; Semichem Inc.: Shawnee Mission, KS, **2007**.

3. IMPACT OF BENZANNULATION SITE AT THE DIIMINE (N^N) LIGAND ON THE PHOTOPHYSICS AND REVERSE SATURABLE ABSORPTION OF CYCLOMETALATED MONOCATIONIC IRIDIUM(III) COMPLEXES

3.1. Introduction

Among the diverse transition–metal complexes, pseudo–octahedral d^6 iridium(III) complexes have attracted growing interest in both academia and industry during the past two decades.^{1–4} The strong spin–orbit coupling induced by the Ir(III) ion enhances the intersystem crossing (ISC) rate and promotes triplet excited–state formation. These characteristics spark research interest in exploring potential binding geometries with novel ancillary ligands. After the seminal work by Watts et. al. on triply ortho–metalated iridium(III) complexes in the 1980s,⁵ diverse mono–, bis– and triscyclometallated complexes with different polypyridine ligands or cyclometallating ligands have been reported.^{6,7} Among these complexes, cyclometalated monocationic Ir(III) complexes have been reported to play a crucial role in various applications, such as sensitized photo–upconversion,³ organic light emitting diodes (OLEDs),^{8–11} light–emitting electrochemical cells (LEECs),^{12,13} photodynamic therapy,^{14–16} nonlinear optics,^{17–19} photocatalysis,^{20–22} and bioimaging and biosensing.²³

In view of the structures of the monocationic Ir(III) complexes $[(N^N)Ir(C^N)_2]^+$ (where N^N refers to the diimine ligand and C^N refers to the cyclometalating ligand), the combination of one N^N ligand and two identical C^N ligands provides the opportunity to tune the photophysical properties of these complexes via a diverse selection and combination of ligands. Generally, the electron–deficient N^N ligand is the major contributor to the lowest unoccupied molecular orbital (LUMO) in these Ir(III) complexes, while the C^N ligands and the d –orbital of

the Ir(III) ion hold the majority of the highest occupied molecular orbital (HOMO).^{24–26} Consequently, extending π -conjugation or introducing electron-donating/withdrawing substituents on the N^N ligand would alter the LUMO exclusively. It has been reported that incorporation of electron-donating substituents, such as an amino or methoxy group, to the N^N ligand raised the LUMO and blue-shifted the low-energy absorption bands of Ir(III) complexes. In contrast, Ir(III) complexes bearing electron-withdrawing substituents at the N^N ligand, such as fluoro or cyano, displayed red-shifted low-energy absorption bands due to the stabilized LUMOs.^{26,27} Another approach to tune the LUMO energy is to bring π -conjugated units to the N^N ligand by benzannulation. It was reported that the energy of the LUMO decreased from -3.15 eV to -3.38 eV for the Ir(III) complex bearing 2-(pyridin-2-yl)quinoline ligand upon benzannulation at the 2,2'-bipyridine ligand.²⁶ Additionally, extending the π -conjugation of the N^N ligand via benzannulation or incorporation of π -conjugated substituents simultaneously induces more $^3\pi,\pi^*$ character into the lowest triplet excited state (T_1).^{17,28–33} In contrast to the charge-transfer based T_1 state (3CT), the $^3\pi,\pi^*$ based T_1 state typically exhibits a longer lifetime, structured emission bands, and a higher emission quantum yield. Therefore, extending π -conjugation on the N^N ligand can serve as an adjuster for both the lowest singlet excited state and the lowest triplet excited state.

In the reported work on benzannulation on organic compounds, either hypsochromic or bathochromic shifts of the absorption and emission bands have been observed depending on the site of benzannulation.^{34–37} Despite finding this unusual phenomenon in small organic molecules, examples featuring the impacts of varied site of benzannulation on the ligands on organometallic complexes are still rare.^{32,38} In seeking a better understanding of the effects of benzannulation site at the ligands on the photophysics of these complexes, the seminal report by Thompson and

Gordon³⁸ on the (N[^]N[^]N)PtCl derivatives has intrigued our interest in other heavy transition-metal complexes, such as the Ir(III) complexes. In our previous work, we explored a series of cyclometalated monocationic Ir(III) complexes employing 1,2-diphenyl-9*H*-pyreno[4,5-*d*]imidazole as the C[^]N ligands, and 2-(pyridin-2-yl)quinoline and its derivatives as the N[^]N ligand.³² Compared to the parent complex bearing the 2-(pyridin-2-yl)quinoline ligand, pronounced red- or blue-shift of the absorption and emission bands was observed via benzannulation at the different sites of the N[^]N ligand. This effect was rationalized by symmetry analysis of the frontier molecular orbitals at the benzannulation site of the parent complex via theoretical calculations. While this phenomenon has been well explained for our previously studied complexes, validation of the prediction from our aforementioned work on tuning the photophysical properties of the Ir(III) complexes through benzannulation at the previously undeveloped sites of N[^]N ligand is still needed. Moreover, because of their readily adjustable ground-state and triplet excited-state absorption, these Ir(III) complexes have the potential for use as reverse saturable absorbers, which is worthy of in-depth study.^{17-19,29-31,33,39-42}

Targeting these goals, we have synthesized ten cyclometalated monocationic Ir(III) complexes (**Chart 3.1**). These complexes utilized 2-phenylquinoline as the cyclometalating ligands and 2,2'-bipyridine (bpy) derivatives with a varied degree of π -conjugation as the diimine ligand. Extending π -conjugation of the bpy ligand was realized *via* benzannulation at one pyridine ring (**3-1 – 3-4**), at the bridge of the two pyridine rings (**3-5 – 3-7**), or at the different sites (*i.e.* 5,6-/5',6'-, 4,5-/4',5'-, or 3,4-/3',4'-) of both pyridine rings (**3-8 – 3-10**). Complexes **3-2 – 3-4**, **3-6**, **3-7**, **3-9** and **3-10** are new complexes that are first reported herein. Although complexes **3-1**,⁴³ **3-5**⁴⁴ and **3-8**⁴⁵ are known in the literature, previous work has focused on their biological/biomedical activities, and no systematic photophysical or reverse saturable absorption

(RSA) studies have been reported for these complexes. More importantly, these complexes fall naturally into our focus on a comprehensive understanding of the impact of benzannulation site at the N^N ligand on the photophysics and RSA of the cyclometalated monocationic Ir(III) complexes.

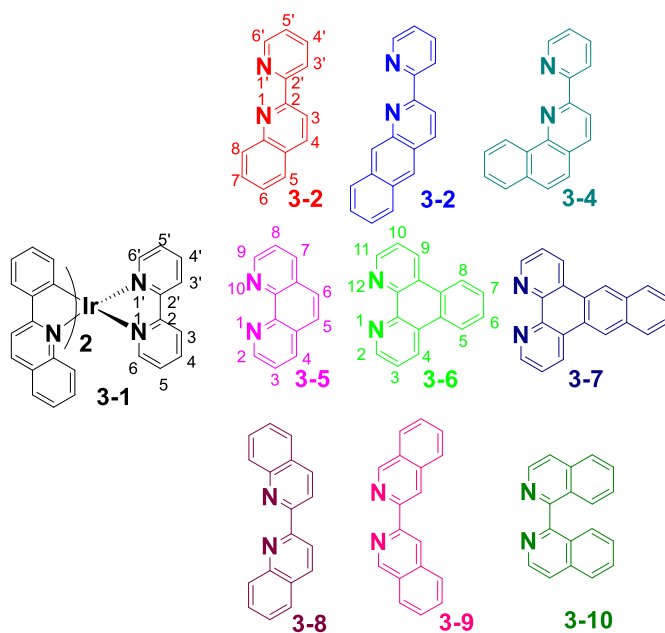


Chart 3.1. Structures of complexes **3-1** – **3-10**.

3.2. Experimental section

3.2.1. Materials and synthesis

All reagents and solvents were purchased from Alfa Aesar or VWR International and used as received unless otherwise stated. Al₂O₃ gels (activated, neutral) and silica gels (230–400 mesh) for column chromatography were purchased from Sorbent Technology. The N^N ligands 2,2'-bipyridine (**L3-1**), phenanthroline (**L3-5**), and 2,2'-bisquinoline (**L3-8**) were obtained from Alfa Aesar. The synthesis of 2-(pyridin-2-yl)quinoline (**L3-2**),⁴⁶ 2-(pyridin-2-yl)[6,7]benzoquinoline (**L3-3**),⁴⁷ and 2-(pyridin-2-yl)-[7,8]benzoquinoline (**L3-4**)⁴⁸ was carried out

using the reported methods. The synthesis of benzo[*f*][1,10]phenanthroline (**L3-6**),⁴⁹ naphtho[2,3-*f*][1,10]phenanthroline (**L3-7**)⁵⁰, 3,3'-biisoquinoline (**L3-9**)⁵¹, and 1,1'-biisoquinoline (**L3-10**)^{51,52} followed published procedures. 2-Phenylquinoline (C[^]N ligand) and its Ir(III) μ -chloro-bridged dimers [Ir(C[^]N)₂Cl]₂ were synthesized following reported procedures.⁵³ ¹H NMR spectroscopy, high-resolution mass spectrometry (HRMS), and elemental analyses were used to characterize these complexes. ¹H NMR spectra were obtained on a Varian Oxford 400 or Bruker 400 spectrometer in CDCl₃ or *d*₆-DMSO using tetramethylsilane (TMS) as the internal standard. A Bruker BioTOF III mass spectrometer was used for ESI-HRMS analyses. Elemental analyses were carried out by NuMega Resonance Laboratories, Inc. in San Diego, California.

General procedure for the synthesis of 3-1 – 3-10. The Ir(III) dimer [Ir(C[^]N)₂Cl]₂ (0.03 mmol), N[^]N ligand (0.06 mmol), and AgSO₃CF₃ (0.06 mmol) were added in the mixed solvent of CH₂Cl₂ and MeOH (v/v = 2:1, 30 mL). The reaction mixture was degassed and heated to reflux under a nitrogen atmosphere for 24 h without light illumination. After cooling to room temperature, NH₄PF₆ (0.3 mmol) was added to the reaction mixture and stirred at r.t. for 2 h. Then, the solvent was removed under vacuum, and the crude product was purified by column chromatography (neutral alumina gel, dichloromethane/hexane (3:1 – 1:0, v/v)) to obtain the target Ir(III) complexes.

Complex 3-1. An orange solid was obtained as the product (36 mg, yield: 66%). ¹H NMR (400 MHz, CDCl₃): δ 8.27 (d, *J* = 8.3 Hz, 2H), 8.23–8.07 (m, 6H), 8.05–7.91 (m, 4H), 7.71 (dd, *J* = 8.1, 1.4 Hz, 2H), 7.43–7.32 (m, 4H), 7.25 (d, 2H), 7.20–7.13 (m, 2H), 6.99 (ddd, *J* = 8.7, 6.1, 1.5 Hz, 2H), 6.86–6.79 (m, 2H), 6.55 (dd, *J* = 7.7, 0.7 Hz, 2H). ESI-HRMS (*m/z*): calcd. for [C₄₀H₂₈N₄Ir]⁺, 757.1943; found, 757.1955. Anal. Calcd. (%) for C₄₀H₂₈F₆IrN₄P: C, 53.27; H, 3.13; N, 6.21. Found: C, 53.59; H, 3.48; N, 5.99.

Complex 3-2. An orange solid was obtained as the product (31 mg, yield: 54%). ^1H NMR (400 MHz, CDCl_3) δ 8.46–8.37 (m, 2H), 8.37–8.21 (m, 3H), 8.18–8.10 (m, 1H), 8.09–8.00 (m, 2H), 7.84 (dd, $J = 7.8, 4.2$ Hz, 2H), 7.79 (d, $J = 7.2$ Hz, 1H), 7.61 (dd, $J = 15.7, 7.9$ Hz, 3H), 7.51 (dd, $J = 14.7, 8.3$ Hz, 2H), 7.45–7.35 (m, 3H), 7.25 (s, 1H), 7.16 (ddd, $J = 15.8, 12.3, 4.7$ Hz, 3H), 7.08 (t, $J = 7.1$ Hz, 1H), 7.02–6.80 (m, 4H), 6.54 (d, $J = 7.2$ Hz, 1H), 6.34 (d, $J = 7.4$ Hz, 1H). ESI–HRMS (m/z): calcd. for $[\text{C}_{44}\text{H}_{30}\text{N}_4\text{Ir}]^+$, 807.2100; found, 807.2136. Anal. Calcd. (%) for $\text{C}_{44}\text{H}_{30}\text{F}_6\text{IrN}_4\text{P}\cdot 0.3\text{C}_6\text{H}_{14}$ (C_6H_{14} : hexane): C, 56.50; H, 3.64; N, 5.68. Found: C, 56.63; H, 3.26; N, 5.46.

Complex 3-3. An orange solid was obtained as the product (34 mg, yield: 57%). ^1H NMR (400 MHz, d_6 -DMSO): δ 8.72 (dt, $J = 9.0, 6.9$ Hz, 3H), 8.67 (s, 1H), 8.38 (d, $J = 7.0$ Hz, 1H), 8.28 (t, $J = 8.0$ Hz, 2H), 8.21–8.09 (m, 4H), 8.06 (ddd, $J = 9.3, 7.1, 1.2$ Hz, 2H), 7.86 (dd, $J = 7.7, 0.8$ Hz, 1H), 7.82–7.70 (m, 3H), 7.66–7.62 (m, 1H), 7.58–7.52 (m, 1H), 7.45–7.35 (m, 2H), 7.24–7.15 (m, 2H), 7.08–6.95 (m, 3H), 6.87 (ddd, $J = 15.5, 12.7, 5.3$ Hz, 4H), 6.38 (dd, $J = 10.8, 7.7$ Hz, 2H). ESI–HRMS (m/z): calcd. for $[\text{C}_{48}\text{H}_{32}\text{N}_4\text{Ir}]^+$, 857.2256; found, 857.2241. Anal. Calcd. for $\text{C}_{48}\text{H}_{32}\text{F}_6\text{IrN}_4\text{P}\cdot 0.9\text{CH}_2\text{Cl}_2$: C, 54.46; H, 3.16; N, 5.20. Found: C, 54.20; H, 3.15; N, 5.39.

Complex 3-4. An orange solid was obtained as the product (52 mg, yield: 87%). ^1H NMR (400 MHz, CDCl_3): δ 9.22 (d, $J = 8.8$ Hz, 1H), 8.63 (d, $J = 8.2$ Hz, 1H), 8.52 (d, $J = 8.6$ Hz, 1H), 8.43 (d, $J = 8.9$ Hz, 1H), 8.31 (d, $J = 8.2$ Hz, 1H), 8.13 (t, $J = 7.8$ Hz, 1H), 8.05 (d, $J = 6.8$ Hz, 1H), 7.93 (dd, $J = 10.4, 8.1$ Hz, 3H), 7.84 (d, $J = 8.7$ Hz, 1H), 7.69–7.58 (m, 3H), 7.48 (dt, $J = 9.5, 6.9$ Hz, 3H), 7.34–7.21 (m, 4H), 7.14–6.99 (m, 3H), 6.77 (d, $J = 8.7$ Hz, 1H), 6.68 (t, $J = 7.5$ Hz, 1H), 6.64–6.54 (m, 2H), 6.50 (t, $J = 7.2$ Hz, 2H), 6.32 (t, $J = 7.6$ Hz, 1H), 6.12 (d, $J = 8.1$ Hz, 1H). ESI–HRMS (m/z): calcd. for $[\text{C}_{48}\text{H}_{32}\text{N}_4\text{Ir}]^+$, 857.2256; found, 857.2289. Anal. Calcd. for $\text{C}_{48}\text{H}_{32}\text{F}_6\text{IrN}_4\text{P}\cdot 0.5\text{CH}_2\text{Cl}_2$: C, 55.77; H, 3.18; N, 5.36. Found: C, 55.37; H, 3.32; N, 5.36.

Complex 3-5. An orange solid was obtained as the product (32 mg, yield: 58%). ^1H NMR (400 MHz, d_6 -DMSO) δ 8.74 (dd, $J = 8.2, 1.4$ Hz, 2H), 8.60 (d, $J = 9.0$ Hz, 2H), 8.51–8.45 (m, 4H), 8.36 (d, $J = 7.3$ Hz, 2H), 8.09 (s, 2H), 8.05 (dd, $J = 8.2, 5.2$ Hz, 2H), 7.81 (dd, $J = 8.1, 1.3$ Hz, 2H), 7.23 (ddd, $J = 15.0, 8.0, 1.0$ Hz, 4H), 7.11 (d, $J = 9.0$ Hz, 2H), 6.91–6.78 (m, 4H), 6.54 (dd, $J = 7.7, 0.8$ Hz, 2H). ESI–HRMS (m/z): calcd. for $[\text{C}_{42}\text{H}_{28}\text{N}_4\text{Ir}]^+$, 781.1943; found, 781.1966. Anal. Calcd. for $\text{C}_{42}\text{H}_{28}\text{F}_6\text{IrN}_4\text{P}$: C, 54.48; H, 3.05; N, 6.05. Found: C, 54.25; H, 2.98; N, 6.02.

Complex 3-6. An orange solid was obtained as the product (41 mg, yield: 70%). ^1H NMR (400 MHz, CDCl_3) δ 9.04 (d, $J = 8.1$ Hz, 2H), 8.51–8.43 (m, 4H), 8.20 (d, $J = 8.9$ Hz, 2H), 8.16 (d, $J = 8.6$ Hz, 2H), 8.06 (d, $J = 8.0$ Hz, 2H), 7.88 (dd, $J = 8.4, 5.2$ Hz, 2H), 7.59–7.51 (m, 4H), 7.23–7.05 (m, 6H), 6.83 (td, $J = 7.5, 1.3$ Hz, 2H), 6.76 (ddd, $J = 8.6, 6.9, 1.4$ Hz, 2H), 6.66–6.55 (m, 2H). ESI–HRMS (m/z): calcd. for $[\text{C}_{46}\text{H}_{30}\text{N}_4\text{Ir}]^+$, 831.2100; found, 831.2123. Anal. Calcd. for $\text{C}_{46}\text{H}_{30}\text{F}_6\text{IrN}_4\text{P}\cdot 0.5\text{C}_6\text{H}_{14}\cdot 2\text{H}_2\text{O}$ (C_6H_{14} : hexane): C, 55.78; H, 3.92; N, 5.31. Found: C, 55.70; H, 4.20; N, 5.64.

Complex 3-7. An orange solid was obtained as the product (51 mg, yield: 83%). ^1H NMR (400 MHz, d_6 -DMSO) δ 9.57–9.46 (m, 4H), 8.63 (d, $J = 9.0$ Hz, 2H), 8.53 (d, $J = 8.7$ Hz, 2H), 8.42–8.32 (m, 4H), 8.20 (dd, $J = 6.3, 3.3$ Hz, 2H), 8.10 (dd, $J = 8.4, 5.2$ Hz, 2H), 7.83 (dd, $J = 8.1, 1.2$ Hz, 2H), 7.76 (dd, $J = 6.4, 3.2$ Hz, 2H), 7.22 (ddd, $J = 8.8, 7.4, 6.3$ Hz, 6H), 6.96–6.85 (m, 4H), 6.54–6.48 (m, 2H). ESI–HRMS (m/z): calcd. for $[\text{C}_{50}\text{H}_{32}\text{N}_4\text{Ir}]^+$, 881.2256; found, 881.2291. Anal. Calcd. for $\text{C}_{50}\text{H}_{32}\text{F}_6\text{IrN}_4\text{P}\cdot 0.3\text{CH}_2\text{Cl}_2$: C, 57.46; H, 3.13; N, 5.33. Found: C, 57.37; H, 3.07; N, 5.37.

Complex 3-8. A red solid was obtained as the product (38 mg, yield: 63%). ^1H NMR (400 MHz, d_6 -DMSO) δ 8.72 (d, $J = 8.6$ Hz, 2H), 8.50 (d, $J = 8.7$ Hz, 2H), 8.32 (d, $J = 8.8$ Hz, 2H), 8.22 (d, $J = 9.0$ Hz, 2H), 8.11–8.03 (m, 2H), 8.01–7.88 (m, 4H), 7.60–7.49 (m, 4H), 7.47–7.35

(m, 4H), 7.10 (ddd, $J = 8.6, 6.9, 1.4$ Hz, 2H), 7.06–6.98 (m, 2H), 6.89–6.79 (m, 4H), 6.36–6.28 (m, 2H). ESI–HRMS (m/z): calcd. for $[C_{48}H_{32}N_4Ir]^+$, 857.2256; found, 857.2233. Anal. Calcd. for $C_{48}H_{32}F_6IrN_4P \cdot 1.1CH_2Cl_2$: C, 53.84; H, 3.15; N, 5.11. Found: C, 53.94; H, 2.95; N, 5.13.

Complex 3-9. An orange solid was obtained as the product (20 mg, yield: 33%). 1H NMR (400 MHz, d_6 -DMSO) δ 9.49 (s, 2H), 9.13 (d, $J = 8.9$ Hz, 2H), 8.68 (d, $J = 8.7$ Hz, 2H), 8.54 (s, 2H), 8.46 (d, $J = 9.0$ Hz, 2H), 8.30 (s, 2H), 8.16 (d, $J = 8.2$ Hz, 2H), 7.96 (d, $J = 7.9$ Hz, 2H), 7.86 (d, $J = 7.3$ Hz, 2H), 7.78–7.66 (m, 6H), 7.27 (s, 2H), 6.87 (s, 2H), 6.58–6.52 (m, 2H), 6.03 (d, $J = 7.8$ Hz, 2H). ESI–HRMS (m/z): calcd. for $[C_{48}H_{32}N_4Ir]^+$, 857.2256; found, 857.2241. Anal. Calcd. for $C_{48}H_{32}F_6IrN_4P \cdot 0.2C_6H_{14}$ (C_6H_{14} : hexane): C, 57.98; H, 3.44; N, 5.50. Found: C, 58.00; H, 3.58; N, 5.20.

Complex 3-10. A red solid was obtained as the product (34 mg, yield: 56%). 1H NMR (500 MHz, d_6 -DMSO) δ 8.52 (d, $J = 9.0$ Hz, 2H), 8.44 (d, $J = 8.8$ Hz, 2H), 8.26 (d, $J = 8.2$ Hz, 2H), 8.03 (dt, $J = 14.1, 5.9$ Hz, 8H), 7.82–7.76 (m, 2H), 7.72 (d, $J = 8.0$ Hz, 2H), 7.48 (d, $J = 6.3$ Hz, 4H), 7.24 (t, $J = 7.5$ Hz, 2H), 7.15 (t, $J = 9.9$ Hz, 4H), 6.83 (t, $J = 7.4$ Hz, 2H), 6.29 (d, $J = 7.4$ Hz, 2H). ESI–HRMS (m/z): calcd. for $[C_{48}H_{32}N_4Ir]^+$, 857.2256; found, 857.2283. Anal. Calcd. for $C_{48}H_{32}F_6IrN_4P \cdot 0.9CH_2Cl_2$: C, 54.46; H, 3.16; N, 5.20. Found: C, 54.59; H, 2.99; N, 5.31.

3.2.2. Photophysical studies

Spectroscopic-grade solvents were used for the photophysical studies and were purchased from VWR International and used as received. A Varian Cary 50 spectrophotometer was used to record UV–vis absorption spectra. The emission spectra of **3-1** – **3-10** were measured on a HORIBA FluoroMax 4 fluorometer/phosphorometer. The absolute emission quantum yields (QY) were measured using a fiber coupled Ocean Optics integrating sphere. On the excitation side, the

sphere was fiber coupled to a set of Delta linear-variable filters (LVFs) and then fiber coupled to a broad white light LED. The set of LVFs were aligned with an in-house modified Ocean Optics LVF mount and positioned to give a narrow excitation band peaked at 450 nm. On the detection side, the integrating sphere was coupled to a bifurcated fiber cable that was coupled to an Ocean Optics UV VIS QE65000 spectrometer and an Ocean Optics NIRQ512 spectrometer yielding an effective detection range of 350 nm to 1700 nm. The samples were degassed and maintained in an oxygen free environment prior to and during each QY measurement.

The nanosecond transient difference absorption (TA) spectra and lifetimes of complexes **3-1** – **3-10** were measured on a laser flash photolysis spectrometer (Edinburgh LP920) in degassed CH₃CN solutions. The excitation source for the measurements was a third-harmonic output (355 nm) of a Nd:YAG laser (Quantel Brilliant; pulse duration: 4.1 ns; repetition rate: 1 Hz). Each sample solution was purged with N₂ for 40 min before measurement. The singlet depletion method⁵⁴ was applied to determine the triplet excited-state molar extinction coefficients (ϵ_T) at the TA band maximum. A benzene solution of SiNc ($\epsilon_{590} = 70,000 \text{ M}^{-1} \text{ cm}^{-1}$, $\Phi_T = 0.20$)⁵⁵ was used as a reference to determine the triplet excited-state quantum yield through the relative actinometry method.⁵⁶

3.2.3. Nonlinear transmission measurement

The nonlinear transmission experiments for all complexes at 532 nm were carried out in CH₃CN solutions in a cuvette (length: 2 mm), which linear transmission of was set to 80%. The 4.1 ns laser (Quantel Brilliant) with a repetition rate of 10 Hz was used as the light source. The As described in previous work, the same experimental setup was used in this paper.⁷⁰ The beam radius at the focal point was approximately 96 μm , focused by an $f = 40 \text{ cm}$ plano-convex lens.

3.2.4. Computational methods

Complexes **3-1** – **3-10** were computationally investigated using density functional theory (DFT) and linear response time-dependent DFT (TDDFT) calculations implemented in Gaussian09 quantum software package.⁵⁷ The ground state optimization and excited state calculations of **3-1** – **3-10** were performed using the B3LYP⁵⁸ functional with mixed basis sets (LANL2DZ for Ir,⁵⁹ and 6-31g* for H, C, and N).⁶⁰ Solvent effects were included via Conductor Polarized Continuum Model (CPCM)^{61,62} for dichloromethane.

The theoretical absorption spectra were generated by computing the lowest 125 singlet excitations from the ground state singlet equilibrium geometry, and the resulting transition energies and oscillator strengths were broadened *via* Equation 2 in Ref. 63 with a line width of 0.12 eV to model the thermal broadening of optical bands to be comparable to experimental spectra. The emission of complexes **3-1** – **3-10** was simulated using TDDFT Δ SCF approach, which computed the phosphorescence energy by calculating the triplet excited state transitions using TDDFT based on the triplet equilibrium geometry.^{38,64} The nature of the triplet and singlet transitions were characterized by computing the natural transition orbitals (NTOs)⁶⁵ *via* Gaussian09 and visualized using VMD with 0.02 isovalue.⁶⁶

3.3. Results and discussion

3.3.1. Electronic absorption

The absorption spectra of complexes **3-1** – **3-10** were measured in different solvents at room temperature. The spectra in dichloromethane are displayed in Figure 3.1 and the absorption band maxima and molar extinction coefficients are tabulated in Table 3.1. The normalized absorption spectra in other solvents are provided in Figure 3.2. These spectra generally can be

divided into four regions: the high-energy, strong absorbing band(s) below 310 nm; the structured medium-energy bands at ca. 310–400 nm; the lower-energy featureless band at ca. 400–500 nm; and the very weakly absorbing band(s) between 500 and 600 nm. According to the shape of these absorption bands and the corresponding molar extinction coefficients, these bands can be attributed to the ligand-localized $^1\pi,\pi^*$ transitions, the dominant $^1\pi,\pi^*$ transitions mixed with charge transfer (^1CT , *i.e.* metal-to-ligand charge transfer ($^1\text{MLCT}$)/ligand-to-ligand charge transfer ($^1\text{LLCT}$)) transitions, the $^1\text{MLCT}/^1\text{LLCT}/^1\text{ILCT}$ (intraligand charge transfer) transitions, and the mixed $^{1,3}\text{MLCT}/^{1,3}\text{LLCT}$ transitions, respectively. These assignments are supported by the TDDFT calculation results (see NTOs in Table 3.2 – 3-4) and are in accordance with the other reported cyclometalated monocationic Ir(III) complexes.^{18,19,27,67}

Examination of the lowest-energy absorption bands (500–600 nm) of complexes **3-1** – **3-10** revealed that benzannulation at the 5,6-position of pyridine (**3-2** vs. **3-1**), 6,7-position of quinoline (**3-3** vs. **3-2**), 5,6- and 5',6'-position of 2,2'-bipyridine (**3-8** vs. **3-1**), and 3,4- and 3',4'-position of 2,2'-bipyridine (**3-10** vs. **3-1**) resulted in a red-shift of the $^{1,3}\text{MLCT}/^{1,3}\text{LLCT}$ absorption bands with an increased molar extinction coefficient compared to their corresponding parent complexes. In contrast, benzannulation at the 7,8-position of quinoline (**3-4** vs. **3-2**), 4,5- and 4',5'-position of 2,2'-bipyridine (**3-9** vs. **3-1**), or 2,2',3,3'-position of 2,2'-bipyridine (**3-5** vs. **3-1**) essentially did not impact the energy of the $^{1,3}\text{MLCT}/^{1,3}\text{LLCT}$ absorption band compared to their corresponding parent complex. In addition, fusing a phenyl or a naphthyl ring to the 5,6-position of 1,10-phenanthroline did not affect the energies of the $^{1,3}\text{MLCT}/^{1,3}\text{LLCT}$ transitions in complexes **3-6** and **3-7** with respect to their corresponding parent compound **3-5**.

The site-dependent benzannulation effect was more clearly evidenced in the calculated S_1 state energies for these complexes. As listed in Table 3.2, benzannulation at the 5,6-/5',6'-position

or 3,4-/3',4'-position of 2,2'-bipyridine stabilized the S_1 states in complexes **3-2**, **3-8**, and **3-10**, respectively, compared to the S_1 state of their parent complex **3-1**; while benzannulation at the 4,5-/4',5'-positions of 2,2'-bipyridine destabilized the S_1 state in **3-9** in comparison to that of **3-1**. In contrast, benzannulation at the 2,2',3,3'-position 2,2'-bipyridine and further benzannulation at phenanthroline essentially had no impact on the S_1 state energies of **3-5** – **3-7** compared to that of **3-1**. While benzannulation at the 6,7-position of quinoline lowered the S_1 state in **3-3**, benzannulation at the 7,8-position of quinoline raised the S_1 state in **3-4**. This trend matched well with experimental observations and was in accordance with that reported by our group earlier for another series of cyclometalated monocationic Ir(III) complexes with different C^N ligands.³²

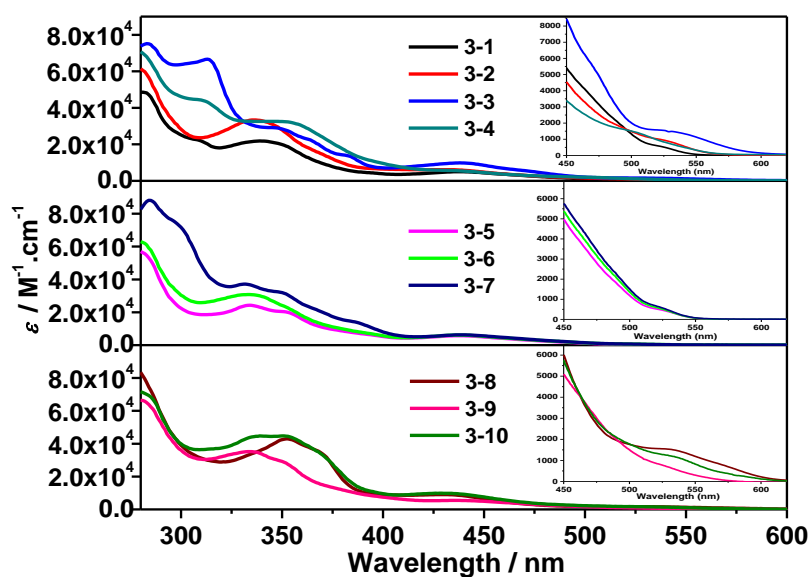


Figure 3.1. UV-vis absorption spectra of **3-1**–**3-10** in CH_2Cl_2 at room temperature. The insets are the expanded spectra in the region of 450–625 nm.

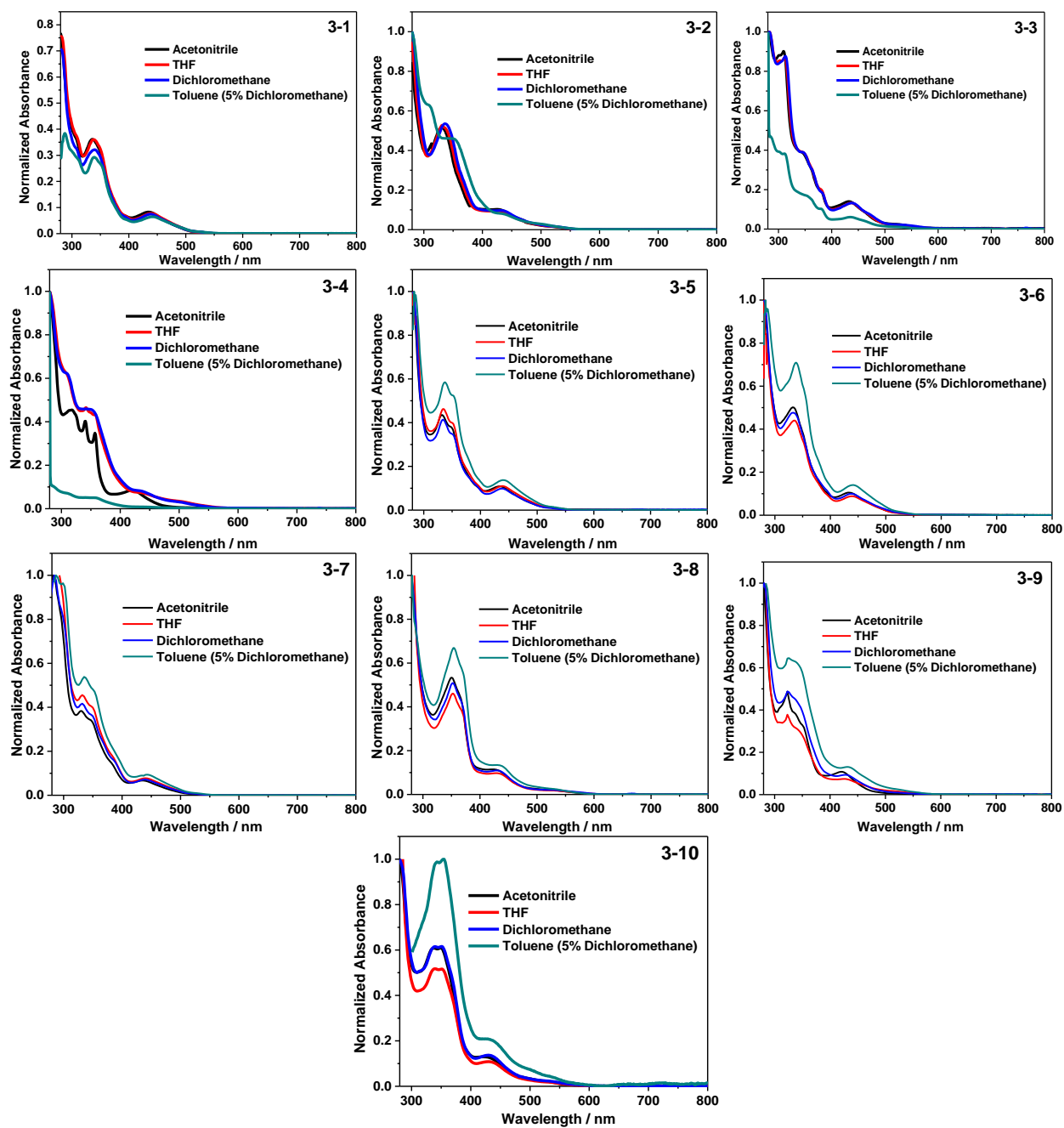


Figure 3.2. Normalized experimental absorption spectra of **3-1** – **3-10** in different solvents.

Table 3.1. Electronic absorption, emission, and triplet excited-state absorption parameters for complexes **3-1**–**3-10**.

	$\lambda_{\text{abs}}/\text{nm}$ ($\log \varepsilon$) ^a	$\lambda_{\text{em}}/\text{nm}$ ($\tau_{\text{em}}/\mu\text{s}$); Φ_{em} ^b	k_r / s^{-1} ^c	$k_{\text{nr}} / \text{s}^{-1}$ ^d	$\lambda_{\text{T1-Tn}}/\text{nm}$ ($\tau_{\text{TA}}/\mu\text{s}$; $\log \varepsilon_{\text{T1-Tn}}$); Φ_{T} ^e
3-1	281 (4.68), 307 (4.35), 339 (4.34), 440 (3.73), 519 (2.79)	553 (2.16); 0.41	1.90×10^5	2.73×10^5	407 (2.14; -), 573 (2.13, -), 783 (-; -); - ^g
3-2	280 (4.79), 337 (4.52), 433 (3.84), 518 (3.02)	613 (0.52); 0.081	1.56×10^5	1.77×10^6	380 (0.30; -), 782 (0.33; -); - ^g
3-3	280 (4.85), 307 (4.65), 351 (4.51), 436 (3.76), 523 (3.20)	738 (2.62); 0.0031	1.18×10^3	3.80×10^5	339 (-, -), 390 (3.42; -), 555 (3.32; -), 660 (3.47; -); - ^g
3-4	283 (4.87), 312 (4.82), 347 (4.46), 438 (3.99), 500 (3.18)	583 (- ^f); 0.0022	–	–	398 (4.52; -), 555 (4.44; -), 795 (4.46; -); - ^g
3-5	280 (4.75), 333 (4.38), 350 (4.31), 438 (3.77), 518 (2.73)	554 (2.77); 0.71	2.56×10^5	1.05×10^5	363 (-; -), 407 (2.82; -), 578 (2.93; -), 797 (2.87; -); - ^g
3-6	281 (4.79), 333 (4.49), 439 (3.78), 518 (2.79)	553 (2.71); 0.78	2.88×10^5	8.12×10^4	360 (-; -), 407 (2.79; -), 575 (2.81; -), 797 (2.79; -); - ^g
3-7	284 (4.94), 331 (4.57), 348 (4.51), 439 (3.79), 518 (2.85)	554 (31.0); 0.27	8.71×10^3	2.35×10^4	412 (sh., 19.6; -), 475 (19.6; -); - ^g
3-8	280 (4.91), 352 (4.63), 365 (4.56), 430 (3.96), 527 (3.19)	645 (1.00); 0.084	1.56×10^5	1.70×10^6	390 (0.61; -), 449 (0.63; -), 641 (0.63; 4.35), 782 (0.63; 4.64); 0.54
3-9	280 (4.82), 334 (4.55), 350 (4.47), 437 (3.75), 517 (2.96)	582 (- ^f); 0.0013	–	–	741 (0.04; -); - ^g
3-10	280 (4.85), 339 (4.65), 350 (4.65), 431 (3.99), 529 (3.10)	651 (0.49); 0.075	5.47×10^5	6.74×10^6	533 (0.25; 4.42), 695 (0.25; 4.40); 0.28

^a Absorption band maxima (λ_{abs}) and molar extinction coefficients ($\log \varepsilon$) of the UV–vis absorption in CH_2Cl_2 at room temperature. ^b The emission band maxima (λ_{em}) and lifetimes (τ_{em}) for **3-1** – **3-10** in CH_2Cl_2 ($c = 1 \times 10^{-5}$ mol/L) at room temperature. A degassed acetonitrile solution of $[\text{Ru}(\text{bpy})_3]\text{Cl}_2$ ($\Phi_{\text{em}} = 0.097$, $\lambda_{\text{ex}} = 436$ nm) was used as reference for the emission quantum yield measurement. The quantum yields were measured using a fiber coupled Ocean Optics integrating sphere. $\lambda_{\text{ex}} = 450$ nm, the emission signals in the wavelength range of 380 – 820 nm were integrated for all of the complexes except for **3-3**. The integration range for **3-3** was 380–900 nm. ^{c,d} Radiative decay rates (k_r) and nonradiative decay rates (k_{nr}) calculated by $k_r = \Phi_{\text{em}}/(\Phi_{\text{T}} \tau_{\text{em}})$ and $k_{\text{nr}} = (1 - \Phi_{\text{em}})/(\Phi_{\text{T}} \tau_{\text{em}})$, respectively. For **3-8** and **3-10**, the estimated triplet quantum yields (Φ_{T}) from the TA measurement were used. For the other complexes, Φ_{T} was assumed to be 1. ^e Nanosecond TA band maxima ($\lambda_{\text{T1-Tn}}$), triplet excited state lifetimes (τ_{TA}), triplet extinction coefficients ($\log \varepsilon_{\text{T1-Tn}}$), and triplet quantum yields (Φ_{T}) measured in CH_3CN at room temperature. ^f Too weak to be measured. ^g Due to lack of bleaching band, the $\varepsilon_{\text{T1-Tn}}$ values cannot be estimated using the singlet depletion method, the Φ_{T} values cannot be determined, either.

Table 3.2. NTOs of the low-energy transitions contributing to the 400–500 nm absorption band of complexes **3-1** – **3-10** in CH_2Cl_2 .

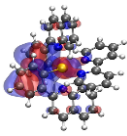
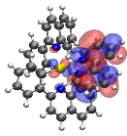
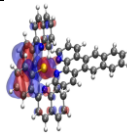
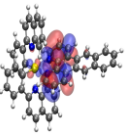
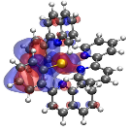
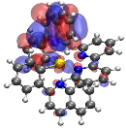
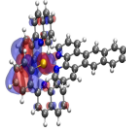
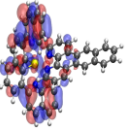
Excited state and properties	Hole	Electron	Excited state and properties	Hole	Electron
3-1 S ₁ 485 nm $f = 0.002$			3-7 S ₁ 482 nm $f = 0.000$		
S ₂ 454 nm $f = 0.047$			S ₂ 458 nm $f = 0.001$		

Table 3.2. NTOs of the low-energy transitions contributing to the 400–500 nm absorption band of complexes **3-1** – **3-10** in CH₂Cl₂. (continued)

Excited state and properties	Hole	Electron	Excited state and properties	Hole	Electron
S ₃ 454 nm <i>f</i> = 0.024			S ₃ 455 nm <i>f</i> = 0.069		
3-2 S ₁ 517 nm <i>f</i> = 0.004			3-8 S ₁ 537 nm <i>f</i> = 0.010		
S ₂ 449 nm <i>f</i> = 0.063			S ₂ 450 nm <i>f</i> = 0.045		
S ₄ 412 nm <i>f</i> = 0.019			S ₃ 439 nm <i>f</i> = 0.016		
S ₅ 399 nm <i>f</i> = 0.003			69%		
3-3 S ₁ 560 nm <i>f</i> = 0.002			29%		
S ₂ 477 nm <i>f</i> = 0.051			29%		
S ₃ 450 nm <i>f</i> = 0.063			S ₄ 433 nm <i>f</i> = 0.015		
S ₅ 436 nm <i>f</i> = 0.008			68%		
			31%		
			31%		
			S ₅ 425 nm <i>f</i> = 0.006		
			S ₆ 402 nm <i>f</i> = 0.038		

Table 3.2. NTOs of the low-energy transitions contributing to the 400–500 nm absorption band of complexes **3-1** – **3-10** in CH₂Cl₂. (continued)

Excited state and properties	Hole	Electron	Excited state and properties	Hole	Electron	
3-4 S ₁ 487 nm <i>f</i> = 0.025			3-9 S ₁ 461 nm <i>f</i> = 0.004			
				56%	56%	
				20%	20%	
S ₂ 449 nm <i>f</i> = 0.005			S ₂ 458 nm <i>f</i> = 0.055			
S ₃ 445 nm <i>f</i> = 0.031			S ₃ 444 nm <i>f</i> = 0.012			
3-5 S ₁ 483 nm <i>f</i> = 0.001			S ₄ 414 nm <i>f</i> = 0.003			
	S ₂ 470 nm <i>f</i> = 0.000			S ₅ 397 nm <i>f</i> = 0.016		
	S ₃ 455 nm <i>f</i> = 0.070			3-10 S ₁ 556 nm <i>f</i> = 0.002		
	S ₄ 427 nm <i>f</i> = 0.007				S ₃ 454 nm <i>f</i> = 0.067	
3-6 S ₁ 483 nm <i>f</i> = 0.000			S ₄ 430 nm <i>f</i> = 0.035			
	S ₂ 460 nm <i>f</i> = 0.001			S ₅ 412 nm <i>f</i> = 0.003		
	S ₃ 455 nm <i>f</i> = 0.070					
	S ₄ 408 nm <i>f</i> = 0.006					

Table 3.3. NTOs for the optical transitions at 300 – 400 nm for **3-1** – **3-10** in CH₂Cl₂. The isovalue is set to 0.03.

	State	Hole	Electron		State	Hole	Electron
3-1	S ₄ 383 nm <i>f</i> = 0.026			3-6	S ₅ 382 nm <i>f</i> = 0.058		
	S ₆ 365 nm <i>f</i> = 0.042				S ₁₀ 354 nm <i>f</i> = 0.055		
	S ₁₀ 347 nm <i>f</i> = 0.081				S ₁₂ 347 nm <i>f</i> = 0.059		
	S ₁₂ 339 nm <i>f</i> = 0.213				S ₁₃ 344 nm <i>f</i> = 0.191		
	S ₁₉ 320 nm <i>f</i> = 0.229				S ₂₃ 321 nm <i>f</i> = 0.129		
		54%	54%			56%	56%
		39%	39%			27%	27%
3-2	S ₆ 379 nm <i>f</i> = 0.055			S ₂₄ 321 nm <i>f</i> = 0.164			
	S ₁₀ 351 nm <i>f</i> = 0.077						
	S ₁₅ 341 nm <i>f</i> = 0.124				54%	54%	
	S ₁₆ 341 nm <i>f</i> = 0.083						
					32%	32%	
				S ₂₉ 310 nm <i>f</i> = 0.188			
					58%	58%	
					27%	27%	

Table 3.3. NTOs for the optical transitions at 300 – 400 nm for **3-1** – **3-10** in CH₂Cl₂. The isovalue is set to 0.03. (continued)

State	Hole	Electron	State	Hole	Electron
S ₂₃ 318 nm <i>f</i> = 0.130			3-7 S ₅ 400 nm <i>f</i> = 0.034		
S ₂₄ 317 nm <i>f</i> = 0.204				S ₇ 383 nm <i>f</i> = 0.066	
	53%	53%	S ₉ 369 nm <i>f</i> = 0.101		
	28%	28%	S ₁₀ 368 nm <i>f</i> = 0.043		
3-3 S ₇ 395 nm <i>f</i> = 0.014				75%	75%
S ₈ 391 nm <i>f</i> = 0.010				22%	22%
S ₉ 383 nm <i>f</i> = 0.013			S ₁₄ 354 nm <i>f</i> = 0.073		
S ₁₂ 362 nm <i>f</i> = 0.030			S ₁₅ 349 nm <i>f</i> = 0.073		
S ₁₃ 361 nm <i>f</i> = 0.026			S ₁₆ 348 nm <i>f</i> = 0.075		
S ₁₅ 355 nm <i>f</i> = 0.077			S ₁₈ 343 nm <i>f</i> = 0.194		
	69%	69%			

Table 3.3. NTOs for the optical transitions at 300 – 400 nm for **3-1** – **3-10** in CH₂Cl₂. The isovalue is set to 0.03. (continued)

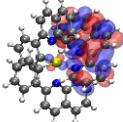
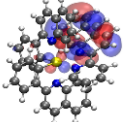
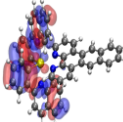
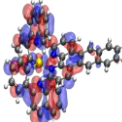
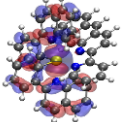
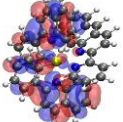
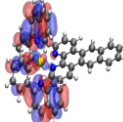
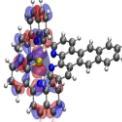
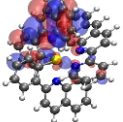
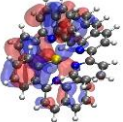
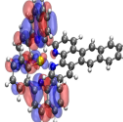
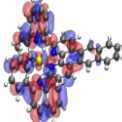
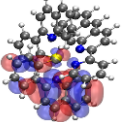
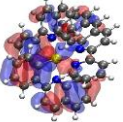
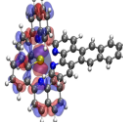
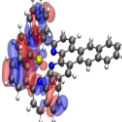
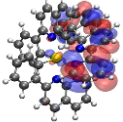
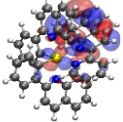
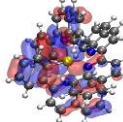
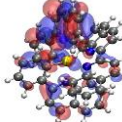
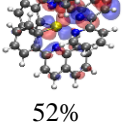
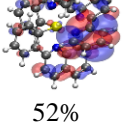
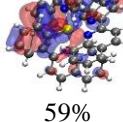
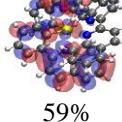
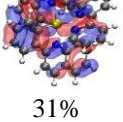
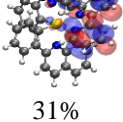
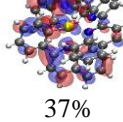
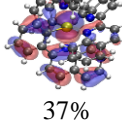
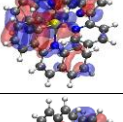
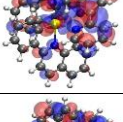
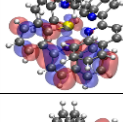
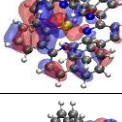
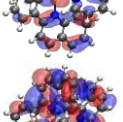
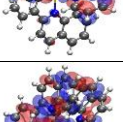
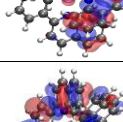
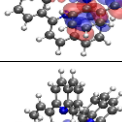
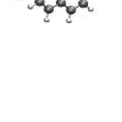



State	Hole	Electron	State	Hole	Electron
			S ₂₄ 328 nm <i>f</i> = 0.123		
	21%	21%		57%	57%
S ₁₆ 351 nm <i>f</i> = 0.109					
				32%	32%
S ₂₁ 335 nm <i>f</i> = 0.105			S ₂₈ 321 nm <i>f</i> = 0.297		
				54%	54%
S ₂₂ 335 nm <i>f</i> = 0.142					
				27%	27%
S ₂₅ 319 nm <i>f</i> = 0.515			3-8 S ₈ 374 nm <i>f</i> = 0.034		
S ₃₀ 308 nm <i>f</i> = 0.291			S ₁₄ 352 nm <i>f</i> = 0.097		
	52%	52%		59%	59%
					
	31%	31%		37%	37%
3-4 S ₄ 391 nm <i>f</i> = 0.009			S ₁₇ 344 nm <i>f</i> = 0.115		
S ₅ 381 nm <i>f</i> = 0.036			S ₁₈ 336 nm <i>f</i> = 0.241		
S ₈ 365 nm <i>f</i> = 0.106			S ₂₃ 326 nm <i>f</i> = 0.111		

Table 3.3. NTOs for the optical transitions at 300 – 400 nm for **3-1** – **3-10** in CH₂Cl₂. The isovalue is set to 0.03. (continued)

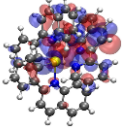
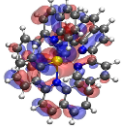
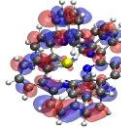
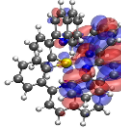
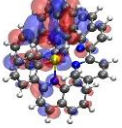
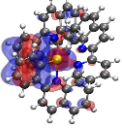
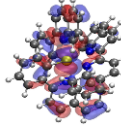
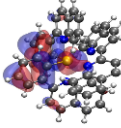
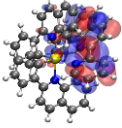
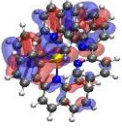
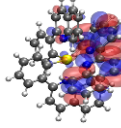
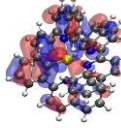
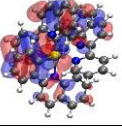
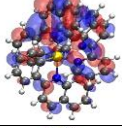
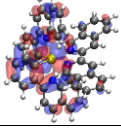
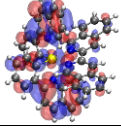
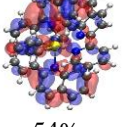
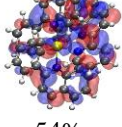
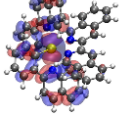
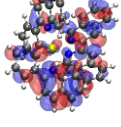
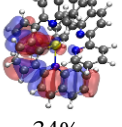
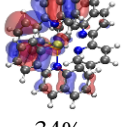
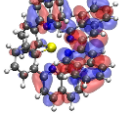
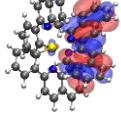
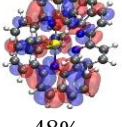
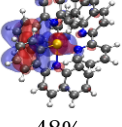
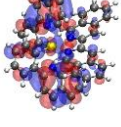
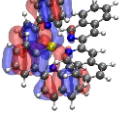
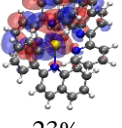
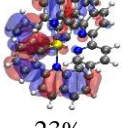
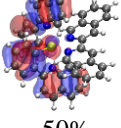
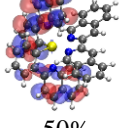
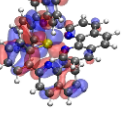
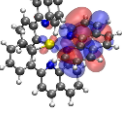
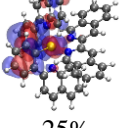
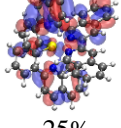
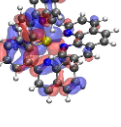
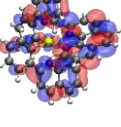
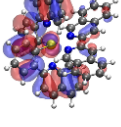
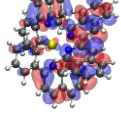
State	Hole	Electron	State	Hole	Electron
S ₁₁ 355 nm <i>f</i> = 0.107			S ₂₈ 314 nm <i>f</i> = 0.126		
	38%	38%		43%	43%
					
	29%	29%		29%	29%
			S ₃₂ 304 nm <i>f</i> = 0.108		
	21%	21%			
S ₁₇ 341 nm <i>f</i> = 0.119			3-9 S ₆ 373 nm <i>f</i> = 0.040		
S ₂₀ 328 nm <i>f</i> = 0.098					
	54%	54%			
			S ₁₃ 344 nm <i>f</i> = 0.114		
	34%	34%			
S ₂₆ 315 nm <i>f</i> = 0.191			S ₁₄ 343 nm <i>f</i> = 0.174		
	48%	48%			
			S ₂₃ 328 nm <i>f</i> = 0.116		
	23%	23%		50%	50%
3-5 S ₅ 382 nm <i>f</i> = 0.046					
				25%	25%
S ₆ 376 nm <i>f</i> = 0.045			S ₂₄ 323 nm <i>f</i> = 0.374		

Table 3.3. NTOs for the optical transitions at 300 – 400 nm for **3-1** – **3-10** in CH₂Cl₂. The isovalue is set to 0.03. (continued)

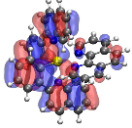
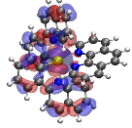
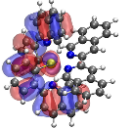
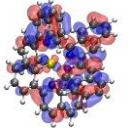
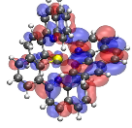
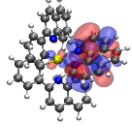
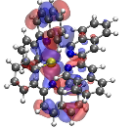
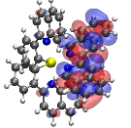
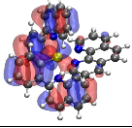
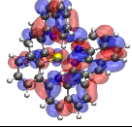
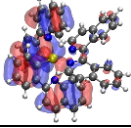
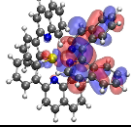
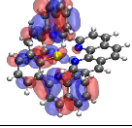
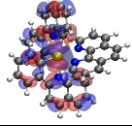
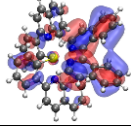
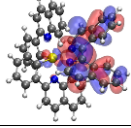
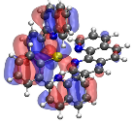
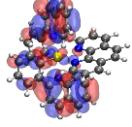
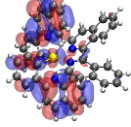
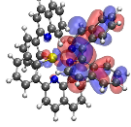
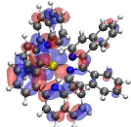
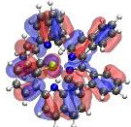
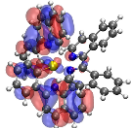
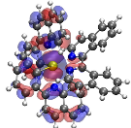
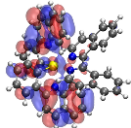
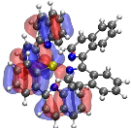
State	Hole	Electron	State	Hole	Electron
S ₉ 356 nm <i>f</i> = 0.043			S ₂₈ 319 nm <i>f</i> = 0.143		
	46%	46%			
			S ₃₈ 299 nm <i>f</i> = 0.210		
	33%	33%			
S ₁₂ 348 nm <i>f</i> = 0.114			3-10 S ₆ 389 nm <i>f</i> = 0.015		
S ₁₃ 346 nm <i>f</i> = 0.099			S ₇ 377 nm <i>f</i> = 0.119		
S ₂₂ 322 nm <i>f</i> = 0.274			S ₁₀ 368 nm <i>f</i> = 0.117		
				57%	57%
					
				40%	40%
			S ₁₄ 349 nm <i>f</i> = 0.098		
			S ₁₈ 339 nm <i>f</i> = 0.131		

Table 3.4. NTOs for the high energy optical transitions (<300 nm) of **3-1** – **3-10** in CH₂Cl₂. The isovalue is set to 0.03.

	State	Hole	Electron		State	Hole	Electron	
3-1	S ₃₃ 282 nm <i>f</i> = 0.194			3-6	S ₅₃ 269 nm <i>f</i> = 0.458			
		45%	45%				37%	37%
							29%	29%
	S ₃₇ 276 nm <i>f</i> = 0.170				S ₇₂ 252 nm <i>f</i> = 0.346			
						40%	40%	
	S ₄₃ 267 nm <i>f</i> = 0.283							
						22%	22%	
3-2	S ₅₈ 271 nm <i>f</i> = 0.330			3-7	S ₄₂ 296 nm <i>f</i> = 0.279			
		39%	39%					
							73%	73%
		31%	31%		S ₄₄ 293 nm <i>f</i> = 0.295			
						23%	23%	
3-3	S ₄₇ 272 nm <i>f</i> = 0.341							
						23%	23%	
3-4	S ₄₉ 275 nm <i>f</i> = 0.178				S ₅₄ 278 nm <i>f</i> = 0.264			
		37%	37%			58%	58%	
						26%	26%	
		33%	33%					

Table 3.4. NTOs for the high energy optical transitions (<300 nm) of **3-1** – **3-10** in CH₂Cl₂. The isovalue is set to 0.03. (continued)

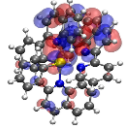
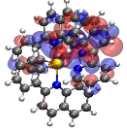
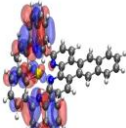
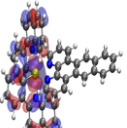
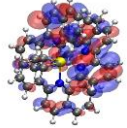
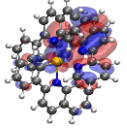
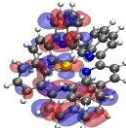
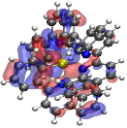
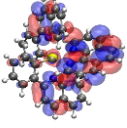
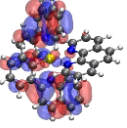
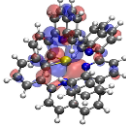
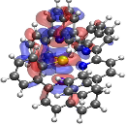
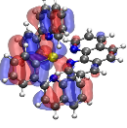
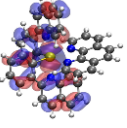
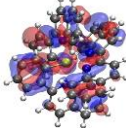
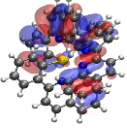
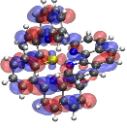
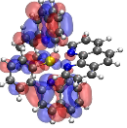
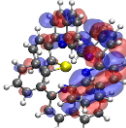
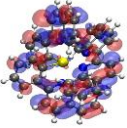
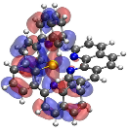
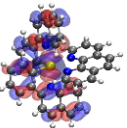
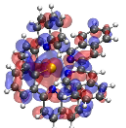
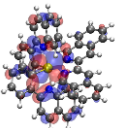
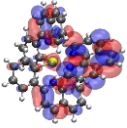
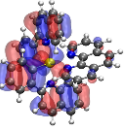
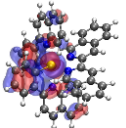
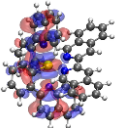
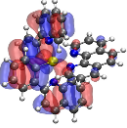
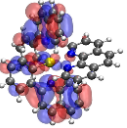
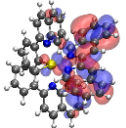
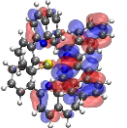
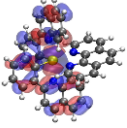
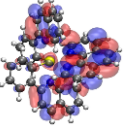
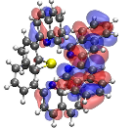
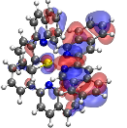
State	Hole	Electron	State	Hole	Electron
S ₅₃ 271 nm <i>f</i> = 0.219	 49%	 49%	S ₆₃ 266 nm <i>f</i> = 0.318		
	 33%	 33%	3-8 S ₅₃ 275 nm <i>f</i> = 0.318		
3-5 S ₄₀ 279 nm <i>f</i> = 0.136	 42%	 42%	S ₅₆ 272 nm <i>f</i> = 0.232		
	 38%	 38%	S ₆₉ 258 nm <i>f</i> = 0.266	 52%	 52%
S ₄₄ 270 nm <i>f</i> = 0.332	 37%	 37%	 34%	 34%	
	 23%	 23%	3-9 S ₅₆ 270 nm <i>f</i> = 0.395	 45%	 45%
	 21%	 21%	 23%	 23%	
S ₄₅ 270 nm <i>f</i> = 0.298			S ₆₆ 256 nm <i>f</i> = 0.384	 57%	 57%
S ₅₀ 263 nm <i>f</i> = 0.383			 21%	 21%	

Table 3.4. NTOs for the high energy optical transitions (<300 nm) of **3-1** – **3-10** in CH₂Cl₂. The isovalue is set to 0.03. (continued)

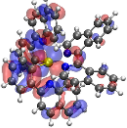
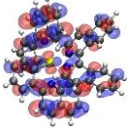
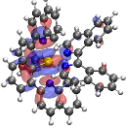
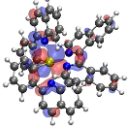
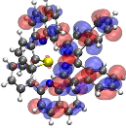
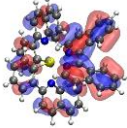
	State	Hole	Electron
3-10	S ₅₆ 272 nm <i>f</i> = 0.317		
	S ₅₉ 269 nm <i>f</i> = 0.143		
	S ₇₀ 256 nm <i>f</i> = 0.152		

Table 3.5. HOMOs and LUMOs of **3-1** – **3-10** in CH₂Cl₂ and the contribution of HOMO→LUMO transition to the S₁ state.

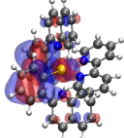
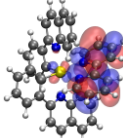
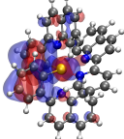

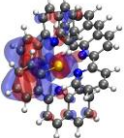

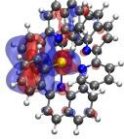
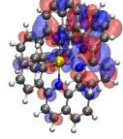
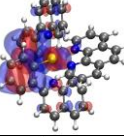
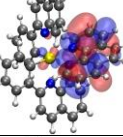
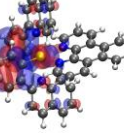
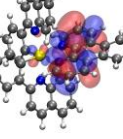
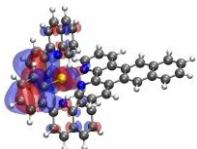
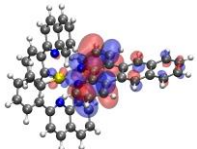
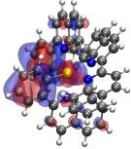
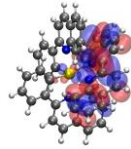
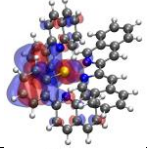
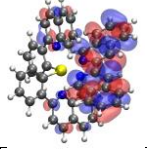
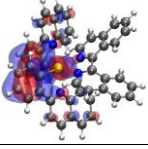
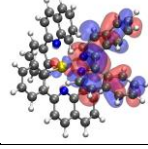
	HOMO	LUMO	Percentage Contribution of H/L Transition to S ₁ State
3-1			70%
3-2			70%
3-3			70%
3-4			68%
3-5			70%
3-6			70%

Table 3.5. HOMOs and LUMOs of **3-1** – **3-10** in CH₂Cl₂ and the contribution of HOMO→LUMO transition to the S₁ state. (continued)

	HOMO	LUMO	Percentage Contribution of H/L Transition to S ₁ State
3-7			69%
3-8			70%
3-9			S ₁ H/L 0%; H/L+1 69% S ₂ H/L 43% S ₃ H/L 56% S ₄ H/L 70%
3-10			70%

The DFT calculation showed that the HOMO→LUMO transition was the dominant contributor (~70%) to the S₁ states of all of the complexes except for **3-9** (see Table 3.5). Electron density distribution plots of the HOMOs and LUMOs in **3-1** – **3-10** (Table 3.5) clearly demonstrated that the HOMOs of these complexes were predominantly distributed on the phenyl rings of the 2-phenylquinoline ligands and the *d*-orbital of the Ir(III) center, while the LUMOs were exclusively localized on the diimine ligand. Thus, benzannulation at the diimine ligand would mainly impact the LUMO energies. As depicted in Figure 3.3, the ground-state MO energy diagram for **3-1** – **3-10** manifested that benzannulation drastically changed the LUMO energies but had a minor effect on the HOMO energies. Benzannulation at the 5,6-/5',6'-position or 3,4-/3',4'-position of 2,2'-bipyridine or at the 6,7-position of quinoline significantly stabilized the LUMOs in complexes **3-2**, **3-3**, **3-8**, and **3-10**; whereas benzannulation at the other sites of

2,2'-bipyridine or the 7,8-position of quinoline either did not affect or slightly raised the LUMOs in **3-4** – **3-7** and **3-9** compared to that of **3-1**.

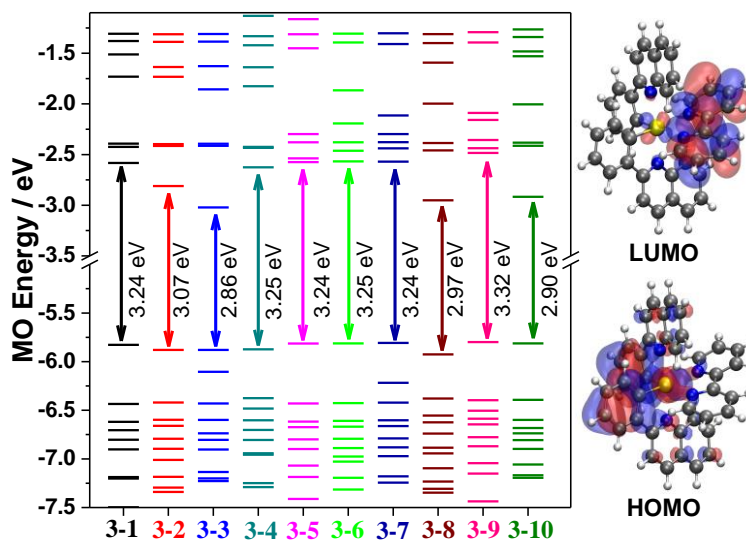


Figure 3.3. Ground-state molecular orbital diagram for **3-1** – **3-10** in CH_2Cl_2 (HOMO and LUMO of **3-1** are plotted as representative).

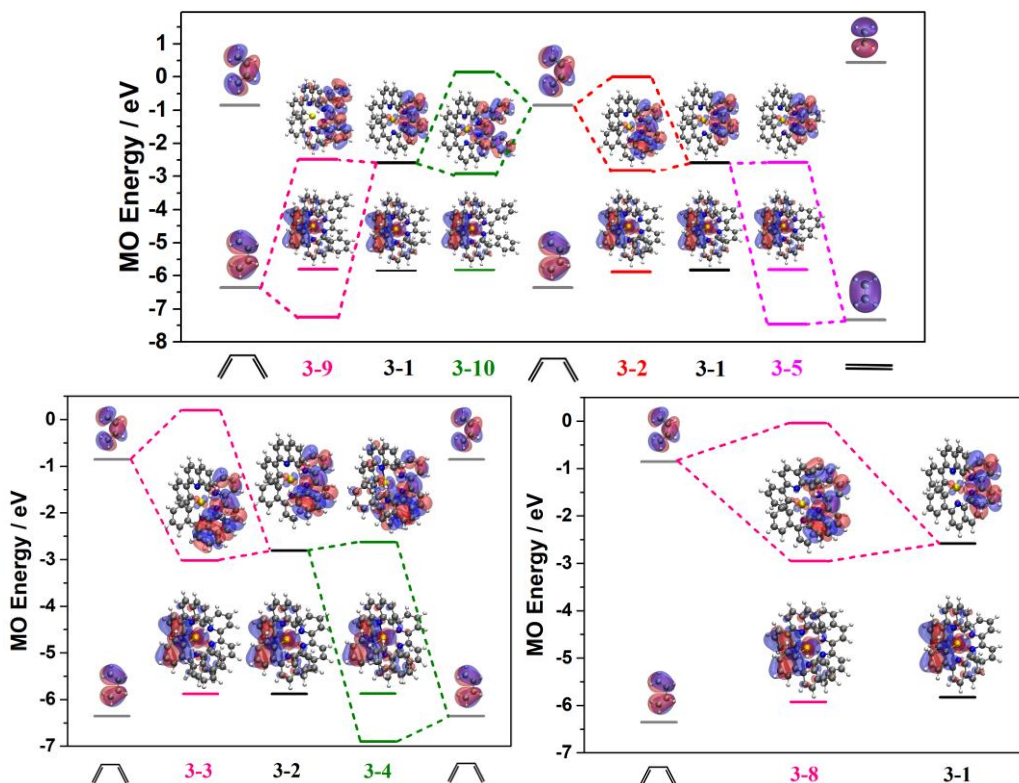


Figure 3.4. Frontier molecular orbital mixing between *cis*-1,3-butadiene or ethene and parent molecules.

According to Thompson / Gordon's work³⁸ and our previous work,³² benzannulation on the diimine ligand can be viewed as the interaction between the LUMO of the parent compound and the HOMO or LUMO of *cis*-1,3-butadiene or ethene, depending on the MO symmetry at the site of benzannulation. As exemplified in Figure 3.4, when benzannulation occurred at the 5,6-position of one of the pyridine rings, the symmetry of the **3-1** LUMO at this site matched the symmetry of the LUMO of *cis*-1,3-butadiene and led to a LUMO-LUMO interaction. The LUMO-LUMO interactions resulted in a stabilized LUMO in **3-2** and thus the red-shifted CT absorption band in its UV-vis absorption spectrum compared to that of **3-1**. Similarly, the symmetry of the LUMO of **3-1** at the 5',6'-position and the 3,4-/3',4'-position matched the symmetry of LUMO of *cis*-1,3-butadiene, resulting in stabilized LUMOs and red-shifted CT absorption bands in complexes **3-8** and **3-10** (Figure 3.4). In contrast, when benzannulation occurred at the 4,5-/4',5'-position of 2,2'-bipyridine in **3-1**, the symmetry of the LUMO of **3-1** at these positions matched the symmetry of the HOMO of *cis*-1,3-butadiene. The HOMO-LUMO interactions gave rise to a destabilized LUMO in complex **3-9** and thus an enlarged HOMO-LUMO energy gap and a blue-shifted CT absorption band. From complex **3-1** to **3-5**, benzannulation at the 2,2',3,3'-position of 2,2'-bipyridine in **3-1** can be considered as the interaction between the LUMO of **3-1** and the HOMO of ethene due to symmetry matching requirement. Such an interaction showed a negligible impact on the LUMO of **3-5** and essentially did not affect the CT transition in **3-5** compared to that of **3-1**. A similar MO symmetry analysis was applied to the other complexes and the results are provided in Figure 3.4.

3.3.2. Photoluminescence

To evaluate the site-dependent benzannulation effect on the triplet excited states of complexes **3-1**–**3-10**, the emission characteristics of these complexes were investigated in different solvents at room temperature. The emission spectra in CH₂Cl₂ are displayed in Figure 3.5 and the emission parameters (lifetime and quantum yield) in CH₂Cl₂ are tabulated in Table 3.1. The normalized emission spectra in other solvents are presented in Figure 3.6 and the emission parameters are compiled in Table 3.6. The emission of these complexes was sensitive to oxygen quenching and was moderately long-lived (0.52–31.0 μs) (except for **3-4** and **3-9**, in which the emission signals were too weak to be measured), indicating the phosphorescent nature of the emission. These features are consistent with the other reported Ir(III) complexes.^{17-19,24-33,39-42} Except for **3-3** that exhibited emission in the near-IR region with clear vibronic structures, the emission of all of the other complexes were broad and almost featureless.

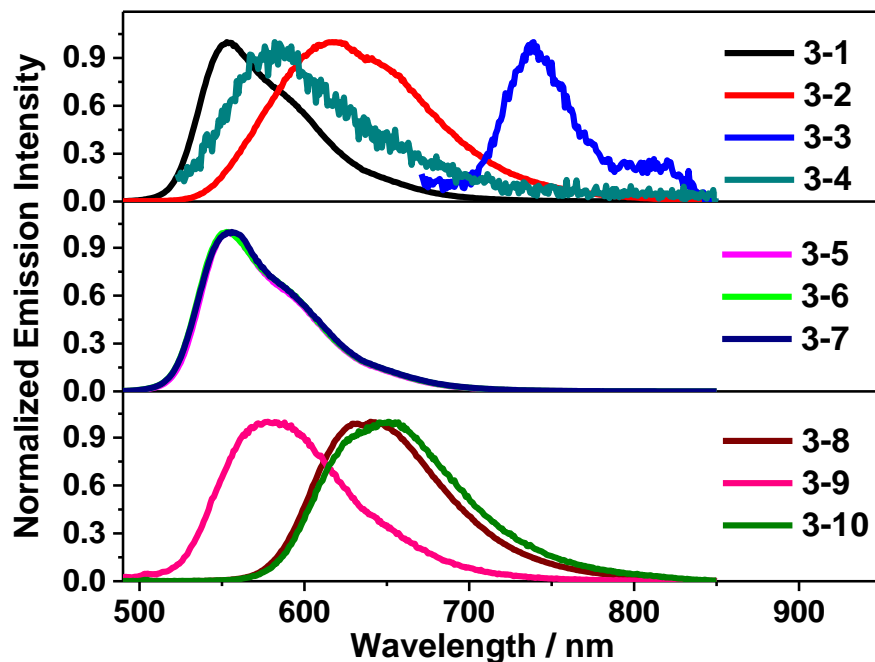


Figure 3.5. Normalized emission spectra of **3-1** – **3-10** in CH₂Cl₂ at room temperature. (λ_{ex} = 438 nm for **3-1**, 430 nm for **3-2**, 439 nm for **3-3**, 436 nm for **3-4**, 438 nm for **3-5**, 437 nm for **3-6**, 440 nm for **3-7**, 428 nm for **3-8**, 436 nm for **3-9**, and 437 nm for **3-10**).

Table 3.6. Emission characteristics of complexes **3-1** – **3-10** in different solvents at room temperature.

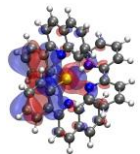
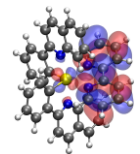
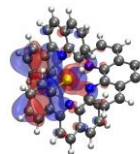
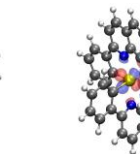
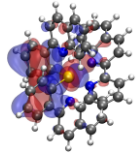

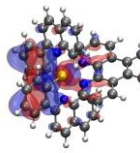
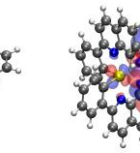
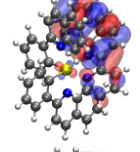
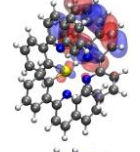
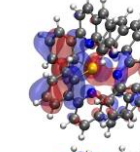
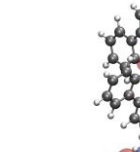
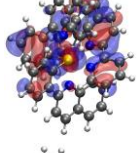
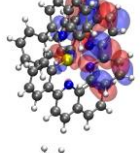
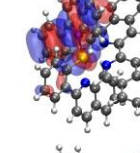
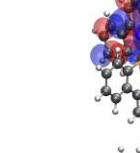
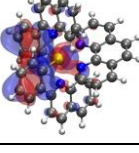
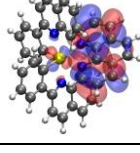
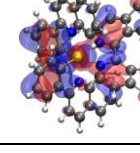
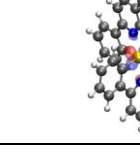
	λ_{em}/nm ($\tau_{em}/\mu s$) ^a ; Φ_{em} ^b		
	Acetonitrile	THF	Toluene/5% CH ₂ Cl ₂
3-1	557 (2.48); 0.47	555 (2.22); 0.75	557 (2.15); 0.34
3-2	608 (0.30); 0.035	618 (0.36); 0.050	616 (0.18); 0.045
3-3	733 (0.63); 0.0044	735 (2.06); 0.0098	733 (-) ^c ; 0.0061
3-4	572 (-) ^c ; - ^c	587 (1.10); 0.0032	562 (-) ^c ; - ^c
3-5	558 (2.91); 0.59	556 (2.47); 0.62	560 (2.09); 0.56
3-6	557 (2.69); 0.56	556 (2.37); 0.65	562 (2.11); 0.61
3-7	559 (19.2); 0.22	558 (16.2); 0.17	562 (11.9); 0.24
3-8	649 (0.64); 0.037	644 (0.69); 0.042	653 (0.41); 0.032
3-9	560 (-) ^c ; 0.0026	596 (-) ^c ; 0.0013	560 (-) ^c ; 0.0038
3-10	653 (0.25); 0.035	656 (0.28); 0.076	596 (0.03); 0.025

^a The emission band maxima (λ_{em}) and lifetimes (τ_{em}) for **3-1** – **3-10** at room temperature. ^b Absolute QY measurements were performed using a fiber coupled Ocean Optics integrating sphere. λ_{ex} = 450 nm, detection wavelength range was 350 – 1700 nm. The integration range was 380-820 nm for **3-1** – **3-10** except for **3-3**, for which the integration was done in the range of 380-900 nm. ^c Too weak to be measured.

In comparison to the parent complex **3-1**, benzannulation at the 3,4-/3',4'-position, 4,5-/4',5'-position, or 5,6-/5',6'-position of 2,2'-bipyridine all caused a red-shift of the emission spectra for **3-2**, **3-8**, **3-9**, and **3-10**, accompanied by a shortened lifetime and a reduced emission quantum yield; while benzannulation at the 2,2',3,3'-position of 2,2'-bipyridine essentially had no impact on the emission energy of **3-5**, but with a slightly longer lifetime and an increased emission quantum yield. A drastically red-shifted emission into the NIR region was observed for **3-3** after fusion of an additional phenyl ring at the 6,7-position of quinoline in **3-2**. In contrast, benzannulation at the 7,8-position of quinoline in **3-2** induced a salient blue-shift of the emission of **3-4** and a lower quantum yield compared to those of **3-2** and **3-3**. Going from **3-5** to **3-7**, further extending the π -conjugation along the 5,6-position of 1,10-phenanthroline did not alter the emission energies of complexes **3-6** and **3-7**. However, the emission lifetime of **3-7** was more than one order of magnitude longer than those of **3-5** and **3-6**, but its emission quantum yield is less than half of those for **3-5** and **3-6**. Similar to the trend discovered for the S₁ states in these

complexes based on the electronic absorption, the site-dependent benzannulation influenced the energies of the lowest triplet excited states (T_1) in a similar manner, but the impact is more pronounced on the T_1 state than on the S_1 state.

Table 3.7. NTOs representing the lowest triplet transitions (T_1) of **3-1** – **3-10** in CH_2Cl_2 .

	T_1/nm	Hole	Electron		T_1/nm	Hole	Electron
3-1	625			3-6	606		
3-2	659			3-7	610		
3-3	1146			3-8	733		
3-4	647			3-9	647		
3-5	600			3-10	744		

To understand the electronic configurations of the emitting states for **3-1** – **3-10**, TDDFT calculations were performed and the NTOs representing the emitting T_1 states are displayed in Table 3.7. The trend of the calculated emission energies matched the trend of the experimental energies very well Figure 3.6. For complexes **3-1**, **3-2**, **3-5** – **3-7**, their holes are almost exclusively distributed on the phenyl rings of the $\text{C}^{\wedge}\text{N}$ ligands and on the metal d -orbital; while the electrons are localized on the diimine ligands and the d -orbital. Therefore, the emitting states in these complexes are assigned to predominantly the ${}^3\text{MLCT}/{}^3\text{LLCT}$ states, mixed with some ${}^3\text{LMCT}/{}^3\text{d,d}$

configurations. For complex **3-3**, both the hole and electron are almost exclusively on the benzoquinoline part of the N[^]N ligand, with minor contribution from the metal d orbitals. This indicates the dominant ${}^3\pi, \pi^*$ nature with minor ${}^3d, d$ character for the emitting state in **3-3**. The NTOs show that the emitting state of **3-9** also has predominant ${}^3\pi, \pi^*$ configuration with minor ${}^3d, d$ contribution. However, both the hole and electron are mainly distributed on one of the C[^]N ligands. The remaining complexes **3-4**, **3-8** and **3-10** all have holes on the phenyl rings of the C[^]N ligands and the *d*-orbitals, with some contributions from the N[^]N ligands; while their electrons are distributed on the N[^]N ligands and the *d*-orbitals. Therefore, the emitting states in these complexes have mixed ${}^3\text{MLCT}/{}^3\text{LLCT}/{}^3\pi, \pi^*$ configurations with minor contribution from the ${}^3\text{LMCT}/{}^3d, d$ configurations. It is noted that the electrons in **3-5** – **3-7** are only localized on the phenanthroline motif, they did not extend to the additional phenyl ring(s). Therefore, the emission energies in these three complexes are essentially the same.

For complexes **3-1**, **3-2**, **3-8** and **3-10** that have dominant charge transfer configurations in their emitting states, benzannulation reduced the energies of their emitting states, which significantly increased the nonradiative decay rate constants (see k_{nr} in Table 3.1) in **3-2**, **3-8**, and **3-10** compared to that in **3-1** without pronouncedly altering their radiative decay rate constants (k_{r}). This trend is in accordance with the energy gap law.^{68,69} For complexes **3-5** and **3-6**, they have the similar k_{r} s to that of **3-1**, but their k_{nr} s are smaller than that of **3-1**. The reduced k_{nr} s in **3-5** and **3-6** can be attributed to the rigidity of phenanthroline and its derivatives compared to bipyridine. Consequently, their emission quantum yields are higher than that of **3-1**. Interestingly, the emission energy and the T₁ state configuration of **3-7** resemble those of **3-5** and **3-6**, but its lifetime is one order of magnitude longer than those of **3-5** and **3-6** and its emission quantum yield is less than half of those for **3-5** and **3-6**. Examination of the triplet energy diagram obtained from the TDDFT

calculation (Figure 3.7) reveals that unlike the other complexes, the second triplet excited state (T_2) in **3-7** lies closely to its T_1 state, which makes it possible to be configurationally mixed with T_1 state and reaches an equilibrium. Because the T_2 state of **3-7** has a ${}^3\pi, \pi^*$ configuration (Table 3.8), admixing T_2 with T_1 drastically reduces the k_r and k_{nr} in **3-7** compared to those in **3-5** and **3-6**, which dramatically prolongs the emission lifetime of **3-7**.

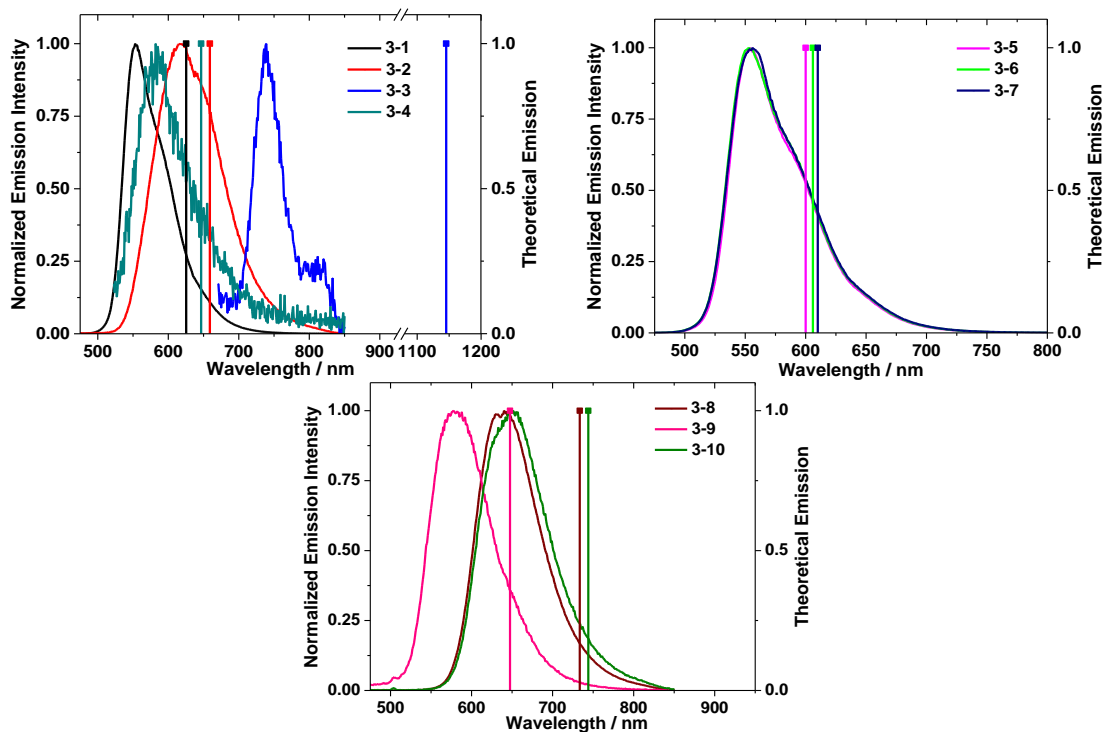


Figure 3.6. Comparing experimental emission spectra to TDDFT Δ SCF energy for **3-1** – **3-10** in dichloromethane.

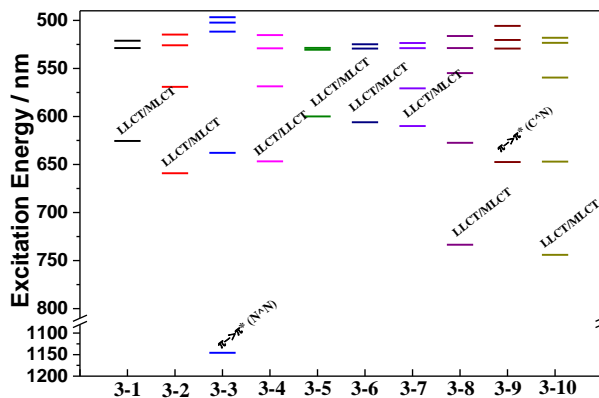
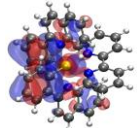
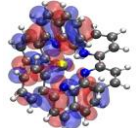
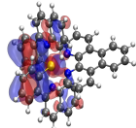
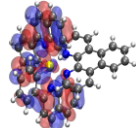
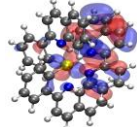
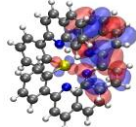
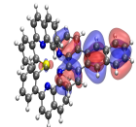
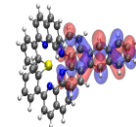
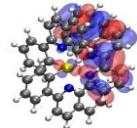
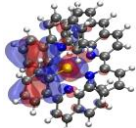
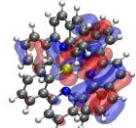
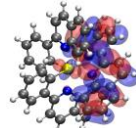
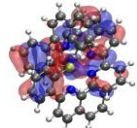
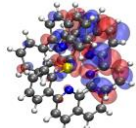
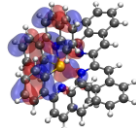
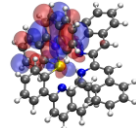
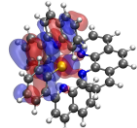
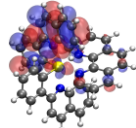
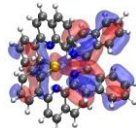
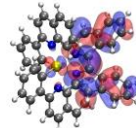


Figure 3.7. Triplet excited state energy diagram for **3-1** – **3-10** in CH_2Cl_2 .

Table 3.8. NTOs for the second triplet excited states (T_2) of **3-1** – **3-10** in CH_2Cl_2 .

	HOTO	LUTO		HOTO	LUTO
3-1			3-6		
3-2			3-7		
3-3			3-8		
3-4			3-9		
3-5			3-10		

3.3.3. Transient absorption (TA)

The nanosecond TA of complexes **3-1** – **3-10** in acetonitrile was investigated to further understand their triplet excited state characteristics. The TA spectra of **3-1** – **3-10** immediately after laser excitation are shown in Figure 3.8, and the time-resolved TA spectra are presented in Figure 3.9. The TA band maxima, triplet excited-state lifetimes, triplet extinction coefficients and quantum yields (when applicable), are listed in Table 3.1. The triplet excited-state lifetimes deduced from the decay profiles of the TA signals resembled the lifetimes obtained from the decay of emission in acetonitrile. Accordingly, we can tentatively assign the transient absorbing excited states to the emitting excited states except for **3-7**.

The TA spectra in Figure 3.8 and the data in Table 3.1 manifested that **3-1**, **3-5** and **3-6** possessed identical TA spectra, and their triplet lifetimes were on the same order. The TA spectral feature of **3-4** appeared to resemble those of **3-1**, **3-5** and **3-6**, but was somewhat blue-shifted

accompanied by a longer lifetime. The TA spectra of **3-2** and **3-8** were similar in shape but the TA band maximum was red-shifted for **3-8** compared to **3-2**, and the lifetime of **3-8** is longer than that of **3-2**. The TA spectra of **3-3** and **3-10** were similar in the region of 450–800 nm with very broad and moderately strong absorption. However, the triplet lifetime of **3-3** is one order of magnitude longer than that of **3-10**, reflecting the different natures of the T₁ states in these two complexes. In addition, the spectra of **3-2**, **3-3**, **3-4**, and **3-8** all resembled those of their corresponding Ir(III) complexes bearing the same N[^]N ligand but with different C[^]N ligands.³² Considering the natures of the T₁ states in these complexes (discussed in the photoluminescence section) and comparing these spectra to those of their corresponding N[^]N ligands and those of their Zn²⁺ perturbed ligands (Figure 3.10), we attribute the observed TA to ³MLCT/³LLCT for **3-1**, **3-2**, **3-5**, and **3-6**, to N[^]N localized ³π, π* to **3-3** and **3-7**, to ³π, π*/³MLCT/³LLCT to **3-4**, and to ³MLCT/³LLCT/³π, π* for **3-8** and **3-10**. No TA signals were observed from **3-9**, which is consistent with the C[^]N ligand localized ³π, π* nature for its T₁ state because we reported earlier that neither 2-phenylquinoline (pq) nor its chloro-bridged dinuclear Ir(III) precursor [(Ir(pq)₂Cl)₂] produced any TA signals.³¹ The drastically different TA spectra and lifetimes of **3-8**, **3-9** and **3-10** clearly manifested the distinct effects that variations of the benzannulation site at the N[^]N ligand exerted on the triplet excited-state absorption.

Complex **3-7** exhibited a quite distinct TA spectrum from the other complexes, with a very strong absorption band at 475 nm and a quite long triplet lifetime. This TA spectral feature was identical to that of its N[^]N ligand (Figure 3.10). Therefore, the observed TA for **3-7** is ascribed to the ³π, π* state localized on the N[^]N ligand. As discussed in the previous section, the T₂ state in **3-7** has the N[^]N ligand localized ³π, π* configuration and is energetically closed to its T₁ state. Thus, it can configurationally mix with the T₁ state and predominantly contribute to the TA of **3-7**.

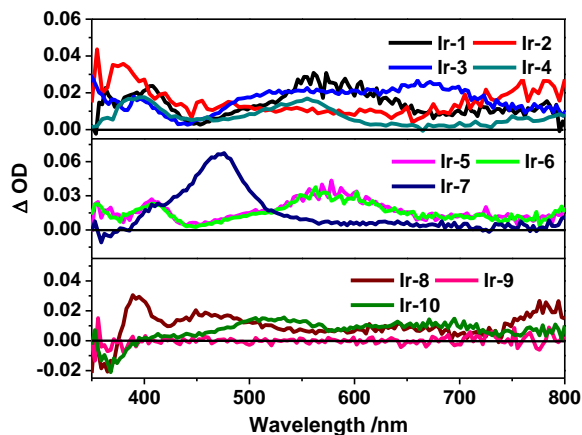


Figure 3.8. Nanosecond transient differential absorption spectra of complexes **3-1** – **3-10** in acetonitrile solution immediately after laser pulse excitation ($A_{355} = 0.4$ in a 1-cm cuvette, $\lambda_{\text{ex}} = 355$ nm).

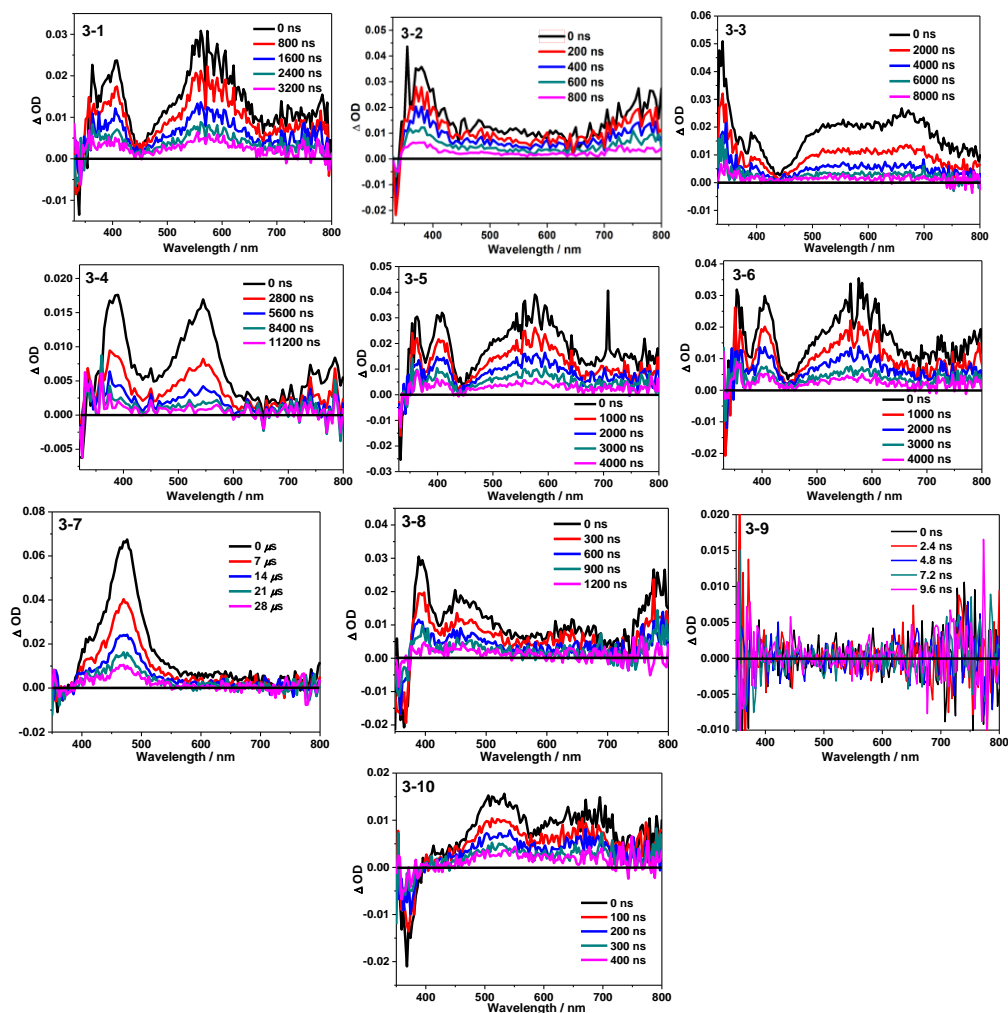


Figure 3.9. Nanosecond time-resolved transient differential absorption spectra of **3-1** – **3-10** at zero-time decay in acetonitrile. $\lambda_{\text{ex}} = 355$ nm, $A_{355} = 0.4$ in a 1-cm cuvette.

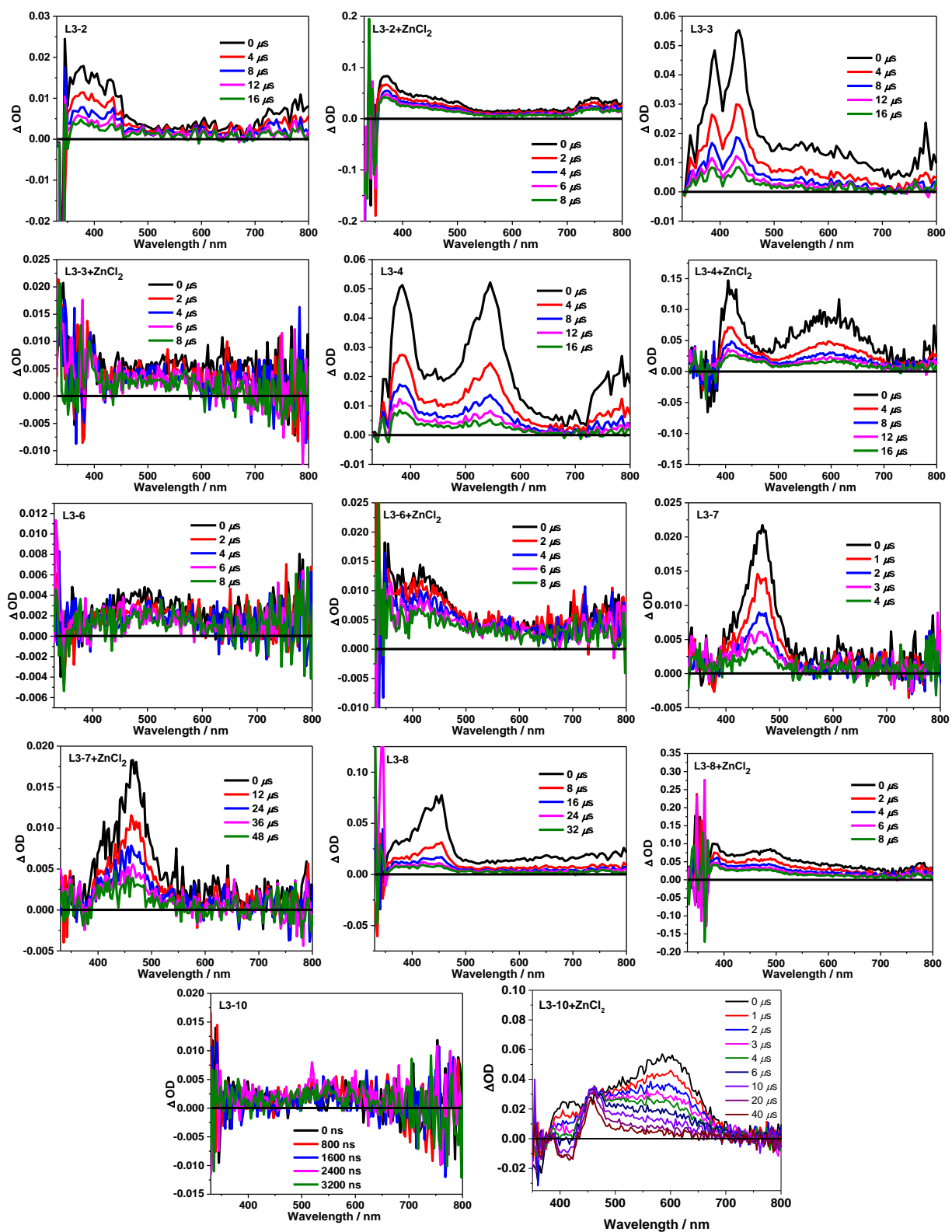


Figure 3.10. Nanosecond time-resolved transient absorption (TA) spectra of the diimine ligands used in complexes 3-2 – 3-4, 3-6 – 3-8 and 3-10 and their corresponding ZnCl_2 complexes in CH_3CN . The diimine ligands used in 3-1, 3-5 and 3-9 and their corresponding ZnCl_2 complexes did not show any TA signals. $\lambda_{\text{ex}} = 355 \text{ nm}$, and $A_{355} = 0.4$ in a 1-cm cuvette.

3.3.4. Reverse saturable absorption

The results and discussions in the previous sections revealed that the ground-state and excited-state absorption and the triplet lifetimes were affected remarkably by the site of benzannulation at the N[^]N ligand in complexes **3-1** – **3-10**. In addition, the TA signals for all complexes except for **3-9** were positive at 532 nm, implying a stronger excited-state absorption than the ground-state absorption at this wavelength. This phenomenon set up the condition for reverse saturable absorption (RSA, a nonlinear optical phenomenon in which the absorptivity of a compound increases with increased incident fluence) to occur. To demonstrate the RSA, nonlinear transmission measurement for all complexes was performed in acetonitrile solutions in a 2-mm cuvette using the 532 nm 4.1 ns laser pulses as the light source. For convenient comparison, the linear transmission of each sample solution was adjusted to 80% at 532 nm in the 2-mm cuvette. The resultant transmission vs. incident energy curves are presented in Figure 3.11. With increased incident energy, the transmission of all complexes decreased pronouncedly, indicating the occurrence of RSA. The strength of the RSA decreased following the sequence of **3-7** > **3-5** ≈ **3-6** > **3-1** > **3-3** > **3-2** > **3-4** > **3-10** > **3-8** > **3-9**, with **3-7** exhibiting the strongest RSA by reducing the transmission from 80% to 25% at the incident energy of 709 μJ. The RSA trend matched well with their ΔOD values at 532 nm (see Table 3.9). It is well known that the strength of RSA is mainly determined by the ratio of the excited-state absorption cross section vs. the ground-state absorption cross section ($\sigma_{\text{ex}}/\sigma_0$) at the interested wavelength. A decreased ground-state absorption and/or increased excited-state absorption would induce a strong RSA. The σ_0 values can be obtained by converting the molar extinction coefficients at 532 nm using the equation $\sigma = 2303\epsilon/N_A$ (where N_A is the Avogadro's constant). Unfortunately, the σ_{ex} values for most of the complexes could not be obtained due to the lack of obvious bleaching bands in the TA

measurement so that the singlet depletion method could not be applied to estimate the ϵ_{ex} values. Nevertheless, the ΔOD values that measure the absorptivity difference between the excited state and the ground state can serve as a good indicator for the strength of the excited-state absorption. A general trend is that the complexes with increased ground-state absorption at 532 nm due to benzannulation, *i.e.* **3-2**, **3-4**, **3-8**, **3-9** and **3-10**, exhibited weaker excited-state absorption at 532nm. The combination of these changes reduced the RSA strength for these complexes. Although **3-3** had an increased σ_0 value at 532 nm, its much stronger excited-state absorption at this wavelength counteracted the increased ground-state absorption and consequently gave rise to a stronger RSA than **3-2**, **3-4**, **3-8**, **3-9** and **3-10**.

Table 3.9. Ground-state absorption cross sections (σ_0) and ΔOD values of **3-1** – **3-10** at 532 nm.

	3-1	3-2	3-3	3-4	3-5	3-6	3-7	3-8	3-9	3-10
$\sigma_0/10^{-18} \text{ cm}^2$	1.39	3.06	5.65	2.47	1.28	1.37	1.52	5.80	2.42	4.61
$\Delta\text{OD}^{\text{b}}$	0.018	0.011	0.020	0.014	0.020	0.020	0.024	0.007	— ^c	0.015

^a Measured in CH_2Cl_2 . ^b Measured in CH_3CN . ^c Too weak to be measured.

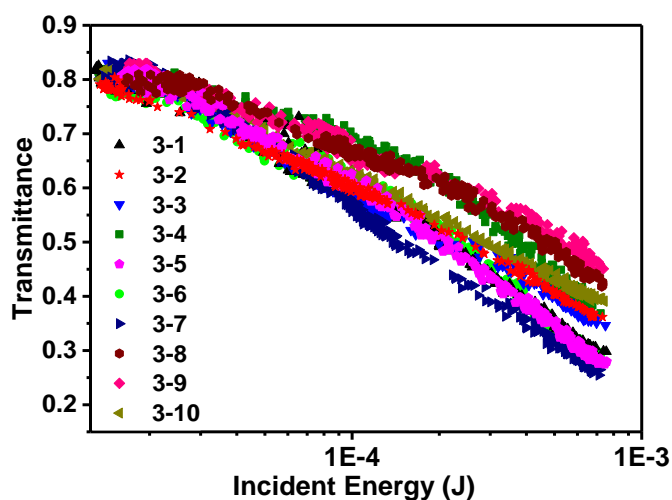


Figure 3.11. Transmission vs incident energy curves for **3-1** – **3-10** at the linear transmittance of 80% in 2 mm cuvette (in acetonitrile solution) using the 532 nm 4.1 ns laser pulses. The radius of the beam at the focal point was approximately 96 μm .

3.4. Conclusions

Ten monocationic iridium(III) complexes featuring various N[^]N ligands were synthesized and their photophysical properties were systematically investigated. Extending π -conjugation of the N[^]N ligand via benzannulation caused either a red- or blue-shift in their absorption and emission spectra compared to their corresponding parent complex. This phenomenon was rationalized by analyzing the molecular orbital symmetry at the site of benzannulation *via* DFT calculations. Depending on the site of benzannulation, destabilization (when benzannulation occurred at the 3,4-/3',4'-position or 5,6-/5',6'-position of 2,2'-bipyridine ligand or at the 6,7-position of the quinoline ring on the N[^]N ligand) or stabilization (when benzannulation occurred at the 4,5-/4',5'-position of 2,2'-bipyridine ligand or at the 7,8-position of the quinoline ring on the N[^]N ligand) or no change (when benzannulation occurred at the 2,2',3,3'-position of 2,2'-bipyridine or 5,6-position of phenanthroline ligand) of the LUMO was found upon interaction with *cis*-1,3-butadiene. Consequently, an enlarged or narrowed or identical HOMO-LUMO gap was produced compared to the parent complex and a blue- or red-shifted or no-changed charge transfer absorption band was observed. The similar trend was observed in the emission spectra of these complexes. The site of benzannulation also impacted the ns TA of these complexes drastically. Due to the site-dependent benzannulation effects on the ground- and excited-state absorption, RSA strength of these complexes at 532 nm also varied, which followed the trend of **3-7 > 3-5 \approx 3-6 > 3-1 > 3-3 > 3-2 > 3-4 > 3-10 > 3-8 > 3-9**. This trend correlated well with their Δ OD values at 532 nm and their ground-state absorption cross sections at 532 nm. Benzannulation that increased ground-state absorption but reduced the excited-state absorption resulted in reduced RSA, while benzannulation that had minor impact on the ground-state absorption but increased the excited-state absorption gave rise to enhanced RSA. A detailed

understanding of the benzannulation site-dependent red- or blue- shift of the absorption and emission spectra is vital for designing organometallic complexes with predetermined photophysical properties for applications in OLEDs, dye-sensitized solar cells, phosphorescent probes, and photosensitizers for upconversion or photodynamic therapy.

3.5. References

- ¹ Dixon, I. M.; Collin, J.-P.; Sauvage, J.-P.; Flamigni, L.; Encinas, S.; Barigelletti, F. *Chem. Soc. Rev.* **2000**, *29*, 385.
- ² Goldsmith, J. I.; Hudson, W. R.; Lowry, M. S.; Anderson, T. H.; Bernhard, S. *J. Am. Chem. Soc.* **2005**, *127*, 7502.
- ³ Zhao, J.; Wu, W.; Sun, J.; Guo, S. *Chem. Soc. Rev.* **2013**, *42*, 5323.
- ⁴ Holder, E.; Langeveld, B. M. W.; Schubert, U. S. *Adv. Mater.* **2005**, *17*, 1109.
- ⁵ King, K. A.; Spellane, P. J.; Watts, R. J. *J. Am. Chem. Soc.* **1985**, *107*, 1431.
- ⁶ Goswami, S.; Sengupta, D.; Paul, N. D.; Mondal, T. K.; Goswami, S. *Chem. – Eur. J.* **2014**, *20*, 6103.
- ⁷ Radwan, Y. K.; Maity, A.; Teets, T. S. *Inorg. Chem.* **2015**, *54*, 7122.
- ⁸ Müllen, K.; Scherf, U. Wiley-VCH: Weinheim, Germany, **2006**.
- ⁹ Mao, H.-T.; Zang, C.-X.; Shan, G.-G.; Sun, H.-Z.; Xie, W.-F.; Su, Z.-M. *Inorg. Chem.* **2017**, *56*, 9979.
- ¹⁰ Xu, H.; Chen, R.; Sun, Q.; Lai, W.; Su, Q.; Huang, W.; Liu, X. *Chem. Soc. Rev.* **2014**, *43*, 3259.
- ¹¹ Wang, Y.; Wang, S. M.; Ding, J. Q.; Wang, L. X.; Jing, X. B.; Wang, F. S. *Chem. Commun.* **2017**, *53*, 180.

- ¹² Mydlak, M.; Bizzarri, C.; Hartmann, D.; Sarfert, W.; Schmid, G.; De Cola, L. *Adv. Funct. Mater.* **2010**, *20*, 1812.
- ¹³ Sunesh, C. D.; Mathai, G.; Choe, Y. *ACS Appl. Mater. Interfaces* **2014**, *6*, 17416.
- ¹⁴ McKenzie, L. K.; Sazanovich, I. V.; Baggaley, E.; Bonneau, M.; Guerchais, V.; Williams, J. A. G.; Weinstein, J. A.; Bryant, H. E. *Chem. –Eur. J.* **2017**, *23*, 234.
- ¹⁵ Stacey, O. J.; Pope, S. J. A. *RSC Adv.* **2013**, *3*, 25550.
- ¹⁶ Maggioni, D.; Galli, M.; D'Alfonso, L.; Inverso, D.; Dozzi, M. V.; Sironi, L.; Iannacone, M.; Collini, M.; Ferruti, P.; Ranucci, E.; D'Alfonso, G. *Inorg. Chem.* **2015**, *54*, 544.
- ¹⁷ Li, Y.; Dandu, N.; Liu, R.; Li, Z.; Kilina, S.; Sun, W. *J. Phys. Chem. C* **2014**, *118*, 6372.
- ¹⁸ Liu, R.; Dandu, N.; Chen, J.; Li, Y.; Li, Z.; Liu, S.; Wang, C.; Kilina, S.; Kohler, B.; Sun, W. *J. Phys. Chem. C* **2014**, *118*, 23233.
- ¹⁹ Sun, W.; Pei, C.; Lu, T.; Cui, P.; Li, Z.; McCleese, C.; Fang, Y.; Kilina, S.; Song, Y.; Burda, C. *J. Mater. Chem. C* **2016**, *4*, 5059.
- ²⁰ Lang, X.; Zhao, J.; Chen, X. *Chem. Soc. Rev.* **2016**, *45*, 3026.
- ²¹ Huo, H.; Wang, C.; Harms, K.; Meggers, E. *J. Am. Chem. Soc.* **2015**, *137*, 9551.
- ²² Huo, H.; Shen, X.; Wang, C.; Zhang, L.; Röse, P.; Chen, L.-A.; Harms, K.; Marsch, M.; Hilt, G.; Meggers, E. *Nature* **2014**, *515*, 100.
- ²³ Chen, Y.; Guan, R.; Zhang, C.; Huang, J.; Ji, L.; Chao, H. *Coord. Chem. Rev.* **2016**, *310*, 16.
- ²⁴ Okada, S.; Okinaka, K.; Iwawaki, H.; Furugori, M.; Hashimoto, M.; Mukaide, T.; Kamatani, J.; Igawa, S.; Tsuboyama, A.; Takiguchi, T.; Ueno, K. *Dalton Trans.* **2005**, *9*, 1583.
- ²⁵ Nazeeruddin, Md. K.; Wegh, R. T.; Zhou, Z.; Klein, C.; Wang, Q.; De Angelis, F.; Fantacci, S.; Grätzel, M. *Inorg. Chem.* **2006**, *45*, 9245.

- ²⁶ Skorka, L.; Filapek, M.; Zur, L.; Małecki, J. G.; Pisarski, W.; Olejnik, M.; Danikiewicz, W.; Krompiec, S. *J. Phys. Chem. C* **2016**, *120*, 7284.
- ²⁷ Zhao, Q.; Liu, S.; Shi, M.; Wang, C.; Yu, M.; Li, L.; Li, F.; Yi, T.; Huang, C. *Inorg. Chem.* **2006**, *45*, 6152.
- ²⁸ Zeng, X.; Tavasli, M.; Perepichka, I. F.; Batsanov, A. S.; Bryce, M. R.; Chiang, C.-J.; Rothe, C.; Monkman, A. P. *Chem. Eur. J.* **2008**, *14*, 933.
- ²⁹ Kim, K.-Y.; Farley, R. T.; Schanze, K. S. *J. Phys. Chem. B* **2006**, *110*, 17302.
- ³⁰ Li, Y.; Dandu, N.; Liu, R.; Hu, L.; Kilina, S.; Sun, W. *ACS Appl. Mater. Interfaces* **2013**, *5*, 6556.
- ³¹ Wang, L.; Cui, P.; Kilina, S.; Sun, W. *J. Phys. Chem. C* **2017**, *121*, 5719.
- ³² Liu, B.; Lystrom, L.; Kilina, S.; Sun, W. *Inorg. Chem.* **2017**, *56*, 5361.
- ³³ Wang, C.; Lystrom, L.; Yin, H.; Hetu, M.; Kilina, S.; McFarland, S. A.; Sun, W. *Dalton Trans.* **2016**, *45*, 16366.
- ³⁴ Adachi, M.; Murata, Y. *J. Phys. Chem. A* **1998**, *102*, 841.
- ³⁵ Adachi, M.; Nagao, Y. *Chem. Mater.* **2001**, *13*, 662.
- ³⁶ Martin, N.; Segura, J. L.; Seoane, C. *J. Mater. Chem.* **1997**, *7*, 1661.
- ³⁷ Jensen, B. S.; Parker, V. D. *J. Am. Chem. Soc.* **1975**, *97*, 5211.
- ³⁸ Hanson, K.; Roskop, L.; Djurovich, P. I.; Zahariev, F.; Gordon, M. S.; Thompson, M. E. *J. Am. Chem. Soc.* **2010**, *132*, 16247.
- ³⁹ Li, Z.; Cui, P.; Wang, C.; Kilina, S.; Sun, W. *J. Phys. Chem. C* **2014**, *118*, 28764.
- ⁴⁰ Zhu, X.; Cui, P.; Kilina, S.; Sun, W. *Inorg. Chem.* **2017**, *56*, 13715.
- ⁴¹ Pei, C.; Cui, P.; McCleese, C.; Kilina, S.; Burda, C.; Sun, W. *Dalton Trans.* **2015**, *44*, 2176.
- ⁴² Li, Z.; Li, H.; Gifford, B. J.; Peiris, W. D. N.; Kilina, S.; Sun, W. *RSC Adv.* **2016**, *6*, 41214.

- 43 Xiang, H.; Chen, H.; Tham, H. P.; Phua, S. Z. F.; Liu, J.-G.; Zhao, Y. *ACS Appl. Mater. Interfaces* **2017**, *9*, 27553.
- 44 Ma, D.-L.; Leung, C.-H.; Zhong, H.-J.; He, B. U. S. Patent US20170145472A1. May 25, **2017**.
- 45 Yang, H.; P.-Y. Ma, V.; S.-H. Chan, D.; He, H.-Z.; Leung, C.-H.; Ma, D.-L. *Curr. Med. Chem.* **2013**, *20*, 576.
- 46 Li, A. H.; Beard, D. J.; Coate, H.; Honda, A.; Kadalbajoo, M.; Kleinberg, A.; Sherman, D. *Synthesis* **2010**, *10*, 1678.
- 47 Karim, M.; Jahng, Y. *Molecules* **2014**, *19*, 12842.
- 48 Riesgo, E. C.; Hu, Y.-Z.; Bouvier, F.; Thummel, R. P.; Scaltrito, D. V.; Meyer, G. J. *Inorg. Chem.* **2001**, *40*, 3413.
- 49 Verhoeven, J. W.; Van D. T. E. B.; Steemers F. J.; Verboom W.; Reinhoudt D. N.; Hofstraat J. W. PCT Int. Appl., 9849163, Nov 05, **1998**.
- 50 Lu, W.; Vicic, D. A.; Barton, J. K. *Inorg. Chem.* **2005**, *44*, 7970.
- 51 Nelson, T. D.; Crouch, R. D. *Org. React.* **2004**, *63*, 265–555.
- 52 Milstein, D.; Stille, J. K. *J. Am. Chem. Soc.* **1979**, *101*, 4992.
- 53 Gao, R.; Ho, D. G.; Hernandez, B.; Selke, M.; Murphy, D.; Djurovich, P. I.; Thompson, M. *J. Am. Chem. Soc.* **2002**, *124*, 14828.
- 54 Carmichael, I.; Hug, G. L. *J. Phys. Chem. Ref. Data* **1986**, *15*, 1.
- 55 Firey, P. A.; Ford, W. E.; Sounik, J. R.; Kenney, M. E.; Rodgers, M. A. J. *J. Am. Chem. Soc.* **1988**, *110*, 7626.
- 56 Kumar, C. V.; Qin, L.; Das, P. K. *J. Chem. Soc., Faraday Trans. 2* **1984**, *80*, 783.

- ⁵⁷ Frisch, M. J.; Trucks, G. W.; Schlegel, H. B.; Scuseria, G. E.; Robb, M. A.; Cheeseman, J. R.; Scalmani, G.; Barone, V.; Mennucci, B.; Peterson, G. A.; et. al. *Gaussian 09*, revision B.1; Gaussian, Inc.: Wallingford, CT, **2009**.
- ⁵⁸ Lee, C.; Yang, W.; Parr, R. G. *Physical review B* **1988**, *37*, 785.
- ⁵⁹ Hay, P. J.; Wadt, W. R. *J. Chem. Phys.* **1985**, *82*, 270.
- ⁶⁰ Adamo, C.; Barone, V. *J. Chem. Phys.* **1999**, *110*, 6158.
- ⁶¹ Barone, V.; Cossi, M.; Tomasi, J. *J. Comput. Chem.* **1998**, *19*, 404.
- ⁶² Cossi, M.; Barone, V.; Cammi, R.; Tomasi, J. *Chem. Phys. Lett.* **1996**, *255*, 327.
- ⁶³ Bjorgaard, J. A.; Sifain, A. E.; Nelson, T.; Myers, T. W.; Veauthier, J. M.; Chavez, D. E.; Scharff, R. J.; Tretiak, S. *J. Phys. Chem. A* **2016**, *120*, 4455.
- ⁶⁴ Li, Y.; Dandu, N.; Liu, R.; Kilina, S.; Sun, W. *Dalton Trans.* **2014**, *43*, 1724.
- ⁶⁵ Martin, R. L. *J. Chem. Phys.* **2003**, *118*, 4775.
- ⁶⁶ Humphrey, W., Dalke, A. and Schulten, K. *J. Molec. Graphics*, **1996**, *4*, 33.
- ⁶⁷ Wu, S.-H.; Ling, J.-W.; Lai, S.-H.; Huang, M.-J.; Cheng, C. H.; Chen, I.-C. *J. Phys. Chem. A* **2010**, *114*, 10339.
- ⁶⁸ Caspar, J. V.; Kober, E. M.; Sullivan, B. P.; Meyer, T. J. *J. Am. Chem. Soc.* **1982**, *104*, 630.
- ⁶⁹ Caspar, J. V.; Meyer, T. J. *J. Phys. Chem.* **1983**, *87*, 952.
- ⁷⁰ Guo, F.; Sun, W.; Liu, Y.; Schanze, K. *Inorg. Chem.* **2005**, *44*, 4055.

4. EFFECTS OF VARYING THE BENZANNULATION SITE AND π CONJUGATION OF THE CYCLOMETALATING LIGAND ON THE PHOTOPHYSICS AND REVERSE SATURABLE ABSORPTION OF MONOCATIONIC Iridium(III) COMPLEXES

4.1. Introduction

In the past two decades, heavy-transition-metal complexes, especially octahedral d_6 iridium(III) complexes, have attracted extensive interest because of the strong spin-orbit coupling of the iridium(III) ion, which enhances the intersystem crossing rate and thus facilitates the formation of a triplet excited state and increases the phosphorescence quantum yield.^{1,2} This feature holds great potential for a variety of applications, such as organic light-emitting devices,^{3,4} light-emitting electro-chemical cells,⁵⁻⁸ low-power upconversion,^{9,10} luminescent biological labeling,¹¹ and nonlinear optics.¹²⁻¹⁵ In addition, iridium(III) complexes exhibit excellent chemical and thermal stabilities, facilitating the practical applications of these complexes in photonic and biophotonic areas. More importantly, the excited-state properties of the iridium(III) complexes can be readily tuned via ligand structural modifications for tailoring a specific application.¹⁶⁻³³

The facile tunability of monocationic cyclometalated iridium(III) complexes, $[(N^{\wedge}N)Ir(C^{\wedge}N)_2]^+$, distinguishes them from their bicationic ruthenium(II) analogues, $[Ru(N^{\wedge}N)_3]^{2+}$, because the cyclometalating ($C^{\wedge}N$) and diimine ($N^{\wedge}N$) ligands can be altered independently to tune the photophysical properties of the iridium(III) complexes.¹⁶⁻³³ One of the commonly applied strategies is to incorporate electron-donating or -withdrawing substituents on the ligand(s).¹⁶⁻²² Another efficient strategy is to extend the π conjugation of the $N^{\wedge}N$ and/or $C^{\wedge}N$ ligand(s).²³⁻³³ In comparison to the former approach, extending the ligand π conjugation can alter the nature of the lowest singlet or triplet excited state independently. In 2006, Huang's group

reported that the emission wavelength of the heteroleptic iridium(III) complexes with N[^]N ligands bearing different degrees of π conjugation can be adjusted drastically from 586 to 732 nm.²³ Bryce's group,²⁶ Schanze's group,²⁷ and our group^{12,13,21,24,28,30-33} reported that incorporating π -conjugated substituents or benzannulation to extend the π -conjugation of the N[^]N ligand dramatically changed the triplet lifetime and enhanced the triplet excited-state absorption. This was achieved by admixing the N[^]N-ligand-localized $^3\pi,\pi^*$ character with the charge-transfer (3 CT) character in the T₁ state or even completely switching the T₁ state to the $^3\pi,\pi^*$ state in the [(N[^]N)Ir(C[^]N)₂]⁺ complexes. Interestingly, we have previously discovered that different sites of benzannulation on the N[^]N ligand caused either a red or blue shift of the absorption and emission spectra in the [(N[^]N)Ir(C[^]N)₂]⁺ complexes.²⁸ This unusual phenomenon was rationalized by analyzing the symmetry of the frontier molecular orbitals (FMOs) at the site of benzannulation on the N[^]N ligand.

Alongside the studies on the impact of the π conjugation of the N[^]N ligand, variation of the π -conjugation of the C[^]N ligands also influences the singlet and triplet excited-state characteristics significantly.^{12,13,25,29,31-33} Particularly, benzannulation at the C[^]N ligand resulted in a strong red shift of the lowest-energy ground-state absorption band and a drastically increased contribution of the C[^]N-ligand-localized $^3\pi,\pi^*$ / intraligand CT (3 ILCT) configuration(s) to the lowest triplet excited state of iridium(III) complexes.^{25,29,33} However, it is not clear whether the impact of benzannulation at the C[^]N ligands is also site-dependent, similar to benzannulation at the N[^]N ligand.

To thoroughly understand the impact of benzannulation at the C[^]N ligand on the excited-state properties of the iridium(III) complexes for a rational design of iridium(III) complexes for photonic applications, a series of monocationic iridium(III) complexes bearing C[^]N ligands

derived from 2-phenylpyridine (ppy; structures shown in Chart 4-1), i.e., 2-phenylquinoline (**L4-1**), 3-phenylisoquinoline (**L4-2**), 1-phenyl-isoquinoline (**L4-3**), benzo[h]quinoline (**L4-4**), 2-(pyridin-2-yl)naphthalene (**L4-5**), 1-(pyridin-2-yl)naphthalene (**L4-6**), 2-(phenanthren-9-yl)pyridine (**L4-7**), 2-phenylbenzo[g]quinoline (**L4-8**), 2-(naphthalen-2-yl)quinoline (**L4-9**), and 2-(naphthalen-2-yl)benzo[g]quinoline (**L4-10**), were synthesized. These C^N ligands were obtained by varying the site of benzannulation either on the pyridine ring (ligands **L4-1** – **L4-4**) or on the benzene ring (ligands **L4-4** – **L4-6**) of the ppy ligand or through expansion of the π -conjugation of **L4-1** (ligands **L4-8** – **L4-10**) or **L4-5/L4-6** (ligand **L4-7**). Complex **4-0** with the ppy ligand was used as a reference complex for comparison purposes. To demonstrate how this change influences the potential applications of the [(N^N)Ir-(C^N)₂]⁺ complexes, reverse saturable absorption (RSA, a nonlinear absorption phenomenon in which the absorptivity of a material increases with an increase of the incident light fluence due to stronger excited-state absorption than the ground-state absorption) of the synthesized complexes was studied using a nanosecond laser pulse at 532 nm.

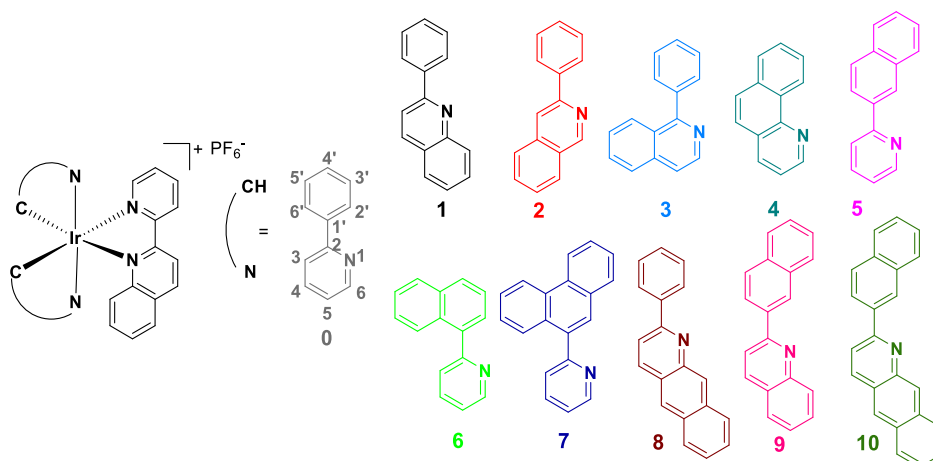


Chart 4.1. Structures of heteroleptic cationic Ir(III) complexes **4-0** – **4-10**.

4.2. Experimental section

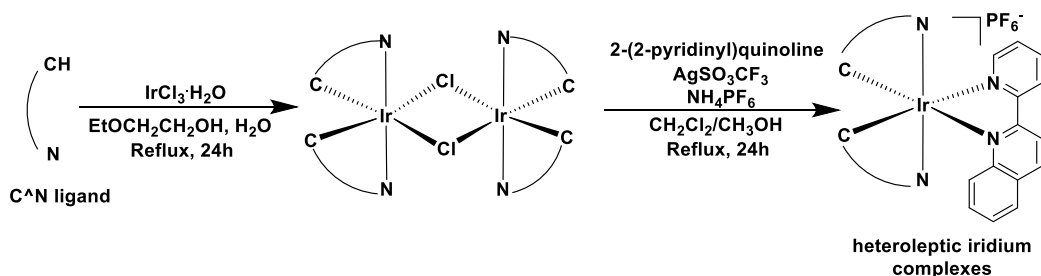
4.2.1. Materials and synthesis

All chemicals and solvents were purchased from Aldrich Chemical Co. or Alfa Aesar and used as received unless otherwise noted. Silica gel (60 Å, 230–400 mesh) and Al₂O₃ gel (neutral) used for column chromatography were purchased from Sorbent Technology. The diimine ligand 2-(pyridin-2-yl)-quinoline (N^N ligand) and C^N ligands **L4-1** and **L4-8 – L4-10** were synthesized by a Friedländer condensation reaction according to or by modification of the literature procedure.^{34–36} 3-Aminonaphthalene-2-carboxaldehyde was prepared according to the reported method.³⁷ Ligand **L4-2** was synthesized by a copper(I)-mediated cyclization reaction from 2-bromobenzaldehyde and ethynylbenzene.³⁸ Ligands **L4-3** and **L4-4** were purchased from Alfa Aesar and used as received. Ligands **L5–L7** were synthesized by Stille coupling reactions from 1-bromonaphthalene, 2-bromonaphthalene, and 9-bromophenanthrene, respectively.^{39,40} The synthesized ligands were characterized by ¹H NMR spectroscopy, while the synthesized complexes **4-1 – 4-10** were confirmed by ¹H NMR spectroscopy, electrospray ionization high-resolution mass spectrometry (ESI-MS), and elemental analysis. ¹H NMR was obtained on Varian Oxford VNMR spectrometers (400 or 500 MHz). ESI-MS analyses were conducted on a Bruker BioTOF III mass spectrometer. Elemental analyses were carried out by NuMega Resonance Laboratories, Inc. (San Diego, CA).

Ligand L4-7. The mixture of 9-bromophenanthrene (0.64 g, 2.5 mmol), 2-(tributylstannyl)pyridine (1.1 g, 3 mmol), Pd(PPh₃)₄ (40 mg, 0.035 mmol), and toluene (50 mL) was heated to reflux under nitrogen for 24 h. After reaction, toluene was removed by distillation, and the resultant dark oil was purified by a silica gel column eluted with hexane/ethyl acetate (v/v = 20/1). A colorless oil was obtained as the product (290 mg, 45%). ¹H NMR (CDCl₃, 400 MHz): δ 8.74-

8.86 (m, 3H), 8.10 (dd, $J = 8.0, 1.2$ Hz, 1H), 8.22 (dd, $J = 8.0, 1.2$ Hz, 1H), 7.86-8.11 (m, 2H), 7.59-7.72 (m, 5H), 7.40 (ddd, $J = 7.6, 3.2, 1.2$ Hz, 1H).

Ligand L4-10. To a solution of 2-acetylnaphthalene (40 mg, 0.23 mmol) and 3-aminonaphthalene-2-carboxaldehyde (40 mg, 0.23 mmol) in absolute EtOH (20 mL), saturated ethanolic KOH (2 mL) was added. The solution was refluxed under Ar for 24 h. After evaporation of the solvent, the residue was purified by chromatography on alumina gel column, eluting with CH_2Cl_2 /hexanes (1:3), to obtain the title compound as a yellow powder (51 mg, 72%). ^1H NMR (CDCl_3 , 400 MHz): δ 8.79 (s, 1H), 8.65 (s, 1H), 8.46-8.41 (m, 3H), 8.12-8.07 (m, 1H), 8.05-7.98 (m, 4H), 7.92-7.88 (m, 1H), 7.54-7.48 (m, 4H).



Scheme 4-1. Synthetic routes for Ir(III) complexes.

General synthetic procedure for Ir(III) complexes 4-1 – 4-10. The synthetic scheme for complexes 4-1 – 4-10 is illustrated in Scheme 4-1. The synthesis required two steps. First, the corresponding cyclometalating ligand (**L4-1 – L4-10**; 0.5 mmol) and $\text{IrCl}_3 \cdot 3\text{H}_2\text{O}$ (46.5 mg, 0.25 mmol) were added to a mixed solvent of 2-methoxyethanol (15 mL) and water (5 mL). The mixture was degassed and then heated to 100 °C for 24 h to allow for complexation to occur under a nitrogen atmosphere. After the reaction, the mixture was cooled to room temperature, and the precipitate was filtered and washed with water and alcohol to give the crude cyclometalated chloro-bridged iridium(III) dimer. The crude iridium(III) dimer was directly used for the following step reaction without further purification. Then, the mixture of obtained iridium(III) dimer (1 equiv),

N[^]N ligand (2 equiv), AgSO₃CF₃ (2 equiv), and CH₂Cl₂/methanol (2:1, v/v; 30 mL) was degassed and heated to reflux for 24 h. After cooling to room temperature, NH₄PF₆ (10 equiv) was added and the mixture was stirred for 2 h at room temperature. The resulting precipitate was filtered and purified by column chromatography on alumina gel eluted with CH₂Cl₂. The crude product was further purified by recrystallization in CH₂Cl₂ and hexane (or toluene) to obtain the pure complex. The reported yield for each complex is for the two-step reactions based on the starting C[^]N ligand.

4-1. An orange powder was obtained as the product (69 mg, yield: 29%). ¹H NMR (400 MHz, CDCl₃) δ 8.46-8.37 (m, 2H), 8.37-8.21 (m, 3H), 8.18-8.10 (m, 1H), 8.09-8.00 (m, 2H), 7.84 (dd, *J* = 7.8, 4.2 Hz, 2H), 7.79 (d, *J* = 7.2 Hz, 1H), 7.61 (dd, *J* = 15.7, 7.9 Hz, 3H), 7.51 (dd, *J* = 14.7, 8.3 Hz, 2H), 7.45-7.35 (m, 3H), 7.25 (s, 1H), 7.16 (ddd, *J* = 15.8, 12.3, 4.7 Hz, 3H), 7.08 (t, *J* = 7.1 Hz, 1H), 7.02-6.80 (m, 4H), 6.54 (d, *J* = 7.2 Hz, 1H), 6.34 (d, *J* = 7.4 Hz, 1H). ESI-HRMS (*m/z*): calcd. for [C₄₄H₃₀N₄Ir]⁺, 807.2103; found, 807.2136. Anal. calcd. (%) for C₄₄H₃₀F₆IrN₄P·0.3C₆H₁₄ (C₆H₁₄: Hexane): C, 56.50; H, 3.64; N, 5.68. Found: C, 56.63; H, 3.26; N, 5.46.

4-2. An orange powder was obtained as the product (112 mg, yield: 47%). ¹H NMR (400 MHz, CDCl₃): δ 8.99 (d, *J* = 7.6 Hz, 1H), 8.86 (d, *J* = 8.8 Hz, 1H), 8.67 (d, *J* = 8.4 Hz, 1H), 8.52 (s, 1H), 8.42 (d, *J* = 8.8 Hz, 1H), 8.31-8.28 (m, 2H), 8.14 (s, 1H), 8.09 (s, 1H), 8.05 (dd, *J* = 6.4, 1.2 Hz, 1H), 7.95-7.90 (m, 2H), 7.83 (d, *J* = 8.8 Hz, 2H), 7.77-7.68 (m, 4H), 7.56-7.44 (m, 5H), 7.24 (td, *J* = 7.2, 1.2 Hz, 1H), 7.13-7.03 (m, 2H), 6.91 (td, *J* = 7.2, 1.2 Hz, 1H), 6.89 (td, *J* = 7.2, 1.2 Hz, 1H), 6.32 (d, *J* = 7.6 Hz, 1H), 6.05 (d, *J* = 7.6 Hz, 1H). ESI-HRMS (*m/z*): calcd. for [C₄₄H₃₀N₄Ir]⁺, 807.2103; found, 807.2106. Anal. calcd. (%) for C₄₄H₃₀F₆IrN₄P·0.7CH₂Cl₂: C, 53.08; H, 3.13; N, 5.54. Found: C, 52.89; H, 3.48; N, 5.87.

4-3. A red powder was obtained as the product (135 mg, yield: 57%). ^1H NMR (400 MHz, DMSO- d_6) δ 9.18-9.05 (m, 2H), 8.99 (d, $J = 8.9$ Hz, 1H), 8.88 (dd, $J = 15.9, 8.3$ Hz, 2H), 8.44 (d, $J = 7.5$ Hz, 1H), 8.34 (dd, $J = 12.4, 8.5$ Hz, 2H), 8.09 (dd, $J = 8.3, 5.0$ Hz, 2H), 8.00 (d, $J = 9.4$ Hz, 2H), 7.97-7.89 (m, 2H), 7.88-7.78 (m, 2H), 7.73-7.63 (m, 2H), 7.58 (dd, $J = 16.3, 7.4$ Hz, 2H), 7.51 (d, $J = 6.3$ Hz, 1H), 7.42 (d, $J = 6.5$ Hz, 1H), 7.16 (dt, $J = 14.1, 8.0$ Hz, 3H), 7.01-6.89 (m, 2H), 6.28 (d, $J = 7.8$ Hz, 1H), 6.14 (d, $J = 6.5$ Hz, 1H), 5.76 (s, 1H). ESI-HRMS (m/z): calcd. for $[\text{C}_{44}\text{H}_{30}\text{N}_4\text{Ir}]^+$, 807.2103; found, 807.2121. Anal. calcd. (%) for $\text{C}_{44}\text{H}_{30}\text{F}_6\text{IrN}_4\text{P}\cdot 0.8\text{CH}_2\text{Cl}_2\cdot 0.3\text{H}_2\text{O}$: C, 52.48; H, 3.17; N, 5.46. Found: C, 52.47; H, 3.57; N, 5.35.

4-4. A brown powder was obtained as the product (108 mg, yield: 48%). ^1H NMR (400 MHz, CDCl_3) δ 8.94 (d, $J = 8.2$ Hz, 1H), 8.83 (d, $J = 8.9$ Hz, 1H), 8.66 (d, $J = 8.7$ Hz, 1H), 8.43 (d, $J = 9.0$ Hz, 1H), 8.31 (dd, $J = 8.1, 1.2$ Hz, 1H), 8.27-8.17 (m, 2H), 8.14 (dd, $J = 5.4, 1.2$ Hz, 1H), 7.92 (d, $J = 8.8$ Hz, 1H), 7.89-7.78 (m, 3H), 7.79-7.71 (m, 2H), 7.61 (d, $J = 8.8$ Hz, 1H), 7.56-7.49 (m, 1H), 7.49-7.41 (m, 3H), 7.37 (dd, $J = 8.1, 5.4$ Hz, 1H), 7.32 (ddd, $J = 7.6, 5.5, 1.1$ Hz, 1H), 7.22-7.16 (m, 1H), 7.16-7.10 (m, 1H), 7.04 (ddd, $J = 8.2, 4.8, 1.4$ Hz, 1H), 6.35 (d, $J = 6.6$ Hz, 1H), 6.04 (d, $J = 6.6$ Hz, 1H). ESI-HRMS (m/z): calcd. for $[\text{C}_{40}\text{H}_{26}\text{N}_4\text{Ir}]^+$, 755.1789; found, 755.1821. Anal. calcd. (%) for $\text{C}_{40}\text{H}_{26}\text{F}_6\text{IrN}_4\text{P}\cdot 1.4\text{H}_2\text{O}$: C, 51.93; H, 3.14; N, 6.06. Found: C, 51.74; H, 3.48; N, 5.99.

4-5. An orange powder was obtained as the product (109 mg, yield: 46%). ^1H NMR (DMSO- d_6 , 400 MHz): δ 9.06 (d, $J = 7.9$ Hz, 1H), 8.96 (d, $J = 7.8$ Hz, 1H), 8.88 (d, $J = 7.9$ Hz, 1H), 8.55 (d, $J = 8.2, 3.1$ Hz, 2H), 8.50 (s, 1H), 8.38 (d, $J = 8.1$ Hz, 1H), 8.30-8.26 (m, 2H), 8.07-8.05 (m, 2H), 7.96-7.93 (m, 2H), 7.86 (d, $J = 8.4$ Hz, 1H), 7.81-7.76 (m, 2H), 7.62 (t, $J = 7.6$ Hz, 2H), 7.48 (t, $J = 7.6$ Hz, 1H), 7.26-7.15 (m, 8H), 6.89 (t, $J = 8.0$ Hz, 1H), 6.57 (s, 1H), 6.33 (s,

1H). ESI-HRMS (m/z): calcd. for $[C_{44}H_{30}N_4Ir]^+$, 807.2103; found, 807.2090. Anal. calcd. (%) for $C_{40}H_{30}F_6IrN_4P$: C, 55.52; H, 3.18; N, 5.89. Found: C, 55.14; H, 3.58; N, 5.73.

4-6. A red powder was obtained as the product (119 mg, yield: 50%). 1H NMR ($CDCl_3$, 400 MHz): δ 8.89 (d, $J = 7.8$ Hz, 1H), 8.77 (d, $J = 8.2$ Hz, 1H), 8.62 (dd, $J = 8.2, 3.1$ Hz, 2H), 8.55 (d, $J = 8.1$ Hz, 1H), 8.33-8.38 (m, 2H), 8.36 (td, $J = 8.1, 1.2$ Hz, 1H), 7.97 (d, $J = 8.0$ Hz, 1H), 7.83-7.90 (m, 3H), 7.68-7.73 (m, 3H), 7.57 (t, $J = 7.8$ Hz, 2H), 7.24-7.46 (m, 7H), 7.22 (d, $J = 8.0$ Hz, 1H), 6.88-6.98 (m, 3H), 6.37 (d, $J = 8.1$ Hz, 1H), 6.23 (d, $J = 8.1$ Hz, 1H). ESI-HRMS (m/z): calcd. for $[C_{44}H_{30}N_4Ir]^+$, 807.2103; found, 807.2123. Anal. calcd. (%) for $C_{44}H_{30}F_6IrN_4P \cdot 0.8CH_2Cl_2 \cdot 0.5H_2O$: C, 52.30; H, 3.19; N, 5.45. Found: C, 52.31; H, 3.55; N, 5.58.

4-7. A red powder was obtained as the product (110 mg, yield: 40%). 1H NMR (400 MHz, $CDCl_3$) δ 8.90 (d, $J = 8.1$ Hz, 1H), 8.69 (dd, $J = 27.7, 8.7$ Hz, 2H), 8.62-8.58 (m, 1H), 8.55 (d, $J = 8.0$ Hz, 1H), 8.53-8.41 (m, 3H), 8.39 (dd, $J = 6.1, 3.5$ Hz, 1H), 8.24 (td, $J = 8.0, 1.6$ Hz, 1H), 8.15 (dd, $J = 5.8, 1.0$ Hz, 1H), 8.13-7.99 (m, 2H), 7.88-7.76 (m, 2H), 7.65-7.56 (m, 3H), 7.49-7.43 (m, 1H), 7.41 (ddd, $J = 8.2, 6.9, 1.4$ Hz, 1H), 7.37-7.26 (m, 5H), 7.21 (ddd, $J = 8.0, 7.0, 0.8$ Hz, 1H), 7.06 (d, $J = 5.0$ Hz, 1H), 6.93 (dd, $J = 8.3, 1.1$ Hz, 1H), 6.88-6.78 (m, 2H), 6.77-6.65 (m, 2H), 6.50 (dd, $J = 8.5, 1.1$ Hz, 1H), 6.42 (ddd, $J = 8.6, 6.9, 1.5$ Hz, 1H). ESI-HRMS (m/z): calcd. for $[C_{52}H_{34}N_4Ir]^+$, 907.2416; found, 907.2442. Anal. calcd. (%) for $C_{52}H_{34}F_6IrN_4P \cdot C_6H_{14} \cdot 3H_2O$: C, 58.43; H, 4.57; N, 4.70. Found: C, 58.70; H, 4.92; N, 4.72.

4-8. A brown powder was obtained as the product (118 mg, yield: 43%). 1H NMR (400 MHz, $CDCl_3$) δ 8.82 (s, 1H), 8.52 (d, $J = 8.6$ Hz, 1H), 8.41 (s, 1H), 8.32-8.24 (m, 2H), 8.24-8.14 (m, 2H), 8.14-8.05 (m, 2H), 7.92 (t, $J = 8.9$ Hz, 3H), 7.82 (dd, $J = 17.5, 8.7$ Hz, 2H), 7.74-7.44 (m, 6H), 7.40 (d, $J = 8.3$ Hz, 2H), 7.28-7.18 (m, 4H), 7.12 (dd, $J = 13.9, 6.8$ Hz, 2H), 6.90-6.81 (m, 2H), 6.73 (d, $J = 8.9$ Hz, 1H), 6.60 (d, $J = 7.7$ Hz, 1H), 6.54 (d, $J = 6.8$ Hz, 1H), 6.09 (d, $J = 8.5$

Hz, 1H). ESI-HRMS (m/z): calcd. for $[\text{C}_{52}\text{H}_{34}\text{N}_4\text{Ir}]^+$, 907.2416; found, 907.2460. Anal. calcd. (%) for $\text{C}_{52}\text{H}_{34}\text{F}_6\text{IrN}_4\text{P}\cdot 0.5\text{C}_6\text{H}_{14}\cdot 3\text{H}_2\text{O}$: C, 57.48; H, 4.12; N, 4.88. Found: C, 57.39; H, 4.26; N, 5.25.

4-9. A red powder was obtained as the product (94 mg, yield: 34%). ^1H NMR (400 MHz, CDCl_3) δ 8.66-8.52 (m, 2H), 8.51-8.40 (m, 2H), 8.37 (d, $J = 8.9$ Hz, 1H), 8.31 (d, $J = 8.5$ Hz, 1H), 8.20 (s, 1H), 8.17-8.01 (m, 3H), 7.96 (d, $J = 8.6$ Hz, 1H), 7.90 (d, $J = 8.1$ Hz, 2H), 7.84-7.73 (m, 3H), 7.68 (d, $J = 7.3$ Hz, 1H), 7.53-7.38 (m, 3H), 7.33 (dd, $J = 13.3, 6.8$ Hz, 2H), 7.25 (t, $J = 4.6$ Hz, 3H), 7.23-7.15 (m, 3H), 7.10 (d, $J = 8.9$ Hz, 1H), 6.96 (dt, $J = 8.6, 7.1$ Hz, 3H), 6.88 (s, 1H), 6.69 (s, 1H). ESI-HRMS (m/z): calcd. for $[\text{C}_{52}\text{H}_{34}\text{N}_4\text{Ir}]^+$, 907.2416; found, 907.2454. Anal. calcd. (%) for $\text{C}_{52}\text{H}_{34}\text{F}_6\text{IrN}_4\text{P}\cdot 1.8\text{H}_2\text{O}$: C, 57.59; H, 3.49; N, 5.17. Found: C, 57.21; H, 3.79; N, 5.55.

4-10. A red powder was obtained as the product (149 mg, yield: 52%). ^1H NMR (400 MHz, CDCl_3) δ 8.93 (s, 1H), 8.67-8.58 (m, 2H), 8.53-8.44 (m, 2H), 8.39 (s, 1H), 8.28 (d, $J = 7.0$ Hz, 3H), 8.25-8.08 (m, 4H), 8.03-7.87 (m, 5H), 7.83 (d, $J = 8.8$ Hz, 2H), 7.64 (s, 1H), 7.57 (ddd, $J = 8.0, 7.0, 0.9$ Hz, 1H), 7.48 (dd, $J = 14.2, 6.9$ Hz, 2H), 7.44-7.33 (m, 3H), 7.32 (dd, $J = 4.8, 3.4$ Hz, 1H), 7.27-7.21 (m, 2H), 7.19-7.12 (m, 2H), 7.12-7.03 (m, 2H), 6.94 (s, 1H), 6.89 (s, 1H), 6.69 (d, $J = 8.1$ Hz, 1H), 6.06 (d, $J = 8.4$ Hz, 1H). ESI-HRMS (m/z): calcd. for $[\text{C}_{60}\text{H}_{38}\text{N}_4\text{Ir}]^+$, 1007.2731; found, 1007.2746. Anal. Calcd. (%) for $\text{C}_{60}\text{H}_{38}\text{F}_6\text{IrN}_4\text{P}\cdot 1.4\text{H}_2\text{O}$: C, 61.21; H, 3.49; N, 4.76. Found: C, 60.94; H, 3.86; N, 4.77.

4.2.2. Photophysical and nonlinear transmission measurements

All spectroscopic-grade solvents used for photophysical measurement were purchased from Alfa Aesar and used as received. The ultraviolet–visible (UV–vis) absorption spectra of complexes **4-1** – **4-10** were recorded on a Varian Cary 50 spectrophotometer. The steady-state emission spectra in different solvents [acetonitrile (CH_3CN), acetone, CH_2Cl_2 , and toluene] were

collected on a Horiba FluoroMax 4 fluorometer/phosphorometer. The full spectra of **4-8** and **4-10** in CH₂Cl₂ were detected with an InGaAs detector from 670 to 1225 nm ($\lambda_{\text{ex}} = 473$ nm) with a 500-nm-long pass filter. [Ru(bpy)₃]Cl₂ ($\Phi_{\text{em}} = 0.097$ in CH₃CN; $\lambda_{\text{ex}} = 436$ nm)⁴¹ was used as the reference for determination of the emission quantum yields for complexes **4-1** – **4-10** using relative actinometry.⁴² In degassed CH₃CN solutions, the time-resolved nanosecond transient absorption (TA) spectra and the triplet lifetimes were measured on an Edinburgh LP920 laser flash photolysis spectrometer. The third harmonic output (355 nm) from a Nd:YAG laser (Quantel Brilliant; pulse width = 4.1 ns; repetition rate = 1 Hz) was used as the excitation source for the TA measurements. Before each measurement, the sample solutions were purged with argon for 40 min.

The nonlinear transmission of complexes **4-1** – **4-10** at 532 nm was studied using a Quantel Brilliant 4.1 ns laser with a repetition rate of 10 Hz as the light source. The linear transmission of complexes **4-1** – **4-10** in CH₃CN solution was set to 80% at 532 nm in the 2 mm cuvette. The experimental setup and details were described previously.⁴³ The beam radius at the focal point was approximately 96 μm , focused by an $f = 40$ cm plano-convex lens.

4.2.3. Quantum chemistry calculations

Theoretical investigations of all iridium(III) complexes were performed using density functional theory (DFT) and time-dependent DFT (TDDFT), implemented in a Gaussian09 quantum software package.⁴⁴ These calculations include ground-state geometry optimization using DFT and absorption spectral calculations using TDDFT. DFT and TDDFT calculations were carried out using the hybrid functional PBE1PBE⁴⁵ with a mixed basis set (LANL2DZ for iridium⁴⁶ and 6-31g* for hydrogen, carbon, and nitrogen⁴⁷). The solvent effects were implicitly included via a conductor polarized continuum model^{48,49} for CH₂Cl₂. This methodology has been

proven to provide reasonable agreement to experimental results for the structural and electronic absorption of iridium(III) complexes.^{22,24,30,31,50} Ground-state optimization at the singlet and triplet states was performed and used as a structural input for TDDFT calculations of the emission energies.

UV–vis absorption spectra were obtained by computing the lowest 60 singlet transitions using TDDFT, which were then broadened by a Gaussian function with a line width of 0.1 eV to reproduce homogeneous broadening caused by thermal vibrations to coincide with the experimental spectra of these complexes. To investigate the nature of the emissive states of the iridium(III) complexes, a TDDFT self-consistent-field (SCF) approach was applied using the triplet ground-state geometry optimized using unrestricted DFT as the input for the TDDFT calculations of the spin-flip transition from T_1 to S_0 .^{22,28,30,50} Characterization of relevant optical transitions was performed by computing the natural transition orbitals (NTOs),⁵¹ as implemented in Gaussian09, and visualized using VMD⁵² and GaussView 5.09⁵³ with the default isovalue of 0.02. In addition, the spin-density was calculated as the difference between the SCF density for the lowest singlet and triplet states for each complex.

4.3. Results and discussion

4.3.1. Effect of benzannulation on the ground-state equilibrium geometry

The main geometrical parameters characterizing the structural changes upon benzannulation were obtained from our DFT calculations and are shown in Table 4.1. The bond lengths between the coordinated atoms on the C^N ligands and the iridium(III) center showed that the C–Ir bonds were insignificantly affected by benzannulation, varying from 1.98 to 2.02 Å for all complexes. In contrast, the effect of benzannulation at the C^N ligands was more pronounced on the coordination bonds between nitrogen atoms and iridium(III), with the N–Ir bonds in

complexes **4-1** and **4-8 – 4-10** being 0.05–0.07 Å longer compared to those in complexes **4-2 – 4-7**. This trend aligns with the fact that complexes **4-1** and **4-8 – 4-10** have benzannulation at the 5 and 6 positions of the pyridine ring of the C[^]N ligands, resulting in a slight elongation of the N–Ir coordination bond. It was noted that the C₂–Ir and N₂–Ir bond lengths from the C₂[^]N₂ ligand were slightly longer than those from the C₁[^]N₁ ligand. Moreover, the bond lengths between the two nitrogen atoms on the N[^]N ligand and the iridium(III) ion were quite distinct, with the N₄–Ir bonds being not only obviously longer than those of the N₃–Ir bonds but also more affected by benzannulation at the 5 and 6 positions of the C[^]N ligands (i.e., the N₄–Ir bonds in complexes **4-1** and **4-8 – 4-10** were 0.05–0.06 Å longer than those in complexes **4-2 – 4-7**).

The dihedral angles between the two pyridine rings (N₃[^]N₄) in the N[^]N ligand also pointed out that benzannulation at the 5 and 6 positions of the C[^]N ligands caused significant conformational changes, with the two pyridine rings being twisted to ~20° in complexes **4-1** and **4-8 – 4-10** compared to the ~10° angles in complexes **4-2 – 4-7** (Table 4.1). It is interesting to note that the dihedral angles between the phenyl and pyridine rings in the two C[^]N ligands were both impacted pronouncedly by benzannulation at the 3 and 4 or 5' and 6' positions of the C[^]N ligands as well. This effect was clearly reflected by the much larger C₁[^]N₁ and C₂[^]N₂ angles in complexes **4-3**, **4-6**, and **4-7** compared to those in the other complexes.

The benzannulation sites at the C[^]N ligands influenced the bond angles around the iridium(III) ion distinctively. Benzannulation at the 5 and 6 positions of the C[^]N ligands reduced both the N₁–Ir–N₃ and N₁–Ir–N₂ angles while increasing the N₂–Ir–N₃ angles in complexes **4-1** and **4-8 – 4-10** compared to those in the other complexes. In contrast, benzannulation at either the 5 and 6 or 5' and 6' positions of the C[^]N ligands increased the C₁–Ir–C₂ angles in complexes **1** and **4-6 – 4-10** compared to those in **4-2 – 4-5**. Benzannulation at the 3 and 4 positions of the C[^]N

ligands also slightly increased the C₁–Ir–C₂ angle in **4-3** with respect to those in **4-2**, **4-4**, and **4-5**. These trends indicate that benzannulation at the 5 and 6 positions of the C[^]N ligands in **4-1** and **4-8 – 4-10** rotate both C[^]N ligands away from the quinoline rings of the N[^]N ligand to reduce steric hindrance. Additionally, benzannulation at the 5' and 6' positions of the C[^]N ligands expanded the C₁–Ir–C₂ angles in **4-6** and **4-7**, especially in **4-7**, as a result of avoiding steric hindrance.

Table 4.1. Geometrical characteristics of complexes **4-1 – 4-10**: bond length (B), dihedral angle (D) and bond angle (A) between atoms numbered in the Chart 4-1.

	4-1	4-2	4-3	4-4	4-5	4-6	4-7	4-8	4-9	4-10
B(Ir-C ₁) / Å	1.98	2.00	1.99	2.01	2.00	1.99	2.01	1.98	1.99	1.98
B(Ir-C ₂) / Å	2.00	2.01	2.01	2.02	2.02	2.01	2.02	2.00	2.00	2.00
B(Ir-N ₁) / Å	2.10	2.05	2.05	2.06	2.05	2.04	2.05	2.10	2.10	2.10
B(Ir-N ₂) / Å	2.11	2.06	2.06	2.06	2.06	2.05	2.05	2.11	2.11	2.11
B(Ir-N ₃) / Å	2.18	2.16	2.16	2.15	2.16	2.16	2.18	2.18	2.18	2.18
B(Ir-N ₄) / Å	2.32	2.27	2.26	2.26	2.27	2.26	2.26	2.32	2.32	2.32
D(C ₁ [^] N ₁) (°)	0.2	0.7	11.4	0.3	1.0	11.1	11.6	0.3	0.6	0.6
D(C ₂ [^] N ₂) (°)	6.2	1.1	12.5	0.7	1.1	10.3	10.7	5.7	6.7	6.3
D(N ₃ [^] N ₄) (°)	19.5	10.0	9.9	9.1	10.8	11.1	9.2	20.0	20.4	20.2
A(N ₁ –Ir–N ₃) (°)	83.3	87.9	88.6	89.1	88.1	88.5	86.5	83.6	84.1	84.0
A(N ₂ –Ir–N ₃) (°)	103.8	96.5	96.9	95.6	96.8	96.8	91.5	103.9	103.3	103.5
A(N ₁ –Ir–N ₂) (°)	171.5	174.6	174.1	174.2	174.2	173.5	178.0	171.2	171.5	171.2
A(C ₁ –Ir–C ₂) (°)	86.6	84.5	85.3	83.9	84.3	86.4	94.7	86.8	86.9	86.9

4.3.2. Electronic absorption

The UV–vis absorptions of complexes **4-1 – 4-10** were studied in solvents with different polarities, such as CH₃CN, tetrahydrofuran (THF), CH₂Cl₂, and toluene. The spectra in CH₂Cl₂ are displayed in Figure 4.1, and the absorption parameters, i.e., absorption band maxima and molar extinction coefficients, are tabulated in Table 4.2. The absorption follows Beer's law in the concentration range of 1×10⁻⁶ to 1×10⁻⁴ mol/L, suggesting the absence of ground-state aggregation in this tested concentration range. The spectra of all complexes were generally divided into three regions: (a) the major absorption bands at wavelengths of 270–400 nm in complexes **4-1 – 4-7**, 270–475 nm in **4-8** and **4-10**, and 270–425 nm in **4-9** being predominantly attributed to the C[^]N

or N^N ligand-centered spin-allowed ¹π,π* transitions, likely mixed with some CT character, in view of the large molar extinction coefficients and the NTOs from the TDDFT calculations (Tables 4-5 and 4-6); (b) a weaker featureless low-energy band at 400–500 nm in **4-1** – **4-7**, 475–550 nm in **4-8** and **4-10**, and 425–550 nm in **4-9** originating mainly from the CT transitions [i.e., metal-to-ligand CT (¹MLCT), ligand-to-ligand CT (¹LLCT), and also ¹LLCT in **4-1** – **4-3** and **4-8** – **4-10**] with minor ¹π,π* character (Table 4.4); (c) a very weak tail beyond 500/ 550 nm attributing to spin-forbidden ³CT/¹π,π* transitions according to literature reports for other iridium(III) complexes.^{23,24,28,29,31–33,54,55}

Table 4.2. Electronic absorption, emission, and excited-state absorption parameters for complexes **4-1** – **4-10**.

	$\epsilon_{\text{abs}}/\text{nm} (\log \epsilon)^{\text{a}}$	$\lambda_{\text{em}}/\text{nm} (\tau_{\text{em}}/\mu\text{s}); \Phi_{\text{em}}^{\text{b}}$	$\lambda_{\text{T1-Tn}}/\text{nm} (\tau_{\text{TA}}/\mu\text{s})^{\text{c}}$
4-1	280 (4.79), 337 (4.52), 433 (3.84)	613 (0.52); 0.075	380 (0.30), 759 (0.31), 782 (0.33)
4-2	292 (4.85), 329 (4.48), 345 (4.40), 381 (4.13)	642 (0.16); 0.033	371 (0.10), 432 (0.11), 773 (0.11)
4-3	290 (4.74), 337 (4.54), 377 (4.25), 432 (3.98)	618 (0.31); 0.11	363 (0.33), 393 (0.34), 511 (0.34)
4-4	280 (4.73), 329 (4.55), 415 (3.95)	615 (0.27); 0.070	377 (0.15), 437 (0.12), 749 (0.13)
4-5	280 (4.79), 330 (4.58), 423 (3.58)	650 (0.07); 0.020	377 (0.03), 438 (0.02), 773 (0.02)
4-6	280 (4.80), 338 (4.53), 416 (3.91), 440 (3.88)	649 (0.08); 0.024	382 (0.04), 501 (0.04), 758 (0.03)
4-7	280 (4.86), 325 (4.66), 343 (4.52), 442 (4.10)	663 (0.06); 0.002	390 (0.01), 502 (0.01), 792 (0.01)
4-8	280 (4.85), 311 (4.91), 383 (4.30), 498 (3.76)	894 (3.11); 0.015	371 (2.93), 462 (2.92), 657 (2.89)
4-9	280 (4.92), 352 (4.68), 473 (3.52)	649 (0.13); 0.019	385 (0.06), 439 (0.06), 735 (0.05)
4-10	280 (5.03), 333 (5.02), 408 (4.65), 445 (4.13)	898 (4.33); 0.009	458 (4.11), 683 (4.15)

^a Absorption band maxima and molar extinction coefficients of the UV-vis absorption in CH₂Cl₂ at room temperature. ^b Emission band maxima and decay lifetimes in CH₂Cl₂ at room temperature, $c = 1 \times 10^{-5}$ mol/L. The reference used was a degassed CH₃CN solution of [Ru(bpy)₃]Cl₂ ($\Phi_{\text{em}} = 0.097$, $\lambda_{\text{ex}} = 436$ nm). ^c Nanosecond TA band maxima and triplet excited-state lifetimes measured in CH₃CN at room temperature.

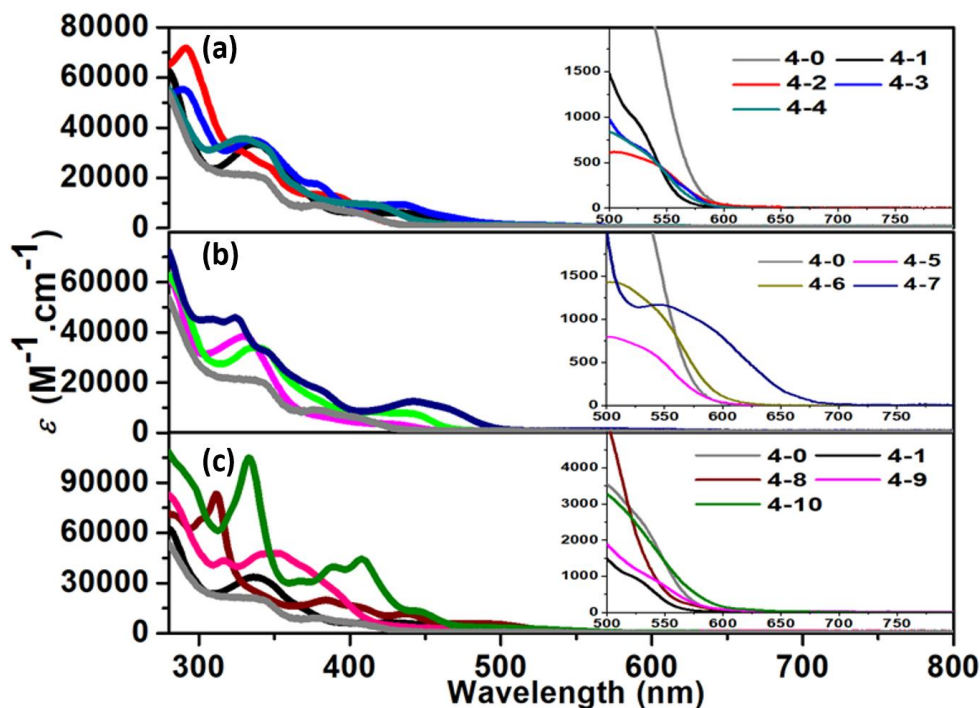


Figure 4.1. Experimental UV-vis absorption spectra of (a) **4-0** – **4-4**, (b) **4-5** – **4-7** and (c) **4-0**, **4-1**, and **4-8** – **4-10** at room temperature in dichloromethane. The inset shows the expanded spectra at 500-800 nm.

Examination of the low-energy CT bands of **4-1** – **4-10** (i.e., 400 / 425 / 475–500 / 550 nm) and their comparison to that of the parent complex **4-0** revealed that benzannulation at the C^N ligands induced a red shift of these bands and increased molar extinction coefficients except for those in **4-2** and **4-5**. Such changes became more distinct when benzannulation occurred at the phenyl ring of the ppy ligand or upon fusion of the naphthyl ring to the 5 and 6 positions of the pyridyl ring. This observation was partially validated by the TDDFT calculation results. According to our calculations, the lowest-energy transition (S_1 state; Table 4.3) appeared to be more site-dependent when benzannulation occurred at the phenyl ring. Extending π -conjugation at the phenyl ring of the ppy ligand drastically decreased the energies of the S_1 states in complexes **4-5** – **4-7**, **4-9**, and **4-10**, while benzannulation at the pyridyl ring of the ppy ligand showed a minor impact on the S_1 state energies in complexes **4-1** – **4-4** and **4-8**. This trend can be rationalized by the electron-density distribution of the holes in these complexes. As indicated by the NTOs in Table 4-3, the

holes in these complexes were primarily localized on the phenyl rings of the C^N ligands and the d orbital of the iridium(III) ion. Benzannulation at the phenyl rings of the C^N ligands thus drastically altered the energy of the holes, while benzannulation at the pyridyl rings had a minor impact on the hole energy.

Table 4.3. NTOs contributing to the lowest-energy singlet transitions (S_1) of complexes **4-1** – **4-10** in CH₂Cl₂.

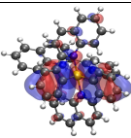
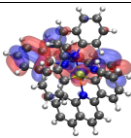
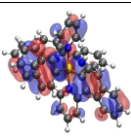
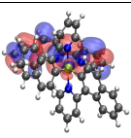
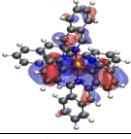
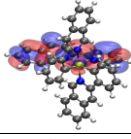
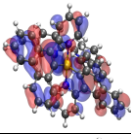
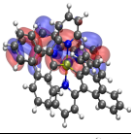
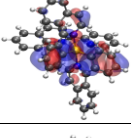
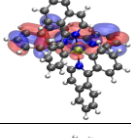
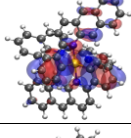
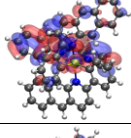
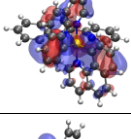
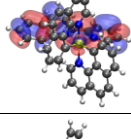
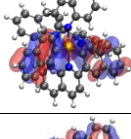
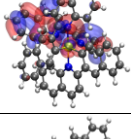
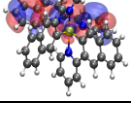
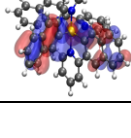
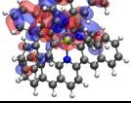
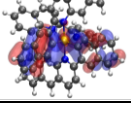
	S_1	Hole	Electron		S_1	Hole	Electron
4-1	486 nm $f = 0.006$ 100%			4-6	530 nm $f = 0.008$ 100%		
4-2	511 nm $f = 0.002$ 100%			4-7	606 nm $f = 0.010$ 100%		
4-3	497 nm $f = 0.005$ 100%			4-8	496 nm $f = 0.013$ 100%		
4-4	499 nm $f = 0.002$ 100%			4-9	516 nm $f = 0.003$ 100%		
4-5	517 nm $f = 0.001$ 100%			4-10	528 nm $f = 0.004$ 100%		

Table 4.4. NTOs representing singlet transitions responsible for the low-energy absorption bands of complexes **4-1** – **4-10** in CH₂Cl₂.

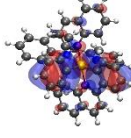
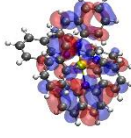
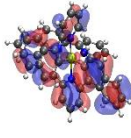
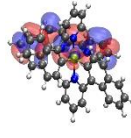
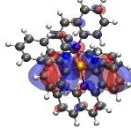
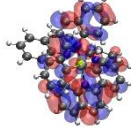
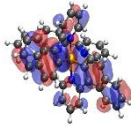
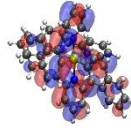
	$S_0 \rightarrow S_n$	Hole	Electron		$S_0 \rightarrow S_n$	Hole	Electron
4-1	S_2 424 nm $f = 0.072$ 99%			4-6	S_2 445 nm $f = 0.001$ 100%		
	S_3 421 nm $f = 0.003$ 98%				S_3 408 nm $f = 0.115$ 98%		

Table 4.4. NTOs representing singlet transitions responsible for the low-energy absorption bands of complexes **4-1** – **4-10** in CH₂Cl₂. (continued)

$S_0 \rightarrow S_n$	Hole	Electron	$S_0 \rightarrow S_n$	Hole	Electron
S ₄ 391 nm $f = 0.028$ 97%			S ₇ 370 nm $f = 0.122$ 97%		
4-2 S ₂ 417 nm $f = 0.005$ 100%			S ₈ 357 nm $f = 0.074$ 97%		
S ₃ 404 nm $f = 0.001$ 99%			S ₉ 352 nm $f = 0.096$ 95%		
S ₄ 390 nm $f = 0.011$ 98%			4-7 S ₂ 474 nm $f = 0.002$ 99%		
4-3 S ₂ 427 nm $f = 0.100$ 99%			S ₃ 446 nm $f = 0.024$ 99%		
S ₃ 415 nm $f = 0.013$ 91%			S ₄ 431 nm $f = 0.190$ 99%		
S ₄ 409 nm $f = 0.020$ 89%			4-8 S ₂ 462 nm $f = 0.051$ 98%		
4-4 S ₂ 413 nm $f = 0.002$ 100%			S ₃ 456 nm $f = 0.020$ 96%		
S ₃ 400 nm $f = 0.000$ 99%			S ₄ 445 nm $f = 0.028$ 95%		
S ₄ 388 nm $f = 0.066$ 97%			S ₆ 419 nm $f = 0.101$ 94%		
4-5 S ₂ 433 nm $f = 0.002$ 100%			S ₇ 415 nm $f = 0.038$ 96%		

Table 4.4. NTOs representing singlet transitions responsible for the low-energy absorption bands of complexes **4-1** – **4-10** in CH₂Cl₂. (continued)

$S_0 \rightarrow S_n$	Hole	Electron	$S_0 \rightarrow S_n$	Hole	Electron
S_3 415 nm $f = 0.002$ 99%			S_8 402 nm $f = 0.044$ 92%		
S_4 401 nm $f = 0.036$ 98%			4-9 S_2 459 nm $f = 0.011$ 100%		
S_5 386 nm $f = 0.013$ 95%			S_3 456 nm $f = 0.013$ 99%		
S_6 378 nm $f = 0.005$ 99%			S_4 423 nm $f = 0.006$ 99%		
			S_5 404 nm $f = 0.013$ 99%		
			S_7 388 nm $f = 0.066$ 98%		
			4-10 S_2 503 nm $f = 0.008$ 100%		
			S_3 488 nm $f = 0.005$ 100%		
			S_4 453 nm $f = 0.035$ 98%		
			S_6 429 nm $f = 0.117$ 91%		
			S_7 425 nm $f = 0.074$		

Table 4.5. NTOs representing singlet transitions responsible for the medium energy absorption bands of complexes **4-1** – **4-10** in CH₂Cl₂.

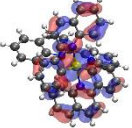
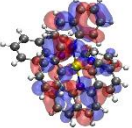
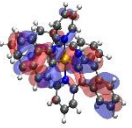
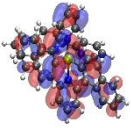
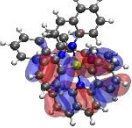
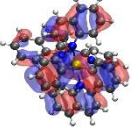
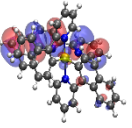
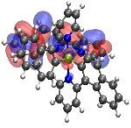
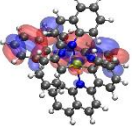
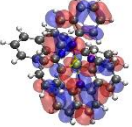
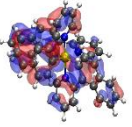
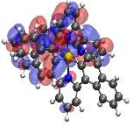
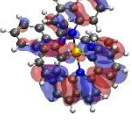
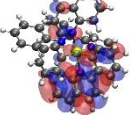
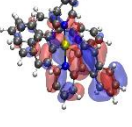
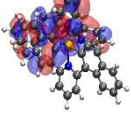
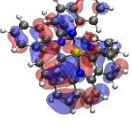
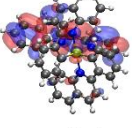
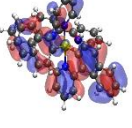
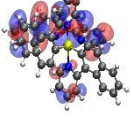
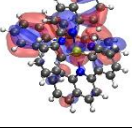
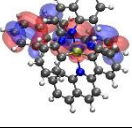
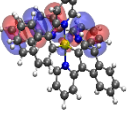
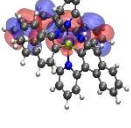
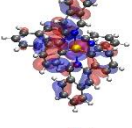
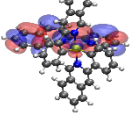
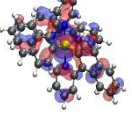
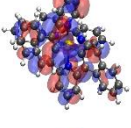
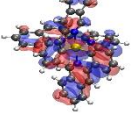
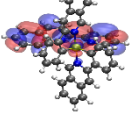
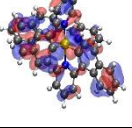
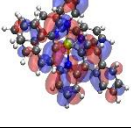
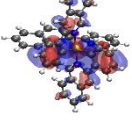
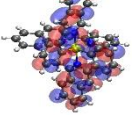
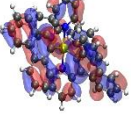
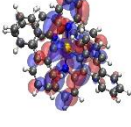
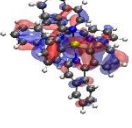
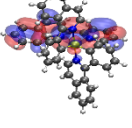
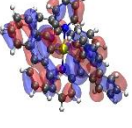
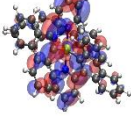
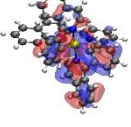
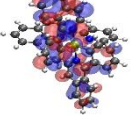
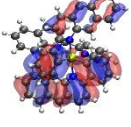
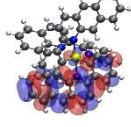
	S ₀ →S _n	Hole	Electron		S ₀ →S _n	Hole	Electron
4-1	S ₁₀ 335 nm <i>f</i> = 0.080 95%			4-6	S ₁₅ 322 nm <i>f</i> = 0.158 90%		
	S ₁₃ 329 nm <i>f</i> = 0.111 58%				S ₂₀ 311 nm <i>f</i> = 0.208 43%		
	25%				33%		
	S ₂₀ 311 nm <i>f</i> = 0.144 59%				21%		
	23%				S ₂₁ 309 nm <i>f</i> = 0.149 58%		
	S ₂₁ 307 nm <i>f</i> = 0.191 77%				29%		
4-2	S ₆ 376 nm <i>f</i> = 0.028 98%			S ₂₂ 308 nm <i>f</i> = 0.124 73%			
	S ₇ 374 nm <i>f</i> = 0.048 98%			21%			
	S ₈ 357 nm <i>f</i> = 0.212 95%			4-7	S ₉ 371 nm <i>f</i> = 0.153 93%		
4-3	S ₆ 374 nm <i>f</i> = 0.084 97%				S ₁₂ 359 nm <i>f</i> = 0.100 83%		
	S ₉ 351 nm <i>f</i> = 0.088 65%			4-8	S ₁₃ 355 nm <i>f</i> = 0.200 90%		

Table 4.5. NTOs representing singlet transitions responsible for the medium energy absorption bands of complexes **4-1** – **4-10** in CH₂Cl₂. (continued)

$S_0 \rightarrow S_n$	Hole	Electron	$S_0 \rightarrow S_n$	Hole	Electron
34%			S ₁₄ 352 nm $f = 0.140$ 80%		
S ₁₀ 349 nm $f = 0.101$ 59%			4-9 S ₉ 367 nm $f = 0.124$ 87%		
40%			S ₁₀ 363 nm $f = 0.201$ 92%		
S ₁₅ 325 nm $f = 0.128$ 62%			S ₁₁ 362 nm $f = 0.154$ 85%		
31%			S ₁₇ 334 nm $f = 0.276$ 79%		
S ₁₈ 320 nm $f = 0.150$ 80%			S ₁₈ 331 nm $f = 0.122$ 74%		
S ₂₀ 311 nm $f = 0.329$ 84%			4-10 S ₁₃ 390 nm $f = 0.247$ 94%		
4-4 S ₉ 332 nm $f = 0.046$ 81%			S ₁₄ 379 nm $f = 0.407$ 96%		
S ₁₄ 322 nm $f = 0.072$ 54%			S ₁₅ 373 nm $f = 0.172$ 84%		
41%					
S ₁₅ 316 nm $f = 0.073$ 55%					

Table 4.5. NTOs representing singlet transitions responsible for the medium energy absorption bands of complexes **4-1** – **4-10** in CH₂Cl₂. (continued)

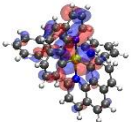
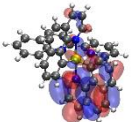
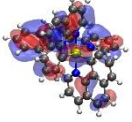
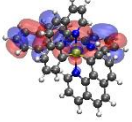
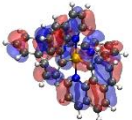

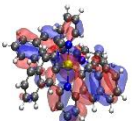
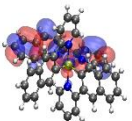
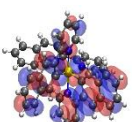
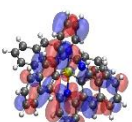
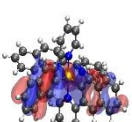
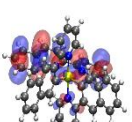
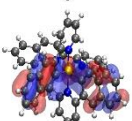
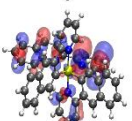
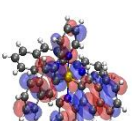
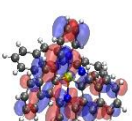
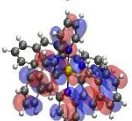
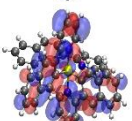
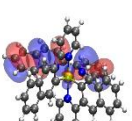
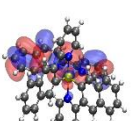
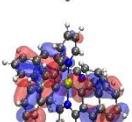
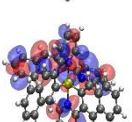
$S_0 \rightarrow S_n$	Hole	Electron
23%		
S ₁₈ 310 nm $f = 0.124$ 80%		
S ₁₉ 309 nm $f = 0.118$ 93%		
4-5 S ₈ 360 nm $f = 0.125$ 96%		
S ₁₂ 336 nm $f = 0.112$ 55%		
42%		
S ₁₃ 334 nm $f = 0.099$ 65%		
32%		
S ₁₄ 325 nm $f = 0.123$ 73%		
S ₁₉ 311 nm $f = 0.168$ 55%		
36%		

Table 4.6. NTOs representing singlet transitions responsible for the main absorption bands of complexes **4-1** – **4-10** in CH₂Cl₂.

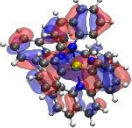
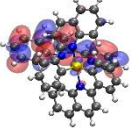
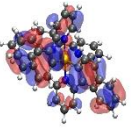
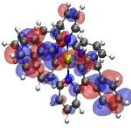
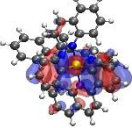
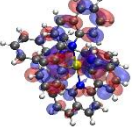
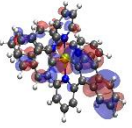
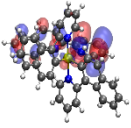
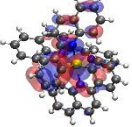
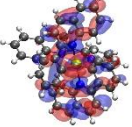
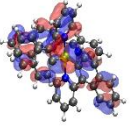
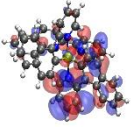
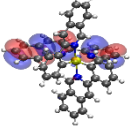
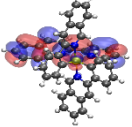
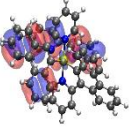
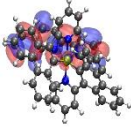
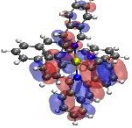
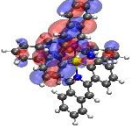
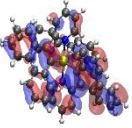
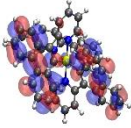
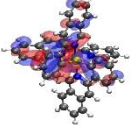
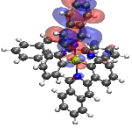
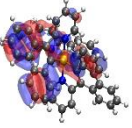
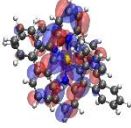

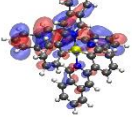
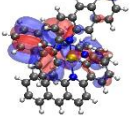
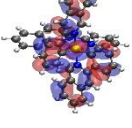
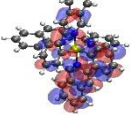
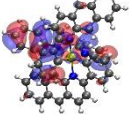
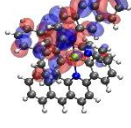
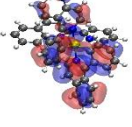
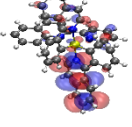
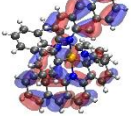
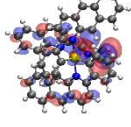
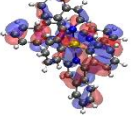
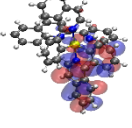
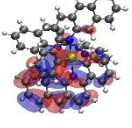
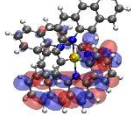
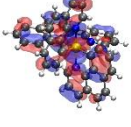

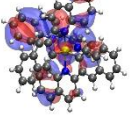
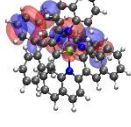
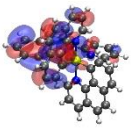
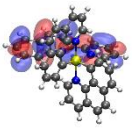
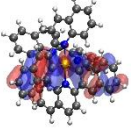
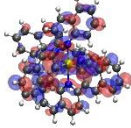
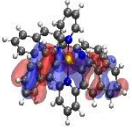
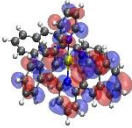
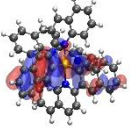
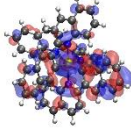
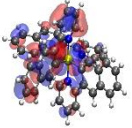
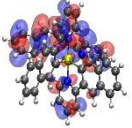
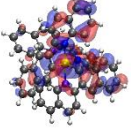
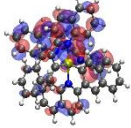
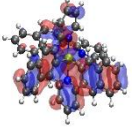
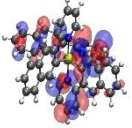
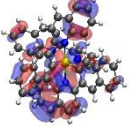
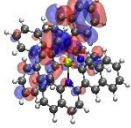
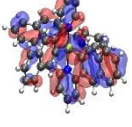
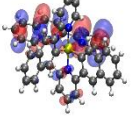
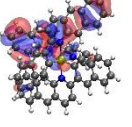
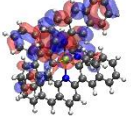
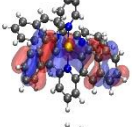
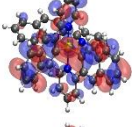
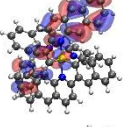
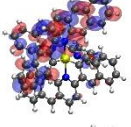
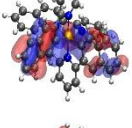
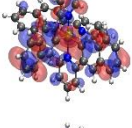
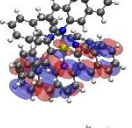
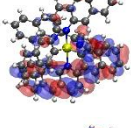
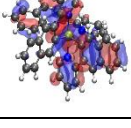
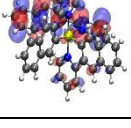
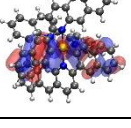
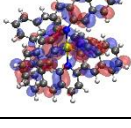
	$S_0 \rightarrow S_n$	Hole	Electron		$S_0 \rightarrow S_n$	Hole	Electron
4-1	S_{38} 269 nm $f = 0.208$ 45%			4-6	S_{38} 270 nm $f = 0.353$ 43%		
	S_{46} 260 nm $f = 0.249$ 44%				22%		
	36%				S_{50} 257 nm $f = 0.161$ 82%		
4-2	S_{20} 311 nm $f = 0.297$ 80%			4-7	S_{25} 312 nm $f = 0.507$ 62%		
	S_{24} 298 nm $f = 0.227$ 64%				S_{43} 276 nm $f = 0.154$ 41%		
	30%				30%		
	S_{27} 293 nm $f = 0.460$ 70%				4-8	S_{29} 309 nm $f = 0.199$ 41%	
S_{32} 284 nm $f = 0.213$ 72%			27%				
4-3	S_{37} 272 nm $f = 0.418$ 62%			S_{34} 301 nm $f = 0.195$ 88%			
	20%			S_{37} 292 nm $f = 0.393$ 73%			
4-4	S_{34} 272 nm $f = 0.110$ 81%			4-9	S_{26} 308 nm $f = 0.148$ 81%		

Table 4.6. NTOs representing singlet transitions responsible for the main absorption bands of complexes **4-1** – **4-10** in CH₂Cl₂. (continued)

$S_0 \rightarrow S_n$	Hole	Electron	$S_0 \rightarrow S_n$	Hole	Electron
S ₄₂ 259 nm $f = 0.194$ 65%			S ₃₆ 288 nm $f = 0.257$ 63%		
4-5 S ₃₅ 276 nm $f = 0.185$ 69%			S ₄₃ 279 nm $f = 0.175$ 36%		
S ₃₆ 275 nm $f = 0.192$ 59%			23%		
22%			21%		
S ₃₇ 273 nm $f = 0.173$ 50%			4-10 S ₂₉ 325 nm $f = 0.123$ 55%		
28%			37%		
S ₃₉ 272 nm $f = 0.242$ 40%			S ₃₁ 318 nm $f = 0.478$ 74%		
22%			S ₄₃ 295 nm $f = 0.510$ 69%		

The DFT calculations indicated that the highest occupied molecular orbital (HOMO) → lowest unoccupied molecular orbital (LUMO) transition played the major role (68–70%; Table 4.7) in generating the S₁ excited state. Therefore, analyzing how structural modifications influenced the HOMO and LUMO energies became important. As the ground-state energy diagram (Figure 4.2) displayed, extending π -conjugation of the C^N ligand mainly influenced the HOMO,

especially when benzannulation occurred at the phenyl ring. The HOMO energy was also affected by the benzannulation site at the phenyl ring. When benzannulation occurred at the 3' and 4' positions, the HOMO of complex **4-7** was significantly raised, while destabilization of the HOMOs in complexes **4-5**, **4-6**, **4-9**, and **4-10** with benzannulation at the 4' and 5' or 5' and 6' positions was less pronounced.

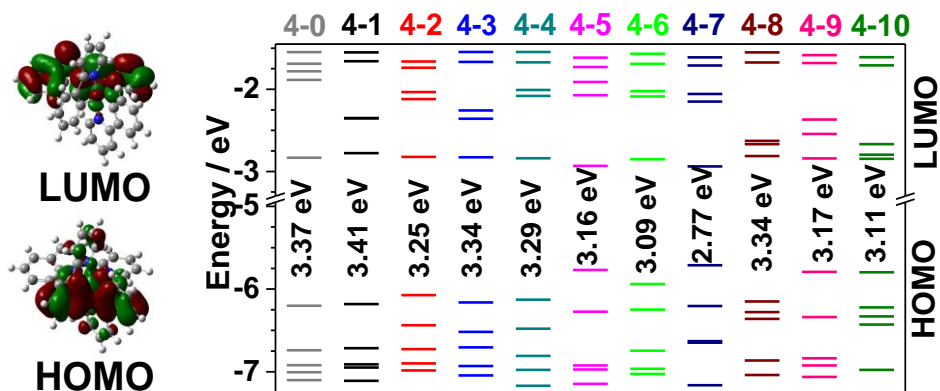


Figure 4.2. HOMO and LUMO plots for **4-0** and ground-state molecular orbital diagram for **4-0** – **4-10** in CH_2Cl_2 .

Table 4.7. Electron density distribution plots for HOMOs and LUMOs of complexes **4-1** – **4-10** in CH_2Cl_2 and the percentage contribution of the HOMO-LUMO transition to the S_1 excited state.

	HOMO	LUMO		HOMO	LUMO
4-1			4-6		
70%			70%		
4-2			4-7		
70%			70%		
4-3			4-8		
70%			68%		
4-4			4-9		
70%			70%		
4-5			4-10		
70%			69%		

In order to rationalize the effect of site-dependent benzannulation at the C[^]N ligands on the HOMO and LUMO energies, orbital symmetry analysis was applied. This method had been applied to benzannulation of the N[^]N[^]N ligand for platinum(II) complexes by Thompson/Gordon⁵⁶ and to benzannulation of the N[^]N ligand for iridium(III) complexes by our group²⁸ to successfully explain the observed site-dependent blue or red shift of the absorption and emission spectra. Here, it was applied to benzannulation at the C[^]N ligand of the iridium(III) complexes. In this method, benzannulation is viewed as the interactions between the FMOs of the parent compound and the FMOs of cis-1,3-butadiene or ethene. Because the HOMOs of the iridium(III) complexes studied are essentially localized on the C[^]N ligand and d orbital of the iridium(III) ion, benzannulation at the C[^]N ligand should mainly consider the interactions between the HOMO of the parent compound and the HOMO (and/or LUMO+1) or LUMO (and/or HOMO-1) of cis-1,3-butadiene (or ethene) depending on the orbital symmetry at the site of benzannulation.

As exemplified in Figure 4.3a, when benzannulation occurred at the 5 and 6 positions of the pyridyl ring of the parent complex **4-0**, the symmetry of HOMO at this position matched the symmetry of LUMO and HOMO-1 of cis-1,3-butadiene. However, because the HOMO-1 of cis-1,3-butadiene is more energetically close to the HOMO of **4-0** than the LUMO of cis-1,3-butadiene is, the HOMO-1 played the major role in interacting with the HOMO of **4-0**. Such an interaction gave rise to a slightly raised (0.02 eV) HOMO in complex **4-1** compared to that in the parent complex **4-0**. Meanwhile, the LUMO of **4-1** was destabilized by 0.05 eV, giving rise to a slightly enlarged HOMO-LUMO gap and consequently a minor hypsochromic shift of the S₁ state. In contrast, when benzannulation took place at the 4 and 5 positions of the pyridyl ring of complex **4-0**, the HOMO symmetry at this position matched the symmetry of the HOMO and LUMO+1 of

cis-1,3-butadiene (Figure 4.3b). Because of the much larger energy gap between the HOMO of complex **4-0** and the LUMO+1 of cis-1,3-butadiene, the HOMO of complex **4-0** predominantly interacted with the HOMO of 1,3-butadiene. This interaction raised the HOMO of complex **4-2** by 0.13 eV, while the LUMO energy of **4-2** essentially remained the same (only an 0.01 eV increase). This narrowed the HOMO–LUMO gap and caused a slight bathochromic shift of the S₁ state in complex **4-2** compared to that in complex **4-0**.

The similar molecular orbital symmetry analysis on complexes **4-5** and **4-6** revealed that benzannulation at the 4' and 5' positions of the phenyl ring of the ppy ligand in complex **4-0** raised the HOMO energy of complex **4-5** by 0.22 eV as a result of the HOMO–HOMO–1 interaction (Figure 4.3c), while the HOMO–HOMO–1 interaction gave rise to a 0.26 eV increase of the HOMO in complex **4-6** (Figure 4.3d). However, the LUMO of **4-6** was 0.02 eV more stabilized than that of **4-5**, resulting in a more red-shifted S₁ state in **4-6** compared to that of **4-5**. The molecular orbital symmetry analyses for the other complexes were carried out, and the results are provided in Figures 4-4 – 4-7.

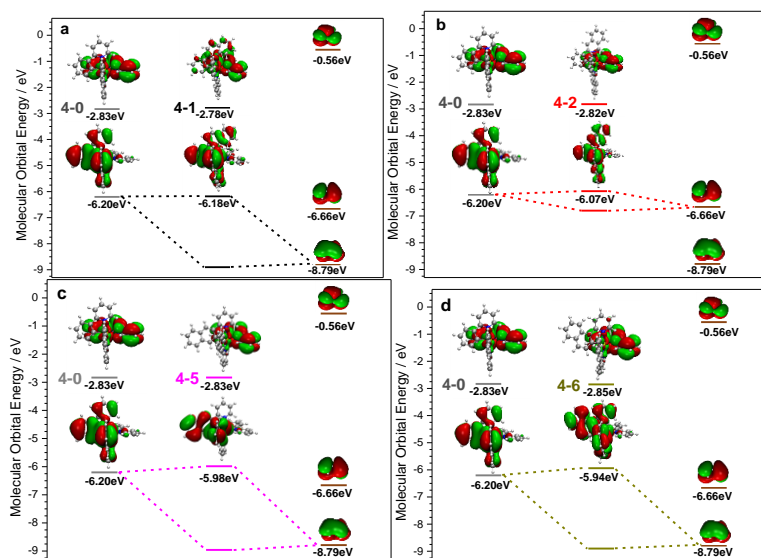


Figure 4.3. FMO mixing between the HOMO of the parent complex **4-0** and the HOMO–1 or HOMO of cis-1,3-butadiene to generate the FMOs of **4-1** (a), **4-2** (b), **4-5** (c), or **4-6** (d), respectively.

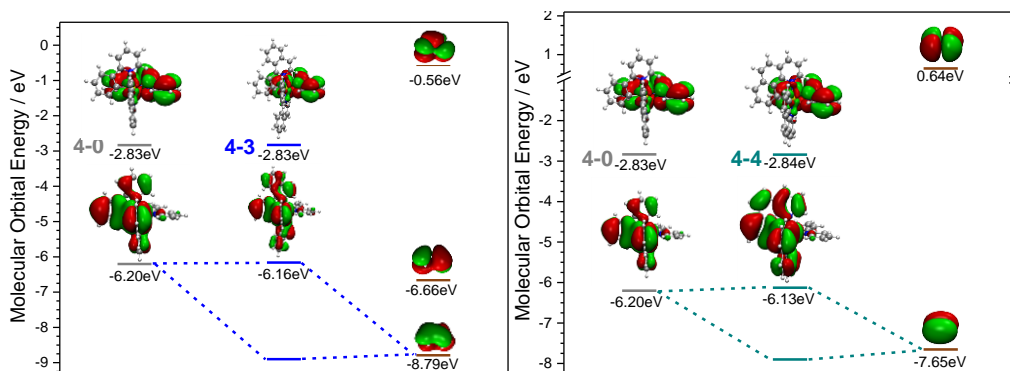


Figure 4.4. FMO mixing between the HOMO of the parent complex **4-0** and HOMO-1/LUMO of *cis*-1,3-butadiene or HOMO of ethane to generate the FMOs of **4-3** and **4-4**, respectively.

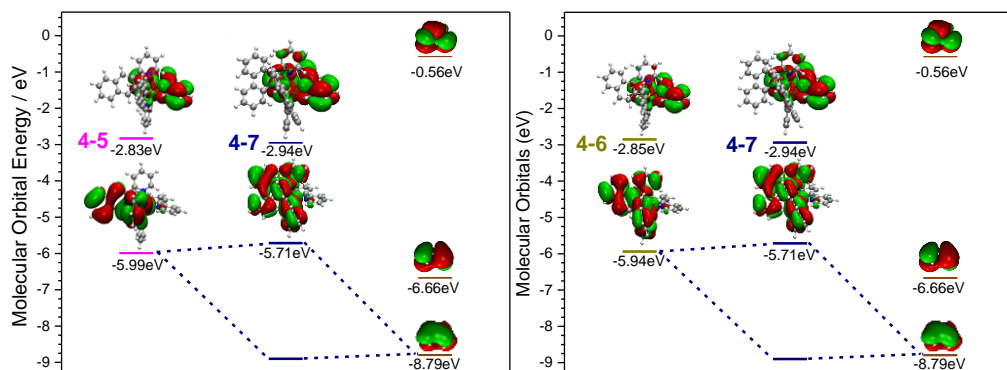


Figure 4.5. FMO mixing between the HOMO of the parent complex **4-5** or **4-6** and HOMO-1/LUMO or HOMO of *cis*-1,3-butadiene to generate the FMOs of **4-7**.

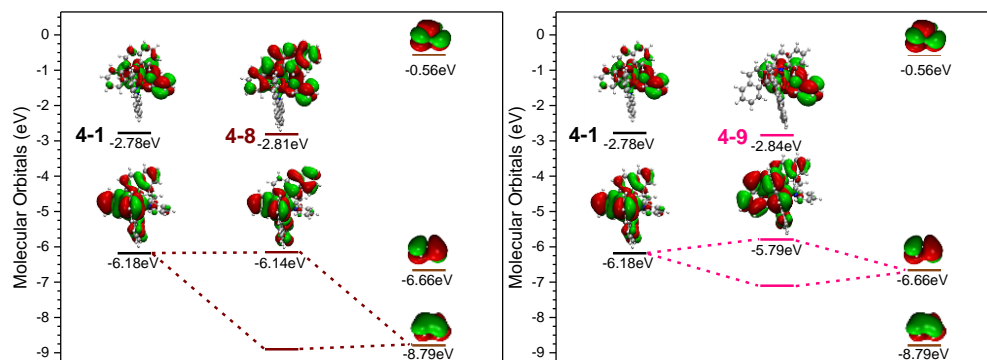


Figure 4.6. FMO mixing between the HOMO of the parent complex **4-1** and HOMO-1/LUMO of *cis*-1,3-butadiene to generate the FMOs of **4-8** and **4-9**.

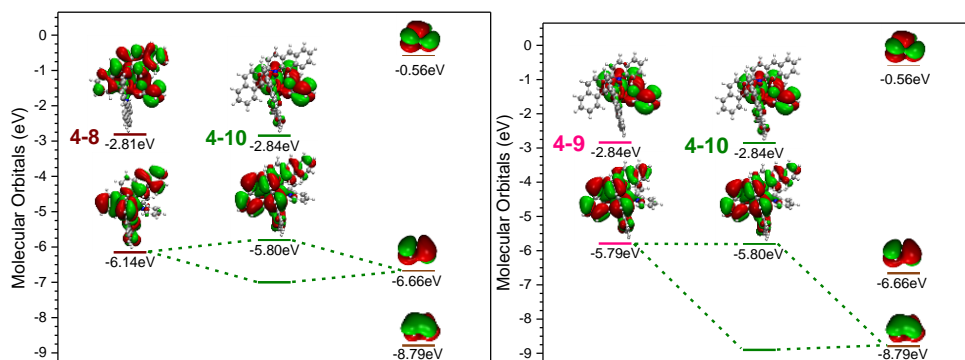


Figure 4.7. FMO mixing between the HOMO of the parent complex **4-8** or **4-9** and HOMO or HOMO-1/LUMO of cis-1,3-butadiene to generate the FMOs of **4-10**.

4.3.3. Photoluminescence

To understand the impacts of benzannulation at the different sites of the C^N ligand on the triplet excited states, the emission characteristics of **4-1** – **4-10** at room temperature in different solvents [CH₃CN, THF, CH₂Cl₂, and toluene (with 10% CH₂Cl₂)] were investigated because the emission of iridium(III) complexes typically originates from the triplet excited state. The emission spectra of **4-1** – **4-10** in CH₂Cl₂ are shown in Figure 4.8 and displayed in Figure 4.9 for the spectra in other solvents. The emission lifetimes and quantum yields are tabulated in Tables 4-2 and 4-8. A quick survey of these data revealed that the emissions band maxima of these complexes spanned from ca. 610 to 900 nm, which are drastically red-shifted with respect to their UV–vis absorption spectra. The emission was prone to quenching by oxygen, and the lifetimes varied from tens of nanoseconds to several microseconds. All of these features confirmed the phosphorescence nature of the emission from these complexes.

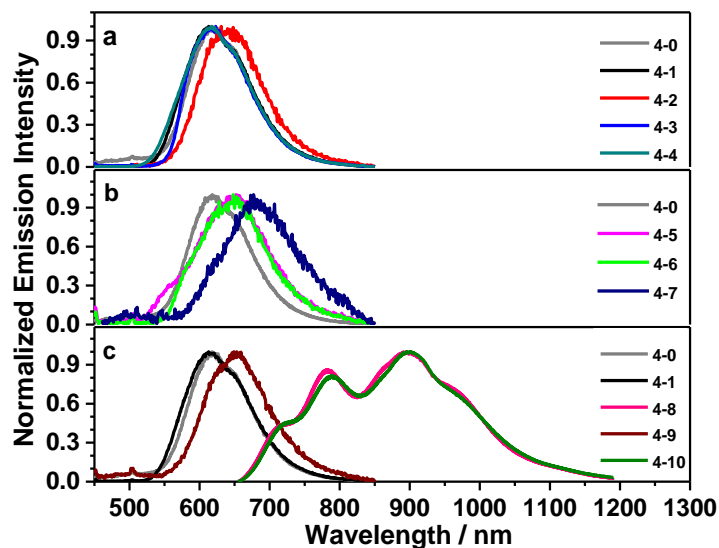


Figure 4.8. Experimental emission spectra of **4-1** – **4-10** at room temperature in dichloromethane. The spectra of **4-1** – **4-7** and **4-9** were measured on a HORIBA FluoroMax 4 fluorometer /phosphorometer with a Hamamatsu PMT R928 as the detector, while the spectra of **4-8** and **4-10** were detected with an InGaAs sensor from 670 to 1225 nm ($\lambda_{\text{ex}} = 473$ nm) with a 500 nm long pass filter.

The emission spectra of **4-1** – **4-7** and **4-9** were structureless, and their lifetimes were tens to hundreds of nanoseconds, which are the characteristics of CT emission. With reference to the emission of other iridium(III) complexes,^{23–33,54,55,57} the emitting states of these complexes are tentatively assigned to the ^3CT states ($^3\text{MLCT}/^3\text{LLCT}$). In contrast, the emission spectra of **4-8** and **4-10** were remarkably red-shifted compared to the other complexes and exhibited clear vibronic structures. Their lifetimes were 3–4 μs , which were almost 1–2 orders of magnitude longer than the other complexes. All of these features suggest that the emission of these two complexes emanates from the ligand-centered $^3\pi,\pi^*$ state.^{28,57} This assignment is supported by the solvent-dependent study and by the TDDFT calculation results being discussed *vide infra*.

The emission characteristics of complexes **4-1** – **4-10** in different solvents are depicted in Figure 4.9 and Table 4.8. Complexes **4-1** – **4-7** and **4-9** generally exhibited somewhat more solvent dependence than complexes **4-8** and **4-10** did, which is in line with the predominant ^3CT attribution for the emission of **4-1** – **4-7** and **4-9** and $^3\pi,\pi^*$ emission for **4-8** and **4-10**. The TDDFT calculation

results further supports these assignments. As the NTOs in Table 4.8 displayed, the holes in **4-1** – **4-7** and **4-9** were primarily localized on the C[^]N ligands and one of the d orbitals of the iridium(III) ion, while the electrons were on the N[^]N ligand and a different d-orbital of the iridium(III) ion. Thus, the emitting states of **4-1** – **4-7** and **4-9** possess predominantly ³MLCT/³LLCT transitions. In contrast, for complexes **4-8** and **4-10**, both the electrons and holes were exclusively distributed on the benzo[g]quinoline (bq) moiety of one of the C[^]N ligands and on the d orbital. This indicates a predominant ³ π,π^* character in the emitting states of **4-8** and **4-10**. The spin-density distributions shown in Table 4.9 for these complexes agree well with the NTOs representing the excitation from S₀ to T₁.

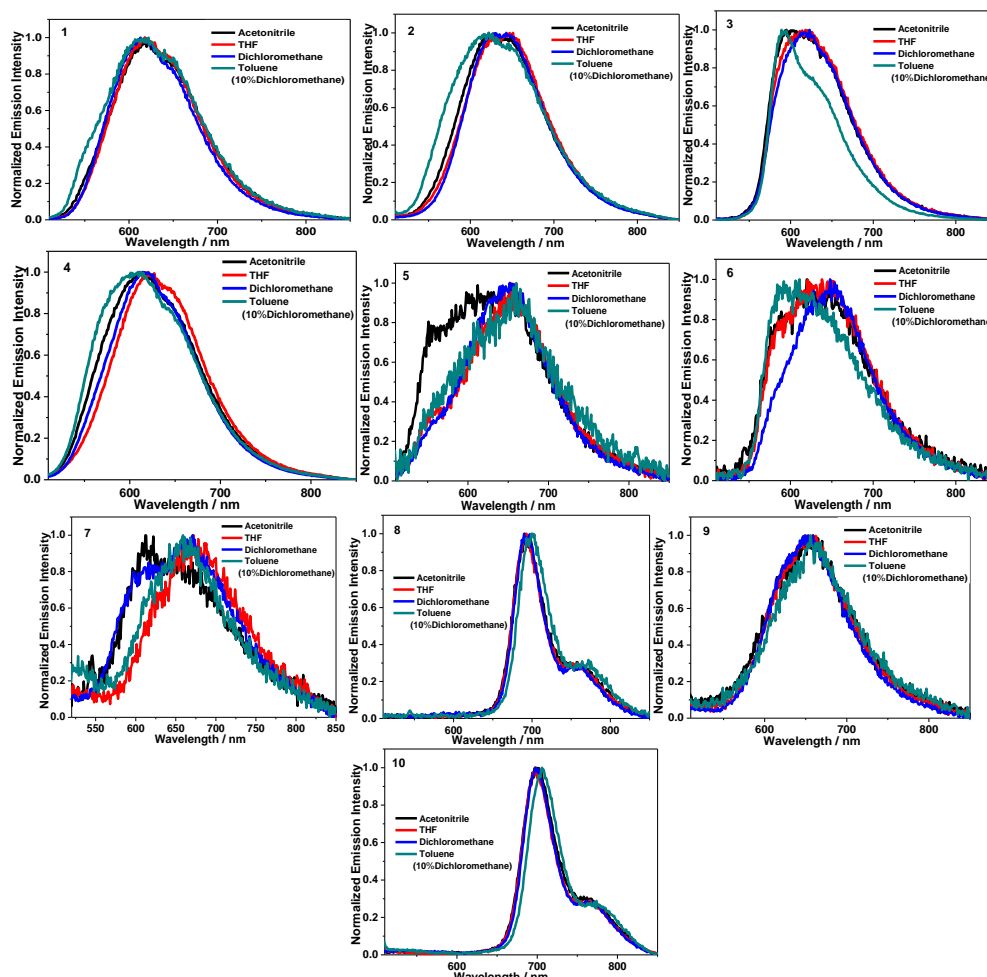


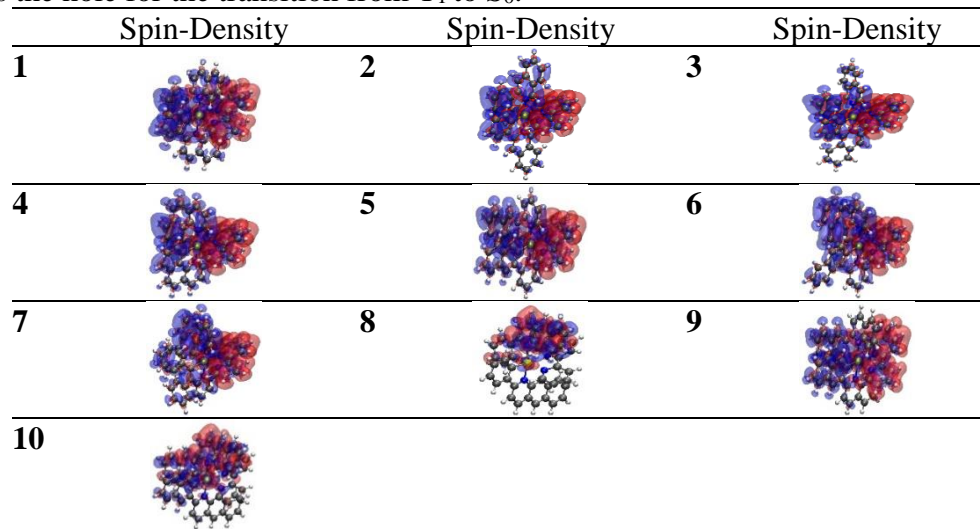
Figure 4.9. Normalized emission spectra of **4-1** – **4-10** (1–10) in different solvents ($\lambda_{ex} = 436$ nm).

Table 4.8. Emission characteristic of complexes **4-1** – **4-10** in different solvents at room temperature.^a

	λ_{em}/nm ($\tau_{em}/\mu s$); Φ_{em}			
	Acetonitrile	THF	Dichloromethane	Toluene ^b
4-1	618 (0.30); 0.033	618 (0.36); 0.047	613 (0.52); 0.075	622 (0.18); 0.042
4-2	623 (0.12); 0.019	646 (0.11); 0.019	642 (0.16); 0.033	620 (0.15); 0.016
4-3	608 (0.34); 0.045	615 (0.31); 0.042	618 (0.31); 0.110	593 (1.07); 0.150
4-4	610 (0.14); 0.025	623 (0.15); 0.032	615 (0.27); 0.070	606 (0.16); 0.041
4-5	610 (0.04); 0.011	655 (0.04); 0.012	650 (0.07); 0.020	661 (0.02); 0.010
4-6	620 (0.04); 0.011	637 (0.04); 0.017	649 (0.08); 0.024	604 (0.03); 0.012
4-7	613 (0.03); 0.001	673 (0.03); 0.001	663 (0.06); 0.002	658 (0.03); 0.002
4-8	693 (2.66); 0.011	691 (3.28); 0.015	693 (3.11); 0.015	700 (1.86); 0.012
4-9	655 (0.06); 0.009	655 (0.09); 0.013	649 (0.13); 0.019	656 (0.05); 0.011
4-10	700 (3.70); 0.005	697 (4.35); 0.007	699 (4.33); 0.009	706 (0.20); 0.005

^a Ru(bpy)₃Cl₂ in acetonitrile was used as the reference ($\lambda_{ex} = 436$ nm, $\Phi_{em} = 0.097$) for the emission quantum yield measurements. The quantum yield for **4-8** and **4-10** are for the emission in the region of 700-850 nm detected by the Hamamatsu photomultiplier tube (PMT) R928. ^b With 10% CH₂Cl₂.

Table 4.9. Spin-density for the single and triplet SCF calculations for **4-1** – **4-10**. The red translucent isosurface represents the electron distribution, whereas the blue translucent isosurface represents the hole for the transition from T₁ to S₀.

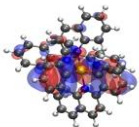
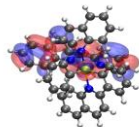
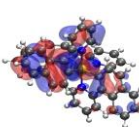
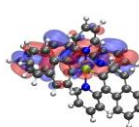
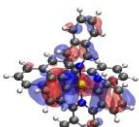
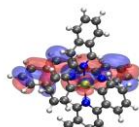
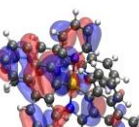
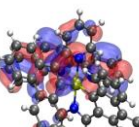
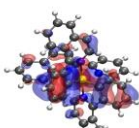
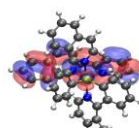
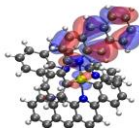
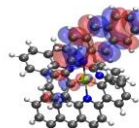
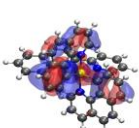
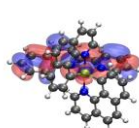
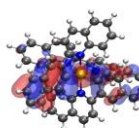
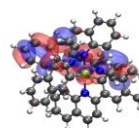
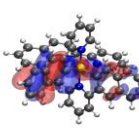
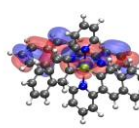
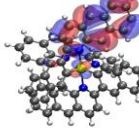
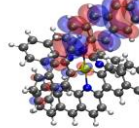


Examination of the emission energies, lifetimes, and quantum yields of **4-1** – **4-10** found that benzannulation at the phenyl ring of the ppy or **L4-1** ligand caused a red shift of the emission spectra in **4-5** – **4-7** and **4-9**, with shorter emission lifetimes and lower emission quantum yields

compared to complexes **4-1** – **4-4** with benzannulation at the pyridyl ring of the ppy ligand. The reduced emission lifetime and quantum yield are the results of increased nonradiative decay when the emitting state is lowered, which follows the energy gap law.^{58,59} In contrast, although the emission energies of complexes **4-8** and **4-10** were dramatically red-shifted compared to the other complexes, their lifetimes were much longer than those of the other complexes. This is attributed to the parentage change of the emission in these two complexes compared to the others. The trend of the emission energy variation of **4-1** – **4-10** is also in accordance with that observed for the S₁ state transitions despite the fact that the nature of the emitting states of **4-8** and **4-10** changed to ³ π,π states. In addition to the aforementioned site-dependent effects of benzannulation at the phenyl versus pyridyl ring, the emission energy was also found to depend on the benzannulation position at the phenyl or pyridyl ring. Among the four complexes **4-1** – **4-4** with benzannulation at the pyridyl ring, complex **4-2**, which has benzannulation at the 4 and 5 positions of the pyridyl ring of the ppy ligand, showed a ~20 nm red shift of the emission maximum compared to the parent complex **4-0** and the other three complexes **4-1**, **4-3**, and **4-4**. For the three complexes **4-5** – **4-7** with benzannulation at the phenyl ring of the ppy ligand, benzannulation at either the 4' and 5' or 5' and 6' positions of the phenyl ring caused red shifts (~37 nm) of the emission in **4-5** and **4-6** compared to that in complex **4-0**. Benzannulation at both the 3' and 4' and 5' and 6' positions of the phenyl ring of the ppy ligand induced a further 14 nm red shift in **4-7** with respect to those in **4-5** and **4-6**. However, fusion of the naphthyl motif to the 5 and 6 positions of the pyridyl ring of the ppy ligand completely changed the emitting states in **4-8** and **4-10** to the bq-localized ³ π,π^* state (see the NTOs in Table 4.10, in which both the holes and electrons for **4-8** and **4-10** were exclusively on the bq motif). When the bq-localized ³ π,π^* state became the emitting triplet excited state in **4-8** and **4-10**, benzannulation at the phenyl ring of the C[^]N ligand did not impact the

emission energy. It is worth noting that, even though complexes **4-7** – **4-9** had the same number of aromatic rings in their C^N ligands, their emission characteristics were drastically different. This provided another piece of evidence manifesting the significant impact of the benzannulation site at the C^N ligand on the photophysics of the iridium(III) complexes.

Table 4.10. NTOs representing the triplet transitions contributing to the emission of complexes **4-1** – **4-10** in CH₂Cl₂^a. The NTOs were calculated by TDDFT using the triplet minimum-energy geometry optimized by unrestricted DFT as described in the quantum chemistry calculations section.

	T ₁ / nm	Hole	Electron		T ₁ / nm	Hole	Electron
4-1	619 99%			4-6	724 98%		
4-2	688 99%			4-7	841 98%		
4-3	642 99%			4-8	1176 100%		
4-4	658 99%			4-9	745 98%		
4-5	693 100%			4-10	1196 97%		

4.3.4. TA

Nanosecond TA spectroscopy is a powerful technique to investigate the triplet excited-state properties, such as the triplet excited-state absorption, triplet lifetime, and quantum yield. In

this work, the TA measurements of complexes **4-1** – **4-10** were carried out in CH₃CN to further understand their triplet excited-state characteristics. CH₃CN was chosen as the solvent for the TA study rather than CH₂Cl₂ because of the better stability of the complexes in CH₃CN than in CH₂Cl₂ upon 355 nm laser excitation. The TA spectra of **4-1** – **4-10** at zero delay after excitation and the time-resolved spectra for complexes **4-1** – **4-3**, **4-5**, **4-8**, and **4-10** are shown in Figure 4.10, and the time-resolved TA spectra for complexes **4-4**, **4-6**, **4-7**, and **4-9** are provided in Figure 4.11. The triplet excited-state lifetimes (τ_{TA}) are tabulated in Table 4.2. The τ_{TA} values of these complexes were similar to their emission lifetimes in CH₃CN (Table 4.8), implying that the observed TA originated from the emitting excited states.

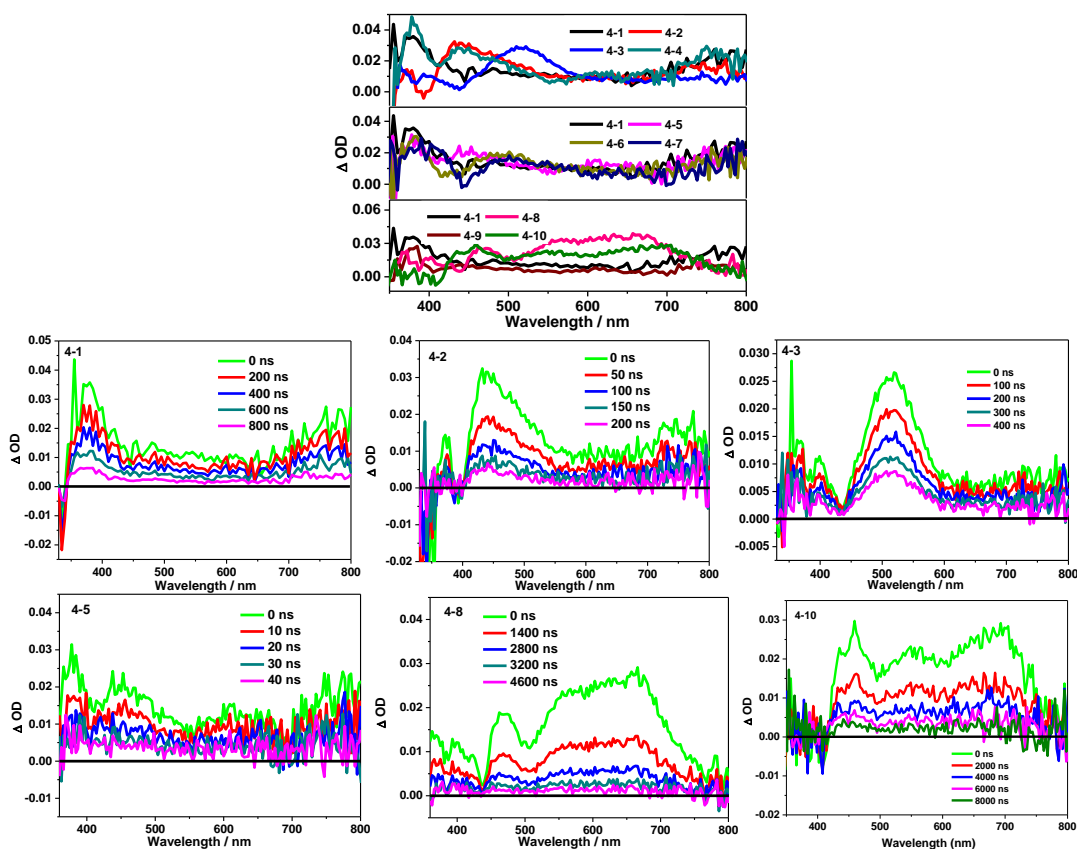


Figure 4.10. Comparison of the nanosecond TA difference spectra of complexes **4-1** – **4-10** in a CH₃CN solution immediately after laser excitation (the top figure) and the time-resolved TA spectra of complexes **4-1** – **4-3**, **4-5**, **4-8**, and **4-10** in CH₃CN ($\lambda_{ex} = 355$ nm; $A_{355} = 0.4$ in a 1 cm cuvette).

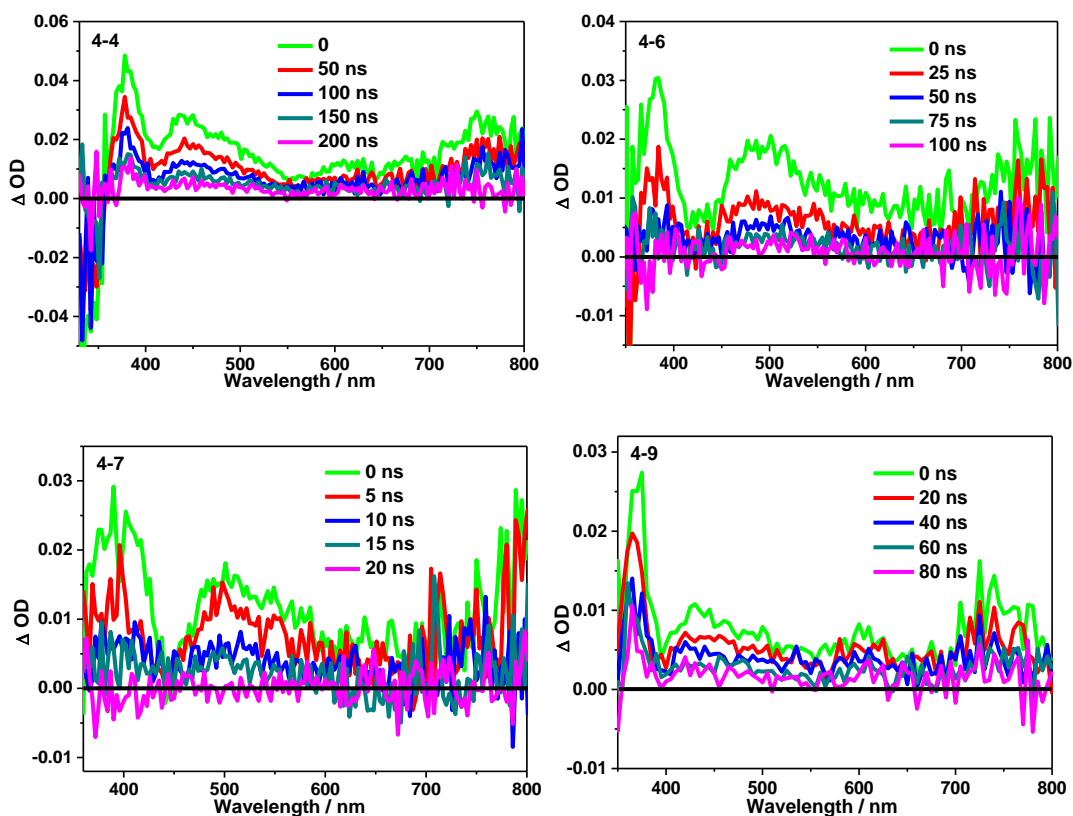


Figure 4.11. Nanosecond time-resolved transient difference absorption spectra of **4-4**, **4-6**, **4-7**, and **4-9** in acetonitrile. $\lambda_{\text{ex}} = 355 \text{ nm}$, $A_{355} = 0.4$ in a 1-cm cuvette.

The TA spectra of **4-1** – **4-10** essentially possessed positive absorption bands in the entire 360–800 nm region, except for very narrow and weak ground-state bleaching band being observed for **4-2** in 386–392 nm, **4-7** in 440–448 nm, and **4-10** in 386–417 nm. For the four complexes **4-1** – **4-4** with benzannulation at the pyridyl ring of the ppy ligand, the TA band maxima of **1–3** gradually bathochromically shifted. While the TA spectrum of **4-4** resembled that of **4-2**, the relative intensities of the two bands were different. The maximum TA band of **4-2** was at 432 nm, while the maximum intensity band appeared at 377 nm in **4-4** (Figure 4.10). For complex **4-3**, its TA spectrum resembled that of its corresponding iridium(III) dimeric precursor $[\text{Ir}(\text{piq})_2\text{Cl}]_2$.²⁹ In view of the structural difference among **4-1** – **4-4** and the different shapes of their TA spectra, it is reasonable to speculate that the observed TA of these complexes could be related to the difference in the heteroatom-containing motif. The similarity between the TA spectra of **4-3** and

its precursor $[\text{Ir}(\text{piq})_2\text{Cl}]_2$ complex also implies that the TA spectra of these complexes are indeed associated with the complexed C^N ligand.

The three complexes **4-5** – **4-7** with benzannulation at the phenyl ring of the ppy ligand exhibited similar TA spectral features with very short lifetimes. Their TA spectra all consisted of a strong but narrow band below 400 nm, a broader but weaker band at 450nm for **4-5** and ca. 500nm for **4-6** and **4-7**, and an emerging near-IR (NIR) band around 800 nm (Figure 4.10). A comparison of the TA spectrum of **4-9** to that of **4-1** (Figure 4.10) revealed similar spectral features, but **4-9** had a much shorter lifetime. The similar spectral features seemed to be related to the identical quinoline motifs in the C^N ligand, while the shorter lifetime appeared to be a common feature when benzannulation occurred at the phenyl ring of the ppy ligand (similar to the shorter lifetimes observed in complexes **4-5** – **4-7**). Additional evidence to support the association of the TA spectrum with the heteroatom-containing aromatic motif came from the TA spectra of **4-8** and **4-10**. The TA spectra of these two complexes were similar to each other and consistent with that of their dimeric iridium(III) precursor complex $[\text{Ir}(\text{pbq})_2\text{Cl}]_2$ (pbq refers to the 2-phenylbenzo[g]quinoline ligand) and the other iridium(III) complex bearing the same pbq ligand.²⁹

Combining the TA and emission studies on complexes **4-1** – **4-10**, we discovered that benzannulation at the phenyl ring of ppy mainly affected the lowest triplet excited-state energy and lifetime, whereas benzannulation at the pyridyl ring mainly impacted the spectral feature of TA. Especially, fusion of the naphthyl group to the pyridyl ring switched the lowest-energy triplet excited state to the bq motif of the C^N ligand, which gave rise to much stronger TA in the red spectral regions.

4.3.5. RSA

To demonstrate that benzannulation at the C^N ligand influences not only the photophysics of the Ir(III) complexes, but also their potential applications, the reverse saturable absorptions (RSA) of complexes **4-1** – **4-10** in CH₃CN solutions were investigated. RSA is a nonlinear optical phenomenon in which the absorptivity of the material increases with increased incident fluence. RSA is closely related to the ground and excited state absorptions. The inherent reason for RSA is that the excited-state absorption is stronger than the ground-state absorption of the absorber.⁶⁰⁻
⁶³ In the past one decade, our group and other groups chose Ir(III) complexes as candidate materials for RSA because the rapid intersystem crossing induced by the heavy Ir(III) ion helps populating the triplet excited state. This property along with many closely-spaced triplet excited state present in Ir(III) complexes induce considerably wide and strong excited-state absorption.^{12,13,20-22,24,25,27,29,30,31,33,50} For lasers with pulse width longer than the intersystem crossing time, the triplet excited state is populated primarily instead of the singlet excited state. In such a case, compounds with a higher triplet quantum yield, a strong excited-state absorption with respect to ground-state absorption, and a longer triplet excited-state lifetime are ideal candidates for RSA.

The positive TA spectra of complexes **4-1** – **4-10** (Figure 4.10) imply that all complexes possess stronger excited-state absorption than the ground-state absorption in the visible and NIR spectral region. They also have longer triplet excited- state lifetimes (Table 4.2) than the nanosecond laser pulse width (4.1 ns). Therefore, RSA of **4-1** – **4-10** is expected to occur at 532 nm for the 4.1-ns laser pulses. RSA was demonstrated for complexes **4-1** – **4-10** in a CH₃CN solution with an identical linear transmittance of 80% in a 2 mm cuvette at 532 nm for an easy comparison of the RSA strength. With the same linear transmission at 532 nm, the same number of molecules would be excited to the singlet excited state. Then the degree of RSA would be

determined by the degree of triplet excited- state absorption, which is a composite of the triplet excited- state quantum yield and the excited-state absorption cross section. As shown in Figure 4.12, complexes **4-1** – **4-10** all exhibited strong RSA. The strength of RSA decreased in the order of **4-3** > **4-7** \approx **4-4** \approx **4-9** \approx **4-6** > **4-8** \approx **4-1** \approx **4-2** \approx **4-5** > **4-10**, which are related to their ground-state absorption cross sections (σ_0 values; Table 4.11) and ΔOD values at 532 nm (Table 4.11).

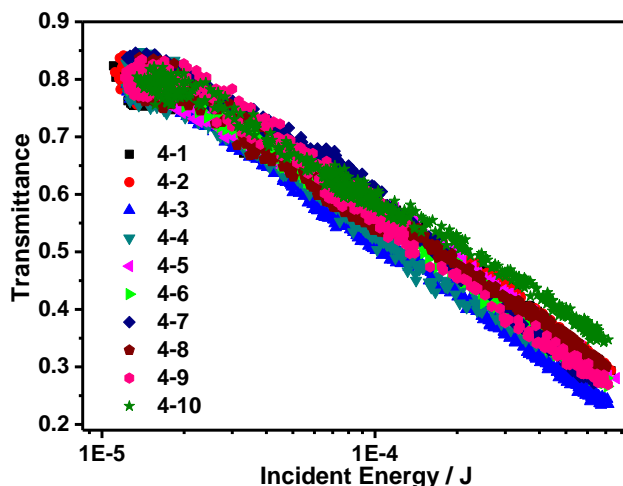


Figure 4.12. Nonlinear transmission plots of **4-1** – **4-10** at 80% linear transmittance in a 2-mm cuvette in CH_3CN solutions for 532 nm 4.1 ns laser pulses.

Table 4.11. Ground-state absorption cross sections (σ_0) and ΔOD values of **4-1** – **4-10** in CH_3CN at 532 nm

	4-1	4-2	4-3	4-4	4-5	4-6	4-7	4-8	4-9	4-10
$\sigma_0/10^{-18} \text{ cm}^2$	3.0	1.8	2.5	2.3	2.5	4.6	4.4	5.0	3.5	7.4
$\Delta OD/10^{-2}$	1.0	1.4	2.8	1.1	1.2	1.5	1.3	2.4	0.6	1.9

A key parameter for assessing the strength of RSA is the ratio of the excited-state absorption cross section to that of the ground state ($\sigma_{\text{ex}}/\sigma_0$). The σ values can be obtained by converting the ε values at 532 nm according to the equation $\sigma = 2303\varepsilon/N_A$ (N_A = Avogadro's constant). The ground-state molar extinction coefficient (ε_0) was readily deduced from the UV–vis absorption spectra. However, the ε_{ex} values at 532 nm were unable to be obtained because of the lack of obvious bleaching bands in most of the complexes. Consequently, a singlet depletion

method⁶⁴ was unable to be used to deduce the ϵ_{ex} values. Nonetheless, the ΔOD values obtained from the TA measurement reflected the absorbance difference between the excited- and ground-state absorptions at a given wave-length. Complex **4-3** possessed one of the smallest ground-state absorption cross sections but the largest ΔOD value at 532 nm, implying the strongest excited-state absorption among this series of complexes. As a result, **4-3** gave rise to the strongest RSA at 532 nm. For complex **4-10**, although the ΔOD value was the third largest, its largest σ_0 value among this series of complexes counterplayed its excited-state absorption and decreased its RSA. Although the RSA strengths of these complexes were affected by the ligand structural variations, overall this series of complexes all exhibited quite strong RSA for nanosecond laser pulses at 532 nm.

4.4. Conclusion

We have synthesized 10 cationic iridium(III) 2-(pyridin-2-yl)quinoline complexes bearing cyclometalating C^N ligands with different degrees of π -conjugation via benzannulation at different positions of the phenyl and/or pyridyl ring. Their site-dependent electronic absorption and emission characteristics were systematically investigated. Benzannulation on the phenyl ring of the C^N ligand raised the HOMO energies in complexes **4-5 – 4-7**, **4-9**, and **4-10** pronouncedly and thus lowered the energies of the S₁ states in these complexes. In contrast, benzannulation on the pyridyl ring of the C^N ligand showed minor effects on the HOMOs of **4-1**, **4-3**, **4-4**, and **4-8**, except for the fact that the HOMO of **4-2** was destabilized. This trend was followed by the triplet emission in all complexes other than **4-8**, with the emission spectra of complexes **4-2** and **4-5 – 4-10** being red-shifted and those of **4-1**, **4-3**, and **4-4 – 4-4** remaining similar to that of the parent complex **4-0**. Accompanying the decreased emission energies in **4-2**, **4-5 – 4-7**, and **4-9**, the emission lifetimes and quantum yields of these complexes were significantly shortened or

decreased, which was consistent with the energy gap law. However, further extending the π conjugation at the pyridyl ring of the C^N ligand in **4-8** and **4-10** changed the parentage of the lowest triplet excited state from the ³MLCT/³LLCT states in the other complexes to the bq-originated ³ π,π^* states, which prolonged the emission lifetimes in these two complexes. It appeared that benzannulation at the phenyl ring of the C^N ligand mainly influenced the lowest singlet and triplet excited-state energies and the triplet lifetimes but did not affect the triplet excited-state absorption spectral feature pronouncedly.

On the contrary, fusion of only one phenyl ring on the pyridyl group of the C^N ligand, in most cases, did not influence the singlet and triplet excited-state energies noticeably but significantly impacted the triplet excited-state absorption spectral feature. Fusion of the naphthyl group to the pyridyl ring completely changed the nature of the lowest triplet excited state, causing drastic changes in the emission and triplet excited-state absorption characteristics. The changes in the ground-state and triplet excited-state absorptions consequently affected the RSA in these complexes, although all of the studied complexes exhibited strong RSA for nanosecond laser pulses at 532 nm. The conclusion drawn from this work could shed light on the rational design of monocationic iridium(III) complexes with predetermined photophysical properties.

4.5. References

- ¹ Jung, Y.; Lippard, S. J. *Chem. Rev.* **2007**, *107*, 1387.
- ² You Y.; Nam W. *Chem. Soc. Rev.* **2012**, *41*, 7061.
- ³ Fan, C.; Yang, C. L. *Chem. Soc. Rev.* **2014**, *43*, 6439.
- ⁴ Liang, A. H.; Zhang, K.; Zhang, J.; Huang, F.; Zhu, X. H.; Cao, Y. *Chem. Mater.* **2013**, *25*, 1013.

- ⁵ Nazeeruddin, M. K.; Wegeh, R. T.; Zhou, Z.; Klein, C.; Wang, Q.; De Angelis, F.; Fantacci, S.; Grätzel, M. *Inorg. Chem.* **2006**, *45*, 9245.
- ⁶ He, L.; Qiao, J.; Duan, L.; Dong, G.; Zhang, D.; Wang, L.; Qiu, Y. *Adv. Funct. Mater.* **2009**, *19*, 2950.
- ⁷ Costa, R. D.; Ortí, E.; Bolink, H. J.; Monti, F.; Accorsi, G.; Armaroli, N. *Angew. Chem. Int. Ed.* **2012**, *51*, 8178.
- ⁸ Tang, S.; Pan, J.; Buchholz, H. A.; Edman, L. *J. Am. Chem. Soc.* **2013**, *135*, 3647.
- ⁹ Zhao, J.; Ji, S.; Guo, H. *RSC Adv.* **2011**, *1*, 937.
- ¹⁰ Duan, P.; Yanai, N.; Kimizuka, N. *Chem. Commun.* **2014**, *50*, 13111.
- ¹¹ Lo, K. K.-W. *Acc. Chem. Res.* **2015**, *48*, 2985.
- ¹² Li, Y.; Dandu, N.; Liu, R.; Li, Z.; Kilina, S.; Sun, W. *J. Phys. Chem. C* **2014**, *118*, 6372.
- ¹³ Li, Y.; Dandu, N.; Liu, R.; Hu, L.; Kilina, S.; Sun, W. *ACS Appl. Mater. Interfaces.* **2013**, *5*, 6556.
- ¹⁴ Massue, J.; Olesiak-Banska, J.; Jeanneau, E.; Aronica, C.; Matczyszyn, K.; Samoc, M.; Monnereau, C.; Andraud, C. *Inorg. Chem.* **2013**, *52*, 10705.
- ¹⁵ Ho, C.-L.; Wong, K.-L.; Kong, H.-K.; Ho, Y.-M.; Chan, C. T.-L.; Kwok, W.-M.; Leung, K. S.-Y.; Tam, H.-L.; Lam, M. H.-W.; Ren, X.-F.; Ren, A.-M.; Feng, J.-K.; Wong, W.-Y. *Chem. Commun.* **2012**, *48*, 2525.
- ¹⁶ Yuan, Y.-J.; Zhang, J.-Y.; Yu, Z.-T.; Feng, J.-Y.; Luo, W.-J.; Ye, J.-H.; Zou, Z.-G. *Inorg. Chem.* **2012**, *51*, 4123.
- ¹⁷ Okada, S.; Okinaka, K.; Iwawaki, H.; Furugori, M.; Hashimoto, M.; Mukaide, T.; Kamatani, J.; Igawa, S.; Tsuboyama, A.; Takiguchi, T.; Ueno, K. *Dalton Trans.* **2005**, *9*, 1583.

- 18 Nazeeruddin, Md. K.; Wegeh, R. T.; Zhou, Z.; Klein, C.; Wang, Q.; Angelis, F. De; Fantacci, S.; Graetzel; M. *Inorg. Chem.* **2006**, *45*, 9245.
- 19 Sunesh, C. D.; Mathai, G.; Choe, Y. *ACS Appl. Mater. Interfaces* **2014**, *6*, 17416.
- 20 Zhu, X.; Lystrom, L.; Kilina, S.; Sun, W. *Inorg. Chem.* **2016**, *55*, 11908.
- 21 Zhu, X.; Cui, P.; Kilina, S.; Sun, W. *Inorg. Chem.* **2017**, *56*, 13715.
- 22 Li, Y.; Dandu, N.; Liu, R.; Kilina, S.; Sun, W. *Dalton Trans.* **2014**, *43*, 1724.
- 23 Zhao, Q.; Liu, S. J.; Shi, M.; Wang, C. M.; Yu, M. X.; Li, L.; Li, F. Y.; Yi, T.; Huang, C. H. *Inorg. Chem.* **2006**, *45*, 6152.
- 24 Liu, R.; Dandu, N.; Chen, J.; Li, Y.; Li, Z.; Liu, S.; Wang, C.; Kilina, S.; Kohler, B.; Sun, W. *J. Phys. Chem. C* **2014**, *118*, 23233.
- 25 Li, Z.; Cui, P.; Wang, C.; Kilina, S.; Sun, W. *J. Phys. Chem. C* **2014**, *118*, 28764.
- 26 Zeng, X.; Tavasli, M.; Perepichka, I. F.; Batsanov, A. S.; Bryce, M. R.; Chiang, C.-J.; Rothe, C.; Monkman, A. P. *Chem. Eur. J.* **2008**, *14*, 933.
- 27 Kim, K.-Y.; Farley, R. T.; Schanze, K. S. *J. Phys. Chem. B* **2006**, *110*, 17302.
- 28 Liu, B.; Lystrom, L.; Kilina, S.; Sun, W. *Inorg. Chem.* **2017**, *56*, 5361.
- 29 Wang, L.; Cui, P.; Kilina, S.; Sun, W. *J. Phys. Chem. C* **2017**, *121*, 5719.
- 30 Pei, C.; Cui, P.; McCleese, C.; Kilina, S.; Burda, C.; Sun, W. *Dalton Trans.* **2015**, *44*, 2176.
- 31 Sun, W.; Pei, C.; Lu, T.; Cui, P.; Li, Z.; McCleese, C.; Fang, Y.; Kilina, S.; Song, Y.; Burda, C. *J. Mater. Chem. C* **2016**, *4*, 5059.
- 32 Wang, L.; Yin, H.; Cui, P.; Hetu, M.; Wang, C.; Monroe, S.; Schaller, R. D.; Cameron, C. G.; Liu, B.; Kilina, S.; McFarland, S. A.; Sun, W. *Dalton Trans.* **2017**, *46*, 8091.
- 33 Wang, C.; Lystrom, L.; Yin, H.; Hetu, M.; Kilina, S.; McFarland, S. A.; Sun, W. *Dalton Trans.* **2016**, *45*, 16366.

- ³⁴ Li, A. H.; Beard, D. J.; Coate, H.; Honda, A.; Kadalbajoo, M.; Kleinberg, A.; Laufer, R.; Mulvihill, K. M.; Nigro, A.; Rastogi, P.; Sherman, D.; Siu, K. W.; Steinig, A. G.; Wang, T.; Werner, D.; Crew, A. P.; Mulvihill, M. J. *Synthesis* **2010**, *10*, 1678.
- ³⁵ Yao, M.; Inoue, H.; Yoshioka, N. *Chem. Phys. Lett.* **2005**, *402*, 11.
- ³⁶ Zhao, Q.; Jiang, C. Y.; Shi, M.; Li, F. Y.; Yi, T.; Cao, Y.; Huang, C. H. *Organometallics* **2006**, *25*, 3631.
- ³⁷ Taffarel, E.; Chirayil, S.; Thummel, R. P. *J. Org. Chem.* **1994**, *59*, 823.
- ³⁸ Dhara, S.; Singha, R.; Nuree, Y.; Ray, J. K. *Tetrahedron Lett.* **2014**, *55*, 795.
- ³⁹ Sunesh, C. D.; Mathai, G.; Choe, Y. *ACS Appl. Mater. Interfaces* **2014**, *6*, 17416.
- ⁴⁰ Okada, S.; Okinaka, K.; Iwawaki, H.; Furugori, M.; Hashimoto, M.; Mukaide, T.; Kamatani, J.; Igawa, S.; Tsuboyama, A.; Takiguchi, T.; Ueno, K. *Dalton Trans.* **2005**, *9*, 1583.
- ⁴¹ Suzuki, K.; Kobayashi, A.; Kaneko, S.; Takehira, K.; Yoshihara, T.; Ishida, H.; Shiina, Y.; Oishi, S.; Tobita, S. *Phys. Chem. Chem. Phys.* **2009**, *11*, 9850.
- ⁴² Demas, J. N.; Crosby, G. A. *J. Phys. Chem.* **1971**, *75*, 991.
- ⁴³ Guo, F.; Sun, W.; Liu, Y.; Schanze, K. *Inorg. Chem.* **2005**, *44*, 4055.
- ⁴⁴ Frisch, M. J.; Trucks, G. W.; Schlegel, H. B.; Scuseria, G. E.; Robb, M. A.; Cheeseman, J. R.; Scalmani, G.; Barone, V.; Mennucci, B.; Peterson, G. A.; et. al. *Gaussian 09*, revision B.1; Gaussian, Inc.: Wallingford, CT, **2009**.
- ⁴⁵ Perdew, J. P.; Burke, K.; Ernzerhof, M. *Phys. Rev. Lett.* **1996**, *77*, 3865.
- ⁴⁶ Hay, P. J.; Wadt, W. R. *J. Chem. Phys.* **1985**, *82*, 270.
- ⁴⁷ Adamo, C.; Barone, V. *J. Chem. Phys.* **1999**, *110*, 6158.
- ⁴⁸ Barone, V.; Cossi, M.; Tomasi, J. *J. Comput. Chem.* **1998**, *19*, 404.
- ⁴⁹ Cossi, M.; Barone, V.; Cammi, R.; Tomasi, J. *Chem. Phys. Lett.* **1996**, *255*, 327.

- 50 Li, Z.; Li, H.; Gifford, B. J.; Peiris, W. D. N.; Kilina, S.; Sun, W. *RSC Adv.* **2016**, *6*, 41214.
- 51 Martin, R. L. Natural Transition Orbitals. *J. Chem. Phys.* **2003**, *118*, 4775.
- 52 Humphrey, W.; Dalke, A.; Schulten, K. *J. Mol. Graphics* **1996**, *14*, 33.
- 53 Dennington, R. II; Keith, T.; Millam, J. *GaussView*; Semichem Inc.: Shawnee Mission, KS, **2007**.
- 54 Wu, S. H.; Ling, J. W.; Lai, S. H.; Huang, M. J.; Cheng, C. H.; Chen, I. C. *J. Phys. Chem. A* **2010**, *114*, 10339.
- 55 Dragonetti, C.; Falciola, L.; Mussini, P.; Righetto, S.; Roberto, D.; Ugo, R.; Valore, A.; Angelis, F. D.; Fantacci, S.; Sgamellotti, A. *Inorg. Chem.* **2007**, *46*, 8533.
- 56 Hanson, K.; Roskop, L.; Djurovich, P. I.; Zahariev, F.; Gordon, M. S.; Thompson, M. E. *J. Am. Chem. Soc.* **2010**, *132*, 16247.
- 57 Constable, E. C.; Neuburger, M.; Rösel, P.; Schneider, G. E.; Zampese, J. A.; Housecroft, C. E.; Monti, F.; Armaroli, N.; Costa, R. D.; Ortí, E. *Inorg. Chem.* **2013**, *52*, 885.
- 58 Caspar, J. V.; Kober, E. M.; Sullivan, B. P.; Meyer, T. J. *J. Am. Chem. Soc.* **1982**, *104*, 630.
- 59 Caspar, J. V.; and Meyer, T. J. *J. Phys. Chem.* **1983**, *87*, 952.
- 60 Perry, J. W.; Mansour, K.; Marder, S. R.; Perry, K. J.; Alvarez, D.; Choong, I. *Opt. Lett.* **1994**, *19*, 625.
- 61 Li, C.; Zhang, L.; Yang, M.; Wang, H.; Wang, Y. *Phys. Rev. A* **1994**, *149*, 1149.
- 62 Zhou, G. J.; Wong W. Y. *Chem. Soc. Rev.* **2011**, *40*, 2541.
- 63 Sun, Y.-P.; Riggs, J. E. *Int. Rev. Phys. Chem.* **1999**, *18*, 43.
- 64 Carmichael, I.; Hug, G. L. *J. Phys. Chem. Ref. Data* **1986**, *15*, 1.

5. MONOCATIONIC IRIDIUM(III) COMPLEXES WITH FAR-RED CHARGE TRANSFER ABSORPTION AND NEAR-IR EMISSION: SYNTHESIS, PHOTOPHYSICS, AND REVERSE SATURABLE ABSORPTION

5.1. Introduction

In the past two decades, octahedral d^6 Ir(III) complexes have attracted a particular attention among chemists and materials scientists due to their high triplet excited-state quantum yield, synthetic versatility, and chemical stability.¹⁻⁴ The rich photophysical properties present in the Ir(III) complexes prompt their potential applications in phosphorescence-based organic light-emitting diodes (OLEDs),^{5,6} low-power upconversion,^{7,8} biomolecular labeling and imaging,^{9,10} photochemical water oxidation,^{11,12} photodynamic therapy (PDT)¹³⁻¹⁵, and nonlinear optics (NLO).^{16,17}

Among the different types of Ir(III) complexes, monocationic Ir(III) complexes featuring diimine (N[^]N) and cyclometalating (C[^]N) ligands are particularly interesting because of the facile synthesis under a mild condition. In addition, the absorption and emission characteristics of this type of complexes can be efficiently tuned via exploiting novel N[^]N and C[^]N ligands.¹⁸⁻²⁰ Based on the reported electrochemical and computational studies, electrons of the lowest unoccupied molecular orbitals (LUMO) of this type of complexes are typically distributed on the N[^]N ligand, whereas the electrons of the highest occupied molecular orbital (HOMO) are mainly delocalized on the C[^]N ligands and d -orbital of the metal center.²¹ Therefore, different N[^]N ligands mainly impact the energy of the LUMO, but have negligible effect on the energy of the HOMO.²² This effect makes it possible to readily tune the lowest-energy charge transfer absorption band corresponding to the HOMO→LUMO transition via alternation of the N[^]N ligand. Meanwhile,

the lowest triplet excited states (T_1 states) of the complexes can be altered simultaneously.²³ For this reason, tremendous efforts have been put on extending the synthetic scope of the $N^{\wedge}N$ ligands, with 2,2'-bipyridine (bpy) and its analogs being the most commonly explored one to date.²⁴⁻²⁶

Reverse saturable absorption (RSA) is a nonlinear optical phenomenon in which the reverse saturable absorbers exhibit a linear absorption at low incident laser fluence, while their absorptivity increases when the incident fluence increase. RSA occurs when the absorbance of the excited state of an absorber is stronger than that of the ground state at the corresponding wavelength. In order to facilitate RSA of nanosecond laser pulses, an absorber should have a weak ground state absorption to populate the excited states, but long-lived triplet excited states, large triplet-triplet excited-state absorption coefficients, and a high quantum yield for triplet excited-state formation. In recent years, the RSA of heavy transition-metal complexes, such as octahedral Ir(III) complexes, have been extensively explored by our group^{14,16,17,24,27-36} and other groups^{23,37-39} because these complexes displayed the aforementioned characteristics that well match the requirements for RSA. In addition, by structural modifications, both the ground-state and the excited-state properties can be readily tuned in these complexes for optimization of the RSA.

Although extensive work has been reported on Ir(III) complexes for RSA, challenges still exist in developing the Ir(III) complexes into broadband reverse saturable absorbers. Among which the lack of considerable ground-state absorption in the red to the NIR region remains to be one of the obstacles. In seeking solutions to red-shift the ground-state absorption, immense effects on exploring $N^{\wedge}N$ or $C^{\wedge}N$ ligands suitable for reverse saturable absorbers have been made by our group.^{14,16,17,24,27-36} We discovered that incorporation of quinoxaline or benzo[*g*]quinoxaline unit into either the $N^{\wedge}N$ or $C^{\wedge}N$ ligand red-shifted the spin-forbidden $^1,^3IL$ (intraligand) / $^1,^3CT$ (charge

transfer) absorption bands into longer wavelengths.^{14,30,35} However, the triplet excited-state lifetimes of these complexes were reduced to tens to hundreds of ns. On the other hand, we have reported that Ir(III) bipyridine complex bearing 1,2-diphenyl-9*H*-pyreno[4,5-*d*]imidazole (dppi) cyclometalating ligands displayed a long-lived strong triplet excited-state absorption in the spectral regions of 410 – 700 nm.²⁴

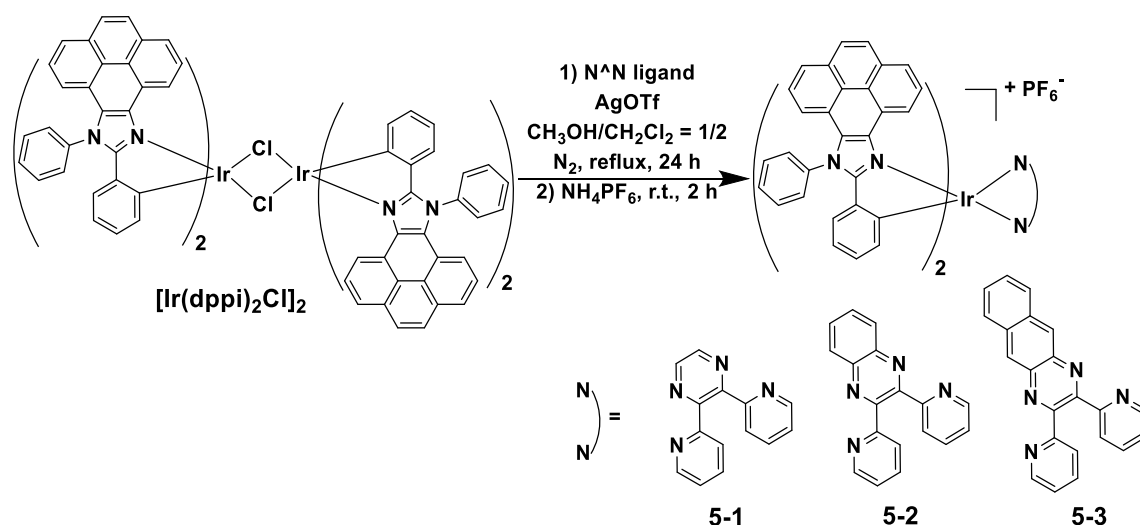
Inspired by these exploration, we combine these two approaches in one system, attempting to red-shift the ground-state absorption to the far-red / NIR regions and meanwhile keep a relatively long-lived and broadly absorbing triplet excited state. In this work, we synthesized and investigated three cationic Ir(III) complexes featuring dppi C[^]N ligands and pyrazine-based N[^]N ligands (structures shown in Scheme 1) as reverse saturable absorbers. The π -conjugation of the N[^]N ligands are gradually extended from **5-1** to **5-3** via benzannulation at the pyrazine unit to red-shift the ^{1,3}IL / ^{1,3}CT absorption bands. The diphyridylpyrazine (dpp) moiety would not only cause the red-shift of the ^{1,3}IL/^{1,3}CT absorption bands but also serve as a bridge to construct a supramolecular system that will be studied in the future. In addition to the spectroscopic studies on the photophysical properties of these complexes, density functional theory (DFT) calculation were performed to provide insight into the natures of the singlet and triplet states of these Ir(III) complexes. RSA of these complexes at 532 nm for ns laser pulses was demonstrated.

5.2. Experimental section

5.2.1. Materials and synthesis.

All chemicals and solvents were purchased from commercial sources and used as received without further purification. The ligands dpp (**L5-1**),⁴⁰ 2,3-di(2-pyridinyl)quinoxaline (**L5-2**),⁴¹ 2,3-di(2-pyridinyl)benzo[*g*]quinoxaline (**L5-3**),⁴² dppi,²⁵ and the Ir(III) dimer [Ir(dppi)₂Cl]₂,²¹

were prepared following the reported procedures. Column chromatography was carried out using silica gel (60 Å, 230–400 mesh) or Al₂O₃ (activated, neutral). The obtained complexes **5-1** – **5-3** were analyzed by ¹H NMR, high-resolution electrospray ionization mass spectrometry (ESI-MS), and elemental analysis. The ¹H NMR spectra were measured on Bruker-400 spectrometer in CDCl₃ using tetramethylsilane [Si(CH₃)₄] as the internal reference. High-resolution mass (HRMS) analyses were carried out on a Waters Synapt G2-Si mass spectrometer. Elemental analyses were performed by NuMega Resonance Laboratories, Inc. in San Diego, California.



Scheme 5-1. Synthetic route for Ir(III) complexes **5-1** – **5-3**.

5.2.2. General procedure for the synthesis of **5-1** – **5-3**

The [Ir(dppi)₂Cl]₂ dimer (61 mg, 0.03 mmol), corresponding N[∧]N ligand (0.06 mmol), and AgSO₃CF₃ (15 mg, 0.06 mmol) were added in the solvent (CH₂Cl₂:MeOH= 2:1 (v/v), 30 mL). The obtained mixture was degassed with N₂ for 30 minutes and then heated to reflux for 24 h. After cooling to room temperature, NH₄PF₆ (49 mg, 0.3 mmol) was added and stirred for another 2 hours. Solvent was then removed in vacuum. The residue was separated by column

chromatography on alumina gel, eluting with CH₂Cl₂/hexanes (3:1 to 1:0 (v/v)) to afford the target complex.

5-1. A red powder was obtained as the product (46 mg, 52%). ¹H NMR (400 MHz, CDCl₃) δ 8.86 (d, *J* = 2.9 Hz, 1H), 8.69 (d, *J* = 4.9 Hz, 1H), 8.59 (d, *J* = 2.9 Hz, 1H), 8.45 – 8.38 (m, 2H), 8.12 (q, *J* = 7.8 Hz, 1H), 8.09 – 7.85 (m, 18H), 7.85 – 7.78 (m, 1H), 7.73 – 7.63 (m, 2H), 7.59 (t, *J* = 7.9 Hz, 1H), 7.45 – 7.36 (m, 2H), 7.34 (d, *J* = 8.1 Hz, 1H), 7.32 – 7.27 (m, 2H), 7.21 (dd, *J* = 10.5, 3.2 Hz, 1H), 7.10 (td, *J* = 7.7, 1.7 Hz, 1H), 7.06 – 6.99 (m, 1H), 6.93 – 6.81 (m, 4H), 6.74 – 6.67 (m, 1H), 6.63 (dt, *J* = 5.0, 3.1 Hz, 1H), 6.47 (d, *J* = 8.1 Hz, 1H), 5.58 (d, *J* = 7.7 Hz, 1H). ESI–HRMS (*m/z*): calcd. for [C₇₂H₄₄N₈Ir]⁺, 1213.3325; found, 1213.3322. Anal. Calcd for C₇₂H₄₄F₆IrN₈P·6H₂O: C, 58.97; H, 3.85; N, 7.64. Found: C, 59.25; H, 3.97; N, 7.70.

5-2. A brownish powder was obtained as the product (47 mg, 54%). ¹H NMR (400 MHz, CDCl₃) δ 8.69 (d, *J* = 6.7 Hz, 2H), 8.41 (d, *J* = 7.1 Hz, 1H), 8.24 (d, *J* = 7.2 Hz, 1H), 8.20 – 8.08 (m, 4H), 8.08 – 7.78 (m, 12H), 7.79 – 7.64 (m, 4H), 7.64 – 7.58 (m, 1H), 7.55 (t, *J* = 7.9 Hz, 1H), 7.45 (d, *J* = 7.4 Hz, 1H), 7.39 – 7.29 (m, 4H), 7.25 – 7.15 (m, 2H), 7.09 (dd, *J* = 6.5, 4.9 Hz, 1H), 7.02 (td, *J* = 7.7, 0.5 Hz, 2H), 6.83 (ddd, *J* = 11.1, 9.0, 4.4 Hz, 4H), 6.78 – 6.72 (m, 1H), 6.71 – 6.66 (m, 1H), 6.34 (t, *J* = 7.8 Hz, 2H), 6.29 (d, *J* = 7.1 Hz, 1H), 5.67 (d, *J* = 7.8 Hz, 1H). ESI–HRMS (*m/z*): calcd. for [C₇₆H₄₆N₈Ir]⁺, 1263.3481; found, 1263.3477. Anal. Calcd for C₇₆H₄₆F₆IrN₈P·3H₂O: C, 63.19; H, 3.49; N, 7.76. Found: C, 62.99; H, 3.72; N, 7.40.

5-3. A brownish powder was obtained as the product (34 mg, 39%). ¹H NMR (CDCl₃, 400 MHz): δ 9.15–9.04 (m, 1H), 8.80–8.67 (m, 2H), 8.59 (s, 1H), 8.50–8.35 (m, 1H), 8.22 (d, *J* = 8.5 Hz, 1H), 8.17–7.88 (m, 12H), 7.89–7.61 (m, 7H), 7.60–7.51 (m, 3H), 7.49–7.38 (m, 2H), 7.33 (t, *J* = 7.8 Hz, 1H), 7.25–7.16 (m, 3H), 7.16–7.07 (m, 2H), 7.05–6.92 (m, 2H), 6.92–6.74 (m, 5H), 6.70 (dd, *J* = 8.0, 1.3 Hz, 1H), 6.20 (dd, *J* = 7.9, 0.9 Hz, 1H), 6.11 (t, *J* = 7.8 Hz, 1H), 5.39 (d, *J* =

7.7 Hz, 1H), 5.24 (d, $J = 8.0$ Hz, 1H). ESI–HRMS (m/z): calcd. for $[C_{80}H_{48}N_8Ir]^+$, 1313.3639; found, 1313.3652. Anal. Calcd for $C_{80}H_{48}F_6IrN_8P \cdot 0.7CH_2Cl_2$: C, 62.50; H, 3.26; N, 7.18. Found: C, 62.37; H, 3.41; N, 7.19.

5.2.3. Photophysical and nonlinear transmission measurements

The UV–vis absorption spectra of **5-1** – **5-3** were recorded on a Varian Cary 50 spectrophotometer. The emission spectra of **5-1** and **5-2** were recorded on a HORIBA FluoroMax-4 fluorometer/phosphorometer. A PTI Quantamaster equipped with a Hamamatsu R5509-42 near-infrared PMT was used to record the NIR emission spectrum of **5-3** in CH_2Cl_2 . The emission quantum yields were obtained in deaerated solutions using relative actinometry method,⁴³ with $[Ru(bpy)_3]Cl_2$ ($\Phi_{em} = 0.097$ in degassed acetonitrile solution, $\lambda_{ex} = 436$ nm)⁴⁴ being used as the reference for **5-1** and **5-2**, and IRF140 ($\Phi_{em} = 0.167$ in degassed ethanol solution, $\lambda_{ex} = 804$ nm)⁴⁵ for **5-3**. The nanosecond transient difference absorption (TA) spectra of **5-1** – **5-3** were measured on an Edinburgh LP920 laser flash photolysis spectrometer in acetonitrile solutions. The third–harmonic output (355 nm) of a Nd:YAG laser (Quantel Brilliant, 4.1 ns, the repetition rate was set to 1 Hz) was used as the excitation source. Each sample solution was degassed with nitrogen for 40 min. before the measurement. By using the singlet depletion method,⁴⁶ the triplet excited–state molar extinction coefficients (ϵ_T) of **5-1** – **5-3** at the TA band maxima were determined. The triplet excited–state quantum yields were then obtained using the relative actinometry method,⁴⁷ with the benzene solution of SiNc ($\epsilon_{590} = 70,000$ $M^{-1} cm^{-1}$, $\Phi_T = 0.20$)⁴⁸ being used as the reference. The setup and details of the nonlinear transmission measurement were the same as those reported earlier by our group.^{28,49}

5.2.4. Computational methodology

The ground and excited-state properties of complexes **5-1** – **5-3** were simulated via density functional theory (DFT) and linear response time-dependent DFT (TDDFT) calculations. Gaussian 09⁵⁰ was used to compute the ground and excited state properties at the B3LYP⁵¹ functional with mixed basis set (LANL2DZ for Ir,⁵² and 6-31g* for H, C, and N⁵³). The effect of dichloromethane solvent was implicitly included through the Conductor Polarized Continuum Model (CPCM).^{54,55}

The oscillator strengths and excitation energies from the singlet ground state (S_0) to singlet excited states (S_n , n is the excited state) were computed via TDDFT. The simulated absorption spectra for **5-1** – **5-3** were then generated following the equation 2 in Ref. 56 by using a line-width of 0.05 eV to broaden the computed transitions. The emission energies of **5-1** – **5-3** were investigated by TDDFT Δ SCF. TDDFT Δ SCF computed the phosphorescence energy at the triplet equilibrium geometry via the spin-flip TDDFT between the singlet ground state (S_0) and first triplet excited state (T_1).²¹ The nature of the singlet absorption ($S_0 \rightarrow S_n$) and emission ($T_1 \rightarrow S_0$) was demonstrated by computing the natural transition orbitals (NTOs)⁵⁶ for relevant transitions. The NTOs were visualized using VMD⁵⁸ with an isosurface of 0.02.

5.3. Results and discussion

5.3.1. Electronic absorption

The ground-state absorption spectra of complexes **5-1** – **5-3** were measured in CH_2Cl_2 (Figure 5.1), and the corresponding data are compiled in Table 5.1. Since the observed absorption obeyed the Beer's law in the concentration range of 5×10^{-6} to 1×10^{-4} mol·L⁻¹, we consider that no ground-state aggregation occurs in this concentration range.

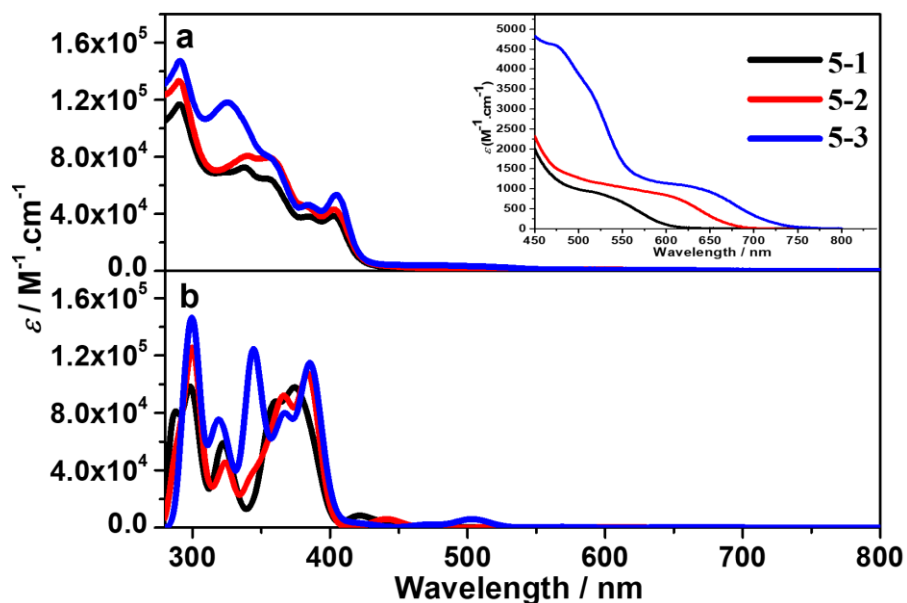


Figure 5.1. Experimental (a) and theoretical (b) UV/Vis absorption spectra of **5-1** – **5-3** at room temperature in CH₂Cl₂. The inset in panel (a) shows the expanded spectra in the regions of 450 – 800 nm. The B3LYP functional was used in the TDDFT calculations and the calculated transitions were broadened by a Gaussian distribution with a linewidth of 0.05 eV.

Table 5.1. Photophysical properties of complexes **5-1** – **5-3**.

	$\lambda_{\text{abs}}/\text{nm}$ ($\log \epsilon$) ^a	$\lambda_{\text{em}}/\text{nm}$ ($\tau_{\text{em}}/\text{ns}$); Φ_{em} ^b	$\lambda_{\text{T1-Tn}}/\text{nm}$ ($\tau_{\text{TA}}/\text{ns}$; $\log \epsilon_{\text{T1-Tn}}$), Φ_{T} ^c
5-1	290 (5.06), 338 (4.86), 356 (4.81), 384 (4.58), 402 (4.57), 507 (2.98)	651 (185); 0.036	390 (119; –), 437 (110; 4.41), 779 (108; –); 0.33
5-2	290 (5.12), 340 (4.91), 355 (4.90), 381 (4.66), 402 (4.63), 544 (3.03)	710 (70); 0.0046	390 (55; –), 444 (56; 5.08), 733 (75; –); 0.032
5-3	290 (5.17), 325 (5.07), 356 (4.90), 384 (4.67), 404 (4.72), 605 (3.04)	825 (380), 919 (–), 1035 (–), 1180 (–); 0.007	423 (392; –), 549 (405; –), 696 (377; –); –

^a Electronic absorption band maxima (λ_{abs}) and molar extinction coefficients ($\log \epsilon$) in CH₂Cl₂ at room temperature. ^b Room temperature emission band maxima (λ_{em}) and lifetimes (τ_{em}) in CH₂Cl₂ ($c = 1 \times 10^{-5}$ mol/L). For emission quantum yields determination, [Ru(bpy)₃]Cl₂ ($\Phi_{\text{em}} = 0.097$, $\lambda_{\text{ex}} = 436$ nm) in a degassed acetonitrile solution was used as the reference for **5-1** and **5-2**, while IRF140 ($\Phi_{\text{em}} = 0.167$, $\lambda_{\text{ex}} = 804$ nm) in a degassed ethanol solution was used as the reference for **5-3**. ^c Nanosecond TA band maxima ($\lambda_{\text{T1-Tn}}$), triplet excited state lifetimes (τ_{TA}) and quantum yields (Φ_{T}) measured in CH₃CN at room temperature.

The UV–vis absorption spectra of **5-1** – **5-3** resemble each other, being all composed of structured, intense absorption bands in the regions of 280 – 420 nm. The molar extinction coefficients of these bands gradually increased from **5-1** to **5-3**, and a new band appearing at 325

nm in **5-3**. Considering the spectral features and the molar extinction coefficients, we tentatively attribute these absorption bands predominantly to the ligand-localized $^1\pi,\pi^*$ transitions. The gradually increased molar extinction coefficients are likely caused by the extended π -conjugation of the N[^]N ligand. All spectra also exhibited weak and broad tails above 420 nm, *i.e.* 420–600 nm for **5-1**, 420–700 nm for **5-2**, and 420–750 nm for **5-3** (see inset in panel (a) of Figure 5.1). Because of the structureless feature and small molar extinction coefficients, these band(s) likely arose from charge transfer (CT) transitions. The gradual red-shift of these bands with increased molar extinction coefficients suggested that the CT transitions likely involved the N[^]N ligands, which could be metal-to-ligand charge transfer (MLCT) and ligand-to-ligand charge transfer (LLCT).

To unambiguously understand the natures of the ground-state absorption, time-dependent density functional theory (TDDFT) calculations were carried out to obtain the natural transition orbitals (NTOs) for each complex. As the NTOs in Table 5.2 shows, the low-energy absorption band(s) at >420 nm exclusively emanate from the ligand-to-ligand charge transfer (1 LLCT) / 1 MLCT transitions. In view of the dark or extremely small oscillator strength of the Table 5.3 and 5-4 transitions in these complexes, the very weak absorption bands beyond 500 nm for **5-1** and **5-2**, and beyond 575 nm for **5-3** could have contributions from the spin-forbidden $^3\pi,\pi^*/^3$ CT transitions that have been reported in many other Ir(III) complexes.^{14,26,28-30,35,59,60} The intense absorption bands at 320–420 nm (Table 5.3) are dominated by the dppl ligand-localized $^1\pi,\pi^*$ transitions, mixed with some 1 MLCT/ 1 LLCT transitions. The NTOs in Table 5.4 indicate that the short wavelength absorption bands at 280–320 nm predominantly arise from the dppl and N[^]N ligand localized spin-allowed $^1\pi,\pi^*$ transitions, admixing with minor 1 MLCT/ 1 LLCT and intraligand charge transfer (1 ILCT) characters.

Table 5.2. Natural transition orbitals (NTOs) corresponding to the transitions contributing to the low-energy absorption bands of **5-1** – **5-3** in CH₂Cl₂.

	State	Hole	Electron	State	Hole	Electron
5-1	S ₁ 601 nm <i>f</i> = 0.003			S ₂ 564 nm <i>f</i> = 0.000		
	S ₃ 502 nm <i>f</i> = 0.003			S ₄ 438 nm <i>f</i> = 0.016		
	S ₆ 421 nm <i>f</i> = 0.014			S ₇ 420 nm <i>f</i> = 0.025		
5-2	S ₁ 640 nm <i>f</i> = 0.000			S ₂ 601 nm <i>f</i> = 0.002		
	S ₃ 525 nm <i>f</i> = 0.002			S ₅ 445 nm <i>f</i> = 0.011		
	S ₆ 442 nm <i>f</i> = 0.014			S ₇ 434 nm <i>f</i> = 0.009		
5-3	S ₁ 707 nm <i>f</i> = 0.000			S ₂ 661 nm <i>f</i> = 0.002		
	S ₃ 568 nm <i>f</i> = 0.003			S ₄ 503 nm <i>f</i> = 0.031		
	S ₆ 471 nm <i>f</i> = 0.010			S ₈ 428 nm <i>f</i> = 0.008	 79%	 79%
				 20%	 20%	

Table 5.3. Natural transition orbitals (NTOs) representing singlet transitions contributing to the medium energy transitions of **5-1** – **5-3** in CH₂Cl₂.

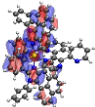
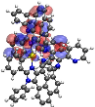
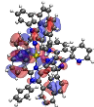
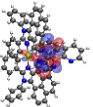
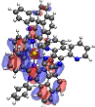
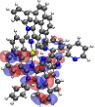
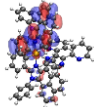
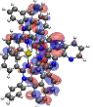
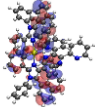
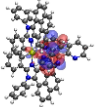
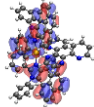
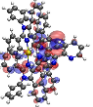
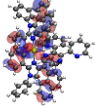
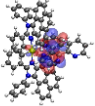
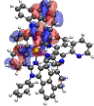
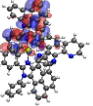
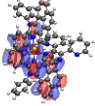
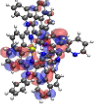
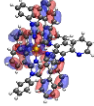
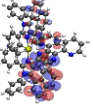
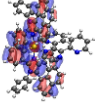
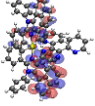
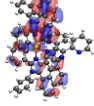
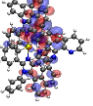
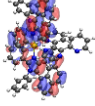
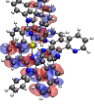
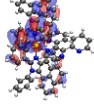
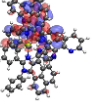
	State	Hole	Electron	State	Hole	Electron
5-1	S ₈ 387 nm <i>f</i> = 0.216			S ₂₁ 355 nm <i>f</i> = 0.103		
					51%	51%
	S ₁₁ 377 nm <i>f</i> = 0.191					
		54%	54%		31%	31%
	S ₁₃ 373 nm <i>f</i> = 0.152			S ₂₃ 346 nm <i>f</i> = 0.048		
		41%	41%			46%
	S ₁₆ 366 nm <i>f</i> = 0.098			S ₂₉ 329 nm <i>f</i> = 0.078		
		54%	54%			44%
	S ₁₈ 359 nm <i>f</i> = 0.161			S ₃₀ 326 nm <i>f</i> = 0.038		
		31%	31%			35%
S ₁₉ 357 nm <i>f</i> = 0.097			S ₃₀ 326 nm <i>f</i> = 0.038			
	47%	47%			24%	24%
S ₁₂ 385 nm <i>f</i> = 0.432			S ₂₆ 342 nm <i>f</i> = 0.052			
	40%	40%			62%	62%

Table 5.3. Natural transition orbitals (NTOs) representing singlet transitions contributing to the medium energy transitions of **5-1** – **5-3** in CH₂Cl₂. (continued)

State	Hole	Electron	State	Hole	Electron
S ₁₅ 371 nm <i>f</i> = 0.111					
				28%	28%
S ₁₉ 365 nm <i>f</i> = 0.209			S ₃₂ 327 nm <i>f</i> = 0.081		
	67%	67%			
			S ₃₃ 324 nm <i>f</i> = 0.052		
	25%	25%			
S ₂₂ 354 nm <i>f</i> = 0.134			S ₃₄ 323 nm <i>f</i> = 0.100		
S ₂₅ 346 nm <i>f</i> = 0.066					
5-3 S ₁₃ 394 nm <i>f</i> = 0.073			S ₂₄ 354 nm <i>f</i> = 0.114		
S ₁₅ 386 nm <i>f</i> = 0.365			S ₂₇ 344 nm <i>f</i> = 0.499		
				53%	53%
S ₁₆ 383 nm <i>f</i> = 0.132					
	69%	69%		33%	33%
			S ₃₆ 327 nm <i>f</i> = 0.070		
	26%	26%			
S ₁₈ 370 nm <i>f</i> = 0.131			S ₃₉ 323 nm <i>f</i> = 0.110		
S ₂₀ 365 nm <i>f</i> = 0.171					

Table 5.4. Natural transition orbitals (NTOs) representing singlet transitions contributing to the high energy transitions of **5-1** – **5-3** in CH₂Cl₂.

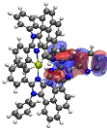
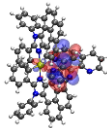
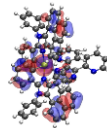
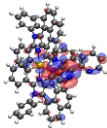
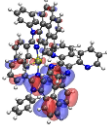
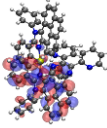
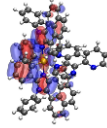
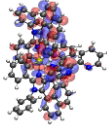
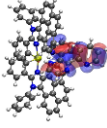
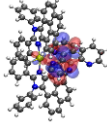
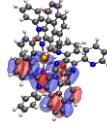
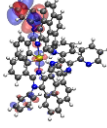
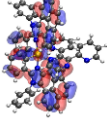
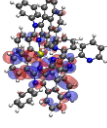
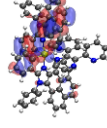
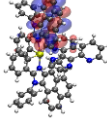
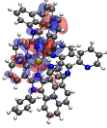
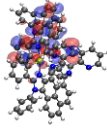
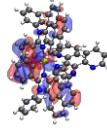
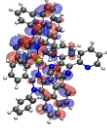
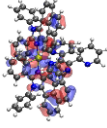
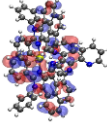
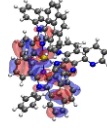
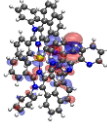
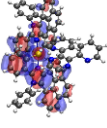
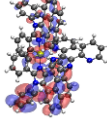
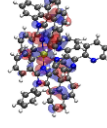
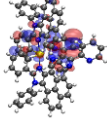
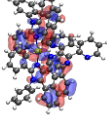
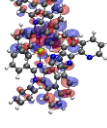
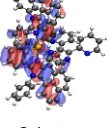
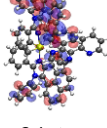
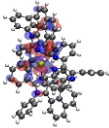
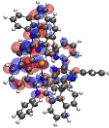
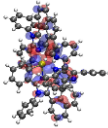
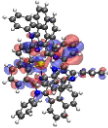
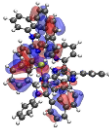
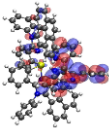
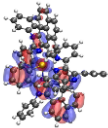
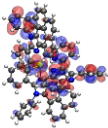
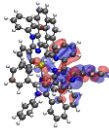
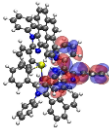
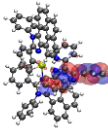
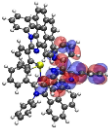
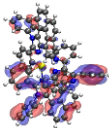
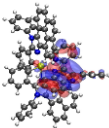
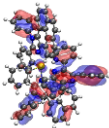
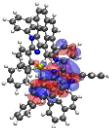
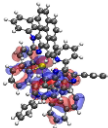
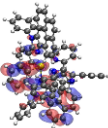
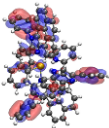
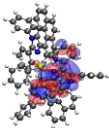
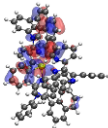
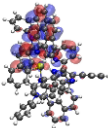
	State	Hole	Electron	State	Hole	Electron	
5-1	S ₃₁ 322 nm <i>f</i> = 0.037			S ₅₃ 296 nm <i>f</i> = 0.098			
		44%	44%			28%	28%
							
		27%	27%			25%	25%
	S ₃₃ 321 nm <i>f</i> = 0.190			S ₆₅ 288 nm <i>f</i> = 0.066			
		41%	41%			44%	44%
							
		33%	33%			26%	26%
	S ₄₃ 303 nm <i>f</i> = 0.088			S ₆₇ 286 nm <i>f</i> = 0.084			
						36%	36%
	S ₄₆ 301 nm <i>f</i> = 0.074			S ₇₀ 285 nm <i>f</i> = 0.055			
		42%	42%			25%	25%
	S ₄₇ 299 nm <i>f</i> = 0.134						
		31%	31%				
							38%
					34%	34%	

Table 5.4. Natural transition orbitals (NTOs) representing singlet transitions contributing to the high energy transitions of **5-1** – **5-3** in CH₂Cl₂. (continued)

	State	Hole	Electron	State	Hole	Electron	
5-2	S ₅₀ 302 nm <i>f</i> = 0.108			S ₇₁ 288 nm <i>f</i> = 0.068			
		43%	43%			29%	29%
							
		24%	24%			26%	26%
5-3	S ₅₃ 301 nm <i>f</i> = 0.137			S ₇₄ 286 nm <i>f</i> = 0.053			
		44%	44%				
							
		31%	31%				
5-3	S ₄₁ 317 nm <i>f</i> = 0.084			S ₆₁ 302 nm <i>f</i> = 0.277			
						43%	43%
							
						25%	25%

5.3.2. Photoluminescence

To explore the triplet excited states properties of **5-1** – **5-3**, the emission of these complexes was studied in different solvents at room temperature. The emission spectra and parameters in CH₂Cl₂ are provided in Figure 5.2 and Table 5.1, and the spectra and parameters in other solvents are given in Figure 5.3 and Table 5.5, respectively. The observed luminescence was sensitive to oxygen quenching, and the lifetimes were tens to hundreds of nanoseconds, indicating the

phosphorescence nature of the emission. Going from **5-1** to **5-3**, the emission energy gradually decreased; however, the spectral feature changed from featureless to structured, accompanied by a shortened lifetime from **5-1** to **5-2**, but increased for **5-3**. The lack of monotonic trend for the spectral feature and the emission lifetime are indicative of a different emitting state for **5-3** from those for **5-1** and **5-2**. This notion was supported by the NTOs calculated by TDDFT Δ SCF.

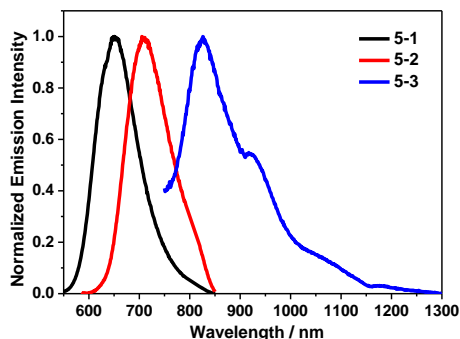


Figure 5.2. Normalized emission spectra of **5-1** – **5-3** in CH_2Cl_2 at room temperature.

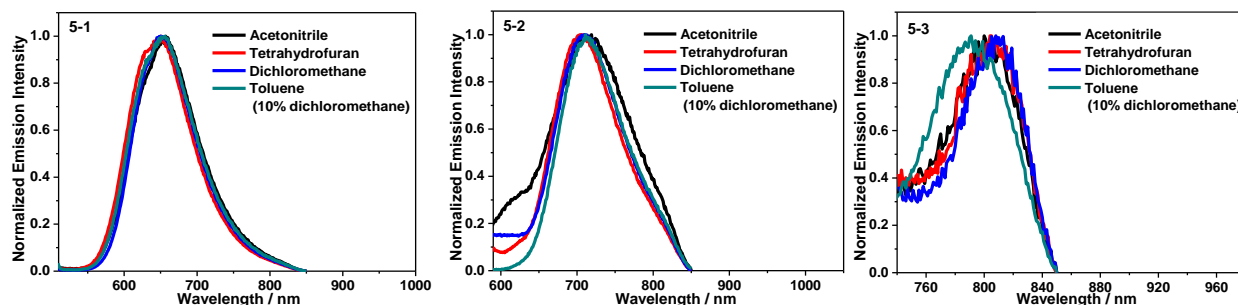


Figure 5.3. Normalized experimental emission spectra of **5-1** – **5-3** at room temperature in different solvents.

As shown in Table 5.6, the electrons in the T_1 states were all localized on the $\text{N}^{\wedge}\text{N}$ ligands and the d orbitals of Ir(III), while the holes were on the dp_{pi} ligands and a different d orbital of Ir(III) in **5-1** and **5-2**, and on the $\text{N}^{\wedge}\text{N}$ and d orbital in **5-3**. Therefore, the emitting states of **5-1** and **5-2** have the $^3\text{LLCT}/^3\text{MLCT}/^3\text{LMCT}$ (ligand-to-metal charge transfer) configurations in nature; whereas the emitting state of **5-3** is the $\text{N}^{\wedge}\text{N}$ ligand-localized $^3\pi, \pi^*$ state. Because the electrons in all three complexes involved the $\text{N}^{\wedge}\text{N}$ ligands, and the extended π -conjugation could stabilize the

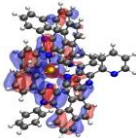
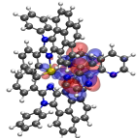
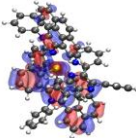
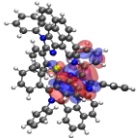
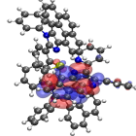
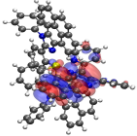
electrons, the reduced electron–hole gap decreased the emission energies going from **5-1** to **5-3**. Moreover, the same charge transfer nature of the emitting states in **5-1** and **5-2** resulted in the shorter emission lifetime and lower emission quantum yield when the emission energy decreased from **5-1** to **5-2**. This trend is consistent with the energy gap law.^{61,62}

Table 5.5. Emission characteristics of **5-1** – **5-3** in different solvents at room temperature.^a

	λ_{em}/nm ($\tau_{em}/\mu s$); Φ_{em}			
	CH ₃ CN	THF	CH ₂ Cl ₂	Toluene (with 10% CH ₂ Cl ₂)
5-1	655 (0.12); 0.014	649 (0.17); 0.026	651 (0.18); 0.036	654 (0.12); 0.019
5-2	714 (0.03); 0.0014	705 (0.04); 0.0033	710 (0.07); 0.0046	712 (0.05); 0.0029
5-3	803 (0.32); - ^b	808 (0.24); - ^b	810 (0.38); - ^b	791 (0.28); - ^b

^a Ru(bpy)₃Cl₂ in CH₃CN was used as the reference ($\lambda_{ex} = 436$ nm, $\Phi_{em} = 0.097$) for the emission quantum yield measurements. ^b Signal was too weak to be measured.

Table 5.6. NTOs representing the transitions contributing to the T₁ states of **5-1** – **5-3** in CH₂Cl₂ calculated by TDDFT Δ SCF method.

	T ₁ / nm	Hole	Electron
5-1	794		
5-2	860		
5-3	1358		

5.3.3. Transient absorption (TA)

The RSA performance of a reverse saturable absorber is closely related to its excited–state absorption, triplet quantum yield, and its triplet lifetime. Thus, the nanosecond transient difference

absorption spectra of **5-1** – **5-3** were investigated in deoxygenated acetonitrile to further understand their triplet excited-state characteristics. The time-resolved TA spectra are presented in Figure 5.4 (a, b, c), and the comparison of the TA spectra immediately after laser excitation are provided in Figure 5.4d. The excited-state absorption parameters, *i.e.* the triplet excited-state lifetimes, extinction coefficients, and quantum yields, are compiled in Table 5.1. Because the TA lifetimes in CH₃CN are similar to the emission lifetimes measured in the same solution for **5-1** – **5-3**, the triplet excited states leading to the observed TA can be attributed to the excited states state that emit, *i.e.* ³LLCT/³MLCT/³LMCT states for **5-1** and **5-2**, and ³ π, π^* state for **5-3**.

The TA spectra of **5-1** and **5-2** resembled each other, both with bleaching at ca. 360 nm and 405 nm, which are consistent with the UV-vis absorption band maxima in the same spectral regions; and positive absorption bands at 371–397 and 414–800 nm. The similar spectral feature reflected the similar configuration of their T₁ states. The positive absorption bands are similar to those observed in other Ir(III) complexes bearing the dppe ligands.^{21,24} Taking into account the fact that the T₁ state contains the ³LLCT/³LMCT characters, the observed positive absorption bands could be ascribed to the absorption from the dppe cation radical. In contrast, the TA spectrum of **5-3** featured a broad positive absorption band in the 363–800 nm regions except for the very narrow and shallow bleaching bands centered at 370 and 405 nm. The TA spectrum of **5-3** is similar to those observed from the other Ir(III) complex bearing the benzoquinoxaline motif in the C[^]N ligand.^{35,60} This feature along with the predominantly benzoquinoxaline-localized ³ π, π^* nature of the T₁ state support the assignment that the observed TA of **5-3** was originated from the benzoquinoxaline-localized ³ π, π^* state.

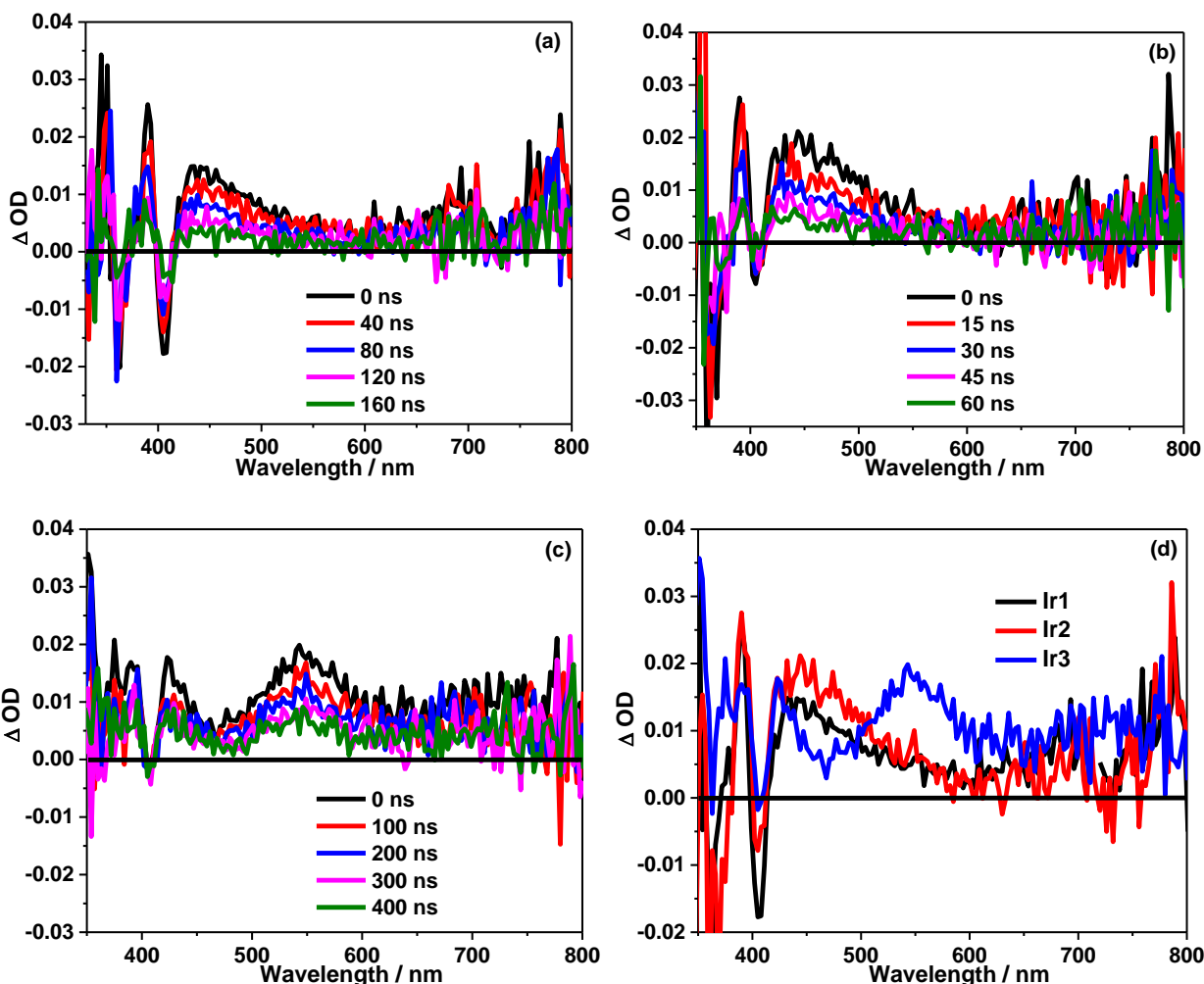


Figure 5.4. Time-resolved nanosecond TA spectra of complexes **5-1** – **5-3** in deoxygenated acetonitrile solution (a–c), and comparison of the TA spectra of **5-1** – **5-3** immediately after laser excitation. $A_{355} = 0.4$ in a 1 cm cuvette, $\lambda_{ex} = 355$ nm.

5.3.4. Reverse saturable absorption

As the TA spectra in Figure 3 displayed, complexes **5-1** – **5-3** all exhibited positive TA signals at 532 nm, implying a stronger triplet excited-state absorption at this wavelength than that of the ground state. Thus, RSA is anticipated to occur upon laser excitation at 532 nm. To ensure that identical number of complexes are excited to the singlet excited state, the concentration of each sample solution was adjusted to reach an 80% linear transmission in a 2 mm cuvette at 532 nm. At this condition, the observed difference in RSA should arise from the different

characteristics of the triplet excited state. Using the 4.1 ns laser pulses, the nonlinear transmission experiment of **5-1** – **5-3** in acetonitrile was carried out and the results are provided in Figure 5.5.

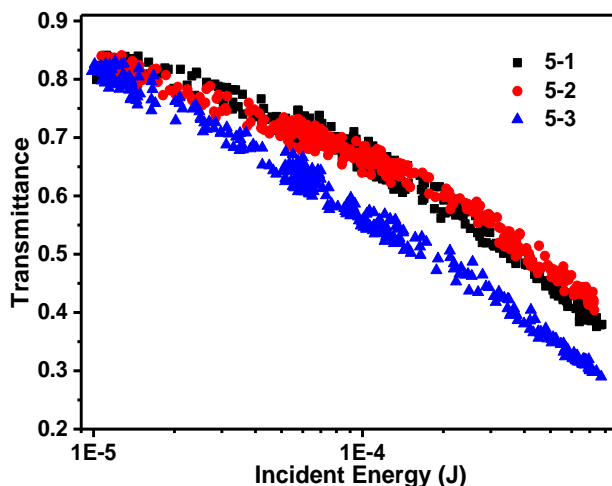


Figure 5.5. Nonlinear transmission plot of **5-1** – **5-3** at the linear transmittance of 80% in 2 mm cuvette in acetonitrile solution using the 4.1 ns laser pulses duration at 532 nm.

It is apparent that all complexes exhibited strong RSA, with the strength of RSA decreasing in the order of **5-3** > **5-1** ≥ **5-2**. The RSA strength of **5-1** – **5-3** approximately paralleled the intensity of the TA signals immediately after laser pulse excitation at 532 nm (*i.e.* 0.005 for **5-1** and **5-2**, and 0.017 for **5-3**). Although the ΔOD values are the same for **5-1** and **5-2**, a slightly stronger RSA was observed for **5-1** because of its slightly weaker ground–state absorption than that of **5-2** (see the inset in Figure 5.1). This is because the strength of RSA is mainly determined by the ratio of the excited–state absorption cross section (σ_{ex}) vs. that of the ground state (σ_0) at the same wavelength, a weaker ground–state absorption could increase the σ_{ex}/σ_0 ratio and thus enhance the RSA. For **5-3**, the much stronger excited–state absorption at 532 nm compared to **5-1** and **5-2** accounted for its strongest RSA among these three complexes. Moreover, **5-3** possesses the much broader ground–state absorption extending to 750 nm, a broader and stronger

excited-state absorption in the visible spectral regions, and the longer triplet lifetime. These features could make it an attractive candidate as a broadband reverse saturable absorber.

5.4. Conclusions

We have reported the synthesis, photophysics, and RSA of three cationic Ir(III) complexes with dppe as the C^N ligand and different dipyrrolylpyrazine derivatives as the N^N ligand. Spectroscopic methods and TDDFT calculations were used to understand the influence of π -conjugation of the N^N ligand on the UV-vis absorption and emission of the complexes. We found that increasing the π -conjugation of the N^N ligand caused a red-shift of the charge-transfer absorption bands in these complexes and increased the molar extinction coefficients of all of the absorption bands. Meanwhile, this structural variation switched the T₁ states from ³LLCT/³MLCT in **5-1** and **5-2** to the N^N ligand-localized ³ π, π^* state in **5-3**, which not only red-shifted the emission spectrum of **5-3**, but also prolonged the T₁ lifetime and drastically changed the transient absorption spectral features. The impact of the π -conjugation on the ground-state and excited-state absorption consequently influenced the RSA of these complexes for ns laser pulses at 532 nm. The trend of the RSA strength, *i.e.* **5-3** > **5-1** ≥ **5-2**, is the result of the increased excited-state absorption and decreased ground-state absorption when the π -conjugation of the N^N ligand varied. The extended weak charge-transfer absorption band at 420–750 nm, along with the stronger triplet excited-state absorption in this spectral region promoted **5-3** as a potential reverse saturable absorber.

5.5. References

- ¹ Dixon, I. M.; Collin, J.-P.; Sauvage, J.-P.; Flamigni, L.; Encinas, S.; Barigelletti, F. *Chem. Soc. Rev.* **2000**, *29*, 385.
- ² Goldsmith, J. I.; Hudson, W. R.; Lowry, M. S.; Anderson, T. H.; Bernhard, S. *J. Am. Chem. Soc.* **2005**, *127*, 7502.
- ³ Lamansky, S.; Djurovich, P.; Murphy, D.; Abdel-Razzaq, F.; Kwong, R.; Tsyba, I.; Bortz, M.; Mui, B.; Bau, R.; Thompson, M. E. *Inorg. Chem.* **2001**, *40*, 1704.
- ⁴ Holder, E.; Langeveld, B. M. W.; Schubert, U. S. *Adv. Mater.* **2005**, *17*, 1109.
- ⁵ Chou, P.-T.; Chi, Y. *Chem. –Eur. J.* **2007**, *13*, 380.
- ⁶ Wong, W.-Y.; Ho, C.-L. *J. Mater. Chem.* **2009**, *19*, 4457.
- ⁷ Sun, J.; Zhong, F.; Yi, X.; Zhao, J. *Inorg. Chem.* **2013**, *52*, 6299.
- ⁸ Ma, L.; Guo, S.; Sun, J.; Zhang, C.; Zhao, J.; Guo, H. *Dalton Trans.* **2013**, *42*, 6478.
- ⁹ Zhao, Q.; Yu, M.; Shi, L.; Liu, S.; Li, C.; Shi, M.; Zhou, Z.; Huang, C.; Li, F. *Organometallics* **2010**, *29*, 1085.
- ¹⁰ Liu, J.; Liu, Y.; Liu, Q.; Li, C.; Sun, L.; Li, F. *J. Am. Chem. Soc.* **2011**, *133*, 15276.
- ¹¹ McDaniel, N. D.; Coughlin, F. J.; Tinker, L. L.; Bernhard, S. *J. Am. Chem. Soc.* **2008**, *130*, 210.
- ¹² Blakemore, J. D.; Schley, N. D.; Balcells, D.; Hull, J. F.; Olack, G. W.; Incarvito, C. D.; Eisenstein, O.; Brudvig, G. W.; Crabtree, R. H. *J. Am. Chem. Soc.* **2010**, *132*, 16017.
- ¹³ Liu, B.; Monro, S.; Lystrom, L.; Cameron, C. G.; Colón, K.; Yin, H.; Kilina, S.; McFarland, S. A.; Sun, W. *Inorg. Chem.* **2018**, *57*, 9859.
- ¹⁴ Wang, C.; Lystrom, L.; Yin, H.; Hetu, M.; Kilina, S.; McFarland, S. A.; Sun, W. *Dalton Trans.* **2016**, *45*, 16366.

- ¹⁵ He, L.; Li, Y.; Tan, C.-P.; Ye, R.-R.; Chen, M.-H.; Cao, J.-J.; Ji, L.-N.; Mao, Z.-W. *Chem. Sci.* **2015**, *6*, 5409.
- ¹⁶ Li, Y.; Dandu, N.; Liu, R.; Kilina, S.; Sun, W. *Dalton Trans.* **2014**, *43*, 1724.
- ¹⁷ Li, Y.; Dandu, N.; Liu, R.; Li, Z.; Kilina, S.; Sun, W. *J. Phys. Chem. C* **2014**, *118*, 6372.
- ¹⁸ Costa, R. D.; Ortí, E.; Bolink, H. J.; Monti, F.; Accorsi, G.; Armaroli, N. *Angew. Chem., Int. Ed.* **2012**, *51*, 8178.
- ¹⁹ Romanenko, I.; Gajan, D.; Sayah, R.; Crozet, D.; Jeanneau, E.; Lucas, C.; Leroux, L.; Veyre, L.; Lesage, A.; Emsley, L.; Lacôte, E.; Thieuleux, C. *Angew. Chem., Int. Ed.* **2015**, *127*, 13129.
- ²⁰ Schulze, M.; Steffen, A.; Würthner, F. *Angew. Chem., Int. Ed.* **2015**, *54*, 1570.
- ²¹ Liu, B.; Lystrom, L.; Kilina, S.; Sun, W. *Inorg. Chem.* **2017**, *56*, 5361.
- ²² Zeng, X.; Tavasli, M.; Perepichka, I. F.; Batsanov, A. S.; Bryce, M. R.; Chiang, C.-J.; Rothe, C.; Monkman, A. P. *Chem. –Eur. J.* **2008**, *14*, 933.
- ²³ Kim, K.-Y.; Farley, R. T.; Schanze, K. S. *J. Phys. Chem. B* **2006**, *110*, 17302.
- ²⁴ Li, Z.; Cui, P.; Wang, C.; Kilina, S.; Sun, W. *J. Phys. Chem. C* **2014**, *118*, 28764.
- ²⁵ Yi, X.; Yang, P.; Huang, D.; Zhao, J. *Dyes Pigm.* **2013**, *96*, 104.
- ²⁶ Zhao, Q.; Liu, S.; Shi, M.; Wang, C.; Yu, M.; Li, L.; Li, F.; Yi, T.; Huang, C. *Inorg. Chem.* **2006**, *45*, 6152.
- ²⁷ Li, Y.; Dandu, N.; Liu, R.; Hu, L.; Kilina, S.; Sun, W. *ACS Appl. Mater. Interfaces* **2013**, *5*, 6556.
- ²⁸ Liu, B.; Lystrom, L.; Kilina, S.; Sun, W. *Inorg. Chem.* **2019**, *58*, 476.
- ²⁹ Liu, R.; Dandu, N.; Chen, J.; Li, Y.; Li, Z.; Liu, S.; Wang, C.; Kilina, S.; Kohler, B.; Sun, W. *J. Phys. Chem. C* **2014**, *118*, 23233.

- 30 Sun, W.; Pei, C.; Lu, T.; Cui, P.; Li, Z.; McCleese, C.; Fang, Y.; Kilina, S.; Song, Y.; Burda, C. *J. Mater. Chem. C* **2016**, *4*, 5059.
- 31 Pei, C.; Cui, P.; McCleese, C.; Kilina, S.; Burda, C.; Sun, W. *Dalton Trans.* **2015**, *44*, 2176.
- 32 Zhu, X.; Lystrom, L.; Kilina, S.; Sun, W. *Inorg. Chem.* **2016**, *55*, 11908.
- 33 Li, Z.; Li, H.; Gifford, B. J.; Peiris, W. D. N.; Kilina, S.; Sun, W. *RSC Adv.* **2016**, *6*, 41214.
- 34 Zhu, X.; Cui, P.; Kilina, S.; Sun, W. *Inorg. Chem.* **2017**, *56*, 13715.
- 35 Wang, L.; Cui, P.; Kilina, S.; Sun, W. *J. Phys. Chem. C* **2017**, *121*, 5719.
- 36 Liu, R.; Dandu, N.; McCleese, C.; Li, Y.; Lu, T.; Li, H.; Yost, D.; Wang, C.; Kilina, S.; Burda, C.; Sun, W. *Eur. J. Inorg. Chem.* **2015**, *31*, 5241.
- 37 Pritchett, T. M.; Ferry, M. J.; Shensky III, W. M.; Mott, A. G.; Stewart, D. J.; Long, S. L.; Haley, J. E.; Li, Z.; Sun, W. *Opt. Lett.* **2015**, *40*, 186.
- 38 Pritchett, T. M.; Ferry, M. J.; Mott, A. G.; Shensky III, W.; Haley, J. E.; Liu, R.; Sun, W. *Opt. Mater.* **2015**, *39*, 195.
- 39 Zhao, H.; Simpson, P. V.; Barlow, A.; Moxey, G. J.; Morshedi, M.; Roy, N.; Philip, R.; Zhang, C.; Cifuentes, M. P.; Humphrey, M. G. *Chem. Eur. J.* **2015**, *21*, 11843.
- 40 Karle, I. L.; Rajesh, Y. B. R. D.; Ranganathan, S. *J. Chem. Cryst.* **2005**, *35*, 835.
- 41 A. Ohta, S. Masano, S. Iwakura, A. Tamura, H. Watahiki, M. Tsutsui, Y. Akita and T. Watanabe, *J. Heterocycl. Chem.* **1982**, *19*, 465–472.
- 42 Bellam, R.; Jaganyi, D.; Mambanda, A.; Robinson, R. *New J. Chem.*, **2018**, *42*, 12557.
- 43 Demas, J. N.; Crosby, G. A. *J. Phys. Chem.* **1971**, *75*, 991.
- 44 Rurack K.; Spieles, M.; *Anal. Chem.* **2011**, *83*, 1232.
- 45 Suzuki, K.; Kobayashi, A.; Kaneko, S.; Takehira, K.; Yoshihara, T.; Ishida, H.; Shiina, Y.; Oishi, S.; Tobita, S. *Phys. Chem. Chem. Phys.* **2009**, *11*, 9850.

- 46 Carmichael, I.; Hug, G. L. *J. Phys. Chem. Ref. Data* **1986**, *15*, 1.
- 47 Kumar, C. V.; Qin, L.; Das, P. K. *J. Chem. Soc., Faraday Trans. 2* **1984**, *80*, 783.
- 48 Firey, P. A.; Ford, W. E.; Sounik, J. R.; Kenney, M. E.; Rodgers, M. A. J. *J. Am. Chem. Soc.* **1988**, *110*, 7626.
- 49 F. Guo, W. Sun, Y. Liu, K. Schanze. *Inorg. Chem.* **2005**, *44*, 4055.
- 50 Frisch, M. J. T., G. W.; Schlegel, H. B.; Scuseria, G. E.; Robb, M. A.; Cheeseman, J. R.; Scalmani, G.; Barone, V.; Mennucci, B.; Peterson, G. A.; Nakatsuji, H.; Caricato, M.; Li, X.; Hratchian, H. P.; Izmaylov, A. F.; Bloino, J.; Zheng, G.; Sonnenberg, J. L.; Hada, M.; Ehara, M.; Toyota, K.; Fukuda, R.; Hasegawa, J.; Ishida, M.; Nakajima, T.; Honda, Y.; Kitao, O.; Nakai, H.; Vreven, T.; Montgomery, J. A., Jr.; Peralta, J. E.; Ogliaro, F.; Bearpark, M.; Heyd, J. J.; Brothers, E.; Kudin, K. N.; Staroverov, V. N.; Kobayashi, R.; Normand, J.; Raghavachari, K.; Rendell, A.; Burant, J. C.; Iyengar, S. S.; Tomasi, J.; Cossi, M.; Rega, N.; Millam, J. M.; Klene, M.; Knox, J. E.; Cross, J. B.; Bakken, V.; Adamo, C.; Jaramillo, J.; Gomperts, R.; Stratmann, R. E.; Yazyev, O.; Austin, A. J.; Cammi, R.; Pomelli, C.; Ochterski, J. W.; Martin, R. L.; Morokuma, K.; Zakrzewski, V. G.; Voth, G. A.; Salvador, P.; Dannenberg, J. J.; Dapprich, S.; Daniels, A. D.; Farkas, O.; Foresman, J. B.; Ortiz, J. V.; Cioslowski, J.; Fox, D. J. Gaussian 09, revision B.1; Gaussian, Inc.: Wallingford, CT, 2009.
- 51 Lee, C.; Yang, W.; Parr, R. G. *Phys. Rev. B* **1988**, *37*, 785.
- 52 Hay, P. J.; Wadt, W. R. *J. Chem. Phys.* **1985**, *82*, 270.
- 53 Adamo, C.; Barone, V. *J. Chem. Phys.* **1999**, *110*, 6158.
- 54 Barone, V.; Cossi, M.; Tomasi, J. *J. Comput. Chem.* **1998**, *19*, 404.
- 55 Cossi, M.; Barone, V.; Cammi, R.; Tomasi, J. *Chem. Phys. Lett.* **1996**, *255*, 327.

- ⁵⁶ Bjorgaard, J. A.; Sifain, A. E.; Nelson, T.; Myers, T. W.; Veauthier, J. M.; Chavez, D. E.; Scharff, R. J.; Tretiak, S. *J. Phys. Chem. A* **2016**, *120*, 4455.
- ⁵⁷ Martin, R. L. *J. Chem. Phys.* **2003**, *118*, 4775.
- ⁵⁸ Humphrey, W.; Dalke, A.; Schulten, K. *Journal of molecular graphics* **1996**, *14*, 33.
- ⁵⁹ Wu, S.-H.; Ling, J.-W.; Lai, S.-H.; Huang, M.-J.; Cheng, C. H.; Chen, I.-C. *J. Phys. Chem. A* **2010**, *114*, 10339.
- ⁶⁰ L. Wang, H. Yin, P. Cui, M. Hetu, C. Wang, S. Monro, R. D. Schaller, C. G. Cameron, B. Liu, S. Kilina, S. A. McFarland, W. Sun. *Dalton. Trans.* **2017**, *46*, 8091.
- ⁶¹ Caspar, J. V.; Kober, E. M.; Sullivan, B. P.; Meyer, T. J. *J. Am. Chem. Soc.* **1982**, *104*, 630.
- ⁶² Caspar, J. V.; Meyer, T. J. *J. Phys. Chem.* **1983**, *87*, 952.

6. PHOTOPHYSICAL AND PHOTOBIOLOGICAL PROPERTIES OF DINUCLEAR IRIDIUM(III) BIS-TRIDENTATE COMPLEXES

6.1. Introduction

In recent decades transition-metal complexes have come to the forefront in the search for new chemical entities in drug discovery and biological chemistry.¹ Platinum (Pt)-based metal complexes have been investigated extensively for cancer therapy,² with cisplatin being arguably the most successful anticancer drug to date. Nevertheless, there is continued focus on developing alternatives to cisplatin^{3,4} and other nonselective cytotoxic agents in an effort to reduce the systemic side effects associated with conventional chemotherapy approaches. Ruthenium (Ru)-containing compounds have been widely studied as alternatives to the Pt-derived drugs, with a few (*e.g.*, NAMI-A, KP1019, and IT-139) entering clinical trials⁵⁻⁷ but none in the clinic to date. With selectivity being a key consideration for any new drug, Ru(II) coordination complexes and other transition-metal complexes are also being considered for targeted modalities such as photodynamic therapy (PDT).⁸⁻¹¹

PDT has been known for over a hundred years¹² yet remains underexploited in mainstream cancer therapy despite its precise spatiotemporal selectivity. In its narrowest definition, PDT involves activation of an otherwise nontoxic photosensitizer with photons of appropriate energy to produce a triplet excited state that can relax through singlet oxygen (¹O₂) sensitization or the production of other reactive oxygen species (ROS).¹³ Collectively, cytotoxic ROS destroy tumors and tumor vasculature, and can even invoke an antitumor immune response under the right conditions. Porphyrin-based organic compounds (and the related chlorins, bacteriochlorins, and phthalocyanines) have traditionally served as ROS-generating photosensitizers for PDT.^{14,15}

However, transition-metal complex photosensitizers have the potential to both (i) expand the scope of PDT to include oxygen-independent mechanisms of action, and thus improve PDT efficacy in hypoxic tissue, and (ii) broaden the wavelength range that can be used to include deeper tissue-penetrating near-infrared (NIR) light. One recent example is our Ru(II) complex TLD1433,¹⁶ currently in clinical trials for treating bladder cancer with PDT (ClinicalTrials.gov Identifier: NCT03053635), and its transferrin conjugate RutherrinTM.¹⁷

TLD1433 incorporates a special π -expansive ligand derived from imidazo[4,5-*f*][1,10]phenanthroline appended to an α -terthienyl unit, which imparts a long-lived triplet intraligand excited state (³IL) of significant π, π^* character that is lower in energy than the triplet metal-to-ligand charge transfer (³MLCT) state that typically dominates the photophysical dynamics of Ru(II) polypyridyl complexes. The reduced intersystem crossing (ISC) rates characteristic of spin-forbidden ³ π, π^* transitions centered on the organic moiety are responsible for the much longer intrinsic triplet lifetimes in these constructs that are known as metal-organic dyads.^{18,19} The implication is that slow ISC back to the ground state from ³IL states provides ample opportunity for requisite bimolecular processes that constitute the phototoxic effects of PDT. We have demonstrated very potent *in vitro* PDT effects from a variety of Ru(II) dyads with low-lying, long-lived ³IL states, including both contiguously-fused π -extended azaaromatic ligands²⁰ as well as ligands tethered to π -extended aromatic chromophores.^{16,21–23} More recently, we have incorporated π -expansive ligands into Ir(III) metal complexes to extend intrinsic excited state lifetimes for both reverse saturable absorption (RSA) and PDT applications.^{24,25}

Compared to the large number of Ru(II) systems that have been explored, investigations on Ir(III) complexes for *in vitro* PDT have been emerged in recent years.^{24–44} While Ir(III) complexes derived from diimine ligands (N[^]N) may fall short of the optimal absorption window

for PDT, we have demonstrated that incorporation of two cyclometalating ligands (C[^]N) to form biscyclometalated Ir(III) complexes extends the ground-state absorption spectrum significantly, and that installation of a π -extended N[^]N ligand alongside the two C[^]N ligands extends the lifetime through population of ³IL states. The result is nanomolar PDT potency with phototherapeutic indices (PIs) greater than 400.²⁵ We also showed that it was possible to use π -extended C[^]N ligands without compromising the potent *in vitro* PDT effects in Ir(III)-based systems that act as near-infrared-emitting theranostic agents.²⁴

The large luminescence quantum yields for certain Ir(III) complexes combined with their high yields for triplet state formation and good photostability make these metal complexes very attractive for photobiological applications such as PDT. In addition, their excitation and emission energies, as well as other photophysical and biological/chemical properties, can be systematically tuned via minor structural changes to a highly versatile and modular architecture. Despite these attributes, Ir(III) complexes studied to date³⁰ still fall short of some of the best Ru(II)-based *in vitro* PDT agents. The purpose of the present study is to use rational design principles to improve the water-solubility and *in vitro* PDT effects within the Ir(III) class of photosensitizers. Specifically, installing two Ir(III) centers in a single complex might simultaneously amplify photocytotoxicity and increase water solubility.

The solubility of organometallic complexes in aqueous solution can be improved by increasing the number of charges in the complex, which should be applicable to multinuclear iridium(III) complexes with C[^]N and/or N[^]N ligands.⁴⁵ Since the photophysical and biological properties of metal complexes bearing tridentate ligand(s) can be readily tuned by modification of the 4'-position of the tridentate ligand(s), and because the bis-tridentate ligand coordination prevents the formation of stereoisomers upon complexation with transition metals, tridentate

ligands are chosen for this Ir(III) study.^{46,47} Our previous work with bis-terpyridyl dinuclear Pt(II) complexes showed that the fluorenyl bridging group imparted these systems with intense absorption in the visible region (400-500 nm) and reasonably long-lived triplet excited states.⁴⁸ These desirable properties led us to investigate fluorenyl-linked Ir(III) systems as *in vitro* PDT agents.

Herein, we report the synthesis, characterization, and photophysical/photobiological properties of stable dinuclear Ir(III) complexes (Chart 6-1) of +2, +4, or +6 charges, with the charge determined by the identities of the metal coordinating atoms of different terminal tridentate ligands. Fluorene was chosen as the central bridging group for the two Ir-tpy components because it is a rigid π -conjugated linker expected to enhance molar extinction coefficients in the visible spectral region. Complexes **6-1** and **6-3** – **6-5** incorporate 9,9-dioctyl-2,7-di(terpyridyl)-9H-fluorene (**L6-1**) as the bridging ligand, with variation at the terminal tridentate ligands: 4'-phenyl-2,2':6',2''-terpyridine (N[^]N[^]N), 1,3-dipyridyl-4,6-dimethylbenzene (N[^]C[^]N), 4,6-diphenyl-2,2'-bipyridine (C[^]N[^]N), or 2,4,6-triphenyl-pyridine (C[^]N[^]C). Complex **6-2** uses 9,9-dioctyl-2,7-bis(2-phenylethynyl)-9H-fluorene (**L6-2**) as the bridging ligand to extend the π -conjugation length, which is anticipated to facilitate intraligand charge transfer (ILCT) transitions that fall in the PDT window and to also increase visible wavelength absorption.

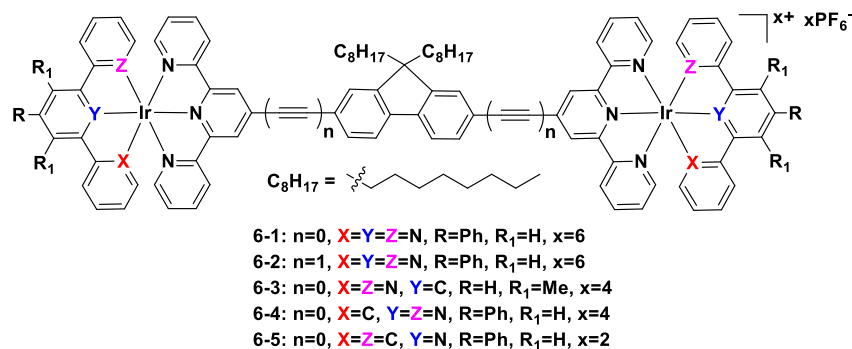


Chart 6-1. The molecule structure of target dinuclear Ir(III) complexes.

6.2. Experimental section

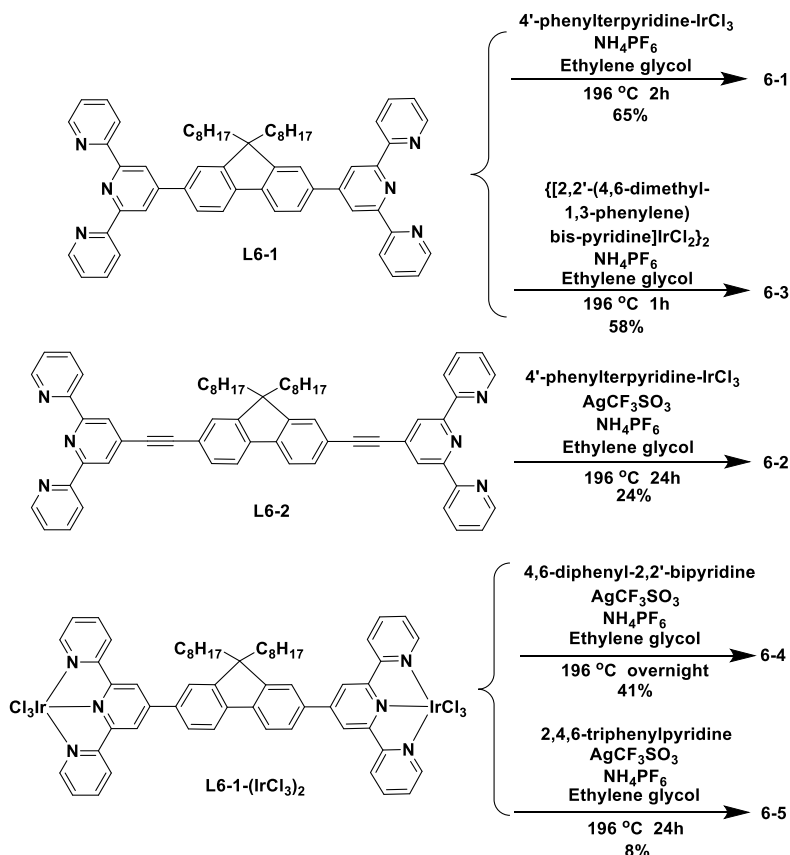
6.2.1. Synthesis and characterizations

All the chemicals and solvents were purchased from Aldrich Chemical Co. or Alfa Aesar and used as received unless otherwise mentioned. The bridging ligands (**L6-1** and **L6-2**) were synthesized following the procedures reported by our group before.⁴⁸ 4'-Phenyl-2,2':6',2''-terpyridine ($N^{\wedge}N^{\wedge}N$),⁴⁹ 1,3-dipyridyl-4,6-dimethylbenzene ($N^{\wedge}C^{\wedge}N$),⁵⁰ 4,6-diphenyl-2,2'-bipyridine ($C^{\wedge}N^{\wedge}N$),⁵¹ 2,4,6-triphenylpyridine ($C^{\wedge}N^{\wedge}C$),⁵² 4'-phenyl-2,2':6',2''-terpyridine- $IrCl_3$ ($N^{\wedge}N^{\wedge}N-IrCl_3$),⁵³ and $\{[1,3-dipyridyl-4,6-dimethylbenzene]IrCl_2\}_2$ ($N^{\wedge}C^{\wedge}N$ Ir-dimer)⁵⁴ were synthesized following literature procedures. The silica gel (60 Å, 230–400 mesh) and Al_2O_3 gel (activated, neutral) used for column chromatography were purchased from Sorbent Technology. Complexes **6-1** – **6-5** were characterized by 1H NMR, high resolution electrospray ionization mass spectrometry (ESI–MS), and elemental analysis. 1H NMR spectra were obtained on Bruker-400 spectrometer or Varian Oxford–500 spectrometer. ESI–MS analyses were conducted on Waters Synapt G2-Si Mass Spectrometer. Elemental analyses were carried out by NuMega Resonance Laboratories, Inc. in San Diego, California.

The synthetic schemes for complexes **6-1** – **6-5** are illustrated in Scheme 6-1.

L6-1-(IrCl₃)₂. A suspension of **L6-1** (170.5 mg, 0.2 mmol) and $IrCl_3 \cdot 3H_2O$ (141 mg, 0.4 mmol) in degassed ethylene glycol (15 mL) was heated to 160 °C without direct light for 30 minutes. After the mixture was cooled to room temperature, the precipitate was filtered out and washed with ethanol, water, and diethyl ether to give **L6-1-Ir(Cl₃)₂** as red solid (254 mg, 88%). 1H NMR (500 MHz, d^6 -DMSO) δ 9.27 (d, $J = 5.0$ Hz, 4H), 9.18 (t, $J = 8.8$ Hz, 4H), 9.06 (dd, $J = 11.3, 3.0$ Hz, 2H), 8.98 – 8.94 (m, 2H), 8.70 (t, $J = 9.8$ Hz, 2H), 8.52 (dd, $J = 8.2, 4.1$ Hz, 2H),

8.38 (t, $J = 7.8$ Hz, 4H), 8.32 (d, $J = 8.5$ Hz, 2H), 8.06 – 8.01 (m, 4H), 2.43 (m, 4H), 0.95 – 0.69 (m, 20H), 0.48 (m, 10H).



Scheme 6.1. Synthetic routes for complexes **6-1** – **6-5**.

6-1. A suspension of 4'-phenylterpyridine-IrCl₃ (60.7 mg, 0.1 mmol) and **L6-1** (42.6 mg, 0.05 mmol) in degassed ethylene glycol (10 mL) was heated to 196 °C without direct light for 2 hours. After the mixture was cooled to room temperature, saturated NH₄PF₆ solution (20 mL) was added to precipitate out the crude product. The crude product was purified by column chromatography (Alumina, eluted with CH₂Cl₂ first to remove unreacted ligand, then using acetone/water gradient elution from 100:0 to 95:5 (v/v)) to give a yellow solid (60 mg, 65%) as the desired product. ¹H NMR (400 MHz, *d*⁶-DMSO) δ 9.76 (s, 4H), 9.67 (s, 4H), 9.50 – 9.34 (m, 4H), 9.29 (d, $J = 8.2$ Hz, 4H), 9.05 (s, 2H), 8.88 – 8.78 (m, 2H), 8.53-8.39 (m, 14H), 8.17 – 7.93

(m, 8H), 7.87 (t, $J = 7.6$ Hz, 4H), 7.78 (t, $J = 7.4$ Hz, 2H), 7.62 (dd, $J = 12.2, 5.8$ Hz, 8H), 2.61 (m, 4H), 0.89 (m, 20H), 0.62 (m, 10H). ESI-HRMS (m/z , in acetone): calcd. for $[\text{C}_{101}\text{H}_{90}\text{Ir}_2\text{N}_{12}]^{6+}$, 309.4445; found, 309.4446. Calcd. for $[\text{C}_{101}\text{H}_{90}\text{Ir}_2\text{N}_{12}\text{PF}_6]^{5+}$, 400.3262; found, 400.3270. Calcd. for $[\text{C}_{101}\text{H}_{90}\text{Ir}_2\text{N}_{12}\text{P}_2\text{F}_{12}]^{4+}$, 536.6489; found, 536.6503. Anal. Calcd. (%) for $\text{C}_{101}\text{H}_{90}\text{F}_{36}\text{Ir}_2\text{N}_{12}\text{P}_6 \cdot 6\text{H}_2\text{O}$: C, 42.80; H, 3.63; N, 5.93. Found: C, 42.61; H, 3.74; N, 5.98.

6-2. A suspension of 4'-phenylterpyridine- IrCl_3 (60.7 mg, 0.1 mmol), **L6-2** (45 mg, 0.05 mmol), and AgOTf (77 mg, 0.3 mmol) in degassed ethylene glycol (10 mL) was heated to 196 °C without direct light for 24 hours. After the mixture was cooled to room temperature, saturated NH_4PF_6 solution (20 mL) was added to precipitate out the crude product. The crude product was purified by column chromatography (Alumina, eluted with CH_2Cl_2 first to remove unreacted ligand, then using acetone/water gradient elution from 100:0 to 95:5 (v/v)) to give a dark red powder (37 mg, 24%) as the desired product. ^1H NMR (400 MHz, d^6 -DMSO) δ 9.62 (t, $J = 7.0$ Hz, 6H), 9.22 (m, 8H), 8.48 (m, 6H), 8.32 (m, 8H), 7.92 (m, 8H), 7.77 (m, 6H), 7.71 (m, 4H), 7.51 (m, 10H), 2.51 (m, 4H), 1.02 (m, 20H), 0.67 (m, 10H). ESI-HRMS (m/z , in acetone): calcd. for $[\text{C}_{105}\text{H}_{90}\text{Ir}_2\text{N}_{12}]^{6+}$, 317.4445; found, 317.4442. Anal. Calcd. (%) for $\text{C}_{105}\text{H}_{90}\text{F}_{36}\text{Ir}_2\text{N}_{12}\text{P}_6 \cdot 13\text{H}_2\text{O} \cdot \text{CH}_2\text{Cl}_2$: C, 41.16; H, 3.85; N, 5.43. Found: C, 40.83; H, 3.47; N, 5.44.

6-3. A suspension of $\{[2,2'-(4,6\text{-dimethyl-1,3-phenylene})\text{bis-pyridine}]\text{IrCl}_2\}_2$ (72 mg, 0.069 mmol) and **L6-1** (59 mg, 0.069 mmol) in ethylene glycol (10 mL) was heated to 196 °C in degassed ethylene glycol without direct light for 1 hour. After cooling to room temperature, the reaction mixture was added to water (10 mL) and filtered. Saturated NH_4PF_6 solution (20 mL) was added to the filtrate, and the resulting yellow precipitate was collected by centrifugation, washed with water (3×10 mL), and dried under vacuum. The crude product was purified by column chromatography (Alumina, eluted with CH_2Cl_2 first to remove unreacted ligand, then using

acetone/water gradient elution from 100:0 to 95:5 (v/v)) to yield a yellow solid (94 mg, 58%) as the desired product. ^1H NMR (400 MHz, d^6 -DMSO) δ 9.65 (td, $J = 5.0, 2.5$ Hz, 4H), 9.18 (t, $J = 9.9$ Hz, 4H), 8.90 (m, 2H), 8.71 (m, 2H), 8.47 (dd, $J = 9.6, 2.6$ Hz, 2H), 8.37 (d, $J = 8.4$ Hz, 4H), 8.30 (dd, $J = 8.8, 4.6$ Hz, 4H), 7.99 (ddd, $J = 7.5, 5.9, 2.7$ Hz, 4H), 7.77 (m, 2H), 7.68 (ddd, $J = 9.7, 4.8, 2.7$ Hz, 4H), 7.52 (ddd, $J = 6.7, 4.1, 1.2$ Hz, 4H), 7.45 (dd, $J = 5.7, 1.8$ Hz, 2H), 7.40 (s, 2H), 7.12 (ddd, $J = 8.4, 6.5, 1.7$ Hz, 4H), 2.93 (s, 12H), 2.52 (m, 4H), 0.90 (m, 20H), 0.62 (m, 10H). ESI-HRMS (m/z, in acetone): calcd. for $[\text{C}_{95}\text{H}_{90}\text{Ir}_2\text{N}_{10}]^{4+}$, 439.1652; found, 439.1668. Calcd. for $[\text{C}_{95}\text{H}_{90}\text{Ir}_2\text{N}_{10}\text{PF}_6]^{3+}$, 633.8750; found, 633.8768. Anal. Calcd. (%) for $\text{C}_{95}\text{H}_{90}\text{F}_{24}\text{Ir}_2\text{N}_{10}\text{P}_4\cdot 5\text{H}_2\text{O}$: C, 47.03; H, 4.15; N, 5.77. Found: C, 46.97; H, 4.32; N, 5.98.

6-4. A suspension of **L6-1**- $(\text{IrCl}_3)_2$ (72.4 mg, 0.05 mmol), 4,6-diphenyl-2,2'-bipyridine (30.8 mg, 0.1 mmol), and AgOTf (77 mg, 0.3 mmol) in degassed ethylene glycol (10 mL) was heated to 196 °C without direct light overnight. After the mixture was cooled to room temperature, saturated NH_4PF_6 solution (20 mL) was added to precipitate out the crude product. The crude product was purified by column chromatography (Alumina, eluted with CH_2Cl_2 first to remove unreacted ligand, then using acetone/water gradient elution from 100:0 to 95:5 (v/v)) to yield a yellow solid (38 mg, 41%) as the desired product. ^1H NMR (400 MHz, d^6 -acetone) δ 10.05 (d, $J = 7.2$ Hz, 2H), 9.49 (d, $J = 8.4$ Hz, 2H), 9.30 (s, 2H), 9.00 (d, $J = 15.3$ Hz, 4H), 8.95 – 8.77 (m, 6H), 8.71 (s, 2H), 8.48 (dd, $J = 18.4, 9.5$ Hz, 8H), 8.36 (s, 2H), 8.28 (d, $J = 6.3$ Hz, 2H), 8.13 – 7.97 (m, 4H), 7.86 (dd, $J = 10.8, 6.6$ Hz, 4H), 7.75 (s, 2H), 7.61 (s, 6H), 7.48 – 7.33 (m, 2H), 7.19 (dd, $J = 13.3, 4.5$ Hz, 4H), 6.91 – 6.69 (m, 4H) 2.41 (m, 4H), 0.86 (m, 20H), 0.55 (m, 10H). ESI-HRMS (m/z, in acetone): calcd. for $[\text{C}_{103}\text{H}_{90}\text{Ir}_2\text{N}_{10}\text{PF}_6]^{3+}$, 655.8756; found, 655.8798. Anal. Calcd. (%) for $\text{C}_{103}\text{H}_{90}\text{F}_{24}\text{Ir}_2\text{N}_{10}\text{P}_4\cdot 9\text{H}_2\text{O}$: C, 47.69; H, 4.20; N, 5.40. Found: C, 47.56; H, 4.46; N, 5.25.

6-5. A suspension of **L6-1**-(IrCl₃)₂ (72.4 mg, 0.05 mmol), 2,4,6-triphenylpyridine (30.7 mg, 0.1 mmol), and AgOTf (77 mg, 0.3 mmol) in degassed ethylene glycol (10 mL) was heated to 196 °C without direct light for 24 hours. After the mixture was cooled to room temperature, saturated NH₄PF₆ solution (20 mL) was added to precipitate out the crude product. The crude product was purified by column chromatography (Alumina, eluted with CH₂Cl₂ first to remove unreacted ligand, then using acetone/water gradient elution from 100:0 to 95:5 (v/v)) to yield a red solid (16 mg, 8%) as the desired product. ¹H NMR (400 MHz, *d*⁶-DMSO) δ 9.56 (s, 4H), 9.19 – 9.09 (m, 4H), 8.95 – 8.85 (m, 4H), 8.60 (s, 4H), 8.33 (d, *J* = 6.6 Hz, 8H), 8.22 (s, 6H), 7.89 (s, 4H), 7.73 (s, 4H), 7.64 (s, 2H), 7.45 (s, 4H), 6.99 (s, 4H), 6.74 (s, 4H), 6.21 (s, 4H), 2.52 (m, 4H), 0.85 (m, 20H), 0.55 (m, 10H). ESI-HRMS (*m/z*, in acetone): calcd. for [C₁₀₅H₉₀Ir₂N₈]²⁺, 924.3283; found, 924.3291. Anal. Calcd. (%) for C₁₀₅H₉₀F₁₂Ir₂N₈P₂·0.6CH₂Cl₂: C, 57.94; H, 4.20; N, 5.12. Found: C, 57.92; H, 3.96; N, 5.27.

6.2.2. Photophysical studies

Spectrophotometric grade solvents purchased from Alfa Aesar were used for the photophysical measurements in this work. The Ultraviolet–visible (UV–vis) absorption spectra of complexes **6-1** – **6-5** were measured on a Varian Cary 50 spectrophotometer. Steady-state emission spectral measurements in different solvents (acetonitrile, acetone, and dichloromethane) were conducted using a HORIBA FluoroMax 4 fluorometer/phosphorometer. The relative actinometry method⁵⁵ was used to determine the emission quantum yields for complexes **6-1** – **6-5** in degassed CH₃CN solution using [Ru(bpy)₃]Cl₂ ($\Phi_{\text{em}} = 0.097$, $\lambda_{\text{ex}} = 436$ nm)⁵⁶ as the reference. The nanosecond transient absorption (TA) spectra and decays, triplet excited-state quantum yields, and triplet lifetimes were recorded in degassed acetonitrile solutions on an Edinburgh LP920 laser flash photolysis spectrometer. The third harmonic output (355 nm) of a Nd:YAG laser (Quantel

Brilliant, pulsewidth ~ 4.1 ns, repetition rate was set to 1 Hz) was used as the excitation light source. Each sample solution was degassed using Ar for 40 minutes before each measurement. The triplet excited-state molar extinction coefficients (ϵ_{T1-Tn}) were determined by the singlet depletion method⁵⁷ at the TA band maxima. The triplet excited-state quantum yields were measured by the relative actinometry method⁵⁸ after obtaining the ϵ_{T1-Tn} values, with SiNc in benzene being used as the reference ($\epsilon_{590} = 70,000 \text{ M}^{-1}\text{cm}^{-1}$, $\Phi_T = 0.20$).⁵⁹

6.2.3. Singlet oxygen quantum yields

Quantum yields for singlet oxygen formation were determined according to the direct method by measuring sensitized singlet oxygen emission centered at 1268 nm using a PTI Quantamaster equipped with a Hamamatsu R5509-42 near-infrared PMT. The PF_6^- salts of the metal complexes were prepared at 5 μM in spectroscopic-grade CH_3CN under an ambient atmosphere (21% O_2). Quantum yields for singlet oxygen emission (Φ_Δ) were calculated relative to the standard $[\text{Ru}(\text{bpy})_3](\text{PF}_6)_2$ ($\Phi_\Delta = 0.56$ in aerated CH_3CN)⁶⁰ according to Eq 1, where I , A , and η are integrated emission intensity, absorbance at the excitation wavelength, and refractive index of the solvent, respectively. The calculated Φ_Δ values were reproducible to within $<5\%$.

$$\Phi_\Delta = \Phi_{\Delta s} \left(\frac{I}{A} \right) \left(\frac{A_s}{I_s} \right) \left(\frac{\eta^2}{\eta_s^2} \right) \quad (6.1.)$$

6.2.4. DFT calculations

Density functional theory (DFT) and time-dependent DFT (TDDFT) calculations on Ir(III) complexes were performed using Gaussian09 quantum software package.⁶¹ The basis sets used in all calculations are LANL2DZ⁶²⁻⁶⁴ for Ir(III) and 6-31G*⁶⁵⁻⁶⁹ for other non-metal atoms. Unlike the previous Ir(III) complexes studied,^{25,70,71} complexes **6-1** – **6-5** have two metal centers

connected by fluorenylbisterpyridyl ligand, which makes long-range interactions critical for the description of both geometry and excited state properties. Therefore, here we used the long-range corrected hybrid function, ω B97XD, which was designed to capture long-range atom-atom dispersion.⁷² Implicit solvent effects were incorporated by the conductor-like polarizable continuous model (CPCM)^{73,74} simulating the effects of acetonitrile. The long aliphatic side chains on fluorene were replaced with butyl groups to reduce the computational cost. This reduction does not affect the optical properties of the complexes in the visible spectral region, since octyl groups do not contribute any electronic transitions in this energy range.

The absorption spectra for the Ir(III) complexes were generated by broadening the lowest 100 singlet vertical excitations computed by TDDFT^{75,76} using the functional and basis sets described above. To broaden the vertical excitation to generate spectra in terms of molar absorptivity units ($\text{L}\cdot\text{mol}^{-1}\cdot\text{cm}^{-1}$) the method described by Bjorgaard and co-workers was followed.⁷⁷ The shape of the spectra generated by broadening the vertical excitation computed by TDDFT quantitatively agreed well, except for about ~ 0.6 eV blue-shift, which is expected for the ω B97XD functional applied to conjugated systems.⁷⁸ To align the theoretical spectra with the experimental spectra, all transitions energy were red-shifted by -0.55 eV. To characterize the type of excitation for the Ir(III) complexes, natural transition orbitals (NTOs)⁷⁹ were generated using Gaussian09 software. NTOs allow for representing an excitation as the electron and hole pair, while preserving the many-body nature of the excited states. Due to the high symmetry of these dinuclear complexes, multiple transition densities that only differ on which metal center electronic density is localized contribute to some excitations. Therefore, only uniquely representative NTOs are shown for those excitations and those states are indicated by “*” in Tables 6-2 and 6-3. The

visualization of the NTOs were done utilizing Visual Molecular Dynamics (VMD)⁸⁰ with isosurface of 0.02.

6.2.5. Photobiological activity studies

The experimental details for cell culture, cytotoxicity and photocytotoxicity studies, confocal microscopy, and DNA mobility-shift assays are the same as those described in our previous published work.^{24,25}

6.3. Results and discussion

6.3.1. Electronic absorption

The experimental UV–vis absorption spectra of complexes **6-1** – **6-5** were recorded in acetonitrile (Figure 6.1a), and the absorption band maxima and molar extinction coefficients are compiled in Table 6.1. The absorption obeys Beer’s law in the concentration range of 5×10^{-6} to 1×10^{-4} mol·L⁻¹, suggesting the absence of ground–state aggregation in the concentration range tested. The strong absorption bands in the range of 250–350 nm and 350–500 nm are predominantly assigned to ¹ π, π^* transitions localized on the terminal tridentate ligands, and the bridging ligand, respectively. These assignments are supported by the NTOs corresponding to the major transitions contributing to these bands (Table 6.2 and Table 6.3). Attribution of the absorption bands of 350–500 nm to the bridging ligand localized ¹ π, π^* transition is in line with that revealed in the dinuclear Ir(III) complexes with trisbidentate ligands and diethynylaryl substituted diketopyrrolopyrrole bridging ligand.^{81,82} However, NTOs of **6-1** – **6-4** in Table 6.2 show that some charge transfer transitions, *i.e.* ¹MLCT, ¹LLCT (ligand-to-ligand charge transfer) or ¹ILCT (intraligand charge transfer) contributed to the 350–500 nm bands as well. Contributions of the charge transfer

configurations to the 350-500 nm absorption bands are partially reflected by the insignificant but noticeable negative solvatochromic effects (Figure 6.2), especially in **6-2** that has more $^1\text{ILCT}$ character (see NTOs in Table 6.2). In contrast, the charge transfer transitions in **6-5** became more distinguishable and energetically separated from the bridging ligand localized $^1\pi,\pi^*$ transition. This is clearly evidenced by the appearance of the new absorption band at 520 nm in **6-5**.

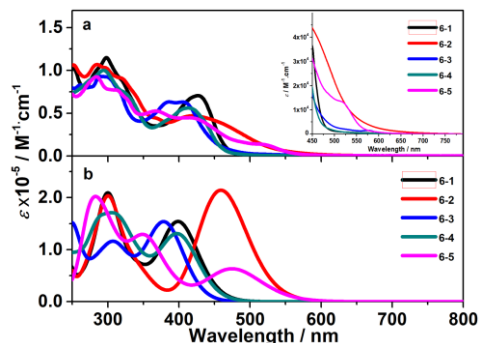


Figure 6.1. Experimental (a) and theoretical (b) UV-vis absorption spectra of **6-1** – **6-5** at room temperature in acetonitrile. The inset in panel (a) is the expansion of the spectra in the region of 450–800 nm. The theoretical spectra were computed using ωB97XD with mixed basis set. A redshift of 0.55 eV for the theoretical spectra in panel (b) was applied for better comparison with the experimental spectra.

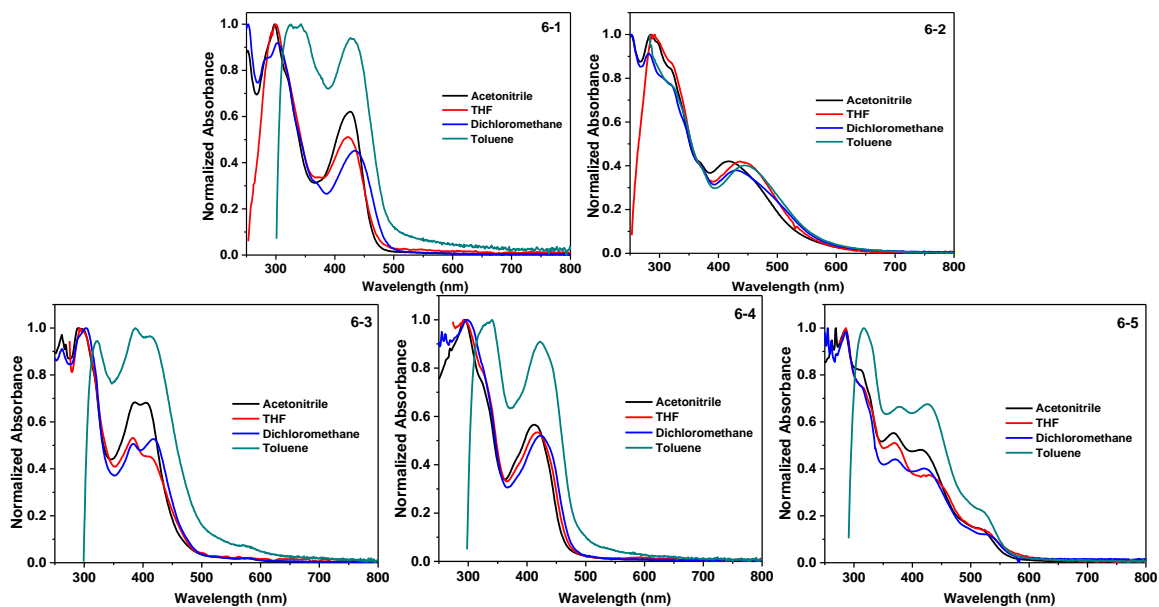


Figure 6.2. Normalized experimental absorption spectra of **6-1** – **6-5** in different solvents.

Table 6.1. Electronic absorption, emission, and triplet excited-state absorption parameters, as well as singlet oxygen quantum yields for complexes **6-1** – **6-5**.

	$\lambda_{\text{abs}}/\text{nm}$ ($\log \varepsilon$ / $\text{L}\cdot\text{mol}^{-1}\cdot\text{cm}^{-1}$) ^a	$\lambda_{\text{em}}/\text{nm}$ ($\tau_{\text{em}}/\mu\text{s}$); $\Phi_{\text{em}}^{\text{b}}$	$\lambda_{\text{T1-Tn}}/\text{nm}$ ($\tau_{\text{TA}}/\mu\text{s}$; $\log \varepsilon_{\text{T1-Tn}} / \text{L}\cdot\text{mol}^{-1}\cdot\text{cm}^{-1}$); $\Phi_{\text{T}}^{\text{c}}$	Φ_{Δ}^{d} ($\lambda_{\text{ex}}/\text{nm}$)
6-1	251 (5.01), 297 (5.06), 427 (4.85)	583 (3.57); 0.024	498 (3.09; -), 765 (3.05; 4.62); 0.44	0.28 (430)
6-2	251 (5.03), 285 (5.03), 364 (4.65), 420 (4.68)	576 (1.99); 0.003	385 (1.72; -), 640 (1.75; 5.04); 0.03	0.26 (468)
6-3	260 (4.92), 289 (4.97), 386 (4.80), 405 (4.80)	608 (1.47); 0.025	513 (0.03 (17%), 1.72 (83%); -), 770 (0.03 (15%), 1.75 (85%)); 4.70); 0.14	0.04 (411)
6-4	294 (5.00), 321 (4.88), 413 (4.75)	578 (53.3); 0.22	498 (48.6; -), 800 (48.3; 4.64); 0.28	0.38 (418)
6-5	283 (4.97), 312 (4.89), 368 (4.72), 416 (4.65), 520 (4.13)	619 (1.92); 0.045	681 (2.68; 4.80), 787 (2.68; -); 0.07	0.22 (418)

^aAbsorption band maxima (λ_{abs}) and molar extinction coefficients ($\log \varepsilon$) of the UV-vis absorption in acetonitrile at room temperature. ^bEmission band maxima (λ_{em}), lifetimes (τ_{em}), and quantum yields (Φ_{em}) measured in acetonitrile ($c = 1 \times 10^{-5} \text{ mol}\cdot\text{L}^{-1}$) at room temperature with $\text{Ru}(\text{bpy})_3\text{Cl}_2$ (in degassed acetonitrile; $\Phi_{\text{em}} = 0.097$, $\lambda_{\text{ex}} = 436 \text{ nm}$) as the reference. ^cNanosecond TA band maxima ($\lambda_{\text{T1-Tn}}$), triplet excited-state lifetimes (τ_{TA}), triplet extinction coefficients ($\varepsilon_{\text{T1-Tn}}$), and quantum yields (Φ_{T}) measured in acetonitrile at room temperature with SiNc (in degassed benzene; $\varepsilon_{590} = 70,000 \text{ L}\cdot\text{mol}^{-1}\cdot\text{cm}^{-1}$, $\Phi_{\text{T}} = 0.20$) as the reference. $\lambda_{\text{ex}} = 355 \text{ nm}$. ^dSinglet oxygen quantum yields in acetonitrile. Values are correct to within $\pm 5\%$.

Table 6.2. NTOs for low energy transitions of **6-1** – **6-5**. For transitions with quasi-degenerate transition orbitals, only one pair of transition densities are shown and are indicated by *.

	S_{n}	Hole	Electron	S_{n}	Hole	Electron
6-1	S_1 340 nm $f = 2.637$			S_1 351 nm $f = 0.003$		
	S_5 303 nm $f = 0.109$			S_2 350 nm $f = 0.004$		
6-2	S_1 381 nm $f = 3.730$			S_3^* 340 nm $f = 2.002$		
	S_2^* 336 nm $f = 0.079$			S_1^* 395 nm $f = 0.933$		
6-3	S_1 333 nm $f = 0.010$			S_6^* 372 nm $f = 0.050$		
	S_3 328 nm $f = 2.189$					
	S_7 311 nm $f = 0.368$					

Table 6.3. Natural transition orbitals (NTOs) for high energy transitions for **6-1** – **6-5**. Transition with quasi-degenerate transition orbitals only one pair of transition densities are shown and are indicated by *.

	State	Hole	Elec.	State	Hole	Elec.	
6-1	S ₇ [*] 291 nm f = 0.717			6-4	S ₈ [*] 302 nm f = 0.650		
	S ₂₇ [*] 264 nm f = 1.256				S ₁₉ 281 nm f = 0.449		
	S ₃₅ [*] 249 nm f = 0.674				S ₂₃ [*] 270 nm f = 0.620		
6-2	S ₇ [*] 292 nm f = 0.707			S ₃₃ [*] 255 nm f = 1.139			
	S ₂₄ [*] 270 nm f = 0.723			6-5	S ₉ [*] 328 nm f = 0.395		
	S ₂₉ [*] 264 nm f = 1.121				S ₁₅ 305nm f = 1.775		
	S ₃₉ [*] 249 nm f = 0.547				S ₃₈ [*] 260 nm f = 0.889		
	S ₂₃ 275 nm f = 0.494				S ₅₃ [*] 247 nm f = 0.718		
S ₃₂ [*] 260nm f = 0.437							
6-3	S ₃₅ [*] 249nm f = 0.571						

Comparison of the absorption spectra of **6-1** and **6-2** revealed that incorporation of the C≡C bonds to the bridging ligand caused a broadening and a red-shift of the bridging ligand localized ¹π,π* absorption band due to the extended π-conjugation. Replacing the terminal terpyridyl ligands in **6-1** by N[^]C[^]N (1,3-dipyridyl-4,6-dimethylbenzene) ligands in **6-3** induced a blue-shift of the 350-500 nm absorption band and incorporated more terminal ligands based ¹π,π* transition and ¹LLCT/¹MLCT character to this band (see NTOs for **6-3** in Table 6.2); while changing the terminal ligands to C[^]N[^]N (4,6-diphenyl-2,2'-bipyridine) ligands in **6-4** only caused a slight blue-shift of this band with respect to that in **6-1**. In contrast, when the terminal ligands were changed to C[^]N[^]C (2,4,6-triphenylpyridine) ligands in **6-5**, the transition energies, intensities, and the shape of the low-energy absorption bands changed pronouncedly from those of **6-1**. This can be attributed to

the distinct nature of the lowest energy optical transition in these two complexes. As the NTOs in Table 6.2 indicated, the stronger σ -donating ability of the phenyl rings on the C^NC ligand delocalized the hole of the S₁ transition mainly to the 2,6-diphenyl rings and to the metal d orbitals, while the electron was predominantly on the terpyridyl ligands. Thus, the lowest-energy optical transition in **6-5** is predominantly the ¹LLCT/¹MLCT transition, which is in contrary to the bridging ligand localized ¹ π,π^* transition in **6-1**. The drastic change of the dominant optical transitions accounts for the different features of the low-energy absorption bands in **6-5** with respect to that in **6-1**.

6.3.2. Photoluminescence

The emission of **6-1** – **6-5** was investigated in different solvents at room temperature. The observed emission all exhibited large Stokes shifts with respect to the corresponding excitation wavelength, they were all long-lived (several to tens of μs), and sensitive to the presence of oxygen. Thus, the emission was attributed to phosphorescence. The normalized emission spectra of **6-1** – **6-5** in acetonitrile are presented in Figure 6.3, and the spectra in other solvents are provided in Figure 6.4. The emission parameters are listed in Table 6.1 and Table 6.4. The emission of **6-1** and **6-4** resembled each other, both showing some vibronic structures, with much longer lifetimes and higher emission quantum yields compared to the other three complexes, and exhibiting minor solvatochromic effects. The vibronic spacing between the 580 nm and 620 nm bands is approximately 1150 cm^{-1} and 1090 cm^{-1} in **6-1** and **6-4**, respectively, which is in accordance with the aromatic vibrational mode of the terpyridyl ligands. Thus, the emission of these two complexes can be assigned predominantly to the ligand localized ³ π,π^* state. However, the lifetime of **6-1** is one order of magnitude shorter than that of **6-4**. This could be attributed to the weaker ligand field

of the terpyridyl ligand with respect to that of the C[^]N[^]N ligand that contains the stronger σ -donating 6-phenyl ring. The nonradiative metal-centered 3d,d state is thus situated more closely to the low-lying emissive $^3\pi,\pi^*$ state and becomes thermally accessible in **6-1** compared to that in **6-4**. This adds an additional decay path for the emitting $^3\pi,\pi^*$ state in **6-1** and consequently reduces its lifetime. For **6-2**, **6-3**, and **6-5**, the emission spectra are featureless and broader, the lifetimes are less than 2 μ s and the emission quantum yields are quite low, and the solvatochromic effect is more pronounced. All these characters imply charge transfer nature of the emitting states in these three complexes. Referring to the NTOs corresponding to the low-energy singlet charge transfer transitions shown in Table 6.2, it is reasonable to speculate that the emitting state of **6-2** could be the 3ILCT state and they are the $^3LLCT/^3MLCT$ states in **6-3** and **6-5**. It appeared that either extending the π -conjugation of the bridging ligand in **6-2**, or varying the terminal tridentate ligands in **6-3** and **6-5** changed the nature of the emitting state from the $^3\pi,\pi^*$ state in **6-1** to 3CT states. In addition, variation of the terminal tridentate ligands impacted the emission energies in **6-3** – **6-5** compared to that in **6-1**, with a slight blue-shift of the emission in **6-4** while a salient red-shift in **6-3** and **6-5**. The red-shifted emission in **6-3** and **6-5** with respect to that in **6-1** could possibly be rationalized by the stronger σ -donating ability of the phenyl rings on the terminal tridentate N[^]C[^]N and C[^]N[^]C ligands, which raised the energies of the terminal ligand and the metal d orbital based holes and thus reduced the energy gaps between the holes and electrons (likely localized on the terpyridyl motifs). Consequently, the $^3LLCT/^3MLCT$ emission energies of **6-3** and **6-5** are reduced.

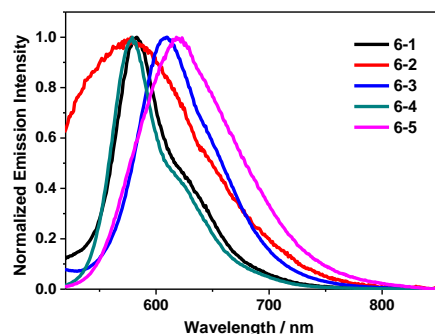


Figure 6.3. Experimental emission spectra of **6-1** ($\lambda_{\text{ex}} = 426$ nm), **6-2** ($\lambda_{\text{ex}} = 420$ nm), **6-3** ($\lambda_{\text{ex}} = 405$ nm), **6-4** ($\lambda_{\text{ex}} = 413$ nm), and **6-5** ($\lambda_{\text{ex}} = 415$ nm) at room temperature in deoxygenated acetonitrile ($c = 1 \times 10^{-5}$ mol·L $^{-1}$).

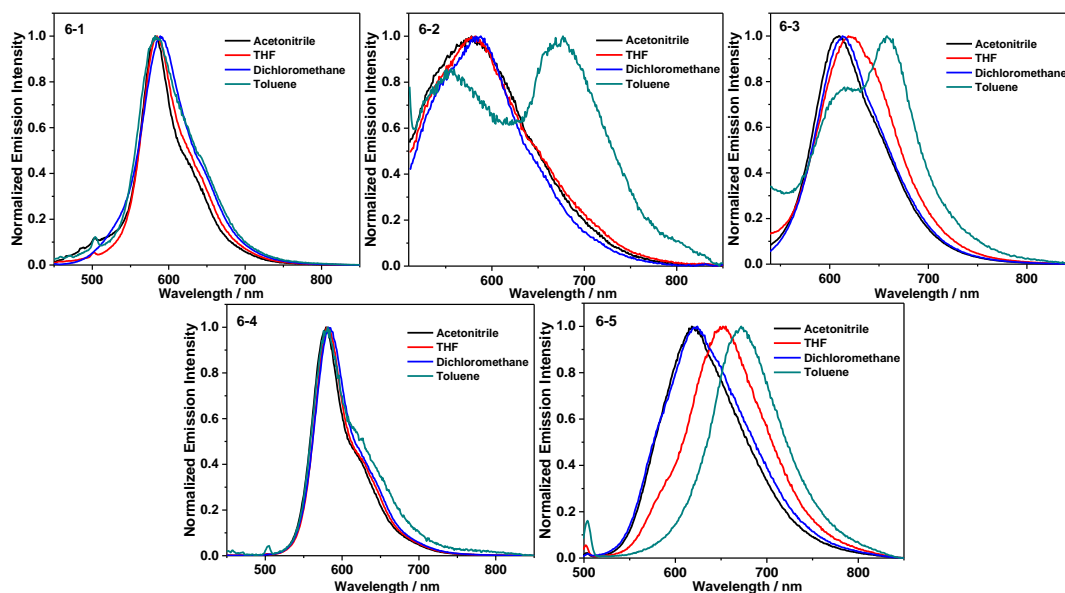


Figure 6.4. Normalized emission spectra of **6-1** – **6-5** in different solvents ($\lambda_{\text{ex}} = 436$ nm).

Table 6.4. Emission characteristics of complexes **6-1** – **6-5** in different solvents at room temperature.

	λ_{em} (nm) (τ_{em} / μs); Φ_{em}		
	THF	DCM	Toluene (5%DCM)
6-1	586 (4.27); 6.82%	590 (2.71); 24.5%	584 (0.06); 1.99%
6-2	579 (1.56); 0.44%	584 (1.78); 0.63%	555 (0.06); 0.35%
6-3	620 (1.64); 3.25%	614 (1.54); 3.65%	659 (0.06); 0.65%
6-4	581 (37.4); 31.8%	583 (69.7); 54.9%	581 (0.04); 3.36%
6-5	651 (1.28); 3.87%	623 (1.61); 5.18%	672 (0.99); 1.15%

6.3.3. Transient absorption

To further understand the triplet excited-state characteristics, the nanosecond transient absorption (TA) studies of complexes **6-1** – **6-5** were carried out in acetonitrile solutions. The TA spectra of **6-1** – **6-5** at zero delay after excitation are presented in Figure 6.5 and the TA parameters are compiled in Table 6.1. The time-resolved TA spectra of **6-1** – **6-5** are provided in Supporting Information Figure 6.6. The triplet lifetimes deduced from the decay of TA for **6-1** – **6-4** are similar to their emission lifetimes in acetonitrile. Therefore, we consider that the observed TA of these complexes was from the excited states that emit. In contrast, **6-3** exhibited a biexponential decay in its TA signals, with the longer lifetime being consistent with the emission lifetime. This implies that the long-lived TA signal in **6-3** could from the emitting excited state as well.

The TA spectra of **6-1** – **6-5** all possessed very broad positive absorption band(s) from the visible to the near-IR region, *i.e.* 463-800 nm for **6-1**, 495-800 nm for **6-2**, 459-800 nm for **6-3**, 455-800 nm for **6-4**, and 538-800 nm for **6-5**. Bleaching occurred in the region corresponding to the low-energy absorption bands. Considering the similar shape of the TA spectra of **6-1** and **6-4** to that of the dinuclear platinum(II) complex with the same bridging ligand reported by our group previously,⁴⁸ and the similar lifetimes to those of emission, we tentatively assign the excited state giving rise to the observed TA predominantly to the bridging ligand localized $^3\pi,\pi^*$ states. While for **6-2** and **6-5**, the transient absorbing states are likely to be the ^3CT state(s), *i.e.* predominantly $^3\text{ILCT}$ for **6-2** and $^3\text{LLCT}/^3\text{MLCT}$ states for **6-5**. In contrast to **6-1**, **6-2**, **6-4** and **6-5** that exhibited monoexponential decays in their TA signals, the TA signal of **6-3** followed a biexponential decay. The short-lived transient species had a lifetime of ~30 ns and gave rise to a spectrum reminiscent to those of **6-1** and **6-4**; while the long-lived species had a lifetime of ~1.7 μs , which is in line with the lifetime obtained from the decay of emission, and the TA was much weaker and featureless. In

view of the different spectral features at the shorter and longer decay time and the reminiscence of the spectra to those of **6-1/6-4** and **6-2/6-5**, respectively, we tentatively assign the short-lived species to the high-lying bridging ligand localized $^3\pi,\pi^*$ state; while the long-lived species to the emitting $^3\text{LLCT}/^3\text{MLCT}$ state. The formation of a rapidly decaying higher excited state that subsequently leads to the lower-lying, long-lived emitting state has been reported for a mononuclear Ir(III) complex $[(\text{dpb})\text{-Ir}(\text{tpy-ph}(t\text{Bu})_2)]^{2+}$ that bears the same N^C^N ligand.⁸³

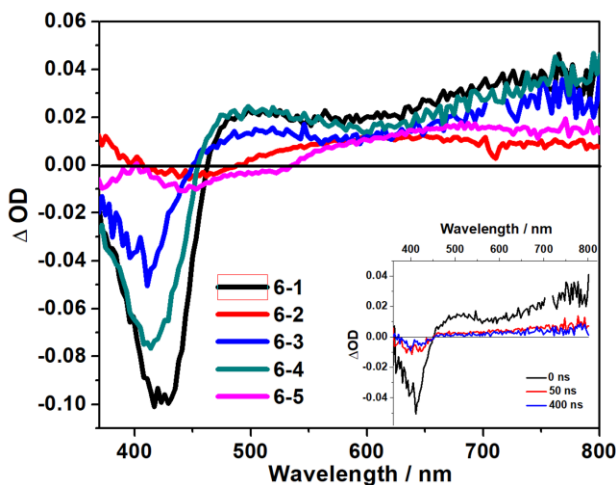


Figure 6.5. Nanosecond transient absorption (TA) spectra of complexes **6-1** – **6-5** in deoxygenated acetonitrile at zero delay after 355 nm excitation. The inset shows the TA spectra of **6-3** at different delay time after excitation. $A_{355\text{ nm}} = 0.4$ in a 1-cm cuvette.

It is noted that the measured triplet quantum yields of these complexes are not quite high, especially for **6-2**, **6-3** and **6-5**. This could be due to the following reasons: (i) The increased π -conjugation of the ligand would decrease the contribution of the transition metal d orbital to the frontier molecular orbitals of the complexes, which would reduce the spin-orbital coupling in the complexes and decrease the triplet quantum yield. Such a phenomenon has been reported in many Pt(II) and Ir(III) complexes.^{25,70,84} (ii) When a transition-metal complex is excited, especially when high-energy excitation is utilized, population of more than one triplet excited states is possible.^{70,85-91} However, not all of the populated triplet excited states contribute to excited-state

absorption. In such a case, the calculated triplet quantum yield based on the observed TA signal could be significantly lower than the actual intersystem crossing quantum yield.

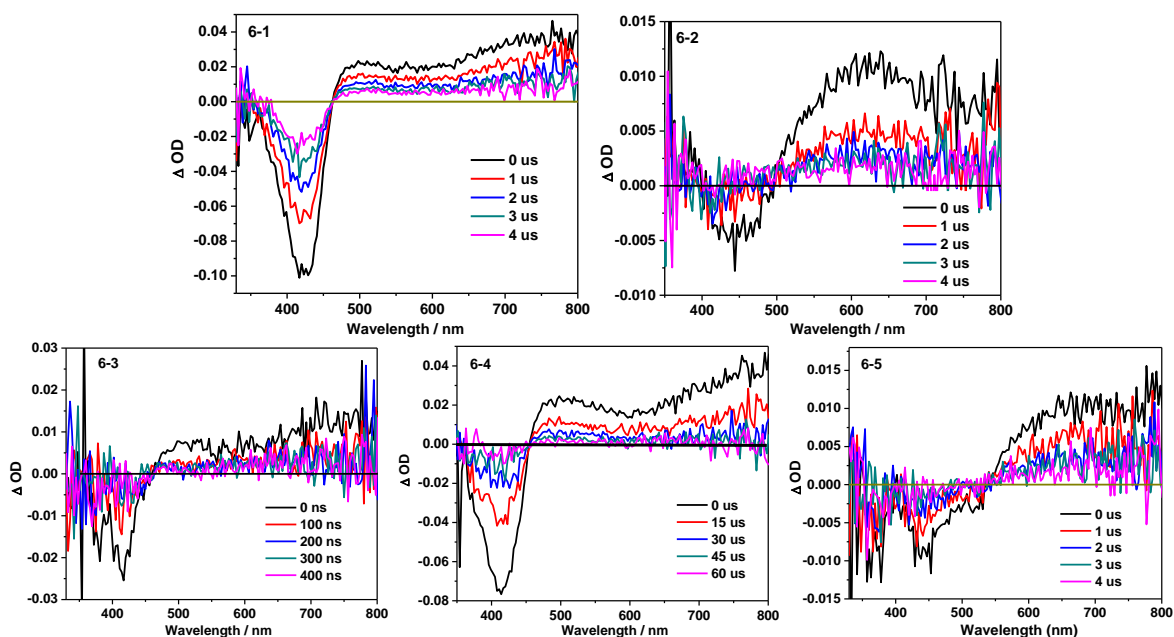


Figure 6.6. Nanosecond time-resolved transient differential absorption spectra of **6-1** – **6-5** at zero-time decay in acetonitrile. $\lambda_{\text{ex}} = 355 \text{ nm}$, $A_{355} = 0.4$ in a 1-cm cuvette.

6.3.4. Singlet oxygen generation

Production of $^1\text{O}_2$ is known to have cytotoxic effects on cells, and thus compounds that generate $^1\text{O}_2$ under cell-free conditions might be expected to act as *in vitro* PDT agents. The Ir(III) complexes **6-1** – **6-5** were assessed for singlet oxygen ($^1\text{O}_2$) sensitization in cell-free conditions through direct measurement of $^1\text{O}_2$ emission at 1270 nm. $[\text{Ru}(\text{bpy})_3](\text{PF}_6)_2$ was used as the standard, with a reported $^1\text{O}_2$ quantum yield (Φ_Δ) of 0.56 in air-saturated CH_3CN .⁶⁰ The calculated Φ_Δ values for all of the complexes were less than 40%. The efficiencies for $^1\text{O}_2$ production ranged from 4% for **6-3** to 38% for **6-4**, with **6-1**, **6-2** and **6-5** yielding similar values (22-28%). Despite having some absorption at wavelengths longer than 500 nm, $^1\text{O}_2$ yields were maximal with blue excitation. For $\text{N}^{\wedge}\text{N}^{\wedge}\text{N}$ terminal tridentate ligands, the presence of the ethynyl groups for extending π -conjugation did not alter the singlet oxygen quantum yield as **6-1** and **6-2** gave very similar

values for Φ_{Δ} . When each terminal tridentate ligand of **6-1** had two of its nitrogens replaced with cyclometalating carbons (C^{^N^C}) as in **6-5**, the ¹O₂ yield decreased only slightly. These limited comparisons appear to indicate that substantial structural changes have little to no effect on Φ_{Δ} . However, when only one nitrogen of each terminal tridentate ligand of **6-1** was replaced by carbon (C^{^N^N}) as in **6-4**, the ¹O₂ yield increased to almost 40%. Clearly, there are structural combinations in this family of complexes that do influence Φ_{Δ} . The most dramatic impact on Φ_{Δ} occurred for **6-3**, where the terminal tridentate ligands were N^{^C^N} with methyl substitution at R₁ but no phenyl group at R. In this case, the ¹O₂ yield decreased by almost tenfold.

It is also worthy of noting that the Φ_{Δ} values for **6-2**, **6-4** and **6-5** are higher than the measured triplet quantum yields (Φ_{T} , Table 6.1). This is not very surprising because population of excited states is wavelength dependent, which could result in different decay pathways.⁹¹ In the Φ_{T} measurement, 355 nm excitation was used; while low-energy excitation (*i.e.* 411 – 468 nm) was used in the Φ_{Δ} measurement. A 355-nm excitation in the TA measurement could populate more than one triplet excited states,^{70,85-91} which might not only impact the Φ_{T} value measurement as discussed in the TA section, but could also reduce the population of the excited state that generates singlet oxygen because of the competing population of the other non-¹O₂-generating triplet excited states. In our previous study on the monocationic tris-bidentate Ir(N^{^N})(C^{^N})₂ complexes, we have demonstrated that the singlet oxygen generation efficiency is wavelength dependent, with lower-energy excitation resulting in higher Φ_{Δ} values in those Ir(III) complexes.²⁴ We speculate the same case for the complexes studied in this work.

6.3.5. Cytotoxicity and photocytotoxicity

To understand whether the photophysical properties of these Ir(III) complexes could lead to photobiological effects, the cytotoxicity profiles of **6-1** – **6-5** were assessed in SK-MEL-28 malignant melanoma cells under three conditions: (i) dark, (ii) illumination with broadband visible light, and (iii) illumination with red LEDs emitting at 625 nm. Cytotoxic and photocytotoxic activities were quantified as the effective concentration required to reduce the cell viability to 50% (EC_{50}) under a given condition. Briefly, cells growing in log phase were dosed with nine concentrations of the complex between 1 nM and 300 μ M, incubated for 16 h, and were then subjected to a sham (dark) or light treatment. The light treatments were delivered at a fluence of 100 $J \cdot cm^{-2}$ with an irradiance of 35.7 $mW \cdot cm^{-2}$ or 32.3 $mW \cdot cm^{-2}$ for visible and red light, respectively. After a 48 h incubation period, cell viability was quantified based on the ability of viable cells to reduce resazurin to resorufin. EC_{50} values were determined from sigmoidal fits of the dose–response curves (Figure 6.7, Table 6.5). The phototherapeutic index (PI), a measure of the therapeutic margin for *in vitro* PDT, was calculated as the ratio of dark to light EC_{50} values and determined for each complex and irradiation condition. The dark toxicities of **6-1** – **6-5** toward normal human skin fibroblasts (CCD-1064Sk) were also measured to determine any selectivity for cancer cells over normal cells. The ratio of the dark CCD-1064Sk EC_{50} value for a given complex and its dark SK-MEL-28 EC_{50} value yielded the selectivity factor (SF), where $SF > 1$ indicates selectivity toward the cancerous cell line. Selective activity toward the cancer cell line is not a requirement for the PDT agent as long as the dark toxicity of the photosensitizer is low, and the PI is relatively large. Rather, the spatiotemporal control of the light treatment provides the selectivity known for PDT. Nevertheless, for *in vivo* applications, selective activity toward cancer cells over normal, healthy cells is an added benefit.

Table 6.5. Comparison of EC₅₀ values (μM) for SK-MEL-28 cancer cells and CCD-1064Sk normal skin fibroblasts dosed with complexes **6-1** – **6-5**.

	SK-MEL-28 cells					CCD-1064Sk cells	
	Dark	Vis ^a	PI ^b	Red ^c	PI ^d	Dark	SF ^e
6-1	82.6 \pm 1.5	0.75 \pm 0.01	111	59.7 \pm 0.4	1.4	102 \pm 2	1.2
6-2	16.9 \pm 0.8	0.83 \pm 0.05	20	16.2 \pm 0.5	1.0	32.0 \pm 2.0	1.9
6-3	49.9 \pm 0.1	0.17 \pm 0.01	288	49.5 \pm 0.1	1.0	49.1 \pm 0.1	1.0
6-4	17.0 \pm 0.7	0.17 \pm 0.01	102	14.3 \pm 0.3	1.2	31.8 \pm 1.8	1.9
6-5	69.5 \pm 1.0	1.05 \pm 0.01	66	85.1 \pm 1.0	0.82	142 \pm 3	2.0

^aVis-PDT: 16 hours drug-to-light interval followed by 100 J·cm⁻² broadband visible light irradiation, ^bPI = phototherapeutic index (ratio of dark EC₅₀ to visible-light EC₅₀), ^cRed-PDT: 16 hours drug-to-light interval followed by 100 J·cm⁻² light irradiation with 625-nm LEDs, ^dPI = phototherapeutic index (ratio of dark EC₅₀ to red-light EC₅₀), ^eSF SK-MEL-28: selectivity factor (ratio of dark CCD-1064Sk EC₅₀ to dark SK-MEL-28 EC₅₀).

The dark cytotoxicities of complexes **6-1** – **6-5** toward SK-MEL-28 melanoma cells ranged from 16.9 to 82.6 μM , with **6-1** being the least cytotoxic in the absence of a light trigger and **6-2** and **6-4** being the most cytotoxic (Table 6.5, Figures 6–7, and Figures 6–8). With the exception of **6-3** (SF = 1), the other dinuclear Ir(III) complexes exhibited some selective cytotoxicity toward the melanoma cancer cells relative to the normal human skin fibroblast cells. SF values followed the order **6-5** > **6-2** \approx **6-4** > **6-1** > **6-3**, with **6-5** exhibiting two-fold greater dark toxicity toward SK-MEL-28 cells and **6-3** showing no selectivity. The selective cytotoxicity observed for **6-2** and **6-4** was almost as great as that for **6-5** (SF = 1.9 versus SF = 2.0). **6-1** and **6-5** had dark EC₅₀ values greater than 100 μM in the CCD-1064Sk cell line, and were thus considered to be completely nontoxic to the normal skin fibroblasts. In both cell lines, the dark toxicity was greatest for **6-2** and **6-4** and least for **6-1** and **6-5**.

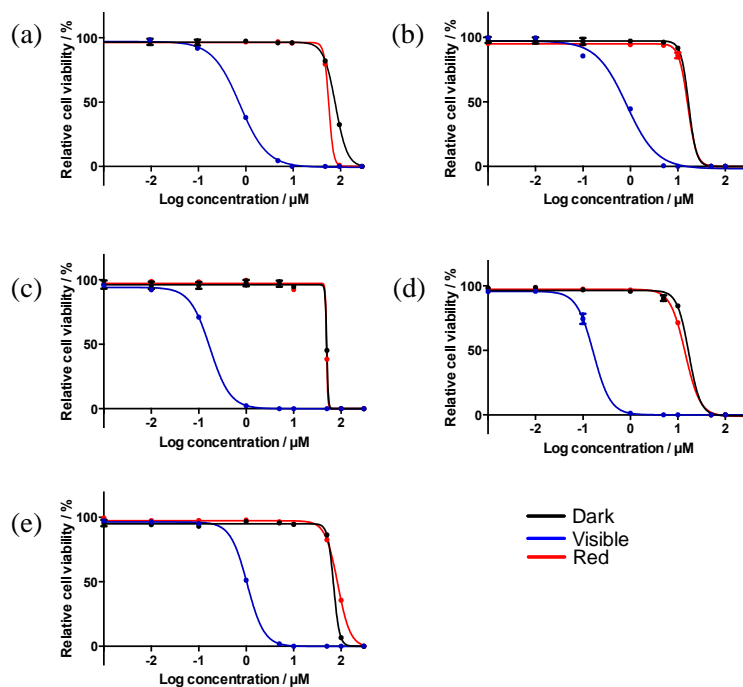


Figure 6.7. *In-vitro* dose-response curves for complexes **6-1** (a), **6-2** (b), **6-3** (c), **6-4** (d), and **6-5** (e) in SK-MEL-28 cells treated in the dark (black) and with visible (blue) or red (red) light activation.

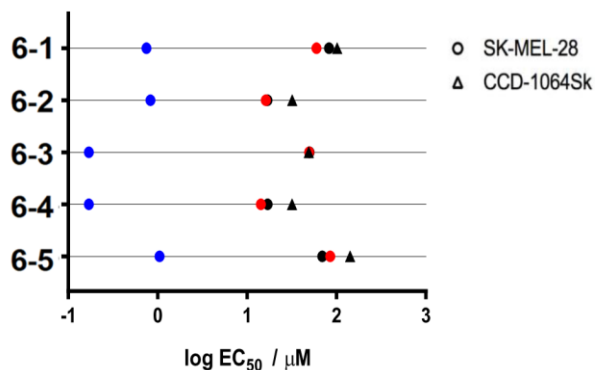


Figure 6.8. Activity plot for complexes **6-1** – **6-5** in SK-MEL-28 and CCD-1064Sk cells treated in the dark (black) and with visible (blue) or red (red) light activation.

All of the complexes in the series could be activated with visible light to become powerful phototoxins, with EC_{50} values ranging from 170 nM to 1 μ M and PIs ranging from 20 to 288. **6-3** and **6-4** were the most phototoxic at 170 nM, while **6-1**, **6-2**, and **6-5** were similar (visible EC_{50} = 0.75–1.0 μ M). Photoactivation of the complexes with red light (625 nm) did not enhance the

cytotoxicity over what was observed in the dark treatment, yielding PIs close to 1.0 in all cases. The photobiological activities of **6-1** – **6-5** were tested with red light, despite their very low molar extinction coefficients in this region, because other metal complex systems with π -expansive ligands have been shown to yield potent *in vitro* red PDT effects even with molar extinction coefficients less than $100 \text{ M}^{-1} \cdot \text{cm}^{-1}$.²⁰

The presence of visible PDT effects (presumably due to the shorter wavelengths) but lack of red PDT effects suggests that direct population of the highly photosensitizing triplet states is not efficient in this class of complexes and that access to these states must be gained through ¹MLCT states. The photocytotoxicity profiles in SK-MEL-28 under two irradiation conditions along with the dark cytotoxicity profiles in two cell lines are summarized in the activity plot in Figure 6.8.

The visible PDT effect followed the order **6-3** > **6-1** > **6-4** > **6-5** > **6-2**, with **6-3** being the most promising photosensitizer based on its PI of 288 and nanomolar photocytotoxicity. **6-1** and **6-4** both had PIs greater than 100, but the dark toxicity associated with **6-4** in both cell lines limits its potential for *in vivo* applications. The source of the PDT effect for this series has not been established. The ¹O₂ quantum yields measured under cell-free conditions followed the order **6-4** > **6-1** > **6-2** > **6-5** > **6-3**, with **6-1** and **6-2** being very similar. **6-3** was the poorest ¹O₂ generator, yet it was one of the most phototoxic complexes of the series. On the other hand, **6-4** was the best sensitizer of ¹O₂ and was as phototoxic as **6-3**. Therefore, ¹O₂ may play a role in the PDT mechanism for some complexes but not others in this series, or the intracellular ¹O₂ quantum yields may differ from those measured under cell-free conditions. Regardless, certain members of this new series of dinuclear Ir(III) complexes have been identified as promising PDT agents for further investigation.

While the structural diversity in such a small library is somewhat limited, it was possible to identify some trends regarding structural features that affect cytotoxicity. For example, incorporation of ethynyl linkers as in **6-2** turned the relatively nontoxic complex **6-1** into one of the most potent dark cytotoxic complexes of the series (Table 6.5). Likewise, replacement of the terminal tridentate N^NN ligands of **6-1** with C^NN as in **6-4** increased the dark cytotoxicity substantially, while replacement with C^NC as in **6-5** had only a very minor effect that differed between the two cell lines. In SK-MEL-28, the dark toxicity increased slightly, and in CCD-106Sk, the dark toxicity decreased slightly. The complex that departed the most structurally from the other complexes in the series and was identified as being the most promising PDT lead, **6-3**, was intermediate in terms of dark cytotoxicity ($EC_{50} \approx 50 \mu\text{M}$) with almost no difference between the two cell lines.

In terms of structural features affecting photocytotoxicity, the nature of the terminal tridentate ligand played some role as **6-4** (C^NN) was more than six-fold more phototoxic than **6-5** (C^NC). While the presence of an ethynyl linker increased the dark cytotoxicity substantially in both cell lines, its presence did not impact the photocytotoxicity toward SK-MEL-28 in any significant way. The differences in dark and light-triggered cytotoxicity toward SK-MEL-28 cells alongside differences in dark cytotoxicity between normal and cancerous cells for certain members of this series indicate that even minor structural modifications can have a major impact on biological activity.

6.3.6. Cellular imaging

The phosphorescence from complexes **6-1** – **6-5** was used to probe cellular uptake by SK-MEL-28 melanoma cells with or without a light treatment (Figure 6.9). The excitation from a

458/488 nm argon-krypton laser matched the excitation maxima of the complexes and was used in conjunction with a 475-nm long pass filter to collect the emission from the complexes. The images were collected after a brief 1-h incubation period to ensure that some viable cells remained. Light-treated cells were illuminated with a broadband visible light ($50 \text{ J} \cdot \text{cm}^{-2}$) that was 50% of the fluence used in the cellular assays in order to capture a fraction of viable cells.

Untreated SK-MEL-28 cells have a dendritic morphology. Treatment with the dinuclear Ir(III) complexes with or without illumination caused a conversion from dendritic to spherical morphology. The complexes showed detectable phosphorescence when associated with or in dead/dying and compromised cells with or without a light treatment. Only **6-1** appeared to be readily taken up into SK-MEL-28 cells in the dark at the observation time point. However, phosphorescence from the Ir(III) complexes in all cells was apparent after a light treatment, suggesting photoactivated uptake. For light-treated cells incubated with **6-1**, it was not possible to discern subcellular localization because only cellular debris was present at the observation time point. However, **6-2** and **6-4** localized to the cytoplasm and multiple nucleoli whereas **6-3** and **6-5** were distributed throughout the cell and phosphoresced with a very intense signal by comparison.

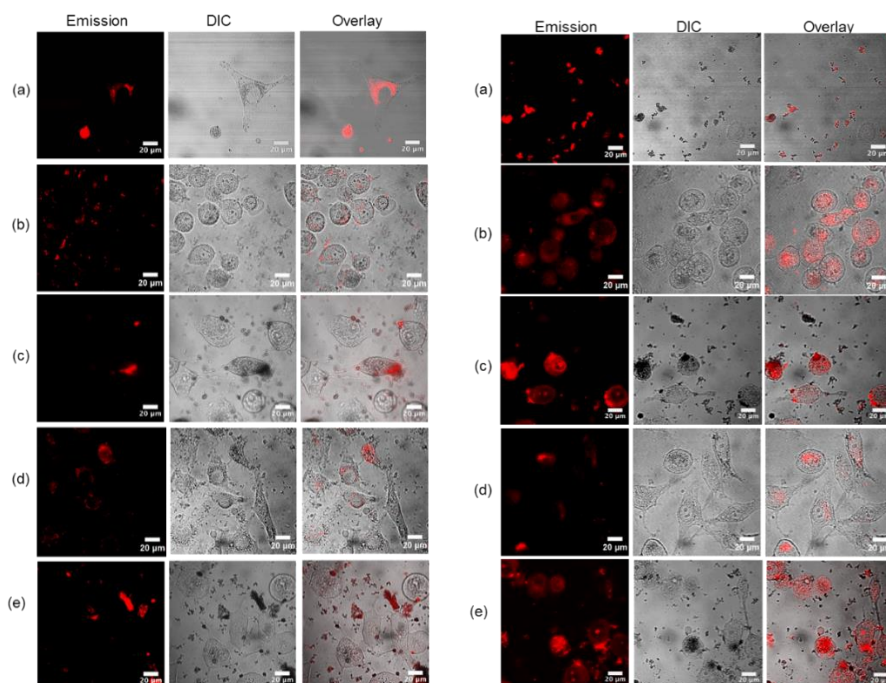


Figure 6.9. Confocal luminescence images of SK-MEL-28 cells dosed with **6-1** – **6-5** (a-e, 50 μM) in the dark (left) and with visible light (50 $\text{J}\cdot\text{cm}^{-2}$) (right).

Qualitatively, SK-MEL-28 cells treated with **6-4** with or without visible illumination appeared the most viable with healthy morphology in the imaging experiments but were the most susceptible in the cellular assays, highlighting the need to exercise caution when reconciling the cellular assay results with confocal imaging performed at different time points post-complex-delivery and post-irradiation and a different light fluence. When the conditions were similar, the imaging experiments did reflect the trends observed in the cellular assays with SK-MEL-28 but did not provide any information regarding uptake and localization since all cells were dead/dying but at slightly different stages. A quantitative comparison of the cellular uptake and induced morphological changes for the five complexes and correlations to cellular cytotoxicity or photocytotoxicity were not attempted given the need to alter incubation and illumination times to preserve some viable cells. Rather, the purpose of the imaging was to highlight the potential of

these new Ir(III) complexes as theranostic agents based on their abilities to yield visible PDT effects and to be simultaneously imaged by their inherent phosphorescence.

6.3.7. DNA interactions

The ability of the Ir(III) complexes to act as DNA photocleaving agents was investigated to establish whether light-mediated DNA damage could contribute to the observed *in vitro* PDT effects for this class of photosensitizers. Supercoiled plasmid DNA (20 μ M bases) was treated with increasing concentrations of **6-1** – **6-5** and then exposed to a visible light treatment of 14 J·cm⁻² (Figure 6.10, lanes 3–8). The fluence is less than what was used in the cellular assays because the DNA is more susceptible to damage by the light treatment alone when not protected by the cellular environment. The photolyzed samples were then electrophoresed and compared to DNA alone with or without a light treatment (Figure 6.10, lanes 1 and 2) and DNA exposed to the highest concentration of the complex without a light treatment (Figure 6.10, lane 15). The gels were cast either with the DNA stain ethidium bromide (EB) incorporated or without EB and stained after electrophoresis (non-EB). EB gels allow detection of photocleavage not compounded by DNA unwinding; the non-EB gels allow detection of DNA unwinding in addition to photocleavage. Under the conditions employed for this gel electrophoretic mobility shift assay, undamaged supercoiled DNA (Form I) migrates the farthest in the gel, while aggregated/condensed DNA (Form IV) migrates very little from the loading well. Plasmid DNA that has undergone single-strand breaks (Form II) will relax and migrate between Forms I and IV, and plasmid DNA with frank double-strand breaks or double-strand breaks that arise from the build-up of single-strand breaks on opposing strands within about 16 base pairs (Form III) will migrate slightly faster than Form II. Forms I, II, and IV were detectable in both EB and non-EB gels. None of the complexes

acted as DNA unwinders on the non-EB gel, indicating that they most likely do not act as DNA intercalators.

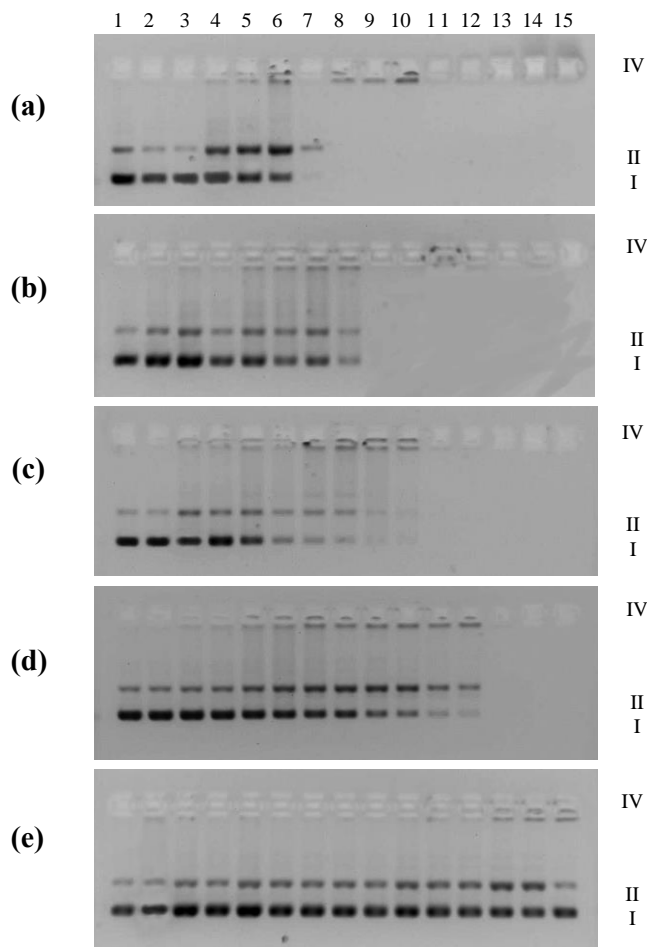


Figure 6.10. DNA photocleavage of pUC19 DNA (20 μM) dosed with metal complex (MC) 6-1 (a), 6-2 (b), 6-3 (c), 6-4 (d), 6-5 (e) and visible light ($14 \text{ J}\cdot\text{cm}^{-2}$). Gel mobility shift assays employed 1% agarose gels ($0.75 \mu\text{g}\cdot\text{mL}^{-1}$ ethidium bromide) electrophoresed in $1\times$ TAE at $8 \text{ V}\cdot\text{cm}^{-1}$ for 30 min. Lane 1, DNA only ($-h\nu$); lane 2, DNA only ($+h\nu$); lane 3, $0.5 \mu\text{M}$ MC ($+h\nu$); lane 4, $1 \mu\text{M}$ MC ($+h\nu$); lane 5, $2 \mu\text{M}$ MC ($+h\nu$); lane 6, $3 \mu\text{M}$ MC ($+h\nu$); lane 7, $5 \mu\text{M}$ MC ($+h\nu$); lane 8, $8 \mu\text{M}$ MC ($+h\nu$); lane 9, $10 \mu\text{M}$ MC ($+h\nu$); lane 10, $12 \mu\text{M}$ MC ($+h\nu$); lane 11, $15 \mu\text{M}$ MC ($+h\nu$); lane 12, $20 \mu\text{M}$ MC ($+h\nu$); lane 13, $50 \mu\text{M}$ MC ($+h\nu$); lane 14, $100 \mu\text{M}$ MC ($+h\nu$); lane 15, $100 \mu\text{M}$ MC ($-h\nu$). Forms I, II and IV DNA refer to supercoiled plasmid, nicked circular plasmid, and aggregated plasmid, respectively.

All of the complexes showed some ability to photocleave DNA (Figure 6.10) in a cell-free environment. Qualitatively, DNA photocleaving ability appeared to increase in the order **6-5** < **6-**

2 \approx **6-3** < **6-4** < **6-1**. The formation of Form IV DNA and the disappearance of gel bands precluded a more quantitative comparison, but some general trends could still be discerned.

Despite its $^1\text{O}_2$ quantum yield of 22%, **6-5** appeared to show the weakest interactions with DNA (although some strand breaks to yield detectable Form II⁹² were observed toward the highest concentrations). On the other hand, **6-1**, with a similar Φ_Δ , acted as a much more potent DNA photocleaving agent, converting a significant amount of supercoiled Form I DNA to Form II DNA at a metal complex (MC) concentration of only 1 μM and 20 μM DNA bases (Table 6.10a, lane 4). At similarly low [MC]:[bases] ratios of 0.05, **6-2** – **6-5** caused no detectable strand breaks, which can be seen by comparing lane 4 for all of the complexes. **6-4**, with the largest value for Φ_Δ , photocleaved DNA in a concentration-dependent manner to yield Form II DNA as expected.

All of the complexes caused DNA aggregation/condensation, although **6-5** produced trace amounts of Form IV DNA only at the highest complex concentrations investigated. Interestingly, **6-5** was the only complex that did not cause the DNA gel bands to disappear. The lack of DNA staining by EB for the other complexes could be due to fluorescence quenching of the EB dye by the complex, their competition for EB intercalation sites, or their distortion of the DNA helix that prevents EB binding.

Clearly, the structural differences between the Ir(III) complexes of this small library resulted in markedly different interactions with DNA, and possibly different photophysical interactions with the EB dye. The observation that **6-5** shows marginal DNA interactions in the gel electrophoretic analysis yet acts as an *in vitro* PDT agent suggests that DNA may not be the intracellular target, at least for this particular complex. In fact, DNA photodamage did not correlate clearly with $^1\text{O}_2$ quantum yields across the series, which also supports the notion that another biological target is likely involved. However, the cell-free experiment does not accurately mimic

the complexity of the cellular environment and dynamic processes (e.g., uptake, efflux, metabolism, and localization), and *in vitro* DNA damage and $^1\text{O}_2$ damage cannot be ruled out completely. What can be gleaned from the DNA photocleavage study is that minor structural changes in this series have profound effects on the complex interactions with biological macromolecules such as DNA, which is in agreement with their different profiles in the cellular assays and imaging studies.

6.4. Conclusions

The synthesis, photophysical and photobiological properties of a family of water-soluble cationic dinuclear iridium(III) complexes (**6-1** – **6-5**) were explored. The influence of the bridging and terminal ligands on the photophysical properties of the complexes was investigated. Compared to **6-1** that had the single bond connection between the fluorenyl motif and the terpyridyl ligands on the bridging ligand, the extended π -conjugation afforded by the ethynyl connectors of the bridging ligand in **6-2** red-shifted the UV-vis absorption markedly, but the low-lying ^3CT state of **6-2** accelerated nonradiative decay and resulted in weak phosphorescence. A considerable bathochromic shift also occurred in the absorption and emission of **6-5**, owing to the stronger σ -donating ability of the negatively charged coordinating carbon relative to nitrogen and thus more charge transfer from the C^NC ligands to the terpyridyl ligands. Complexes **6-1** – **6-5** all featured with broad positive absorption bands spanning the visible region and NIR regions in their nanosecond TA spectra. However, the triplet state TA lifetimes of **6-1** and **6-4** were much longer (3.1 μs and 48 μs , respectively) than those of **6-2**, **6-3** and **6-5**, implying the dominant bridging ligand-localized $^3\pi,\pi^*$ nature for the lowest triplet states in **6-1** and **6-4** rather than the ^3CT states

for the other three complexes. Based on photophysical properties alone, **6-4** was predicted to be the best *in vitro* PDT agent.

All of the Ir(III) complexes of this study exhibited photobiological effects when activated with visible light, but were inactive with single-wavelength red light (625 nm). Thus, the *in vitro* PDT effects with broadband visible light were attributed to the shorter wavelengths. Some of the complexes showed selective cytotoxicity toward cancerous human melanoma cells over normal human skin fibroblasts. The photobiological trends could not be readily correlated to any differences in photophysical properties despite accessible long-lived $^3\pi,\pi^*$ states often resulting in red PDT activity. But the long-lived **6-4** did not yield a red PDT effect, nor did any of the other complexes due to the lack of ground-state absorption in the red. Rather, **6-3** emerged as a promising photosensitizer for further investigation owing to its nanomolar photocytotoxicity and visible PI > 280, with **6-1** and **6-5** also having suitable profiles. This small library of just five complexes proved to be a rich source of photophysical and photobiological diversity with only minor structural modifications. They gave $^1\text{O}_2$ quantum yields that ranged from 4 to 38%, light EC₅₀ values from nanomolar to micromolar, dark toxicities that ranged from 32 to >140 μM , and DNA interactions that were characteristic for a particular cationic complex. For *in vitro* PDT applications in particular, there was a clear indication that the terminal tridentate N^{^C^N} ligand performed best when combined with methyl substituents on the central cyclometalating ring and no ethynyl linkers between terminal ligands and the central fluorene unit. Thus, **6-3** will serve as the lead complex for future studies and as the parent complex of a second-generation library.

6.5. References

- ¹ Storr, T.; Thompson, K. H.; Orvig, C. *Chem. Soc. Rev.* **2006**, *35*, 534.

- ² Dasari, S.; Tchounwou, P. B. *Eur. J. Pharmacol.* **2014**, *740*, 364.
- ³ Bergamo, A.; Gaiddon, C.; Schellens, J. H. M.; Beijnen, J. H.; Sava, G. *J. Inorg. Biochem.* **2012**, *106*, 90.
- ⁴ Dabrowiak, J. C. *In Metals in Medicine*; John Wiley & Sons, Ltd, **2017**, 157.
- ⁵ Trondl, R.; Heffeter, P.; Kowol, C. R.; Jakupec, M. A.; Berger, W.; Keppler, B. K. *Chem. Sci.* **2014**, *5*, 2925.
- ⁶ Schoenhacker-Alte, B.; Mohr, T.; Pirker, C.; Kryeziu, K.; Kuhn, P.-S.; Buck, A.; Hofmann, T.; Gerner, C.; Hermann, G.; Koellensperger, G.; et al. *Cancer Lett.* **2017**, *404*, 79.
- ⁷ Burris, H. A.; Bakewell, S.; Bendell, J. C.; Infante, J.; Jones, S. F.; Spigel, D. R.; Weiss, G. J.; Ramanathan, R. K.; Ogden, A.; Von Hoff, D. *ESMO Open* **2017**, *1*, e000154.
- ⁸ Mari, C.; Gasser, G. *Chim. Int. J. Chem.* **2015**, *69*, 176.
- ⁹ Mari, C.; Pierroz, V.; Ferrari, S.; Gasser, G. *Chem. Sci.* **2015**, *6*, 2660.
- ¹⁰ Knoll, J. D.; Turro, C. *Coord. Chem. Rev.* **2015**, *282–283*, 110.
- ¹¹ Poynton, F. E.; Bright, S. A.; Blasco, S.; Williams, D. C.; Kelly, J. M.; Gunnlaugsson, T. *Chem. Soc. Rev.* **2017**, *46*, 7706.
- ¹² Bonnett, R. *Chemical Aspects of Photodynamic Therapy*; Gordon and Breach Science Publishers, **2000**.
- ¹³ van Straten, D.; Mashayekhi, V.; de Bruijn, H.; Oliveira, S.; Robinson, D. *Cancers* **2017**, *9*, 19.
- ¹⁴ Hamblin, M. R.; Huang, Y.-Y. *Handbook of Photomedicine*; Taylor & Francis, **2014**.
- ¹⁵ Abrahamse, H.; Hamblin, M. R. *Biochem. J.* **2016**, *473*, 347.
- ¹⁶ Shi, G.; Monroe, S.; Hennigar, R.; Colpitts, J.; Fong, J.; Kasimova, K.; Yin, H.; DeCoste, R.; Spencer, C.; Chamberlain, L.; et al. *Coord. Chem. Rev.* **2015**, *282–283*, 127.

- ¹⁷ Kaspler, P.; Lazic, S.; Forward, S.; Arenas, Y.; Mandel, A.; Lilge, L. *Photochem. Photobiol. Sci.* **2016**, *15*, 481.
- ¹⁸ Ford, W. E.; Rodgers, M. A. J. *J. Phys. Chem.* **1992**, *96*, 2917.
- ¹⁹ McClenaghan, N. D.; Leydet, Y.; Maubert, B.; Indelli, M. T.; Campagna, S. *Coord. Chem. Rev.* **2005**, *249*, 1336.
- ²⁰ Yin, H.; Stephenson, M.; Gibson, J.; Sampson, E.; Shi, G.; Sainuddin, T.; Monro, S.; McFarland, S. A. *Inorg. Chem.* **2014**, *53*, 4548.
- ²¹ Lincoln, R.; Kohler, L.; Monro, S.; Yin, H.; Stephenson, M.; Zong, R.; Chouai, A.; Dorsey, C.; Hennigar, R.; Thummel, R. P.; et al. *J. Am. Chem. Soc.* **2013**, *135*, 17161.
- ²² Stephenson, M.; Reichardt, C.; Pinto, M.; Wächtler, M.; Sainuddin, T.; Shi, G.; Yin, H.; Monro, S.; Sampson, E.; Dietzek, B.; et al. *J. Phys. Chem. A* **2014**, *118*, 10507.
- ²³ Arenas, Y.; Monro, S.; Shi, G.; Mandel, A.; McFarland, S.; Lilge, L. *Photodiag. Photodyn. Ther.* **2013**, *10*, 615.
- ²⁴ Wang, L.; Yin, H.; Cui, P.; Hetu, M.; Wang, C.; Monro, S.; Schaller, R. D.; Cameron, C. G.; Liu, B.; Kilina, S.; et al. *Dalton Trans.* **2017**, *46*, 8091.
- ²⁵ Wang, C.; Lystrom, L.; Yin, H.; Hetu, M.; Kilina, S.; McFarland, S. A.; Sun, W. *Dalton Trans.* **2016**, *45*, 16366.
- ²⁶ Majumdar, P.; Yuan, X.; Li, S.; Guennic, B. L.; Ma, J.; Zhang, C.; Jacquemin, D.; Zhao, J. *J. Mater. Chem. B* **2014**, *2*, 2838.
- ²⁷ Ye, R.-R.; Tan, C.-P.; He, L.; Chen, M.-H.; Ji, L.-N.; Mao, Z.-W. *Chem. Commun.* **2014**, *50*, 10945.
- ²⁸ He, L.; Li, Y.; Tan, C.-P.; Ye, R.-R.; Chen, M.-H.; Cao, J.-J.; Ji, L.-N.; Mao, Z.-W. *Chem. Sci.* **2015**, *6*, 5409.

- ²⁹ Kando, A.; Hisamatsu, Y.; Ohwada, H.; Itoh, T.; Moromizato, S.; Kohno, M.; Aoki, S. *Inorg. Chem.* **2015**, *54*, 5342.
- ³⁰ Jiang, X.; Zhu, N.; Zhao, D.; Ma, Y. *Sci. China Chem.* **2016**, *59*, 40.
- ³¹ Zheng, Y.; He, L.; Zhang, D.-Y.; Tan, C.-P.; Ji, L.-N.; Mao, Z.-W. *Dalton Trans.* **2017**, *46*, 11395.
- ³² Liu, J.; Jin, C.; Yuan, B.; Chen, Y.; Liu, X.; Ji, L.; Chao, H. *Chem. Commun.* **2017**, *53*, 9878.
- ³³ Xiang, H.; Chen, H.; Tham, H. P.; Phua, S. Z. F.; Liu, J.-G.; Zhao, Y. *ACS Appl. Mater. Interfaces* **2017**, *9*, 27553.
- ³⁴ Zhang, P.; Chiu, C. K. C.; Huang, H.; Lam, Y. P. Y.; Habtemariam, A.; Malcomson, T.; Paterson, M. J.; Clarkson, G. J.; O'Connor, P. B.; Chao, H.; Sadler, P. J. *Angew. Chem. Int. Ed.* **2017**, *56*, 14898.
- ³⁵ Lv, W.; Zhang, Z.; Zhang, K. Y.; Yang, H.; Liu, S.; Xu, A.; Guo, S.; Zhao, Q.; Huang, W. *Angew. Chem. Int. Ed.* **2016**, *55*, 9947.
- ³⁶ Qiu, K.; Ouyang, M.; Liu, Y.; Huang, H.; Liu, C.; Chen, Y.; Ji, L.; Chao, H. *J. Mater. Chem. B* **2017**, *5*, 5488.
- ³⁷ Ouyang, M.; Zeng, L.; Qiu, K.; Chen, Y.; Li, L.; Chao, H. *Eur. J. Inorg. Chem.* **2017**, 1764.
- ³⁸ Xue, F.; Lu, Y.; Zhou, Z.; Shi, M.; Yan, Y.; Yang, H.; Yang, S. *Organometallics* **2015**, *34*, 73.
- ³⁹ Maggioni, D.; Galli, M.; D'Alfonso, L.; Inverso, D.; Dozzi, M. V.; sironi, L.; Iannacone, M.; Collin, M.; Ferruti, P.; Ranucci, E.; D'Alfonso, G. *Inorg. Chem.* **2015**, *54*, 544.
- ⁴⁰ Nam, J. S.; Kang, M.-G.; Kang, J.; Park, S.-Y.; Lee, S. J. C.; Kim, H.-T.; Seo, J. K.; Kwon, O.-H.; Lim, M. H.; Rhee, H.-W.; Kwon, T.-H. *J. Am. Chem. Soc.* **2016**, *138*, 10968.

- 41 Li, Y.; Lu, X.-R.; Li, M.-F.; Ji, L.-N.; Mao, Z.-W. *Dalton Trans.* **2017**, *46*, 11363.
- 42 Tabrizi, L.; Chiniforoshan, H. *RSC Adv.* **2017**, *7*, 34160.
- 43 McKenzie, L. K.; Sazanovich, I. V.; Baggaley, E.; Bonnneau, M.; Guerchais, V.; Williams, J. A. G.; Weinstein, J. A.; Bryant, H. E. *Chem. Eur. J.* **2017**, *23*, 234.
- 44 Tian, X.; Zhu, Y.; Zhang, M.; Luo, L.; Wu, J.; Zhou, H.; Guan, L.; Battaglia, G.; Tian, Y. *Chem. Commun.* **2017**, *53*, 3303.
- 45 Cui, Y.; Wen, L. L.; Shan, G. G.; Sun, H. Z.; Mao, H. T.; Zhang, M.; Su, Z. M. *Sens. Actuators B.* **2017**, *244*, 314.
- 46 Constable, E. C. *Chem. Soc. Rev.* **2007**, *36*, 246.
- 47 Hofmeier, H.; Schubert, U. S. *Chem. Soc. Rev.* **2004**, *33*, 373.
- 48 Ji, Z.; Li, S.; Li, Y.; Sun, W. *Inorg. Chem.* **2010**, *49*, 1337.
- 49 Tu, S.; Li, T.; Shi, F.; Wang, Q.; Zhang, J.; Xu, J.; Zhu, X.; Zhang, X.; Zhu, S.; Shi, D. *Synthesis* **2005**, *18*, 3045
- 50 Wilkinson, A. J.; Puschmann, H.; Howard, J. A. K.; Foster, C. E.; Williams, J. A. G. *Inorg. Chem.* **2006**, *45*, 8685.
- 51 Basnet, A.; Thapa, P.; Karki, R.; Na, Y.; Jahng, Y.; Jeong, B. S.; Jeong, T. C.; Lee, C. S.; Lee, E. S. *Bioorg. Med. Chem.* **2007**, *15*, 4351.
- 52 Adib, M.; Ayashi, N.; Mirzaei, P. *Synlett* **2016**, *27*, 417.
- 53 Chirdon, D. N.; Transue, W. J.; Kagalwala, H. N.; Kaur, A.; Maurer, A. B.; Pintauer, T.; Bernhard, S. *Inorg. Chem.* **2014**, *53*, 1487.
- 54 Choi, D.; Kim, T.; Reddy, S. M.; Kang, J. *Inorg. Chem. Commun.* **2009**, *12*, 41.
- 55 Demas, J. N.; Crosby, G. A. *J. Phys. Chem.* **1971**, *75*, 991.
- 56 van Houten, J.; Watts, R. J. *J. Am. Chem. Soc.* **1976**, *98*, 4853.

- ⁵⁷ Carmichael, I.; Hug, G. L. *J. Phys. Chem. Ref. Data* **1986**, *15*, 1.
- ⁵⁸ Kumar, C. V.; Qin, L.; Das, P. K. *J. Chem. Soc., Faraday Trans. 2* **1984**, *80*, 783.
- ⁵⁹ Firey, P. A.; Ford, W. E.; Sounik, J. R.; Kenney, M. E.; Rodgers, M. A. J. *J. Am. Chem. Soc.* **1988**, *110*, 7626.
- ⁶⁰ DeRosa, M. C.; Crutchley, R. J. *Coord. Chem. Rev.* **2002**, *233–234*, 351.
- ⁶¹ Frisch, M. J.; Trucks, G. W.; Schlegel, H. B.; Scuseria, G. E.; Robb, M. A.; Cheeseman, J. R.; Scalmani, G.; Barone, V.; Mennucci, B.; Petersson, G. A.; *et al.* *Gaussian 09*, Revision D.01, *Gaussian, Inc.*, Wallingford, CT, **2013**.
- ⁶² Hay, P. J.; Wadt, W. R. *J. Chem. Phys.* **1985**, *82*, 299.
- ⁶³ Hay, P. J.; Wadt, W. R. *J. Chem. Phys.* **1985**, *82*, 270.
- ⁶⁴ Wadt, W. R.; Hay, P. J. *J. Chem. Phys.* **1985**, *82*, 284.
- ⁶⁵ Clark, T.; Chandrasekhar, J.; Spitznagel, G. W.; Schleyer, P. V. R. *J. Comput. Chem.* **1983**, *4*, 294.
- ⁶⁶ Francl, M. M.; Pietro, W. J.; Hehre, W. J.; Binkley, J. S.; Gordon, M. S.; DeFrees, D. J.; Pople, J. A. *J. Chem. Phys.* **1982**, *77*, 3654.
- ⁶⁷ Gill, P. M.; Johnson, B. G.; Pople, J. A.; Frisch, M. J. *Chem. Phys. Lett.* **1992**, *197*, 499.
- ⁶⁸ Hariharan, P. C.; Pople, J. A. *Theor. Chim. Acta* **1973**, *28*, 213.
- ⁶⁹ Krishnan, R.; Binkley, J. S.; Seeger, R.; Pople, J. A. *J. Chem. Phys.* **1980**, *72*, 650.
- ⁷⁰ Liu, B.; Lystrom, L.; Kilina, S.; Sun, W. *Inorg. Chem.* **2017**, *56*, 5361.
- ⁷¹ Zhu, X.; Lystrom, L.; Kilina, S.; Sun, W. *Inorg. Chem.* **2016**, *55*, 11908.
- ⁷² Chai, J.-D.; Head-Gordon, M. *PCCP* **2008**, *10*, 6615.
- ⁷³ Barone, V.; Cossi, M.; Tomasi, J. *J. Comput. Chem.* **1998**, *19*, 404.
- ⁷⁴ Cossi, M.; Rega, N.; Scalmani, G.; Barone, V. *J. Comput. Chem.* **2003**, *24*, 669.

- 75 Marques, M. A.; Gross, E. K. *Annu. Rev. Phys. Chem.* **2004**, *55*, 427.
- 76 Ullrich, C. A. *Time-Dependent Density-Functional Theory: Concepts and Applications*. OUP Oxford: 2011.
- 77 Bjorggaard, J. A.; Sifain, A. E.; Nelson, T.; Myers, T. W.; Veauthier, J. M.; Chavez, D. E.; Scharff, R. J.; Tretiak, S. *J. Phys. Chem. A* **2016**, *120*, 4455.
- 78 Kilina, S.; Kilin, D.; Tretiak, S. *Chem. Rev.* **2015**, *15*, 5929.
- 79 Martin, R. L. *J. Chem. Phys.* **2003**, *118*, 4775.
- 80 Humphrey, W.; Dalke, A.; Schulten, K. *J. Mol. Graph.* **1996**, *14*, 33.
- 81 McCusker, C. E.; Hablot, D.; Ziessel, R.; Castellano, F. N. *Inorg. Chem.* **2012**, *51*, 7957.
- 82 McCusker, C. E.; Hablot, D.; Ziessel, R.; Castellano, F. N. *Inorg. Chem.* **2014**, *53*, 12564.
- 83 Auffrant, A.; Barbieri, A.; Barigelletti, F.; Collin, J.-P.; Flamigni, L.; Sabatini, C.; Sauvage, J.-P. *Inorg. Chem.* **2006**, *45*, 10990.
- 84 Dubinina, G. G.; Price, R. S.; Abboud, K. A.; Wicks G.; Wnuk, P.; Stepanenko, Y.; Drobizhev, M.; Rebane, A.; Schanze, K. S. *J. Am. Chem. Soc.* **2012**, *134*, 19346.
- 85 Liu, R.; Li, Y.; Li, Y.; Zhu, H.; Sun, W. *J. Phys. Chem. A* **2010**, *114*, 12639.
- 86 Liu, R.; Dandu, N.; Li, Y.; Kilina, S.; Sun, W. *Dalton Trans.* **2013**, *42*, 4398.
- 87 Sun, Y.; Joyce, L. E.; Dickson, N. M.; Turro, C. *Chem. Commun.* **2010**, *46*, 2426.
- 88 Liu, Y.; Hammitt, R.; Lutterman, D. A.; Joyce, L. E.; Thummel, R. P.; Turro, C. *Inorg. Chem.* **2009**, *48*, 375.
- 89 Foxon, S. P.; Metcalfe, C.; Adams, H.; Webb, M.; Thomas, J. A. *Inorg. Chem.* **2007**, *46*, 409.
- 90 Foxon, S. P.; Alamiry, M. A. H.; Walker, M. G.; Meijer, A. J. H. M.; Sazanovich, I. V.; Weinstein, J. A.; Thomas, J. A. *J. Phys. Chem. A* **2009**, *113*, 12754.

- ⁹¹ Papanikolaou, P. A.; Tkachenko, N. V. *Phys. Chem. Chem. Phys.* **2013**, *15*, 13128.
- ⁹² Blazek, E. R.; Peak, J. G.; Peak, M. J. *Photochem. Photobiol.* **1989**, *49*, 607.

7. SYNTHESIS, NEUTRAL IRIDIUM(III) COMPLEXES BEARING BODIPY–SUBSTITUTED N–HETEROCYCLIC CARBENE (NHC) LIGANDS: SYNTHESIS, PHOTOPHYSICS, AND PHOTOBIOLOGICAL ACTIVITIES

7.1. Introduction

Photodynamic therapy (PDT) is an emerging cancer treatment modality that combines a photosensitizer (PS), oxygen, and light to destroy tumors and tumor vasculature and induce an immune response.¹⁻⁵ During PDT, reactive oxygen species (ROS) are formed through energy (type II) or electron transfer (type I) reactions that take place between ground state molecular oxygen and the excited triplet state of the PS. The most important mediator of the PDT effect is thought to be singlet oxygen ($^1\text{O}_2$) produced through the type II PDT mechanism, but superoxide ($\text{O}_2^{\bullet-}$) or hydroxyl radical ($\bullet\text{OH}$), generated by the type I PDT mechanism may also play a role.

PDT is inherently selective because toxicity is confined to regions where the PS, oxygen, and light overlap spatiotemporally.^{3,6,7} Therefore, PDT has the potential to be a safe, noninvasive alternative to conventional cancer therapies,⁸ but is not currently the standard of care for any type of cancer. The absence of PDT from mainline therapy stems, in part, from certain drawbacks associated with the porphyrin-based PS Photofrin, which is the only FDA-approved PS for cancer therapy in the USA. There has been significant effort in recent years to develop new PSs and treatment regimens that overcome some of the limitations of Photofrin and its derivatives.

Certain transition metal complexes are among the numerous PSs that have been explored due to their (1) interesting photophysical properties, (2) reduced photobleaching, and (3) improved kinetic stabilities (compared to organic PSs).⁹ Among the metal complexes, Ru(II) systems are probably the most widely studied for PDT.^{11,12} Our Ru(II) complex TLD1433,^{12,13} which

incorporates a π -expansive ligand derived from imidazo[4,5-*f*][1,10]phenanthroline appended to an α -terthienyl unit, just successfully completed a Phase 1b clinical trial for treating bladder cancer with PDT (ClinicalTrials.gov Identifier: NCT03053635). This example demonstrates the utility of lowest-energy π, π^* triplet states, in this case centered on the oligothieryl unit, with extremely long lifetimes for highly efficient photosensitization.

Some transition-metal complexes possess the distinct advantage of having singlet and triplet excited states that can be tuned independently for optimization of their respective characteristics when appropriate π -conjugated ligands are chosen. We have reported that it is possible to shift the singlet charge-transfer absorption to longer wavelengths (for activation by red wavelengths of light) by extending the π -conjugation of the organic ligands, while allowing the lowest triplet excited state (T_1) to be localized on the π -expansive organic ligands.¹⁰ The π, π^* nature of the lowest triplet excited state results in very long triplet excited state lifetimes, which have the potential to facilitate ROS production even at low oxygen tension. Unlike organic PSs, metal complexes possess high quantum yields for triplet state formation due to the heavy atom effect (metal-induced rapid ISC), and their triplet excited states are typically long-lived. All of these properties are desirable features for next-generation PSs.

Ir(III) complexes are also of interest because some have exhibited high efficiency for ROS production *via* electron or energy transfer.¹⁴ Many Ir(III) complexes possess high quantum yields for triplet excited state formation and long-lived triplet excited states for efficient ROS generation even under hypoxia.¹⁴ It has been reported that cationic Ir(III) complexes can target mitochondria,¹⁵⁻¹⁹ lysosomes,^{20,21} the endoplasmic reticulum,^{22,23} or nuclei^{24,25} in a variety of cancer cell lines. A mitochondria-targeted Ir(III) complex PS was reported to show improved PDT effects under hypoxia.¹⁵ These complexes can also display bright intracellular luminescence,

imparting theranostic capacity.^{14-21,24-26} Therefore, Ir(III) complexes have emerged as a new platform for theranostic PDT applications. However, most of the currently studied Ir(III) complexes absorb light maximally in the UV to blue spectral regions, wavelengths of lesser interest for PDT because of their shallow tissue penetration due to tissue scattering and absorption.²⁷

Although it is possible to red-shift the charge transfer ground-state absorption bands of the cyclometalating monocationic Ir(III) complexes $[\text{Ir}(\text{C}^{\wedge}\text{N})_2(\text{N}^{\wedge}\text{N})]^+$ (where $\text{N}^{\wedge}\text{N}$ refers to the diimine ligand and $\text{C}^{\wedge}\text{N}$ refers to the cyclometalating ligand) to longer wavelength by introducing electron-withdrawing substituents on the diimine ligands²⁸ or through benzannulation at the diimine ligands, the molar extinction coefficients of the charge transfer absorption bands are quite low and the lowest triplet excited state (T_1) lifetimes become much shorter (tens of ns).²⁹⁻³³ In contrast, it has been shown that bichromophoric transition-metal complexes with π -conjugated organic chromophores result in long-lived ${}^3\pi, \pi^*$ T_1 states localized at the organic chromophore with simultaneous red-shifting of the ground-state absorption to the longer wavelengths. Metal coordination improves π -conjugation across the organic ligands through planarization, facilitating the interactions between ligands. It also increases the quantum yield of triplet excited-state formation *via* heavy atom induced ISC. Such a strategy has been applied in TLD1433¹² and other Ru(II) complexes for PDT applications,^{13,34-40} but is relatively rare for Ir(III) systems.⁴¹⁻⁴⁴

Borondipyrromethene (BODIPY) and its derivatives, a class of strong light-harvesting fluorophores with facile wavelength tunability, have been extensively explored as potential PSs for PDT applications in recently years.⁴⁵⁻⁴⁸ In addition, BODIPY appears as a promising moiety to be attached to a monodentate or polydentate ligand to tune the absorption wavelength of the transition-metal PSs to the desired spectral region.^{40-42,49} However, BODIPY-Ir(III) dyads for PDT applications are not well-studied.^{41,42,49} One of the few examples used BODIPY tethered cationic

cyclometalated Ir(III) dyads as PSs for PDT and bioimaging applications, and their *in vitro* PDT effects were marginal due to high dark toxicity ($IC_{50} = 8.16 - 16.70 \mu M$ toward 1121 or LLC cell lines). Phototherapeutic index (PI) values (1.3-3.8) were very small.^{41,42}

Recently, *N*-heterocyclic carbene (NHC) based iridium(III) complexes have emerged.⁵⁰⁻⁵⁴ Unlike the numerous well-studied monocationic cyclometalated Ir(III) complexes $[Ir(C^{\wedge}N)_2(N^{\wedge}N)]^+$ (where $N^{\wedge}N$ refers to the diimine ligand and $C^{\wedge}N$ refers to the cyclometalating ligand), monoanionic NHC ligands, such as 1-phenyl-3-alkylbenzimidazole, as the $N^{\wedge}N$ ligand gives rise to neutral complexes.^{54,55} To date, NHC-Ir(III) complexes have largely been studied for their catalytic⁵⁰ and optoelectronic applications.⁵¹⁻⁵⁴ Biological activities were only reported on monocationic Ir(III) complexes with bis(alkylated-NHC) ligands,^{16,50} which possessed high dark toxicity and could only be activated by UV light (365 nm). To date, the biological activities of the neutral $Ir(C^{\wedge}N)_2(NHC)$ complexes remain unexplored.

Herein, a series of neutral iridium(III) complexes bearing BODIPY-NHC ligands (Chart 7-1) were designed and synthesized to explore their photophysical properties and *in vitro* PDT effects. These complexes all contain benzo[*h*]quinoline (*bhq*) as the cyclometalating ligands, but the NHC ligand varies from 1-(4-BODIPY-ethynylphenyl)-3-methyl-1*H*-benzo[*d*]imidazol-3-iumiodide (**L7-1**), 1-(4-BODIPY-phenyl)-3-methyl-1*H*-benzo[*d*]imidazole-3-iumiodide (**L7-2**), 1-(4-BODIPY-ethynylphenyl)-3-(2-(2-(2-methoxyethoxy)ethoxy)ethyl-1*H*-benzo[*d*]imidazol-3-iumiodide (**L7-3**), 5-(4-BODIPY-ethynylphenyl)-3-methyl-1*H*-benzo[*d*]imidazole-3-iumiodide (**L7-4**), to 5-(4-BODIPY-ethynylphenyl)-3-(2-(2-(2-methoxyethoxy)ethoxy)ethyl-1*H*-benzo[*d*]imidazol-3-iumiodide (**L7-5**). BODIPY was incorporated into the NHC ligand scaffold at different sites through a single bond (**7-2**) or a triple bond (**7-1** and **7-3-7-5**) in order to red-shift the absorption of the complexes to longer wavelengths. An oligoether

chain, 2-(2-(2-methoxyethoxy)ethoxy)ethyl, was appended to **7-3** and **7-5** to increase the hydrophilicity of the neutral complexes. The photophysical properties of these five complexes were systematically investigated by various spectroscopic methods and simulated by density functional theory (DFT) calculations. The *in vitro* theranostic PDT effects of the two water-soluble complexes **7-3** and **7-5** were investigated. The impact of the BODIPY attachment site on the photophysics and PDT effects of these dyads was explored.

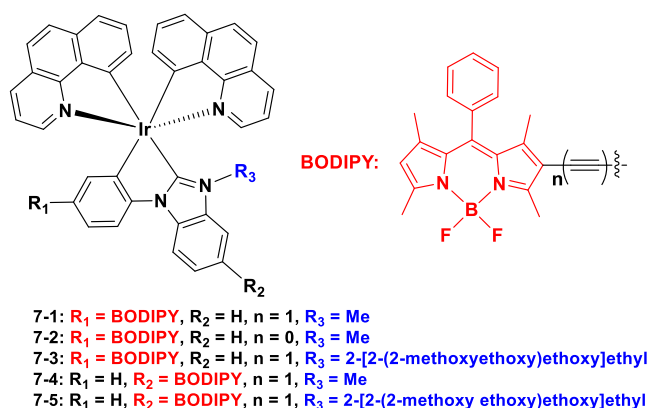


Chart 7.1. Molecular structures of BODIPY-NHC-Ir(III) complexes **7-1** – **7-5**.

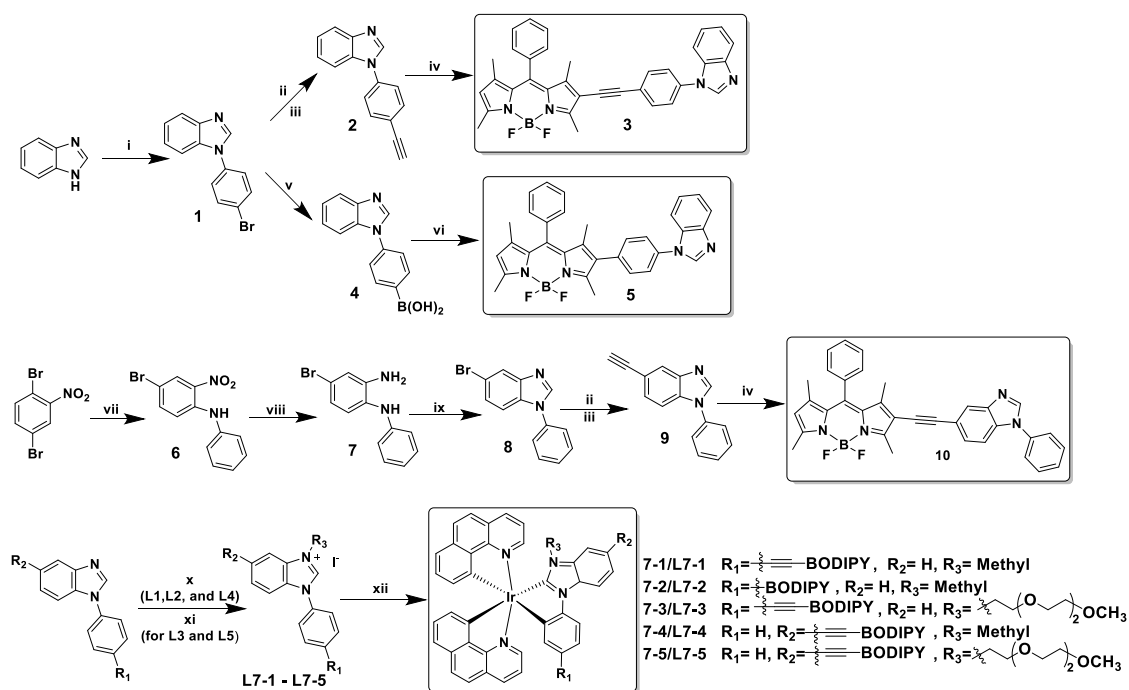
7.2. Experimental

7.2.1. Materials and synthesis

All reagents and solvents were purchased from Alfa Aesar and VWR International and used as received. Al_2O_3 gels (activated, neutral) and silica gels (230–400 mesh) for column chromatography were purchased from Sorbent Technology. Benzo[*h*]quinoline (C[^]N ligand) was obtained from Alfa–Aesar and its Ir(III) μ -chloro-bridged dimers $[\text{Ir}(\text{C}^{\wedge}\text{N})_2\text{Cl}]_2$ was synthesized according to the literature procedure.⁵⁶ Compounds 1-(4-bromophenyl)-1*H*-benzimidazole (compound **1** in Scheme 7-1),⁵⁷ 4-bromo-2-nitro-*N*-phenylaminobenzene (compound **6** in Scheme 7-1),⁵⁸ 4-bromo-*N*¹-phenyl-1,2-benzenediamine (compound **7** in Scheme 7-1),⁵⁹ and 2-iodo-BODIPY⁶⁰ were synthesized following the reported procedures. The synthetic route for

the synthesis of ligands **L7-1** – **L7-5** and complexes **7-1** – **7-5** are provided in Scheme 7-1. ^1H NMR, high-resolution mass spectrometry (HRMS), and elemental analyses were used to characterize these complexes. ^1H NMR spectra were obtained on a Varian Oxford-400 or Bruker-400 spectrometer in CDCl_3 using tetramethylsilane (TMS) as the internal standard. Bruker BioTOF III mass spectrometer was used for ESI-HRMS analyses. NuMega Resonance Laboratories, Inc. in San Diego, California conducted elemental analyses.

Scheme 7-1. Synthetic route for ligands **L7-1**–**L7-5** and complexes **7-1** – **7-5**^a.



^aReagents and conditions: (i) 1-bromo-4-iodobenzene, CuI , Cs_2CO_3 , 1,10-phenanthroline, DMF, 110°C , 40 hrs.; (ii) CuI , $\text{PdCl}_2(\text{PPh}_3)_2$, ethynyltrimethylsilane, TEA/dioxane, 100°C , 1 hr.; (iii) TBAF, THF, 0°C , 1 hr.; (iv) 2-Iodo-BODIPY, CuI , $\text{Pd}(\text{PPh}_3)_4$, TEA, THF, 50°C , 16 hrs.; (v) triisopropyl borate, $^n\text{BuLi}$, anhydrous THF, -78°C , 1 hr., then r.t. overnight, followed by HCl, 100°C , 1 hr.; (vi) 2-iodo-BODIPY, K_2CO_3 , $\text{Pd}(\text{PPh}_3)_4$, toluene, THF, water, 70°C , overnight; (vii) NaOAc , aniline, 160°C , 7 hrs.; (viii) Na_2S , S, water, reflux, 6 hrs.; (ix) formic acid, 100°C , overnight; (x) MeI , THF, 100°C , 24 hrs.; (xi) 1-iodo-3,6,9-trioxadecane, toluene, 100°C , 96 hrs.; (xii) $[\text{Ir}(\text{benzo}[h]\text{quinoline})_2(\mu\text{-Cl})_2]$, Ag_2O , 1,2-dichloroethane, reflux, 24 hrs.

7.2.2. Synthesis of precursor compounds 2 – 5 and 8 – 10

Compound 2. A solution of **1** (544 mg, 2 mmol), CuI (19 mg, 0.1 mmol), PdCl₂(PPh₃)₂ (70 mg, 0.1 mmol) in trimethylamine (TEA)/dioxane (2:1, v/v) was degassed with N₂ at room temperature for 20 minutes. Then, ethynyltrimethylsilane (0.86 mL, 6 mmol) was added and the resulting reaction mixture was heated at 100 °C for 1 hour under N₂. After cooling to room temperature, the mixture was concentrated and purified by column chromatography over silica gel using hexane:ethyl acetate = 1:2 (v/v) as the eluent to give product as pale yellow solid. This pale yellow solid (500 mg, 1.8 mmol) was dissolved in THF (10 ml), and THF solution of tetrabutylammonium fluoride (TBAF) (10 mL, 1 M in THF) was added at 0 °C. The reaction mixture was stirred at room temperature for 1 hour. Then the solution was diluted with ethyl acetate (EA) and washed with water and brine consequently. The organic layer was dried over Na₂SO₄ and concentrated. The residue was purified by column chromatography over silica gel using hexane:ethyl acetate= 1:2 (v/v) as the eluent to give compound **2** as pale yellow solid (360 mg, 81%). ¹H NMR (400 MHz, CDCl₃) δ 8.14 (s, 1H), 7.91 (dd, *J* = 6.4, 2.7 Hz, 1H), 7.73 (d, *J* = 8.4 Hz, 2H), 7.57 (dd, *J* = 6.6, 2.7 Hz, 1H), 7.53 (d, *J* = 8.4 Hz, 2H), 7.43–7.34 (m, 2H), 3.22 (s, 1H).

Compound 3. The solution of 2-iodo-BODIPY (200 mg, 0.44 mmol), compound **2** (97 mg, 0.44 mmol), CuI (17 mg, 0.09 mmol), and Pd(PPh₃)₄ (57 mg, 0.049 mmol) in 10 mL degassed mixed solvent (THF/TEA = 4/1) was heated to 50 °C and stirred for 16 hours in dark. After cooling to room temperature, the solvent was removed under reduced pressure and the residue was extracted with CH₂Cl₂ and washed with brine. After removal of the solvent from the organic layer, the crude product was purified by flash column chromatography with CH₂Cl₂/acetone (v/v = 50/1) being used as the eluent to obtain a dark red solid (200 mg, 83%). ¹H NMR (400 MHz, with

CDCl₃) δ 8.14 (s, 1H), 7.94–7.86 (m, 1H), 7.67 (d, J = 8.4 Hz, 2H), 7.62–7.44 (m, 6H), 7.43–7.30 (m, 4H), 6.08 (s, 1H), 2.75 (s, 3H), 2.62 (s, 3H), 1.55 (s, 3H), 1.44 (s, 3H).

Compound 4. Under -78 °C, ⁿBuLi (0.5 mL, 2.5 M in hexane) was added dropwise to the solution of compound **1** (151 mg, 0.56 mmol) and B(O^{*i*}Pr)₃ (157 mg, 0.83 mmol) in THF (10 mL). The mixture was stirred at -78°C for 1 h, and then allowed to warm up to room temperature, and continued stirring for overnight. The reaction was quenched by addition of concentrated aqueous NH₄Cl (10 mL), and the volatiles were evaporated in vacuum. Then, HCl (10 mL, 37% aq.) was added to the solution and the resultant mixture was heated to reflux for 1 h. After cooling to room temperature, the mixture was carefully adjusted to pH = 7 with NaOH. The white suspension was extracted with CH₂Cl₂. After removal of the solvent, the residue was dried under vacuum. The crude product was purified by column chromatography on silica gel and eluted with acetone to obtain white solid as the product (47 mg, 36%). ¹H NMR (400 MHz, DMSO) δ 8.60 (s, 1H), 8.24 (s, 1H), 8.04 (d, J = 8.0 Hz, 2H), 7.79 (d, J = 7.4 Hz, 1H), 7.67 (d, J = 7.9 Hz, 2H), 7.34 (dt, J = 13.6, 6.8 Hz, 2H).

Compound 5. A solution of compound **4** (44 mg, 0.18 mmol), 2-iodo-BODIPY (56 mg, 0.12 mmol), and K₂CO₃ (166 mg, 1.2 mmol) in toluene (8 mL), THF (8 mL), and water (2 mL) was degassed with N₂ at room temperature for 20 minutes. After that, Pd(PPh₃)₄ (3 mg, 0.0025 mmol) was added, and the mixture was heated to 70 °C for overnight. After evaporation of the volatiles under reduced pressure, water (10 mL) was added, and the mixture was extracted with CH₂Cl₂ (3×10 mL). The combined organic layers were washed with brine (100 mL), and dried over anhydrous MgSO₄. The solvent was then removed, and the crude product was purified by column chromatography on silica gel using hexane/ethyl acetate (v/v = 1:1) as the eluent to obtain orange solid as the target compound (79 mg, 78%). ¹H NMR (400 MHz, CDCl₃) δ 8.13 (d, J =

7.5 Hz, 1H), 7.92–7.84 (m, 1H), 7.62–7.45 (m, 7H), 7.40–7.29 (m, 5H), 6.04 (s, 1H), 2.61 (s, 3H), 2.59 (s, 3H), 1.41 (s, 3H), 1.36 (s, 3H).

Compound 8. The mixture of compound **7** (880 mg, 3.36 mmol) and formic acid (20 mL) was stirred at 100 °C for overnight. The reaction mixture was cooled to room temperature and concentrated under reduced pressure to afford a crude solid. The crude solid was partitioned between ethyl acetate (250 mL) and NH₃/H₂O (25 mL). The ethyl acetate layer was combined, dried with Na₂SO₄, and then concentrated under reduced pressure. The residue was purified by column chromatography (silica gel, eluted with CH₂Cl₂) to get the target compound as off-white solid (860 mg, 98%). ¹H NMR (400 MHz, CDCl₃) δ 8.10 (s, 1H), 8.02 (d, *J* = 1.5 Hz, 1H), 7.59 (dd, *J* = 8.2, 7.4 Hz, 2H), 7.52–7.47 (m, 3H), 7.46–7.36 (m, 2H).

Compound 9. Following the similar synthetic procedure for compound **2**, compound **9** was obtained with 87% yield using compound **8** as the starting material. ¹H NMR (400 MHz, CDCl₃) δ 8.13 (s, 1H), 8.06–7.96 (m, 1H), 7.59 (dd, *J* = 10.0, 5.5 Hz, 2H), 7.49 (dd, *J* = 11.7, 5.7 Hz, 4H), 7.42 (dt, *J* = 13.5, 5.1 Hz, 1H), 3.07 (s, 1H).

Compound 10. Following the similar synthetic procedure for compound **3**, compound **10** was obtained with 41% yield using compound **9** as the starting material. ¹H NMR (500 MHz, CDCl₃) δ 8.14 (s, 1H), 7.97 (s, 1H), 7.59 (t, *J* = 7.7 Hz, 2H), 7.54–7.45 (m, 7H), 7.42 (d, *J* = 8.4 Hz, 1H), 7.33–7.28 (m, 2H), 6.03 (s, 1H), 2.74 (s, 3H), 2.59 (s, 3H), 1.54 (s, 3H), 1.41 (s, 3H).

7.2.3. General synthetic procedure for ligands L7-1 – L7-5

In a round-bottom flask equipped with a gastight Teflon cap, the precursor NHCs compound **3**, **5**, or **10** (1 mmol) was dissolved in 10 mL of THF (for synthesizing **L7-1**, **L7-2**, or **L7-4**) or in 1 mL of toluene (for synthesizing **L7-3** and **L7-5**). Then 1.5 mmol CH₃I (for

synthesizing **L7-1**, **L7-2**, or **L7-4**) or 1-iodo-3,6,9-trioxadecane (for synthesizing **L7-3** and **L7-5**) was added. The mixture was heated to 100 °C for 24 h. After the reaction, the solution was allowed to cool to room temperature. The formed precipitate was collected by filtration and washed with THF, dichloroethane, and Et₂O (10 mL × 2) to obtain the corresponding target compound.

L7-1. A dark red powder was obtained as the product (yield: 73%). ¹H NMR (400 MHz, DMSO) δ 10.16 (s, 1H), 8.18 (d, *J* = 8.4 Hz, 1H), 8.05–7.71 (m, 8H), 7.65 (d, *J* = 3.7 Hz, 2H), 7.46–7.40 (m, 2H), 6.39 (s, 1H), 4.20 (s, 3H), 2.66 (s, 3H), 2.56 (s, 3H), 1.53 (s, 3H), 1.43 (s, 3H).

L7-2. A red powder was obtained as the product (yield: 67%). ¹H NMR (400 MHz, DMSO) δ 10.15 (s, 1H), 8.16 (d, *J* = 8.2 Hz, 1H), 7.94–7.69 (m, 6H), 7.63 (dd, *J* = 12.4, 7.5 Hz, 4H), 7.46 (d, *J* = 7.6 Hz, 2H), 6.29 (s, 1H), 4.17 (s, 3H), 2.52 (s, 3H), 2.50 (s, 3H), 1.38 (s, 3H), 1.36 (s, 3H).

L7-3. A dark red powder was obtained as the product (yield: 53%). ¹H NMR (500 MHz, CDCl₃) δ 10.72 (s, 1H), 7.97 (d, *J* = 7.6 Hz, 1H), 7.88 (d, *J* = 8.7 Hz, 2H), 7.74–7.66 (m, 4H), 7.53 (dd, *J* = 5.0, 1.9 Hz, 2H), 7.33–7.27 (m, 4H), 6.07 (s, 1H), 5.09–5.03 (m, 2H), 4.22–4.14 (m, 2H), 3.74 (dd, *J* = 5.5, 3.4 Hz, 2H), 3.60 (dd, *J* = 5.4, 3.5 Hz, 2H), 3.54 (dd, *J* = 5.6, 3.7 Hz, 2H), 3.41 (dd, *J* = 5.6, 3.7 Hz, 2H), 3.28 (s, 3H), 2.73 (s, 3H), 2.60 (s, 3H), 1.53 (s, 3H), 1.42 (s, 3H).

L7-4. A dark red powder was obtained as the product (yield: 58%). ¹H NMR (400 MHz, DMSO) δ 10.17 (s, 1H), 8.36 (s, 1H), 7.82–7.73 (m, 7H), 7.62 (d, *J* = 3.6 Hz, 3H), 7.53–7.34 (m, 2H), 6.37 (s, 1H), 4.17 (s, 3H), 2.66 (s, 3H), 2.54 (s, 3H), 1.52 (s, 3H), 1.41 (s, 3H).

L7-5. A dark red powder was obtained as the product (yield: 65%). ¹H NMR (400 MHz, CDCl₃) δ 10.61 (s, 1H), 8.19 (s, 1H), 7.97–7.88 (m, 3H), 7.79–7.68 (m, 4H), 7.64–7.54 (m, 4H), 7.35–7.30 (m, 1H), 6.10 (s, 1H), 5.08–4.98 (m, 2H), 4.24–4.14 (m, 2H), 3.81–3.72 (m, 2H),

3.67–3.61 (m, 2H), 3.54 (dd, $J = 5.4, 3.6$ Hz, 2H), 3.45 (dd, $J = 5.7, 3.7$ Hz, 2H), 3.30 (s, 3H), 2.75 (s, 3H), 2.63 (s, 3H), 1.56 (s, 3H), 1.45 (s, 3H).

7.2.4. General synthetic procedure for iridium complexes 7-1 – 7-5

The mixture of the NHC ligand (**L7-1** – **L7-5**, 0.12 mmol), $[\text{Ir}(\text{benzo}[h]\text{quinoline})_2(\mu\text{-Cl})_2]$ (76 mg, 0.06 mmol), Ag_2O (56 mg, 0.24 mmol), and 1,2-dichloroethane (15 mL) was heated to reflux in the dark for 24 h. After the mixture was cooled to room temperature, the solvent was removed under reduced pressure to afford the crude product. Purification of the crude product was carried out on silica gel column chromatography eluted with CH_2Cl_2 . The obtained product was further recrystallized in CH_2Cl_2 / hexane to give the desired pure complex.

7-1. A dark purple powder was obtained as the product (yield: 32%). $^1\text{H NMR}$ (400 MHz, CDCl_3) δ 8.39 (d, $J = 5.2$ Hz, 1H), 8.27 (d, $J = 5.2$ Hz, 1H), 8.17 (d, $J = 8.2$ Hz, 1H), 8.03 (dd, $J = 12.1, 7.6$ Hz, 2H), 7.85–7.66 (m, 3H), 7.57–7.46 (m, 4H), 7.39–7.21 (m, 9H), 7.18–6.99 (m, 4H), 6.87 (s, 1H), 6.74 (d, $J = 6.9$ Hz, 1H), 6.33 (d, $J = 7.0$ Hz, 1H), 5.98 (s, 1H), 3.26 (s, 3H), 2.55 (s, 3H), 2.53 (s, 3H), 1.36 (s, 3H), 1.33 (s, 3H). ESI-HRMS (m/z): calcd. for $[\text{C}_{61}\text{H}_{44}\text{BF}_2\text{IrN}_6+\text{H}]^+$, 1103.3396; found, 1103.3384. Anal. Calcd for $\text{C}_{61}\text{H}_{44}\text{BF}_2\text{IrN}_6 \cdot 5\text{CH}_2\text{Cl}_2 \cdot 2.4\text{C}_6\text{H}_{14}$ (C_6H_{14} : hexane): C, 55.71; H, 5.09; N, 4.85. Found: C, 55.37; H, 5.42; N, 5.15.

7-2. A red powder was obtained as the product (yield: 30%). $^1\text{H NMR}$ (400 MHz, CDCl_3) δ 8.40 (d, $J = 5.2$ Hz, 1H), 8.30 (d, $J = 5.5$ Hz, 1H), 8.18 (d, $J = 8.1$ Hz, 1H), 8.04 (d, $J = 8.0$ Hz, 1H), 7.97 (d, $J = 7.8$ Hz, 1H), 7.83 (d, $J = 7.9$ Hz, 1H), 7.78 (d, $J = 8.7$ Hz, 1H), 7.69 (d, $J = 8.7$ Hz, 1H), 7.60–7.40 (m, 4H), 7.35 (t, $J = 8.1$ Hz, 2H), 7.22 (d, $J = 6.6$ Hz, 6H), 7.10 (ddd, $J = 22.5, 14.7, 6.6$ Hz, 4H), 6.89 (d, $J = 6.9$ Hz, 1H), 6.79 (d, $J = 8.3$ Hz, 1H), 6.43 (s, 1H), 6.26 (d, $J = 7.3$ Hz, 1H), 5.91 (s, 1H), 3.28 (s, 3H), 2.52 (s, 3H), 2.15 (s, 3H), 1.33 (s, 3H), 1.26 (s, 3H). ESI-

HRMS (m/z): calcd. for $[\text{C}_{59}\text{H}_{44}\text{BF}_2\text{IrN}_6+\text{H}]^+$, 1079.3396; found, 1079.3389. Anal. Calcd for $\text{C}_{59}\text{H}_{44}\text{BF}_2\text{IrN}_6 \cdot 0.4\text{CH}_2\text{Cl}_2 \cdot 0.6\text{C}_6\text{H}_{14}$: C, 65.02; H, 4.61; N, 7.22. Found: C, 64.62; H, 4.92; N, 7.19.

7-3. A dark purple powder was obtained as the product (yield: 56%). ^1H NMR (400 MHz, CDCl_3) δ 9.36 (d, $J = 5.4$ Hz, 1H), 8.39 (d, $J = 5.9$ Hz, 1H), 8.27 (dd, $J = 12.3, 7.0$ Hz, 2H), 8.16 (d, $J = 8.5$ Hz, 1H), 8.03 (dd, $J = 16.6, 8.0$ Hz, 2H), 7.83 (d, $J = 8.3$ Hz, 1H), 7.74 (t, $J = 8.2$ Hz, 2H), 7.68 (d, $J = 8.8$ Hz, 1H), 7.56–7.47 (m, 3H), 7.39–7.26 (m, 4H), 7.25–7.00 (m, 6H), 6.87 (d, $J = 1.8$ Hz, 1H), 6.81 (t, $J = 7.6$ Hz, 1H), 6.68 (d, $J = 7.0$ Hz, 1H), 6.28 (d, $J = 7.0$ Hz, 1H), 5.98 (d, $J = 7.1$ Hz, 1H), 4.37–4.17 (m, 2H), 3.75 (dd, $J = 10.5, 5.7$ Hz, 2H), 3.39–3.32 (m, 2H), 3.29 (s, 3H), 3.02–2.83 (m, 2H), 2.75–2.59 (m, 2H), 2.59 (s, 3H), 2.52 (s, 3H), 2.40 (dd, $J = 4.1, 2.8$ Hz, 2H), 1.36 (s, 3H), 1.32 (s, 3H). ESI-HRMS (m/z): calcd. for $[\text{C}_{67}\text{H}_{56}\text{BF}_2\text{IrN}_6\text{O}_3+\text{H}]^+$, 1235.4183; found, 1235.4164. Anal. Calcd for $\text{C}_{67}\text{H}_{56}\text{BF}_2\text{IrN}_6\text{O}_3 \cdot 1.6\text{CH}_2\text{Cl}_2 \cdot 0.3\text{C}_6\text{H}_{14}$: C, 60.57; H, 4.58; N, 6.02. Found: C, 60.74; H, 4.55; N, 5.75.

7-4. A dark purple powder was obtained as the product (yield: 57%). ^1H NMR (400 MHz, CDCl_3) δ 8.27 (d, $J = 4.6$ Hz, 1H), 8.20 (d, $J = 5.5$ Hz, 1H), 8.06 (d, $J = 8.7$ Hz, 1H), 8.02–7.93 (m, 2H), 7.79–7.68 (m, 3H), 7.54–7.42 (m, 5H), 7.38 (t, $J = 8.4$ Hz, 1H), 7.30 (dd, $J = 11.9, 7.4$ Hz, 2H), 7.22 (dd, $J = 6.5, 3.1$ Hz, 3H), 7.11–6.95 (m, 5H), 6.75 (d, $J = 5.7$ Hz, 1H), 6.68 (dd, $J = 11.5, 7.1$ Hz, 2H), 6.28 (d, $J = 7.1$ Hz, 1H), 5.98 (s, 1H), 3.19 (s, 3H), 2.64 (s, 3H), 2.52 (s, 3H), 1.43 (s, 3H), 1.34 (s, 3H). ESI-HRMS (m/z): calcd. for $[\text{C}_{61}\text{H}_{44}\text{BF}_2\text{IrN}_6+\text{H}]^+$, 1103.3396; found, 1103.3385. Anal. Calcd for $\text{C}_{61}\text{H}_{44}\text{BF}_2\text{IrN}_6 \cdot 4.8\text{CH}_2\text{Cl}_2 \cdot 2\text{C}_6\text{H}_{14}$: C, 55.55; H, 4.89; N, 5.00. Found: C, 55.46; H, 5.14; N, 5.26.

7-5. A dark purple powder was obtained as the product (yield: 65%). ^1H NMR (400 MHz, CDCl_3) δ 8.34 (d, $J = 5.5$ Hz, 1H), 8.25 (d, $J = 5.4$ Hz, 1H), 8.11 (d, $J = 8.5$ Hz, 1H), 8.07–8.03 (m, 1H), 8.02–7.98 (m, 1H), 7.83 (dd, $J = 14.7, 8.1$ Hz, 1H), 7.75 (dd, $J = 8.9, 2.0$ Hz, 2H), 7.67

(d, $J = 1.9$ Hz, 1H), 7.59–7.46 (m, 5H), 7.46–7.27 (m, 5H), 7.17–7.00 (m, 5H), 6.80 (dd, $J = 5.1$, 3.6 Hz, 1H), 6.74 (t, $J = 7.6$ Hz, 1H), 6.67 (dd, $J = 6.2$, 2.5 Hz, 1H), 6.29 (dd, $J = 6.3$, 3.3 Hz, 1H), 6.04 (s, 1H), 4.31–4.24 (m, 2H), 3.77–3.71 (m, 2H), 3.42–3.37 (m, 2H), 3.33–3.29 (m, 2H), 3.27 (s, 3H), 3.25–3.22 (m, 2H), 2.96–2.85 (m, 2H), 2.70 (s, 3H), 2.58 (s, 3H), 1.50 (s, 3H), 1.40 (s, 3H). ESI-HRMS (m/z): calcd. for $[\text{C}_{67}\text{H}_{56}\text{BF}_2\text{N}_6\text{O}_3\text{Ir}+\text{H}]^+$, 1235.4183; found, 1235.4169. Anal. Calcd for $\text{C}_{67}\text{H}_{56}\text{BF}_2\text{IrN}_6\text{O}_3 \cdot 0.3\text{H}_2\text{O}$: C, 64.92; H, 4.60; N, 6.78. Found: C, 64.97; H, 4.77; N, 6.49.

7.2.5. Photophysical studies

The spectroscopic grade solvents used for photophysical studies were purchased from VWR International and used as received without further purification. The ultraviolet–visible (UV–vis) absorption spectra of complexes **7-1** – **7-5** were measured on a Varian Cary 50 spectrophotometer. Steady–state emission spectra of complexes **7-1** – **7-5** were recorded using a HORIBA FluoroMax 4 fluorometer/phosphorometer. The relative actinometry method was used for measuring the emission quantum yields of **7-1** – **7-5**. $[\text{Ru}(\text{bpy})_3]\text{Cl}_2$ in degassed acetonitrile ($\lambda_{\text{max}} = 436$ nm, $\Phi_{\text{em}} = 0.097$)⁶¹ was used as the reference. The nanosecond transient absorption (TA) measurements, *i.e.* the TA spectra, triplet lifetimes, and quantum yields, were carried out on a laser flash photolysis spectrometer (Edinburgh LP920). The excitation source was the third–harmonic output (355 nm) of a Quantel Brilliant Nd:YAG laser (pulse duration, 4.1 ns; repetition rate was 1 Hz). Before measurement, each sample solution was purged with nitrogen for 40 min. The singlet depletion method was followed to calculate the triplet excited–state molar extinction coefficients (ϵ_{T}),⁶² and the relative actinometry method⁶³ was used to estimate the triplet excited–state quantum yields using SiNc in benzene as the reference ($\epsilon_{590} = 70,000 \text{ M}^{-1}\text{cm}^{-1}$, $\Phi_{\text{T}} = 0.20$).⁶⁴

7.2.6. Computational methodology

The ground state geometries were optimized using the Density Functional Theory (DFT)⁶⁵ employing PBE1 functional⁶⁶ and the mixed basis set, where LANL2DZ⁶⁷ was used for Ir(III) to incorporate the effective core potential for a heavy element and 6-31G*⁶⁸ basis set was used for all remaining atoms. The solvent effects were modeled by the Conductor-like Polarizable Continuum Model (CPCM) reaction field method⁶⁹ for toluene.

Linear response time dependent DFT (TDDFT)⁷⁰ was employed to calculate excited state properties of the complexes by using the same functional and basis set that were used for the ground state calculations. It was previously reported for other Ir(III) complexes that both the ground and excited state calculations using this methodology show good agreement with the experimental results,⁷¹ which defined our choice of the methodology. To meet the same energy range of the experimental absorption spectra, the lowest 80 states were calculated by TDDFT. The thermal linewidths of spectra were obtained using Gaussian function with the broadening parameter of 0.08 eV, which well fits to the line shape of experimental absorption spectra.

To calculate the emission energies, we have optimized the triplet excited state using the analytical gradient method based on TDDFT, within PBE1 functional and the mixed LANL2DZ/6-31G* basis set. To get a better understanding of the nature of the transitions, natural transition orbitals (NTOs)⁷² were calculated, which is the compact representation of the excited electron-hole pair obtained from the transition density matrices calculated by TDDFT. NTOs were visualized by VMD⁷³ software using 0.02 iso resolution. All quantum chemical calculations were performed using the Gaussian09[®] software package.⁷⁴

7.2.7. Cellular assays

Metal complex solutions. Stock solutions (5 mM) of the chloride salts of **7-3** and **7-5** were prepared by first dissolving the solids in DMSO (10% of total aqueous solution), using sonication and slight heat, then deionized water (dI) water was added to the appropriate volume. The solutions were vortexed to mixed well and stored in the dark at -20°C when not in use. Working solutions were made by diluting the 5 mM stock solutions in pH 7.4 Dulbecco's phosphate buffered saline (DPBS, no Ca²⁺ or Mg²⁺), where DMSO in the final assay wells were kept under 0.1% at the highest complex concentration.

7.2.8. Cell culture

SKMEL28 cells. Adherent SKMEL28 human malignant melanoma cells (HTB-72, ATCC) were cultured in complete growth media EMEM plus 10% FBS and were kept incubated at 37°C under 5% CO₂. The complete growth media was prepared in 500 mL portions by combining 50 mL Seradigm FB Essence (VWR Life Science) and 450 mL Eagle's Minimum Essential Medium (MEM, Corning® 10-009-CV) then filtered in a Nalgene™ rapid-flow sterile disposable bottle top filter with PES 0.2 µm membrane (Thermo Scientific 09-741-07). SK-MEL-28 cells were initiated at about 300,000 cells mL⁻¹ in 75 cm² tissue culture flasks and were subcultured 2-3 times per week under standard aseptic conditions when growth reached approximately 500,000 cells mL⁻¹. Subculturing was done by discarding the spent media, rinsing the cell layer once with cold DPBS, followed with the dissociation of the cell monolayer with cold 1X Trypsin-EDTA solution (VWR Life Science Trypsin, 0.25% EDTA 1X). Complete growth media was added to the cell suspension to dilute and distributed to new cell flasks. Cell assays were performed with cells at no higher than ten cell passages (subcultures).

7.2.9. Cytotoxicity and photocytotoxicity cell assays

Cell viability assays were completed in triplicate in 96-well polystyrene flat bottom TC-treated microplates (Corning Costar 3595). The outer periphery wells were filled with 200 μL DPBS in order to minimize evaporation from inner sample wells. SKMEL28 cells, growing in log phase ($\sim 500,000$ cells mL^{-1}) with at least 95% viability were transferred in 50 μL aliquots to inner wells containing warm complete growth media (25 μL) and placed in a 37°C, 5% CO_2 water-jacketed incubator (Thermo Electron Corp., FormaSeries II, Model 3110, HEPA Class 100) for 3 h to allow for cell attachment. Serial dilutions of **7-3** and **7-5** metal complexes (prepared in DPBS and prewarmed in 37°C incubator) were added in 25 μL volumes to the appropriate microplate wells containing cells. Control wells, with no metal complexes, were included in each microplate with either cells only (25 μL growth media, 50 μL cells, 25 μL DPBS) or no cells (75 μL growth media, 25 μL DPBS). All microplates were kept incubated in the dark at 37°C under 5% CO_2 for a pre-treatment time of 16 h. Control microplates not receiving light treatments were kept in the dark while PS-treated microplates were irradiated under one of the following conditions: visible light (400-700 nm, 33 mW cm^{-2}) from a 190 W BenQ MS 510 overhead projector, or red light (625 nm, 43 mW cm^{-2}) from an LED array (Photodynamic Inc., Halifax, NS). Irradiation times using these two light sources were 51 and 39 min respectively to yield total light doses of 100 J cm^{-2} . After PS treatments, all microplates were returned to the incubator for another 48 h. Cell viability was evaluated using a resazurin fluorescent dye assay according to a standard protocol (reference Hanson 2013 patent and O'Brien 2000 EJB). Briefly, 10 μL aliquots of prewarmed, sterile filtered 0.6 mM resazurin reagent (Sigma Aldrich Canada) were added to all sample wells and subsequently incubated another 3-4 h. Viability was determined based on the ability of the blue resazurin dye to be metabolically reduced (by live cells) to the fluorescent red resorufin.

Fluorescence was recorded with a Cytofluor 4000 fluorescence microplate reader (excitation 530 ± 25 nm, emission 620 ± 40 nm). The concentrations of the metal complexes where cell viability was reduced by 50% (EC_{50} values) for cytotoxicity (dark) and photocytotoxicity (light) were calculated from sigmoidal fits of the dose-response curves using GraphPad Prism 6.0 according to Eq. 1, where y_i and y_f are the initial and final fluorescence signal intensities. Generally, cells growing in log phase and of the same passage number have EC_{50} values reproducible to within $\pm 25\%$ in the submicromolar range, $\pm 10\%$ below $10 \mu\text{M}$, and $\pm 5\%$ above $10 \mu\text{M}$. Phototherapeutic indices (PIs), a measure of the therapeutic window, were represented by the ratio of dark to light EC_{50} values from the dose-response curves.

$$y = y_i + \frac{y_i - y_f}{1 + 10^{(\log EC_{50} - x) \times (\text{Hill slope})}} \quad (1)$$

7.2.10. Confocal microscopy

The influence of the metal complexes **7-3** and **7-5** on SKMEL28 cells, in dark or light conditions, was monitored using confocal fluorescence microscopy. Live cells were imaged in DPBS using poly-L-lysine coated sterile glass-bottom Petri dishes (MatTek) with several treatments: (i) cells with no complex in dark, (ii) cells with no complex with light, (iii) cells with complex in dark, and (iv) cells with complex with light. SK-MEL-28 cells (approximately 100,000) were transferred in 1 mL volumes to the dishes and placed in a 37°C , $5\% \text{CO}_2$ water-jacketed incubator for approximately 3 hr to equilibrate. The cells were then washed with warm PBS followed by the addition of $50 \mu\text{M}$ **7-3** or **7-5** (1 mL, prepared in DPBS and warmed in incubator) to the sample dishes containing cells. The dishes were returned to the incubator for 15 min prior to further treatment. Light treated samples were irradiated with visible light for 26 min from a 190 W BenQ MS 510 projector (400–700 nm, power density 33 mW cm^{-2} for a total light

dose 50 J cm^{-2}), where dark samples were covered with foil and placed in a dark drawer for the same amount of time. Dishes containing both dark and light samples were imaged 15 min post-treatment using a Carl Zeiss LSM 510 laser scanning confocal microscope with a 60X oil objective lens. Excitation was delivered at 458/488 nm from an argon-krypton laser, and signals were acquired through a 505 nm long-pass filter. Pinhole diameters for all the treatments were at 1 AU (airy unit) equaling $98 \mu\text{m}$. The images were collected and analyzed using the Zeiss LSM Image Browser Version 4.2.0.121 software (Carl Zeiss Inc.).

7.2.11. Bacterial survival assays

Photodynamic inactivation (PDI) of *Streptococcus aureus* (ATCC 25923, Cedarlane) growing as planktonic culture, by **7-3** and **7-5**, was probed using a standard broth microdilution method.²⁸ In order to standardize the starting bacterial concentration for all experiments, a standard curve of McFarland barium sulfate turbidity standards was generated, representing approximate bacterial concentrations. McFarland barium sulfate standards 0.5, 1, 2, 3, 4, and 5, were prepared, representing approximately $1.5, 3, 6, 9, 12, 15 \times 10^8$ bacteria mL^{-1} respectively. The absorbance at 562 nm was measured for all McFarland standards, using a BioTek EL800 microplate reader, and a standard curve was generated. An inoculum of *S. aureus* was then prepared by transferring colonies from a room temperature secondary growth plate to a sterile 15 mL conical tube containing 2 mL sterile distilled water, and the contents were mixed well by vortexing. The absorbance at 562 nm was read and the approximate concentration was calculated according to the McFarland barium sulfate standard curve. The solution was further diluted in fresh TSB in order to match a starting bacterial cell concentration of approximately 1×10^6 CFU mL^{-1} and was used within 1 hr of preparation. Dark and light experiments were performed in duplicate in 96-well

microplates (Corning Costar, Acton, MA), where outer wells along the top and bottom contained 200 μL of sterile distilled water to prevent evaporation. Dilutions of **7-3** and **7-5** were prepared in TSB media at 200 μM (twice the desired top concentration of 100 μM) and added to triplicate wells of the microplate and 1:2 serial dilutions were performed in wells containing 50 μL TSB using an electronic multichannel pipettor. (final concentrations were 100, 50, 25, 12.5, 6.3, 3.1, 1.6, 0.8, 0.4, 0.2, 0.1 μM). To sample wells, 50 μL bacterial inoculum was added (final concentration in wells were $\sim 5 \times 10^5$ CFU mL^{-1}). Final assay volumes in the wells were 100 μL . Both plates were incubated for 30 min prior to treatments. Dark treatment microplates were wrapped in foil and placed in a dark drawer, while PDI-treated microplates were irradiated with visible light (400 – 700 nm, 28 ± 0.9 mW cm^{-2}) using a Solla 30W Cree LED light panel. The irradiation time was 60 min to yield a light dose of approximately 100 J cm^{-2} to the microplate wells (lid on). Both dark and PDT-treated microplates were incubated overnight. Sample turbidity was measured as absorbance at 562 nm for all microplates and EC_{50} values (effective concentration at which $\geq 50\%$ of bacterial growth is inhibited) for antibiotic (dark) and antimicrobial PDI (light) activity were calculated from sigmoidal fits of the dose response curves using Graph Pad Prism 6.0 according to Eq 1 (as shown above in cell culture section), where y_i and y_f are the initial and final absorbance intensities. Data was normalized using triplicate control wells containing 50 μL TSB and 50 μL bacterial inoculum and were deemed as 100% growth. Bacteria-free control wells received 100 μL TSB only. Highly colored concentrations of PS were given duplicate control wells containing 50 μL water containing PS and 50 μL TSB (no bacteria). PS controls were prepared due to the color content of high concentration skewing the absorbance values of treated wells. PS control absorbance values were subtracted from the corresponding treated PS absorbance values to show true comparative growth rates.

7.2.12. Measurement of ROS in SKMEL-28 cells

The generation of intracellular ROS was measured using the fluorescent stain 2,7'-Dichlorofluorescein diacetate (DCFDA, Sigma D6883), following a simple microplate assay.²⁹ DCFDA is a cell-permeable probe that measures hydroxyl, peroxy, and other ROS activity within the cell or the cellular environment. SKMEL28 cells were seeded at approximately 25,000 cells per well on two 96-well ultra-low attachment flat bottom microtiter plates (Corning 3595) and incubated overnight. The spent media was carefully removed and the cells were washed with 1X buffer (Hank's 1X Balanced Salt Solutions, HBSS, HyClone SH30268.01), followed by the addition of 100 μ L of 25 μ M DCFDA prepared in 1X buffer. The two microplates were incubated for 45 min (37°C under 5% CO₂). Compound serial dilutions of **7-3** and **7-5** were prepared in 1X supplemented buffer (HBSS + 10% FBS). The supernatant was carefully removed, the cells were washed once with 1X buffer, then 75 μ L 1X supplemented buffer was added to each sample well followed by 25 μ L aliquots of either **7-3** or **7-5** (final 9 concentrations in wells ranged from 4 pM - 120 μ M). Control wells in both microplates included: 1) Ir(III) complexes with DCFDA, no cells, 2) cells only, no DCFH-DA, 3) cells only with DCFDA, 4) Ir(III) complexes with cells, no DCFDA. The microplates were incubated (pre-treatment) for 30 min. The dark-treatment microplate was kept in the dark (foiled and kept in dark place), while the light-treatment microplate was irradiated with visible light (400-700 nm, 33 mW cm⁻²) from a 190 W BenQ MS 510 overhead projector for 26 min, yielding a light dose of 50 J cm⁻². Fluorescence signals were measured at several time periods after irradiation (15 min, 30 min, 60 min, 90 min, 120 min) with a Cytofluor 4000 fluorescence microplate reader (excitation 485 \pm 20 nm, emission 580 \pm 50 nm). Relative ROS production is represented by plotting arbitrary fluorescence units versus the log concentration of test samples in both dark and light treatments.

7.3. Results and discussion

7.3.1. Electronic absorption

The UV–vis absorption spectra of **7-1** – **7-5** were measured in toluene, CH₃CN, THF, and CH₂Cl₂ at room temperature. The spectra in toluene (the preferred solvent due to the high solubility of the neutral complexes in it) are displayed in Figure 7.1, and the normalized spectra in the other solvents are provided in Figure 7.2. The absorption band maxima and molar extinction coefficients are summarized in Table 7.1. **7-1** – **7-5** exhibited strong absorption bands with vibronic structure in the region of 280–460 nm, and broad, intense absorption bands centered between 500–600 nm. The energies and spectral features of these low-energy absorption bands resemble those of the 1,3,5,7-tetramethyl-8-phenyl-BODIPY.⁷⁵ However, the band maxima of **7-1** – **7-5** are approximately 30–40 nm red-shifted compared to the ¹ π, π^* absorption band of the 1,3,5,7-tetramethyl-8-phenyl-BODIPY, and these bands are broader than that of 1,3,5,7-tetramethyl-8-phenyl-BODIPY. These characteristics imply that the NHC ligand interacts with the BODIPY motif and there could be some charge transfer character in this band (see discussion *vide infra*).

Inserting a C \equiv C bond between the BODIPY motif and the phenyl ring in complex **7-1** led to a red-shift of approximately 13-nm compared to that of complex **7-2**. This difference was attributed to the extended π -conjugation within the NHC-BODIPY ligand of **7-1**. Varying the point of attachment of BODIPY on the NHC ligand also showed a noticeable effect on the energy of the low-energy absorption band. Complex **7-4**, with BODIPY attached at C5 of the benzimidazole ring blue shifted the low-energy absorption band by approximately 8 nm compared to the corresponding band in **7-1**, where BODIPY is appended at C4 of the phenyl ring. Replacement the methyl substituents on C3 of benzimidazole in complexes **7-1** and **7-4** by

oligoether substituents as in 7-3 and 7-5 did not impact the energy of the low-energy absorption band but slightly attenuated the molar extinction coefficients for this transition.

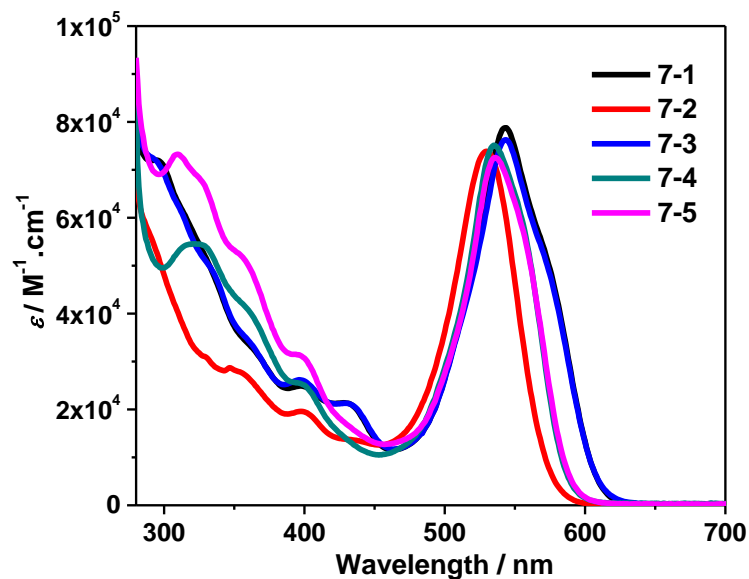


Figure 7.1. UV-vis absorption spectra of 7-1 – 7-5 in toluene at room temperature.

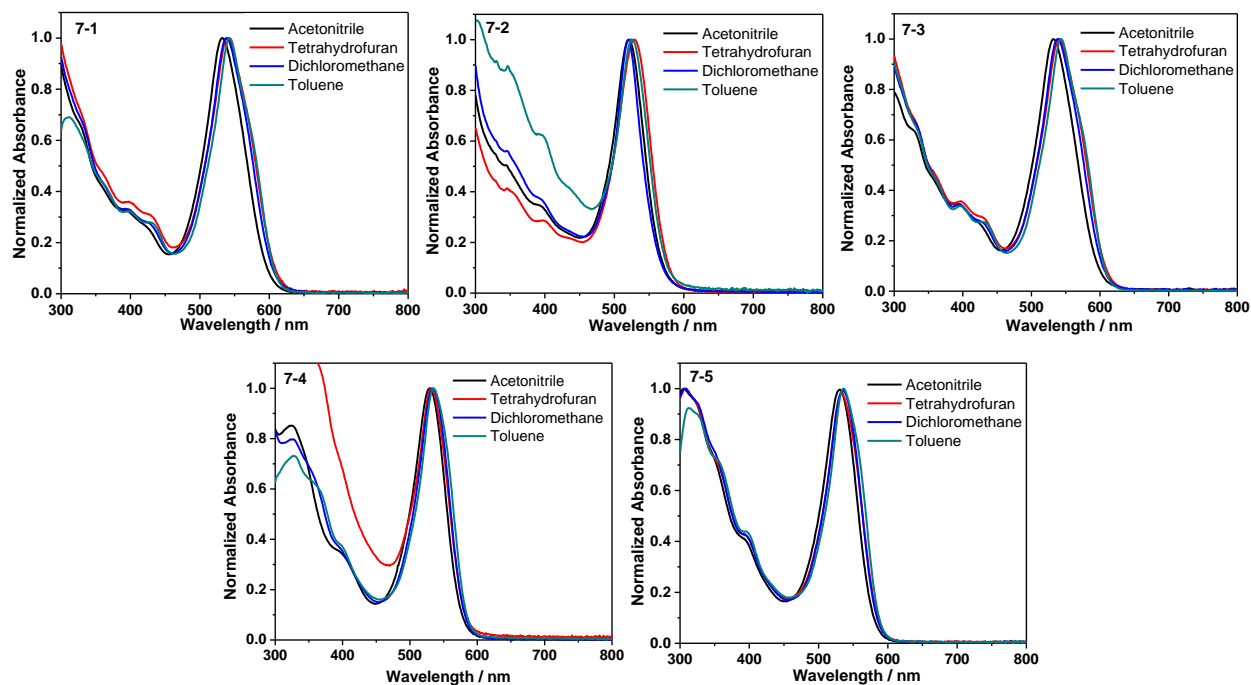


Figure 7.2. Normalized UV-vis absorption spectra of 7-1 – 7-5 in different solvents.

Table 7.1. Photophysical parameters for complexes **7-1 – 7-5**.

	$\lambda_{\text{abs}}/\text{nm}$ ($\log \varepsilon$ / $\text{L}\cdot\text{mol}^{-1}\cdot\text{cm}^{-1}$) ^a	$\lambda_{\text{em}}/\text{nm}$ ($\tau_{\text{em}}/\mu\text{s}$); Φ_{em} ^b	$\lambda_{\text{T1-Tn}}/\text{nm}$ ($\tau_{\text{TA}}/\mu\text{s}$; $\log \varepsilon_{\text{T1-Tn}}/$ $\text{L}\cdot\text{mol}^{-1}\cdot\text{cm}^{-1}$); Φ_{T} ^c	Φ_{Δ} ^d ($\lambda_{\text{ex}}/\text{nm}$)
7-1	294 (4.86), 335 (4.68), 352 (4.56), 398 (4.40), 430 (4.33), 543 (4.90)	610 (4.96); 0.041	457 (42.1; - ^e), 679 (48.0; 4.13); 0.51	n.d. ^f
7-2	286 (4.78), 347 (4.46), 398 (4.29), 530 (4.87)	583 (3.12); 0.063	458 (24.0; - ^e), 681 (28.7; 3.83); 0.86	n.d. ^f
7-3	290 (4.86), 335 (4.69), 352 (4.57), 397 (4.42), 430 (4.33), 543 (4.88)	610 (5.26); 0.047	455 (26.1; - ^e), 690 (32.1; 4.11); 0.51	0.38 (450); 0.37 (534)
7-4	322 (4.74), 350 (4.64), 396 (4.40), 535 (4.88)	587 (4.77); 0.034	449 (28.0; - ^e), 699 (30.9; 4.09); 0.39	n.d. ^f
7-5	309 (4.87), 350 (4.73), 395 (4.50), 535 (4.86)	587 (4.89); 0.010	452 (52.9; - ^e), 690 (55.2; 4.06); 0.40	0.11 (352); 0.22 (450); 0.08 (534)

^aAbsorption band maxima (λ_{abs}) and molar extinction coefficients ($\log \varepsilon$) in toluene at room temperature.

^bEmission band maxima (λ_{em}), lifetimes (τ_{em}), and quantum yields (Φ_{em}) in toluene at room temperature, $c = 1 \times 10^{-5}$ mol/L. The reference used was a degassed acetonitrile solution of $[\text{Ru}(\text{bpy})_3]\text{Cl}_2$ ($\Phi_{\text{em}} = 0.097$, $\lambda_{\text{ex}} = 436$ nm)⁶¹. The emission lifetimes reported are the longer-lived ³ILCT/³MLCT phosphorescence lifetimes. The short-lived ¹IL fluorescence lifetimes were unable to be reliably measured due to the resolution of our instrument. ^cNanosecond TA band maxima ($\lambda_{\text{T1-Tn}}$), triplet excited-state lifetimes (τ_{TA}), triplet extinction coefficients ($\log \varepsilon_{\text{T1-Tn}}$), and quantum yields (Φ_{T}) measured in toluene at room temperature. SiNc in benzene ($\varepsilon_{590} = 7 \times 10^4$ L mol⁻¹cm⁻¹, $\Phi_{\text{T}} = 0.20$)⁶⁴ was used as the reference for calculating Φ_{T} . ^dSinglet oxygen quantum yields (Φ_{Δ}) were measured in acetonitrile and are corrected to within $\pm 5\%$. ^eNot determined due to strong ground-state absorption, which does not satisfy the condition to apply singlet depletion method for estimation of $\varepsilon_{\text{T1-Tn}}$. ^fNot determined.

To better understand the nature of the different absorption bands, time-dependent density functional theory (TDDFT) calculations were carried out for complexes **7-1 – 7-5** in toluene. As shown in Figure 7.2, the calculated spectra matched well with the experimental spectra. The natural transition orbitals (NTOs) corresponding to the major transitions contributing to the major absorption bands of **7-1 – 7-5** are presented from Table 7.2 to Table 7.4. As the NTOs in Table 7.2 indicated, the electrons of the S_1 states were almost exclusively localized on the BODIPY moiety, while the holes were delocalized on the entire BODIPY-substituted NHC ligands and on the metal d orbitals. Therefore, the S_1 states in **7-1 – 7-5** have the mixed ¹ π, π^* / ¹ILCT (intraligand charge transfer, $\pi(\text{NHC}) \rightarrow \pi^*(\text{BODIPY})$) / ¹MLCT (metal-to-ligand charge transfer,

$d(\text{Ir}) \rightarrow \pi^*(\text{BODIPY})$) configurations, which contributed to the intense low-energy absorption bands. For the absorption band(s) in the 370-450 nm region, the NTOs in Table 7.3 suggest major ligand-to-ligand charge transfer (${}^1\text{LLCT}$, $\pi(\text{bhq}) \rightarrow \pi^*(\text{BODIPY})$) / ${}^1\text{MLCT}$ transitions, admixing with some BODIPY-NHC localized ${}^1\text{IL}$ (intraligand transition, *i.e.* ${}^1\pi, \pi^*$ / ${}^1\text{ILCT}$) characters. In contrast, according to the NTOs shown in Table 7.4, the high energy, strong absorption bands at 280-370 nm can be predominantly assigned to the spin-allowed bhq or BODIPY-NHC ligand-centered ${}^1\pi, \pi^*$ transitions, mixed with ${}^1\text{LLCT}$, ${}^1\text{MLCT}$, and minor ${}^1\text{ILCT}$ configurations.

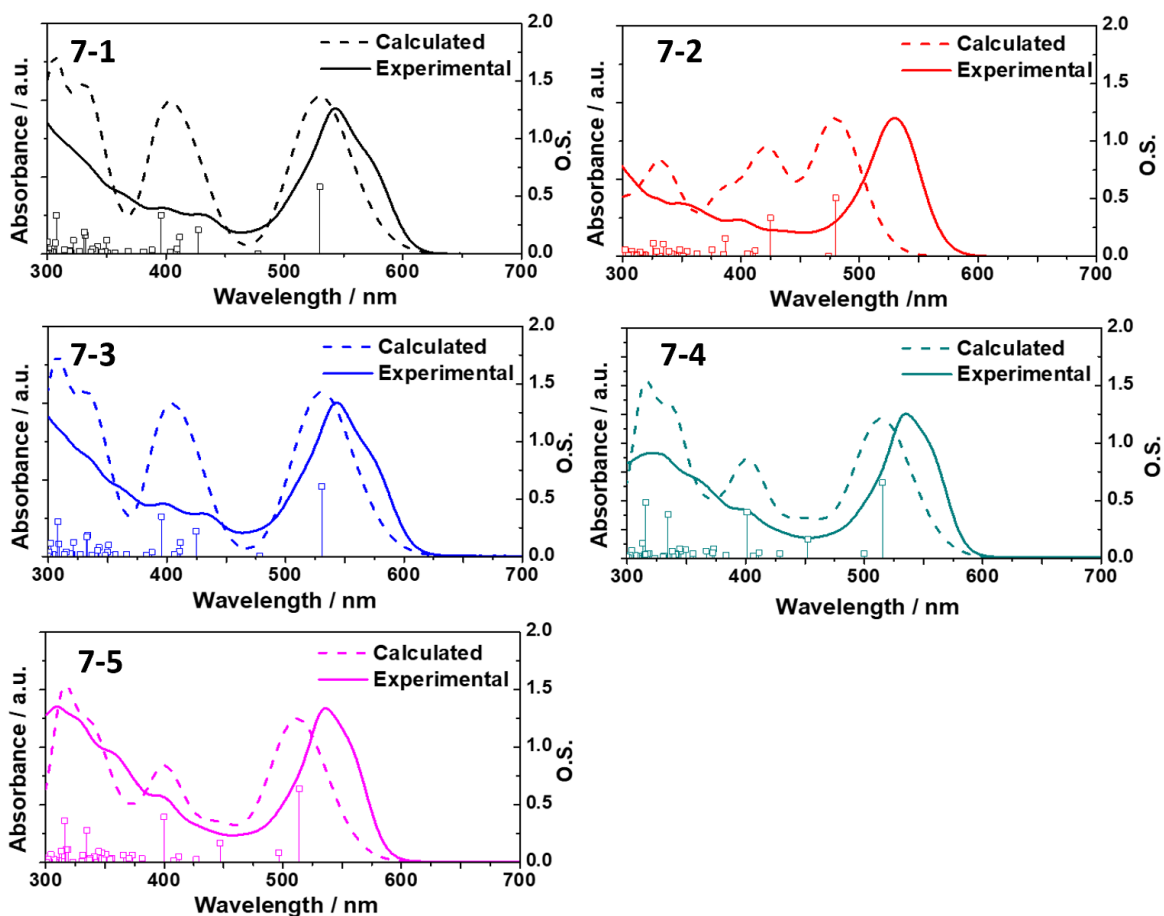


Figure 7.3. Normalized experimental and calculated absorption spectra with the respective oscillation strength. All absorption spectra are calculated by using the linear response time dependent DFT (TD-DFT) with the PBE1 functional and LAN2DZ/6-31G* basis set. Toluene are used as a solvent. Vertical bar indicates the oscillation strength of the transitions.

Table 7.2. NTOs for lowest-energy transitions of complexes **7-1** – **7-5** in toluene.

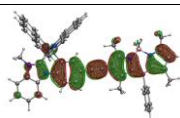
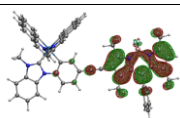
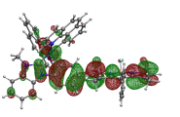
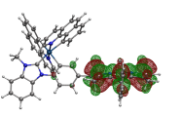
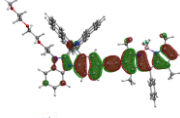
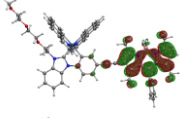
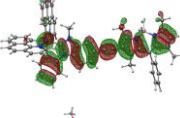
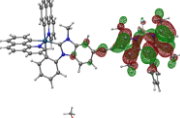
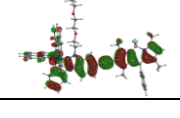
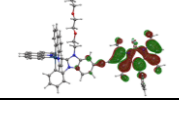
	S_n	Hole	Electron
7-1	S_1 533 nm $f = 0.633$		
7-2	S_1 480 nm $f = 0.507$		
7-3	S_1 531 nm $f = 0.647$		
7-4	S_1 515 nm $f = 0.655$		
7-5	S_1 513 nm $f = 0.641$		

Table 7.3. NTOs of the hole and electron of the moderate energy absorption band transitions of complexes **7-1** – **7-5**, calculated by the TD-DFT method with PBE1PBE functional, LANL2DZ/6-31G* basis and toluene as a solvent.

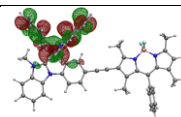
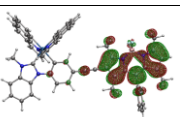
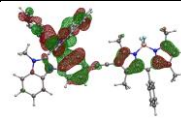
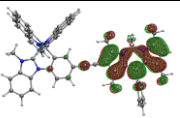
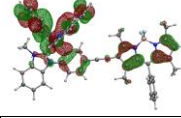
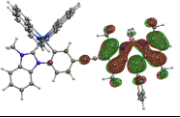
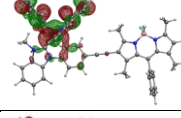
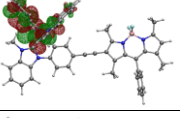
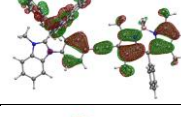
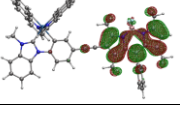
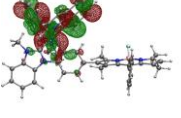
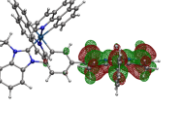
	S_n	Hole	Electron
	S_2 477 nm $f = 0.0017$		
	S_3 429 nm $f = 0.1557$		
7-1	S_4 412 nm $f = 0.1551$		
	S_5 411 nm $f = 0.0442$		
	S_7 396 nm $f = 0.3499$		
7-2	S_2 473 nm $f = 0.0001$		

Table 7.3. NTOs of the hole and electron of the moderate energy absorption band transitions of complexes **7-1** – **7-5**, calculated by the TD-DFT method with PBE1PBE functional, LANL2DZ/6-31G* basis and toluene as a solvent. (continued)


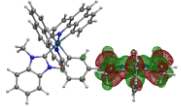

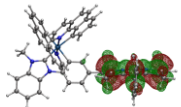
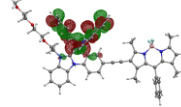
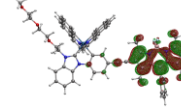
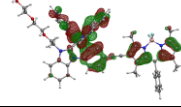
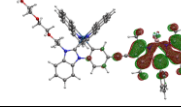
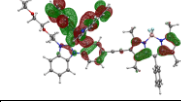
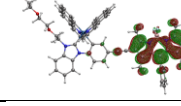
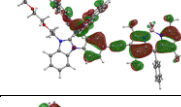
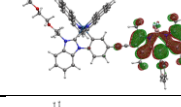
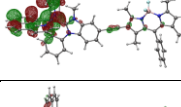
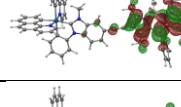
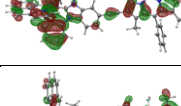
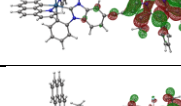
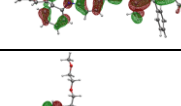
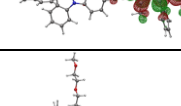
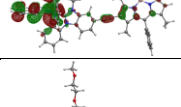
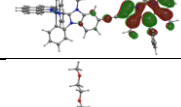
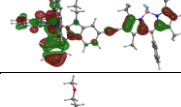
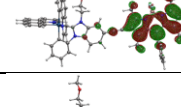
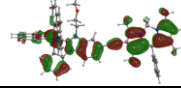
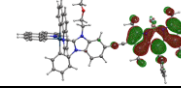
	S_n	Hole	Electron
	S_3 424 nm $f = 0.3307$		
	S_7 387 nm $f = 0.1558$		
7-3	S_2 482 nm $f = 0.0055$		
	S_3 424 nm $f = 0.1796$		
	S_4 413 nm $f = 0.1221$		
	S_7 395 nm $f = 0.3579$		
7-4	S_2 500 nm $f = 0.0396$		
	S_3 452 nm $f = 0.1633$		
	S_7 401 nm $f = 0.3959$		
7-5	S_2 496 nm $f = 0.0862$		
	S_3 447 nm $f = 0.1648$		
	S_7 399 nm $f = 0.3930$		

Table 7.4. NTOs of the hole and electron of the high energy absorption band transitions of complexes **7-1** – **7-5**, calculated by the TD-DFT method with PBE1PBE functional, LANL2DZ/6-31G* basis using toluene as the solvent.

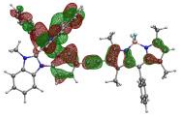
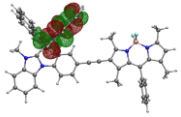
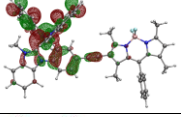
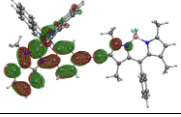
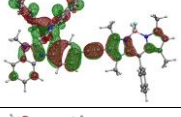
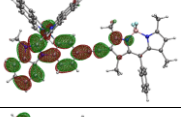
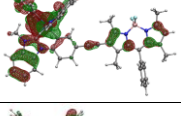
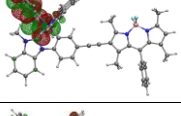
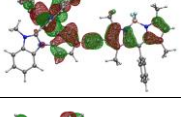
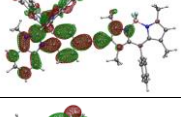
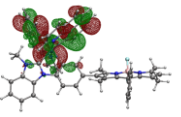
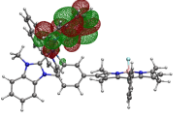
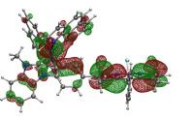
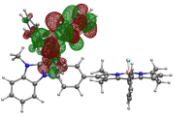

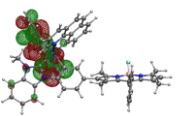
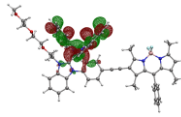
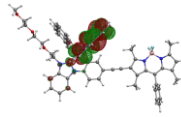
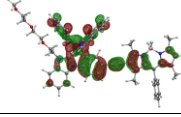
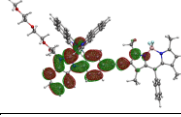
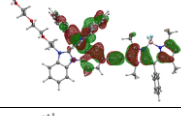
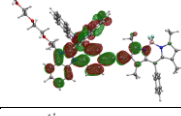
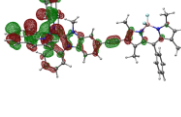
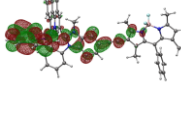
	S_n	Hole	Electron
7-1	S_{13} 350 nm $f = 0.1222$		
	S_{18} 340 nm $f = 0.0389$		
	S_{21} 332 nm $f = 0.2753$		
	S_{23} 322 nm $f = 0.0901$		
	S_{30} 309 nm $f = 0.3708$		
7-2	S_{18} 334 nm $f = 0.1076$ (60%)		
	Homo-1/Lumo+1 (33%)		
	S_{22} 325 nm $f = 0.1125$		
7-3	S_{20} 333 nm $f = 0.1144$		
	S_{21} 332 nm $f = 0.2474$		
	S_{30} 309 nm $f = 0.3345$		
7-4	S_{21} 334 nm $f = 0.3787$ (50%)		

Table 7.4. NTOs of the hole and electron of the high energy absorption band transitions of complexes **7-1** – **7-5**, calculated by the TD-DFT method with PBE1PBE functional, LANL2DZ/6-31G* basis using toluene as the solvent. (continued)

S_n	Hole	Electron
Homo-1/Lumo+1 (28%)		
S_{27} 315 nm $f = 0.4822$		
S_{21} 334 nm $f = 0.2816$		
7-5 S_{27} 316 nm $f = 0.3603$		

7.3.2. Photoluminescence

The steady-state emission spectra for complexes **7-1** – **7-5** were measured in degassed toluene, CH_3CN , THF, and dichloromethane at room temperature. The normalized emission spectra in toluene are presented in Figure 7.3, and the emission maxima and lifetimes are compiled in Table 7.1. The normalized emission spectra and the emission data in other solvents are provided in Figure 7.4 and Table 7.5. As shown in Figure 7.3, all of the complexes exhibited broad and structureless luminescence in toluene ranging from 582 to 610 nm, which were mirror images to their corresponding ^1IL absorption bands. The emission signals showed bi-exponential decays, with a short lifetimes of several nanoseconds and a longer lifetimes of several microseconds. The emission was only partially quenched by air. These characteristics imply that the emission of these complexes could be mixed with ^1IL fluorescence and charge transfer phosphorescence (^3CT). This fluorescence/phosphorescence mixing has been reported for a cationic dinuclear Ir(III) complex linked by BODIPY.⁴²

Table 7.5. Emission characteristics of complexes **7-1** – **7-5** in different solvents at r.t.

	$\lambda_{em} / \text{nm})(\tau_{em} / \mu\text{s}); \Phi_{em}$			
	CH ₃ CN	THF	CH ₂ Cl ₂	Toluene
7-1	575 (0.21); 0.31%	608 (0.07); 0.89%	603 (0.05); 0.97%	610 (4.96); 4.11%
7-2	559 (2.46); 3.01%	561 (4.19); 2.09%	547 (2.83); 5.46%	538 (3.12); 6.32%
7-3	575 (0.61); 0.74%	560 (3.57); 0.91%	563 (0.06); 0.86%	610 (5.26); 4.69%
7-4	578 (2.81); 6.61%	560 (3.57); 6.65%	571 (2.71); 5.27%	579 (4.77); 3.36%
7-5	573 (0.41); 1.27%	561 (3.63); 5.45%	570 (3.61); 11.7%	579 (4.89); 10.1%

Similar to the trend observed from the UV-vis absorption experiments, the emission maxima for **7-1** and **7-3** were identical as were those for **7-4** and **7-5**. This indicates that the oligoether chain did not impact the energies of the emitting states in these complexes. In contrast, the emission of **7-2** with BODIPY singly-bonded to NHC showed a pronounced blue-shift (27 nm) compared to that of **7-1**, with the C≡C linker, due to the shorter π -conjugation and the reduced coplanarity between BODIPY and NHC ligand in **7-2**. The attachment position of BODIPY on the NHC ligand also affected the emission energy as it did for the UV-vis absorption, namely, the emission maxima of **7-4** and **7-5** displayed a blue-shift of 23 nm with respect to those of **7-1** and **7-3**.

To assign the nature of the emitting states for these complexes, TDDFT calculations were performed based on the optimized singlet triplet excited state geometries. The singlet and triplet excited-state NTOs obtained for **7-1** – **7-5** are compiled in Table 7.6 for S₁ and T₂ states, and in Table 7.7 for T₁ states. Because neither the calculated T₁ energies nor the energy trend matched the experimental results, and the emission lifetimes were much shorter than the lifetimes obtained from the ns transient absorption measurement (which will be discussed in the next section), we believe that the phosphorescence components of the observed emission from these complexes are

from the T₂ states. Based on the NTOs provided in Table 7.6, the fluorescent S₁ states have mixed ¹ILCT/¹π,π*/¹MLCT configurations, while the T₂ states are predominantly ³ILCT/³MLCT configurations mixed with minor ³π,π* character. The S₁ states and the T₂ states are in energetic proximity, therefore, they both contribute to the observed emission. However, these two states are not in thermal equilibrium because the emission decay was bi-exponential, with a short component of less than 10 ns and a longer lifetime of several microseconds.

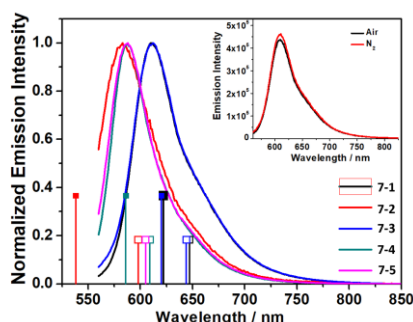


Figure 7.4. Normalized experimental emission spectra of **7-1** – **7-5** in deaerated toluene at room temperature. The excitation wavelength was 543 nm for **7-1** and **7-3**, 530 nm for **7-2**, and 535 nm for **7-4** and **7-5**. The open-headed lines represent the calculated S₁ fluorescence and the solid-headed lines represent the calculated T₂ phosphorescence. The inset shows the comparison of emission intensity in air-saturated and deaerated toluene solutions for **7-1**.

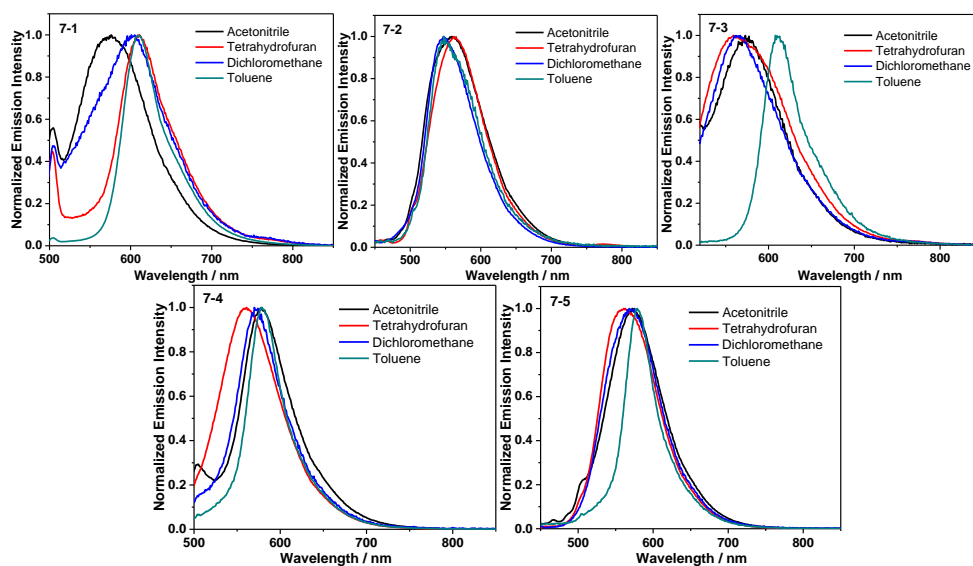


Figure 7.5. Normalized emission spectra of complexes **7-1** – **7-5** in different solvents at r.t. ($\lambda_{ex} = 436$ nm).

Table 7.6. NTOs corresponding to the optimized S_1 and T_2 states of complexes **7-1** – **7-5** in toluene.

S_1			T_2		
Energy	Hole	Electron	Energy	Hole	Electron
7-1 647 nm			623 nm		
7-2 598 nm			538 nm		
7-3 644 nm			621 nm		
7-4 609 nm			586 nm		
7-5 605 nm			584 nm		

Table 7.7. NTOs of the optimized 1st triplet state. All excited state calculations were done with the PBE1 functionals with LAN2DZ/6-31G* basis set and toluene as a solvent.

T_1	Hole	Electron
7-1 1121 nm		
7-2 1192 nm		
7-3 1122 nm		
7-4 1143 nm		
7-5 1143 nm		

7.3.3. Transient absorption (TA)

To further understand the triplet excited state characteristics of **7-1** – **7-5**, especially the non-emitting T_1 states in these complexes, nanosecond TA were collected in deaerated toluene at room temperature. The TA spectra of **7-1** – **7-5** at zero-time delay upon 355-nm excitation are presented in Figure 7.5. The TA parameters, such as the TA band maxima, triplet excited-state lifetimes and quantum yields, and triplet extinction coefficients, are compiled in Table 7.1. Fitting of the TA signals revealed a long-lived species (ca. 28-55 μs). In addition, the TA spectral features of **7-1** – **7-5** were similar, with ground-state bleaching arising from the BODIPY-NHC localized ^1IL absorption. These spectra are also similar to that of the iodo-BODIPY reported in the literature.⁷⁵ Therefore, the triplet excited states that produced the observed TA should have the same nature for all of the complexes, likely from the BODIPY localized $^3\pi, \pi^*$ state. The lifetimes of **7-1** – **7-5** obtained from the decay of the TA signals are distinctively different from their emission lifetimes, indicating that the excited states observed by TA in these complexes are different from their emitting excited states. The long TA lifetimes were assigned to excited states with $^3\pi, \pi^*$ characters. The NTOs for T_1 states in Table 7.5 confirmed that the T_1 states for these complexes are of $^3\pi, \pi^*$ configuration and localized exclusively on the BODIPY motif.

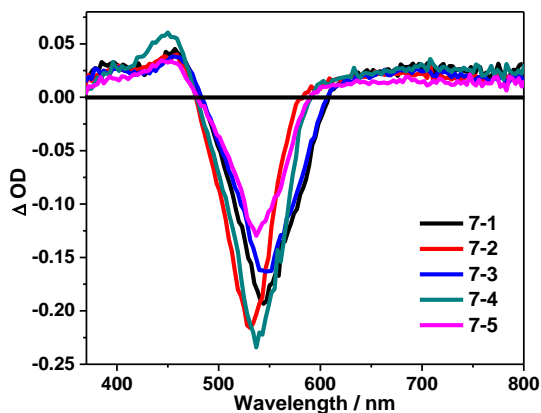


Figure 7.6. Nanosecond transient difference absorption spectra of complexes **7-1** – **7-5** in toluene at room temperature immediately after 355 nm laser pulse excitation. $A_{355} = 0.4$ in a 1-cm cuvette.

7.3.4. Singlet oxygen generation

7-3 and **7-5** were designed with oligoether substituents as R3 (Chart 7-1) to increase the hydrophilicities of these neutral Ir(III) NHC complexes for improved aqueous solubility (which is a desirable property for *in vitro* biological testing). Our detailed photophysical and computational analyses of **7-3** and **7-5** (compared to their corresponding methyl-substituted **7-2** and **7-4** relatives) indicated that the addition of the oligoether groups did not alter the general excited state dynamics observed for these systems. Therefore, the more water-soluble **7-3** and **7-5** were further investigated for their photobiological activities.

The abilities of **7-3** and **7-5** to generate singlet oxygen ($^1\text{O}_2$) were assessed as quantum yields for $^1\text{O}_2$ production (Φ_Δ) in MeCN relative to $[\text{Ru}(\text{bpy})_3](\text{PF}_6)_2$ as the standard ($\Phi_\Delta = 56\%$). The direct method was employed, whereby sensitized $^1\text{O}_2$ was detected by its phosphorescence centered at 1268 nm. MeCN was used as the solvent since $^1\text{O}_2$ phosphorescence is quenched in aqueous solution.⁷⁶ The value of Φ_Δ for **7-3** was near 37% and largely independent of excitation wavelength, whereas that for **7-5** ranged from 8-22% as a function of excitation wavelength. Excitation at 352, 450, and 534 nm yielded values for Φ_Δ of 11, 22, and 8%, respectively.

7-3 was the more efficient $^1\text{O}_2$ generator at all wavelengths investigated, which could be attributed, in part, to the fact that its quantum yield for triplet state formation is larger (51 versus 40%). Clearly, the substitution position of the BODIPY chromophore, either on the *meso*-phenyl versus the benzimidazole portion of the NHC ligand, impacts the excited state dynamics and photophysical properties of the complexes. These structural differences may, therefore, be expected to also alter their photobiological properties.

7.3.5. Cytotoxicity and photocytotoxicity toward cancer cells

Based on their abilities to generate $^1\text{O}_2$ under cell-free conditions, albeit with modest efficiency, it was anticipated that both **7-3** and **7-5** would give rise to in vitro photobiological effects. The human melanoma cell line SKMEL28 was used to probe the cytotoxicities and photocytotoxicities of **7-3** and **7-5**. Briefly, cells were dosed 1 nM-300 μM of **7-3** or **7-5** (dissolved in water supplemented with 10% DMSO (v/v) and serially diluted with phosphate buffered saline (PBS)) and incubated for 16 h before receiving a dark treatment or a light treatment. The illumination condition was 100 J cm^{-2} of either broadband visible or monochromatic red (625 nm) light. After a dark or light treatment, the cells were incubated for 48 h, treated with the resazurin cell viability indicator,⁷⁷ and incubated an additional 2–4 h. The relative cell viabilities for the dark and light treatments of cells dosed with compound were quantified by the metabolic reduction of resazurin to its fluorescent product resorufin (Figure 7.6, Table 7.8).

Table 7.8. Comparison of EC_{50} values (μM) for SKMEL28 cancer cells dosed with complexes **7-3** and **7-5**.

	SKMEL28 cells				
	Dark	Vis ^a	PI ^b	Red ^c	PI ^b
7-3	> 300	9.66 ± 0.28	>31	53.7 ± 2.1	>6
7-5	20.2 ± 1.3	0.15 ± 0.01	135	13.0 ± 0.1	2

^aVis-PDT: 16 h drug-to-light interval followed by 100 J cm^{-2} broadband visible light irradiation, ^bPI = phototherapeutic index (ratio of dark EC_{50} to visible-light EC_{50}), ^cRed-PDT: 16 h drug-to-light interval followed by 100 J cm^{-2} light irradiation with 625 nm LEDs.

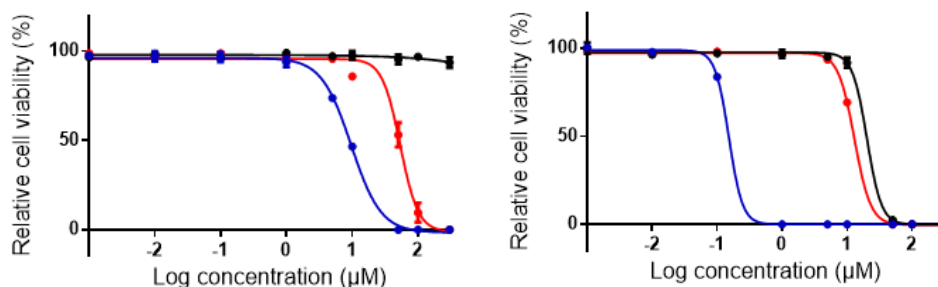


Figure 7.7. In vitro dose-response curves for complexes **7-3** (left) and **7-5** (right) in SKMEL28 cells treated in the dark (black) and with visible (blue) or red (red) light activation.

7-3 was nontoxic toward SKMEL28 cells ($EC_{50} > 300 \mu\text{M}$), while **7-5** was substantially more cytotoxic ($EC_{50} = 20 \mu\text{M}$). With broadband visible light activation, both compounds were photocytotoxic. The photocytotoxicity of **7-5** was submicromolar, with an EC_{50} value of 150 nM and PI of 135, while the visible-light EC_{50} value for **7-3** was approximately 10 μM and its PI was 31. The photocytotoxicities of both compounds with red light were substantially attenuated (5-fold for **7-3** and over 85-fold for **7-5**), giving rise to much smaller PI values (6 for **7-3** and 2 for **7-5**).

Despite having much higher cytotoxicity in the dark, **7-5** was the better in vitro photosensitizing agent according to both the magnitude of its photocytotoxicity and its phototherapeutic margin. This was initially surprising since the value of Φ_{Δ} for **7-3** was significantly larger than that for **7-5**. This discrepancy could be due to differences in $^1\text{O}_2$ production under cell-free conditions versus the in vitro experiment, or that reactive oxygen species (ROS) other than $^1\text{O}_2$ may be involved in the phototoxic mechanism.

To probe for the involvement of ROS, more broadly defined, as a possible source of the photocytotoxic activity for **7-3** and **7-5**, SKMEL28 cells were preincubated with the cell-permeable and highly sensitive 2',7'-dichlorodihydrofluorescein diacetate (DCFDA) fluorogenic dye before performing (photo)cytotoxicity assays (Figure 7.7). The compounds were tested in the range of 4 pM to 126 μM , and a sub-lethal light dose of 50 J cm^{-2} broadband visible light was used for the light condition with a reduced incubation time of 30 min between compound addition and light treatment. DCFDA is deacetylated by cellular esterases to a nonfluorescent compound, which is subsequently oxidized by ROS to the highly fluorescent DCF product that can be detected by its characteristic emission.⁷⁸ ROS that can be detected by this method include superoxide anion ($\text{O}_2^{\cdot-}$), hydrogen peroxide (H_2O_2), hydroxyl radical (HO^{\cdot}), and singlet oxygen ($^1\text{O}_2$), which react directly or indirectly with the deacetylated probe.⁷⁹

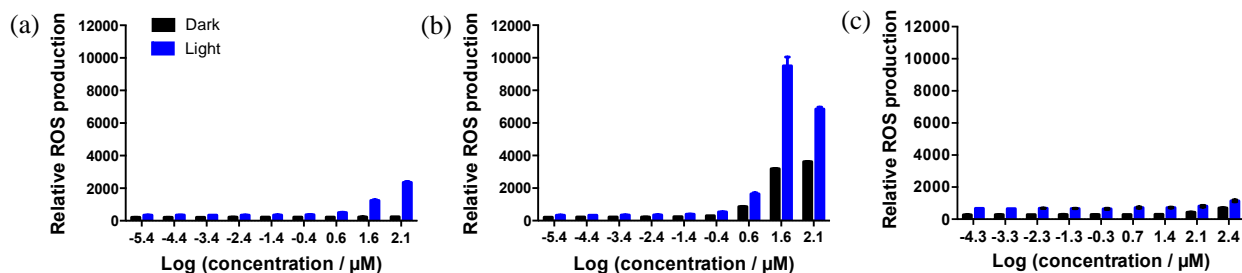


Figure 7.8. Reactive oxygen species assay results for SKMEL28 cells treated with **7-3** (a), **7-5** (b), or the positive control *tert*-butyl hydrogen peroxide TBHP (c) using DCFH-DA as a ROS probe. Cells were treated in the dark (black bars) or with 50 J cm⁻¹ visible light (blue bars). ROS production was measured at 120 min post-treatment.

Dark treatments were included to quantify baseline ROS levels under the assay conditions for comparison, and *tert*-butyl hydrogen peroxide (TBHP) was used as a positive control (Figure 7.7c). The signal produced by TBHP was relatively weak, but sufficient, owing to the short incubation that was necessary to ensure a sub-lethal treatment with photoactivated **7-3** and **7-5**. ROS generation with **7-3** in the dark was minimal at all concentrations tested, while cells treated with **7-5** in the dark showed elevated ROS levels at concentrations greater than 1 μM. This observation may account for the cytotoxicity induced by **7-5** in the absence of a light trigger, whereby **7-5** was at least 15× more cytotoxic (in the dark) than **7-3**.

Light-treated complexes **7-3** and **7-5** increased the detected fluorescence from the DCF product in a dose-dependent manner over the dark controls and also in comparison to the positive control THBP (Figure 7.7). The highest concentration of light-treated **7-5** (126 μM) showed a slight decrease in the DCF fluorescence relative to the second highest concentration (39 μM). This attenuation is typical when the cells begin to lose viability, which is why it is important to choose a sub-lethal dose for ROS quantification. **7-5** produced significantly more DCF fluorescence than **7-3** at the highest concentrations tested. Therefore, the much larger PI measured for **7-5** (compared to **7-3**) may stem from its more efficient light-mediated ROS production. Which ROS is most important for the photocytotoxicity invoked by **7-5** is not known at this time, although we

hypothesize that ROS other than $^1\text{O}_2$ may be involved based on the lower value of Φ_{Δ} measured for **6-5** under the cell-free condition.

Confocal microscopy was used to observe the qualitative effects of **7-3** and **7-5** on SKMEL28 cells with a dark or visible light treatment of 50 J cm^{-2} (Figure 7.8). A concentration of $50 \mu\text{M}$ was chosen because a marked difference in the dark cytotoxicity of **7-3** and **7-5** at this concentration was anticipated (since $50 \mu\text{M}$ is greater than the dark EC_{50} value of **7-3**, but not of **7-5**). The light treatment was chosen to be 50 J cm^{-2} (half the dose of the cell cytotoxicity assays) and imaging was done at 15 min post-treatment to ensure that cells were imaged under sub-lethal conditions, where a comparison of cellular morphologies and uptake might be made.

The differences in the $^3\text{MLCT}$ emission quantum yields for **7-3** and **7-5** were apparent in the dark confocal images, where cellular uptake by **7-3** was detectable as a very weak signal but no signal was detected for **7-5**. Qualitatively, there appeared to be more cellular debris from dead and dying cells treated with **7-5** in the dark (Figure 7.8a, bottom row) but emission was not detected. Both compounds caused a general change in the morphology of a large fraction of the cells treated in the dark, from the typical elongated and spindle shape to spherical.

With light activation, intracellular emission from **7-3** was much more pronounced (Figure 7.8b, top row). If the signal intensity is proportional to concentration, then photoactivated uptake of **7-3** results in accumulation in the cytoplasm and mitochondria but not in the nuclei. Interestingly, **7-5** produced luminescence in the cellular debris from dead and dying cells that were treated with visible light and very faint luminescence from the intact cells. Images of cells treated with **7-3** and light did not exhibit the dark clumps of cellular debris that were observed in the images of **7-5**, possibly reflecting the differences in photocytotoxicities of these two compounds.

Photoactivated uptake also led to a larger concentration of **7-5** in cells (assuming that signal intensity is proportional to concentration), making its detection possible. Given that luminescence from **7-3** is almost five-fold more efficient than that from **7-5** (and this difference could be magnified in cells), the confocal imaging experiment cannot definitively establish that cellular uptake of **7-3** higher than **7-5**. It would be expected that the higher dark toxicity of **7-5** would be correlated with better cellular uptake, but additional intracellular compound quantification methods were not carried out as part of this study.

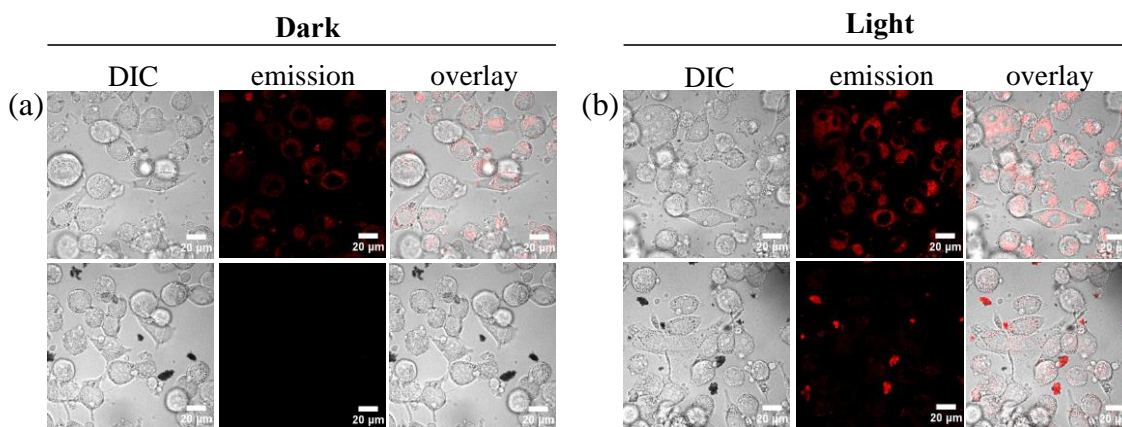


Figure 7.9. Laser scanning confocal microscopy images of SKMEL28 cells dosed with 50 μM **7-3** (top row) or **7-5** (bottom row) in the dark (a) or with 50 J cm^{-2} visible light (b).

7.3.6. Cytotoxicity and photocytotoxicity toward bacteria

The antimicrobial photobiological activities of **7-3** and **7-5** were also assessed using *Streptococcus aureus* (*S. aureus*) growing as planktonic cultures (Table 7.9, Figure 7.9). The compounds were tested at concentrations between 0.4 and 100 μM , and the light treatments were approximately 35 J cm^{-2} of visible light. Despite showing photobiological activity against SKMEL28 melanoma cells, **7-3** was inactive against *S. aureus* both in the dark and with a light treatment. On the other hand, **7-5** was nontoxic to *S. aureus* in the dark but phototoxic with a visible light EC_{50} of approximately 7 μM ($\text{PI} > 15$). The observation that **7-3** was less photobiologically active (inactive) than **7-5** against *S. aureus* agreed with the trend in cancer cells,

further highlighting the discrepancy between the $^1\text{O}_2$ quantum yields and phototoxicities for these two compounds. It appears that ROS other than $^1\text{O}_2$ are also important for the phototoxic mechanism against *S. aureus*. Why **7-5** might be a better ROS generator than **7-3** is not known at this time, but the substitution position of the BODIPY unit on the NHC ligand plays a major role in determining the biological and photobiological activities against the cell lines investigated in this study.

Table 7.9. Comparison of EC_{50} values (μM) for *streptococcus aureus* dosed with **7-3** or **7-5**.

	<i>streptococcus aureus</i>		
	Dark	Vis ^a	PI ^b
7-3	>100	>100	-
7-5	>100	6.67 ± 0.07	>15

^aVis-PDT: 35 J cm^{-2} broadband visible light irradiation; ^bPI = phototherapeutic index (ratio of dark EC_{50} to visible-light EC_{50}).

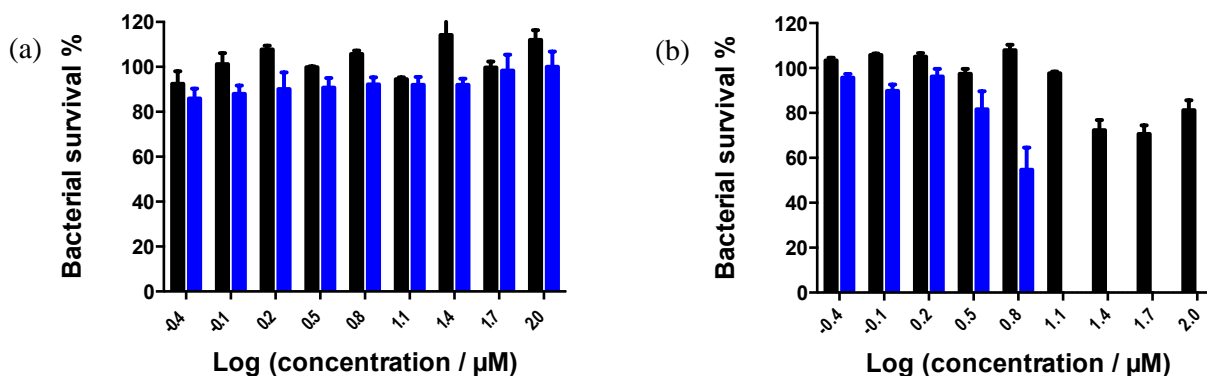


Figure 7.10. Bacterial cell survival dose-response bar graphs for complexes **7-3** (a) and **7-5** (b) in *Streptococcus aureus*, treated in the dark (black) or with 35 J cm^{-1} visible (blue) light.

7.4. Conclusions

New neutral iridium(III) complexes bearing BODIPY-substituted NHC ligands are reported. Their photophysical characteristics were systematically investigated via spectroscopic methods and DFT calculations. All complexes exhibited BODIPY-localized intense $^1\text{IL}/^1\text{MLCT}$ absorption at 530-543 nm and $^1\text{IL}/^3\text{CT}$ emission at 582-610 nm. However, the lowest triplet

excited state of these complexes are the BODIPY-localized $^3\pi, \pi^*$ states. It was demonstrated that the position of the BODIPY pendant on the NHC ligand impacted both the $^1\text{IL}/^1\text{MLCT}$ absorption and $^1\text{IL}/^3\text{CT}$ emission bands. Complexes **7-1** and **7-3**, with the BODIPY-ethynyl motif attached at C4 of the phenyl ring of the NHC ligand, caused a red-shift of the $^1\text{IL}/^1\text{MLCT}$ absorption and $^1\text{IL}/^3\text{CT}$ emission bands compared to those in **7-4** and **7-5** that have BODIPY-ethynyl at C5 of the benzimidazole unit of the NHC ligand. Meanwhile, both the lowest singlet excited state and the emitting states of **7-1** were lowered compared to those in **7-2**, due to the extended π -conjugation induced by the ethynyl linker in **7-1**. In contrast, replacing the methyl substituents on C3 of benzimidazole in complexes **7-1** and **7-4** by oligoether substituents in **7-3** and **7-5**, respectively, did not impact the energies of the lowest singlet and emitting excited states in the corresponding complexes.

7-3 and **7-5** were photobiologically active toward SKMEL28 melanoma cells with visible light activation, with **7-5** possessing a much larger PI and higher photocytotoxicity. The photobiological trends in cancer cells did not correlate with cell-free $^1\text{O}_2$ quantum yields. The DCFDA assay for intracellular ROS detection showed that **7-5** was much more effective at ROS production. **7-5** was also photobiologically active toward *S. aureus*, while **7-3** was not. Therefore, ROS other than $^1\text{O}_2$ may play a role in the phototoxic mechanism toward both cancer cells and bacterial cells. These studies indicate that the substitution position of BODIPY on the NHC ligand plays a profound role in the cytotoxicity and photocytotoxicity of this new class of complexes. C4-phenyl substitution of BODIPY compared to substitution at C5 of benzimidazole leads to lower $^1\text{O}_2$ quantum yields but more effective production of other ROS. Obviously, the impact of BODIPY substitution position at the NHC ligand is more pronounced on the photobiological activities than on the photophysical properties. Future studies are aimed at expanding this

structure-activity relationship in this new class of neutral Ir(III) NHC complexes, identifying the ROS mediator for phototoxic effects, and probing the photobiological activities against a larger number of cancer cell lines.

7.5. References

- ¹ Celli, J. P.; Spring, B. Q.; Rizvi, I.; Evans, C. L.; Samkoe, K. S.; Verma, S.; Pogue, B. W.; Hasan, T. *Chem. Rev.* **2010**, *110*, 2795.
- ² Li, X.; Lee, S.; Yoon J. *Chem. Soc. Rev.* **2018**, *47*, 1174.
- ³ Dolmans, D. E. J. G. J.; Fukumura D.; Jain, R. K. *Nat. Rev. Cancer* **2003**, *3*, 380.
- ⁴ Sharman, W. M.; Allen, C. M.; van Lier, J. E. *Drug Disc. Today* **1999**, *4*, 507.
- ⁵ Moan, J.; Peng, Q. *Anticancer Res.* **2003**, *23*, 3591.
- ⁶ Wilson, B. C. *Can. J. Gastroenterol. Hepatol.* **2002**, *16*, 393.
- ⁷ Vrouenraets, M. B.; Visser, G. W.; Snow, G. B.; van Dongen, G. A. *Anticancer Res.* **2003**, *23*, 505.
- ⁸ Lovell, J. F.; Liu, T. W. B.; Chen, J.; Zheng, G. *Chem. Rev.* **2010**, *110*, 2839.
- ⁹ Stacey, O. J.; Pope, S. J. A. *RSC Adv.* **2013**, *3*, 25550.
- ¹⁰ Wang, C.; Lystrom, L.; Yin, H.; Hetu, M.; Kilina, S.; McFarland, S. A.; Sun, W. *Dalton Trans.* **2016**, *45*, 16366.
- ¹¹ Mari, C.; Pierroz, V.; Ferrari, S.; Gasser, G. *Chem. Sci.* **2015**, *6*, 2660.
- ¹² Monro, S.; Colón, K. L.; Yin, H.; Roque, J.; Konda, P.; Gujar, S.; Thummel, R. P.; Lilge, L.; Cameron, C. G.; McFarland, S. A. *Chem. Rev.* **2018**, DOI:10.1021/acs.chemrev.8b00211.

- ¹³ Shi, G.; Monro, S.; Hennigar, R.; Colpitts, J.; Fong, J.; Kasimova, K.; Yin, H.; DeCoste, R.; Spencer, C.; Chamberlain, L.; Mandel, A.; Lilgec, L.; McFarland, S. A. *Coord. Chem. Rev.* **2015**, 282–283, 127.
- ¹⁴ Zamora, A.; Viguera, G.; Rodríguez, V.; Santana, M. D., Ruiz, J. *Coord. Chem. Rev.* **2018**, 360, 34.
- ¹⁵ Lv, W.; Zhang, Z.; Zhang, K. Y.; Zhang, Y.; Yang, H.; Liu, S.; Xu, A.; Guo, S.; Zhao, Q.; Huang, W. *Angew. Chem. Int. Ed.* **2016**, 55, 9947.
- ¹⁶ Li, Y.; Tan, C.-P.; Zhang, W.; He, L.; Ji, L.-N.; Mao, Z.-W. *Biomaterials* **2015**, 39, 95.
- ¹⁷ Li, S. P.-Y.; Lau, C. T.-S.; Louie, M.-W.; Lam, Y.-W.; Cheng, S. H.; Lo, K. K.-W. *Biomaterials* **2013**, 34, 7519.
- ¹⁸ Qiu, K.; Ouyang, M.; Liu, Y.; Huang, H.; Liu, C.; Chen, Y.; Ji, L.; Chao, H. *J. Mater. Chem. B* **2017**, 5, 5488.
- ¹⁹ Ouyang, M.; Zeng, L.; Qiu, K.; Chen, Y.; Ji, L.; Chao, H. *Eur. J. Inorg. Chem.* **2017**, 1764.
- ²⁰ Zheng, Y.; He, L.; Zhang, D.-Y.; Tan, C.-P.; Ji, L.-N.; Mao, Z.-W. *Dalton Trans.* **2017**, 46, 11395.
- ²¹ He, L.; Li, Y.; Tan, C.-P.; Ye, R.-R.; Chen, M.-H.; Cao, J.-J.; Ji, L.-N.; Mao, Z.-W. *Chem. Sci.* **2015**, 6, 5409.
- ²² Nam, J. S.; Kang, M. G.; Kang, J.; Park, S. Y.; Lee, S. J.; Kim, H. T.; Seo, J. K.; Kwon, O. H.; Lim, M. H.; Rhee, H. W.; Kwon, T. H. *J. Am. Chem. Soc.* **2016**, 138, 10968.
- ²³ Cao, R.; Jia, J.; Ma, X.; Zhou, M.; Fei, H. *J. Med. Chem.* **2013**, 56, 3636.
- ²⁴ Tian, X.; Zhu, Y.; Zhang, M.; Luo, L.; Wu, J.; Zhou, H.; Guan, L.; Battaglia, G.; Tian, Y. *Chem. Commun.* **2017**, 53, 3303.

- ²⁵ Liu, S.; Liang, H.; Zhang, K. Y.; Zhao, Q.; Zhou, X.; Xu, W.; Huang, W. *Chem. Commun.* **2015**, *51*, 7943.
- ²⁶ Zhang, G.; Zhang, H.; Gao, Y.; Tao, R.; Xin, L.; Yi, J.; Li, F.; Liu, W.; Qiao, J. *Organometallics*, **2014**, *33*, 61.
- ²⁷ Escobedo, J. O.; Rusin, O.; Lim, S.; Stromgim, R. M. *Curr. Opin. Chem. Biol.* **2010**, *14*, 64.
- ²⁸ Skorka, L.; Filapek, M.; Zur, L.; Małeckı, J. G.; Pisarski, W.; Olejnik, M.; Danikiewicz, W.; Krompiec, S. *J. Phys. Chem. C* **2016**, *120*, 7284.
- ²⁹ Liu, R.; Dandu, N.; Chen, J.; Li, Y.; Li, Z.; Liu, S.; Wang, C.; Kilina, S.; Kohler, B.; Sun, W. *J. Phys. Chem. C* **2014**, *118*, 23233.
- ³⁰ Wang, L.; Yin, H.; Cui, P.; Hetu, M.; Wang, C.; Monro, S.; Schaller, R. D.; Cameron, C. G.; Liu, B.; Kilina, S.; McFarland S. A.; Sun, W. *Dalton Trans.* **2017**, *46*, 8091.
- ³¹ Sun, W.; Pei, C.; Lu, T.; Cui, P.; Li, Z.; McCleese, C.; Fang, Y.; Kilina, S.; Song, Y.; Burda, C. *J. Mater. Chem. C* **2016**, *4*, 5059.
- ³² Zhao, Q.; Liu, S.; Shi, M.; Wang, C.; Yu, M.; Li, L.; Li, F.; Yi, T.; Huang, C. *Inorg. Chem.* **2006**, *45*, 6152.
- ³³ Liu, B.; Lystrom, L.; Kilina, S.; Sun, W. *Inorg. Chem.* **2017**, *56*, 5361.
- ³⁴ Ford, W. E.; Rodgers, M. A. J. *J. Phys. Chem.* **1992**, *96*, 2917.
- ³⁵ McClenaghan, N. D.; Leydet, Y.; Maubert, B.; Indelli, M. T.; Campagna. S. *Coord. Chem. Rev.* **2005**, *249*, 1336.
- ³⁶ Wang, L.; Yin, H.; Javed, M. A.; Hetu, M.; Monro, S.; Wang, C.; Kilina, S.; McFarland, S. A.; Sun, W. *Inorg. Chem.* **2017**, *56*, 3245.
- ³⁷ Lincoln, R.; Kohler, L.; Monro, S.; Yin, H.; Stephenson, M.; Zong, R.; Chouai, A.; Dorsey, C.; Hennigar, R.; Thummel, R. P.; McFarland, S. A. *J. Am. Chem. Soc.* **2013**, *135*, 17161.

- ³⁸ Stephenson, M.; Reichardt, C.; Pinto, M.; Wächtler, M.; Sainuddin, T.; Shi, G.; Yin, H.; Monro, S.; Sampson, E.; Dietzek, B.; McFarland, S. A. *J. Phys. Chem. A* **2014**, *118*, 10507.
- ³⁹ Arenas, Y.; Monro, S.; Shi, G.; Mandel, A.; McFarland, S.; Lilge, L. *Photodiag. Photodyn. Ther.* **2013**, *10*, 615.
- ⁴⁰ Galletta, M.; Campagna, S.; Quesada, M.; Ulrich, G.; Ziessel, R. *Chem. Commun.* **2005**, *0*, 4222.
- ⁴¹ Majumdar, P.; Yuan, X.; Li, S.; Guennic, B. L.; Ma, J.; Zhang, C.; Jacquemin, D.; Zhao, J. *J. Mater. Chem. B* **2014**, *2*, 2838.
- ⁴² Wang, J.; Lu, Y.; McGoldrick, N.; Zhang, C.; Yang, W.; Zhao, J.; Draper, S. M. *J. Mater. Chem. C* **2016**, *4*, 6131.
- ⁴³ McCusker, C. E.; Hablot, D.; Ziessel, R.; Castellano, F. N. *Inorg. Chem.* **2012**, *51*, 7957.
- ⁴⁴ McCusker, C. E.; Hablot, D.; Ziessel, R.; Castellano, F. N. *Inorg. Chem.* **2014**, *53*, 12564.
- ⁴⁵ Kamkaew, A.; Lim, S. H.; Lee, H. B.; Kiew, L. V.; Chung, L. Y.; Burgess, K. *Chem. Soc. Rev.* **2013**, *42*, 77.
- ⁴⁶ Zhao, J.; Xu, K.; Yang, W.; Wang, Z.; Zhong, F. *Chem. Soc. Rev.* **2015**, *44*, 8904.
- ⁴⁷ Tang, Q.; Xiao, W.; Huang, C.; Si, W.; Shao, J.; Huang, W.; Chen, P.; Zhang, Q.; Dong, X. *Chem. Mater.* **2017**, *29*, 5216.
- ⁴⁸ Turan, I. S.; Cakmak, F. P.; Yildirim, D. C.; Cetin-Atalay, R.; Akkaya, E. U. *Chem. Eur. J.* **2014**, *20*, 16088.
- ⁴⁹ Tabrizi, L.; Chiniforoshan, H. *RSC Adv.* **2017**, *7*, 34160.
- ⁵⁰ Yang, C.; Mehmood, F.; Lam, T. L.; Chan, S. L.-F.; Wu, Y.; Yeung, C.-S.; Guan, X.; Li, K.; Chung, C. Y.-S.; Zhou, C.; Zou, T.; Che, C.-M. *Chem. Sci.* **2016**, *7*, 3123.
- ⁵¹ Jacquemin, D.; Escudero, D. *Chem. Sci.* **2017**, *8*, 7844.

- ⁵² Aghazada, S.; Huckaba, A. J.; Pertegas, A.; Babaei, A.; Grancini, G.; Zimmermann, I.; Bolink, H.; Nazeeruddin, M. K. *Eur. J. Inorg. Chem.* **2016**, *2016*, 5089.
- ⁵³ Lee, J.; Chen, H.-F.; Batagoda, T.; Coburn, C.; Djurovich, P. I.; Thompson, M. E.; Forrest, S. F. *Nat. Mater.* **2016**, *15*, 92.
- ⁵⁴ Li, T.-Y.; Liang, X.; Zhou, L.; Wu, C.; Zhang, S.; Liu, X.; Lu, G.-Z.; Xue, L.-S.; Zheng, Y.-X.; Zuo, J.-L. *Inorg. Chem.* **2015**, *54*, 161.
- ⁵⁵ Tennyson, A. G.; Rosen, E. L.; Collins, M. S.; Lynch, V. M.; Bielawski, C. W. *Inorg. Chem.* **2009**, *48*, 6924.
- ⁵⁶ Li, Z.; Cui, P.; Wang, C.; Kilina, S.; Sun, W. *J. Phys. Chem. C* **2014**, *118*, 28764.
- ⁵⁷ Yang, J.-H.; Yoon, K.-J.; Noh, H.-J.; Yoon, D.-W.; Shin, I.-A.; Kim, J.-Y. US Patent Application Publication No. US 2016/0133856 A1, May 12, **2016**.
- ⁵⁸ Nakano, Y.; Yamamoto, H.; Hashimoto, R.; Nagashima, H. PCT Int. Appl., WO 2013118507, Aug 15, **2013**.
- ⁵⁹ Schelz, D. *Helv. Chim. Acta* **1978**, *61*, 2452.
- ⁶⁰ Wu, W.; Liu, L.; Cui, X.; Zhang, C.; Zhao, J. *Dalton Trans.* **2013**, *42*, 14374.
- ⁶¹ Suzuki, K.; Kobayashi, A.; Kaneko, S.; Takehira, K.; Yoshihara, T.; Ishida, H.; Shiina, Y.; Oishi, S.; Tobita, S. *Phys. Chem. Chem. Phys.* **2009**, *11*, 9850.
- ⁶² Carmichael, I.; Hug, G. L. *J. Phys. Chem. Ref. Data* **1986**, *15*, 1.
- ⁶³ Kumar, C. V.; Qin, L.; Das, P. K. *J. Chem. Soc., Faraday Trans. 2* **1984**, *80*, 783.
- ⁶⁴ Firey, P. A.; Ford, W. E.; Sounik, J. R.; Kenney, M. E.; Rodgers, M. A. J. *J. Am. Chem. Soc.* **1988**, *110*, 7626.
- ⁶⁵ Kohn, W.; Sham, L. J. *Phys. Rev.* **1965**, *140*, A1133.
- ⁶⁶ Gill, P. M. W.; Johnson, B. G.; Pople, J. A.; Frisch, M. J. *Chem. Phys. Lett.* **1992**, *197*, 499.

- ⁶⁷ Hay, P. J.; Wadt, W. R. *J. Chem. Phys.* **1985**, *82*, 299.
- ⁶⁸ Clark, T.; Chandrasekhar, J.; Spitznagel, G. W.; Schleyer, P. V. R. *J. Comput. Chem.* **1983**, *4*, 294.
- ⁶⁹ Barone, V.; Cossi, M.; Tomasi, J. *J. Comput. Chem.* **1998**, *19*, 404.
- ⁷⁰ Casida, M. E.; Jamorski, C.; Casida, K. C.; Salahub, D. R. *J. Chem. Phys.* **1998**, *108*, 4439.
- ⁷¹ Pei, C.; Cui, P.; McCleese, C.; Kilina, S.; Burda, C.; Sun, W. *Dalton Trans.* **2015**, *44*, 2176.
- ⁷² Martin, R. L. *J. Chem. Phys.* **2003**, *118*, 4775.
- ⁷³ Humphrey, W.; Dalke, A.; Schulten, K. *J. Mol. Graph.* **1996**, *14*, 33.
- ⁷⁴ Frisch, M. J.; Trucks, G. W.; Schlegel, H. B.; Scuseria, G. E.; Robb, M. A.; Cheeseman, J. R.; Scalmani, G.; Barone, V.; Mennucci, B.; Petersson, G. A.; Nakatsuji, H.; Caricato, M.; Li, X.; Hratchian, H. P.; Izmaylov, A. F.; Bloino, J.; Zheng, G.; Sonnenberg, J. L.; Hada, M.; Ehara, M.; Toyota, K.; Fukuda, R.; Hasegawa, J.; Ishida, M.; Nakajima, T.; Honda, Y.; Kitao, O.; Nakai, H.; Vreven, T.; Montgomery Jr, J. A.; Peralta, J. E.; Ogliaro, F.; Bearpark, M. J.; Heyd, J.; Brothers, E. N.; Kudin, K. N.; Staroverov, V. N.; Kobayashi, R.; Normand, J.; Raghavachari, K.; Rendell, A. P.; Burant, J. C.; Iyengar, S. S.; Tomasi, J.; Cossi, M.; Rega, N.; Millam, N. J.; Klene, M.; Knox, J. E.; Cross, J. B.; Bakken, V.; Adamo, C.; Jaramillo, J.; Gomperts, R.; Stratmann, R. E.; Yazyev, O.; Austin, A. J.; Cammi, R.; Pomelli, C.; Ochterski, J. W.; Martin, R. L.; Morokuma, K.; Zakrzewski, V. G.; Voth, G. A.; Salvador, P.; Dannenberg, J. J.; Dapprich, S.; Daniels, A. D.; Farkas, Ö.; Foresman, J. B.; Ortiz, J. V.; Cioslowski, J.; Fox, D. J. *Gaussian 09*, Gaussian, Inc.: Wallingford, CT, USA, **2009**.
- ⁷⁵ Wu, W.; Guo, H.; Wu, W.; Ji, S.; Zhao, J. *J. Org. Chem.* **2011**, *76*, 7056.
- ⁷⁶ Ogilby, P. R.; Foote, C. S. *J. Am. Chem. Soc.* **1983**, *105*, 3423.
- ⁷⁷ O'Brien, J.; Wilson, I.; Orton, T.; Pognan, F. *Eur. J. Biochem.* **2000**, *267*, 5421.

- ⁷⁸ Rosenkranz, A. R.; Schmaldienst, S.; Stuhlmeier, K. M.; Chen, W.; Knapp, W.; Zlabinger, G.
J. J. Immunol. Methods **1992**, *156*, 39.
- ⁷⁹ Daghasanli, N. A.; Itri, R.; Baptista, M. S. *Photochem. Photobiol.* **2008**, *84*, 1238.